Author:
Luke, Emily

Title:
The synthesis of nanostructured functional metal oxides

The Synthesis of Nanostructured Functional Metal Oxides

By

EMILY J. LUKE

School of Chemistry
UNIVERSITY OF BRISTOL

A dissertation submitted to the University of Bristol in accordance with the requirements of the degree of DOCTOR OF PHILOSOPHY in the School of Chemistry

FEBRUARY 2023

Word count: fifty thousand

ABSTRACT

This thesis focused on exploring syntheses of metal oxide ceramic materials, particularly syntheses that resulted in some morphological control of the product material. The aim for Chapter 3 was to design facile syntheses of $Na_3Ni_2BiO_6$, $Na_3Ca_2BiO_6$ and $KBa_6Zn_4Ga_7O_{21}$. These materials were predicted to be superconductive by a machine learning algorithm, so the subsequent analysis of the magnetic properties of these materials was also important to explore. From these experiments, highly pure samples of $Na_3Ni_2BiO_6$ and $Na_3Ca_2BiO_6$ were successfully synthesised *via.* two different solution based approaches. $Na_3Ni_2BiO_6$ was found to be antiferromagnetic with a Nèel temperature of 12 K, whereas $Na_3Ca_2BiO_6$ was found to be weakly paramagnetic. The synthesis of $KBa_6Zn_4Ga_7O_{21}$ was not successfully achieved in this work.

For Chapter 4, the synthesis of 2-dimensional nanostructures was attempted for the superconductor $Bi_2Sr_2CaCu_2O_{8+x}$. This was carried out using a solid-state method which was designed to emulate the microcrucible mechanism of superconductor growth. Additionally, the use of a heating stage on a transmission electron microscope was also carried out, where some optimisation of experimental parameters needed to be carried out, before nanowire growth was observed on cooling of one sample.

Finally, Chapter 5 explores the synthesis of a 3D porous network of high-temperature superconductive sponges, utilising a template based on melamine formaldehyde. Three different synthetic methods were used, from simply combining an aqueous solution of metal nitrate salts with the sponge by itself; to first coating the sponge with a biopolymer prior to the addition of the metal salts; to utilising the Pechini method of synthesis. These techniques resulted in varying success in terms of purity and desired resultant morphology. The porosity of the sponges was measured, as well as the superconductive properties *via.* both resistance measurements and magnetometry.

Covid-19 was declared a global pandemic at the beginning of 2020, which resulted in many restrictions over everyday life. Naturally, this also meant that there were some implications on this project. One impact was an initial 3-month lockdown where no lab work was possible. This was challenging, as much of the work herein relied on practical experiments, and thus the lockdown resulted in an inevitable delay in research. After this, the labs returned to work but with reduced occupancy, which resulted in restricted access to the labs and thus further delays to the project. Additionally, access to characterisation techniques was severely limited during this time, with both X-ray diffraction and electron microscopy becoming services instead of being able to carry them out myself. This lead to slower analysis and characterisation of samples, as well as the inability to interface with my samples directly.

Another unfortunate result of the pandemic was key shortages of chemicals and parts. The SQUID magnetometer at the University of Bristol was out of operation for much of the project due to delays sourcing replacement parts. In general, delivery of chemicals and parts was much slower than would ordinarily be the case. Therefore, more comprehensive testing of materials on the SQUID magnetometer was not fully possible and alternative arrangements were necessary such as the use of the Henry Royce institute towards the end of the project.

Finally, another impact of Covid-19 was the disruption of collaboration between research groups and conferences. There were plans for a trip to to Japan towards the beginning of 2020, to share ideas with a research group there and to work on the iron-based superconductors. This was unfortunately cancelled due to stringent travel restrictions to Japan, which were only lifted in October 2022.

There are so many people whom I have to thank for supporting me during these four years. First and foremost, I want to thank my wonderful supervisor, Professor Simon Hall. Your unfailing enthusiasm for everything has been a source of strength throughout my whole PhD. Thank you for all the 'crazy Friday experiments', the pastoral support and for making day-to-day work fun. It has been a bit of a crazy emotional ride for me through these years, but you've always been there with new ideas and passion to keep me going. To my second supervisor, Dr. Sven Friedemann, thank you for giving up so much of your time to show me how to do resistance and SQUID measurements, and your patient guidance in the way of superconductivity research.

I'd also like to thank the School of Chemistry. In particular, to Dr. Jean-Charles Eloi for your excellent training and advice with the SEM and TEM and for trusting me to run samples by myself. Thank you for running all those nanowire samples for us during the dreaded lockdown times! To Dr. Natalie Pridmore, thank you for all your expertise regarding all things X-ray; I could always go to you with a stupid question, and you'd always try your best to point me in the correct direction. Thank you for running my X-ray samples in the aftermath of the COVID lockdowns. Thank you to my collaborators, Dr. Lui Skytree, Dr. Huan Doan, and Dr. Valeska Ting for all of your hard work on our publication together. I'd like to also extend my thanks to the Henry Royce institute for their assistance with the last few SQUID measurements. I'd also like to thank our collaborators at IIT in Pisa, Dr Mauro Gemmi and Dr Iryna Andrusenko, for offering me advice in many aspects. To my CDT, the BCFN, thank you for the opportunity of doing a PhD and for providing such a groundwork of support throughout my PhD. It was comforting knowing there was somewhere I could turn to with any question. Thank you, Annela, Ian, Joanna, Becky, Jake and Tom, for being so supportive.

To my wonderful research group, Jason, Joe, Vicky, Spayne, Charlie, Wil, Torsten, Chen, Rikesh, Jiawei and Michaela: thank you for the camaraderie and the friendship. You all lit up my days in the office, sharing excellent ideas and always giving much-needed advice. I don't think I would have made it this far without you all. In particular, Jason, thank you for being such a font of knowledge through everything. I could always ask you anything and you'd always be able to answer or help me find it. You have all been a wonderful group to work with, and I wish you all the best in your future endeavours. To the excellent students I got to work with, Hector, Jack, Rowena, Sorrel, Jula, Jaz, Chris and Freddie, thank you for working with me so well, and for bringing your boundless passion to your projects. Along the same vein, I'd like to thank my buddies in physics, Sam, Roemer, Jonathan, for welcoming me over there, abiding by my dumb questions, and showing me how to use all of the instruments again and again.

To my family - Mum, Dad, John, Claire, and Lilia thank you for being there for me throughout it all. I needed all those calls and chats, photos, jokes and gatherings. I think you supplied the majority of my thesis-writing playlist, John! Mum and Dad, thank you for reading my paper

I declare that the work in this dissertation was carried out in accordance with the requirements of the University's Regulations and Code of Practice for Research Degree Programmes and that it has not been submitted for any other academic award. Except where indicated by specific reference in the text, the work is the candidate's own work. Work done in collaboration with, or with the assistance of, others, is indicated as such. Any views expressed in the dissertation are those of the author.

SIGNED: ..█████████.............. DATE: 03/02/2023 ....

INTRODUCTION

M aterials encompass every facet of our lives, from the simple floors upon which we walk to the complex, intelligent computers that govern our daily experience. As a result, materials science is vast and comprises everything from developing new materials to improving those we have used for many years. For the optimum design of a new material, many factors must be considered - from the ease of its synthesis to the processability of the material once it has been made. Additional complexity comes from the fact that the morphology of the material can also drastically affect its properties, leading to the necessity for many factors to be considered when designing novel materials.

1.1   Functional Materials

Functional materials are often defined as materials with native properties that can be exploited and utilised as a material with a purpose. For example, many functional materials possess interesting electronic capabilities, such as piezoelectricity (where mechanical stress yields an electric field within a material).[1] In reality, however, any solid material that has been synthesised for a specific use is a functional material, from electroactive organic polymers to magnetic materials, to superconductors; functional materials are present in many facets of life.[2]

Perhaps one of the greatest inspirations in the design of novel functional materials is the natural world. Biomimetics, also known as biomimicry, is the process in which humans artificially create a system that mimics what is found in nature.[3] Biomimetics have been used in many different aspects of life, creating novel technologies through the replication of biological systems with human-synthesised technologies. A straightforward example of this comes from the material Velcro, where George de Mestrel noticed that his dog was covered in burdock burr after a walk in the alps. He noticed that the burdock burr seeds had tiny hooks on them, which got attached

to his dog's fur and was therefore inspired to create a new fastening system that used this hook-and-loop motif, thus forming Velcro.[4] There are many other examples of biomimicry as well; the Japanese bullet train, the Shinkansen, has a front nose designed after the beak of a kingfisher to reduce air resistance; and polar bear fur has inspired thermal clothing.[5,6]

1.1.1 Ceramic materials

In 1976, Kingery defined a ceramic as 'a non-metallic inorganic solid'.[7] This broad definition means that the study of ceramic materials can encompass many material types, from disordered glasses to highly ordered crystals. Historically, ceramics are some of the oldest materials used by ancient civilisations to form figurines and vases, which are archaeologically significant today. These materials were formed from clay, made of ceramic minerals combined with water. This clay can be formed into many shapes for use in pottery and subsequently 'fired', which leads to the formation of a hard, often brittle material. This processing is similar to what is commonly carried out today, where a powdered material is ground together and fired or calcined, resulting in the formation of the product material.[8] Because of the extensive definition of ceramic materials, they encompass many types of material with numerous applications; metal oxides, inorganic semiconductors and even natural minerals can be defined as a 'ceramic' material. Conventionally, ceramic materials are often considered insulating, hard and brittle. However, it must be remembered that there are usually exceptions to these broad characteristics. For example, stating that all ceramics are insulators is invalid, as there are also semiconductive ceramics. Ceramics are prevalent in daily life, with specialist applications such as lasers, dental implants and potential solar cells, to name a few.[9–11] For the purposes of this thesis, crystalline metal oxide ceramic materials will be the focus.

Metal oxides are widespread materials; many are found naturally as common minerals, such as tenorite (CuO), rutile (TiO_2) and corundum (Al_2O_3).[12] Indeed, noble metals are prized as they do not readily react with oxygen, as this corrosion is often an undesirable and difficult-to-reverse process.[13] For example, the formation of Fe_2O_3, or rust, on the surface of pure iron can be detrimental to its properties, resulting in a brittle layer on its surface and corroding the material.[14] There are numerous potential metal oxide compositions, exploiting an extreme range of elements and compositional order. This wide variety of compositions has enabled metal oxides to exhibit various properties such as piezoelectricity and superconductivity.[15–17]

1.1.2 Crystalline materials

In 1611, Johannes Kepler postulated that the hexagonal structure of snowflakes was due to small spheres of water hexagonally packed together.[18] This was one of the first attempts to define why crystalline matter forms into the shapes they do and our understanding has significantly developed since this case. Considering how spheres pack together to form 3D structures can help visualise how inorganic materials crystallise into 3D structures, and a visual representation of

this is given in Figure 1.1. The ideal way for spheres to pack is in a close-packed arrangement (A). The next layer follows that the spheres pack in the centre of the holes from the previous row (B). The third layer is where a choice can occur; either the spheres can be layered so that they are in an identical position to those on the first layer (A), or they can be packed so that the centre of the spheres are in the holes of the spheres on the row below (C). The material with layers packed as ABAB are known as hexagonal close-packed structures, whereas the material with layers packed as ABCA are known as cubic close-packed structures.
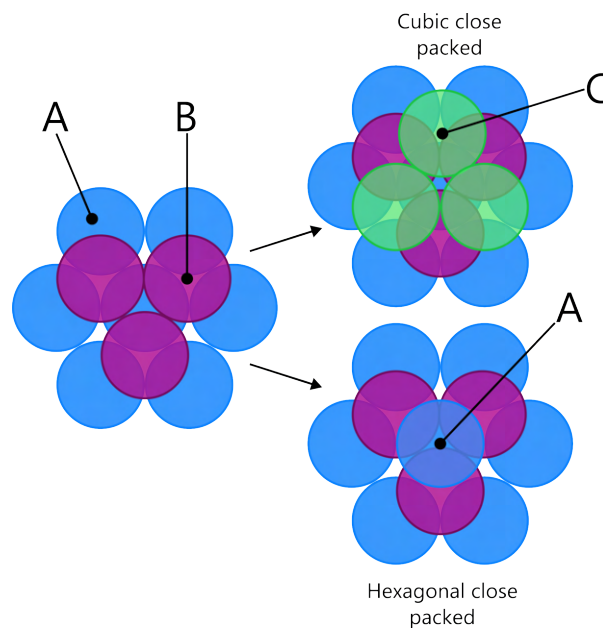
Figure 1.1: Graphical representation of the close packing of spheres into 3D structures.

Crystals are highly ordered materials where atoms or molecules are arranged in a regularly repeating 3D pattern. These ions or molecules can be reduced into single points, known as lattice points, which are extended into a 3D lattice. The smallest repeating unit of this lattice which can be perfectly tessellated in 3D is known as the unit cell. In this way, a crystal is a highly ordered solid with extensive symmetry. There are seven different unit cells which are classified by virtue of their symmetries. This can be further expanded, depending on where the lattice points fall:

- If there are only lattice points on each of the unit cell corners this is known as a primitive unit cell, P.

- If there are lattice points on each unit cell corners, and an additional lattice point in the centre of the unit cell, it is known as body centred, I.

- If there are lattice points on each unit cell corners, and there are additional lattice points on the centre of all the faces of the unit cell, it is known as face-centred, F.
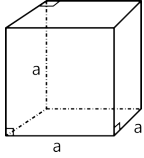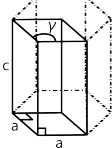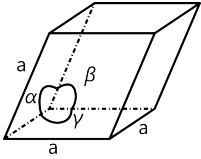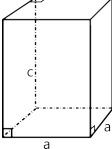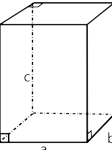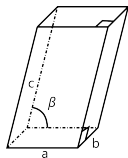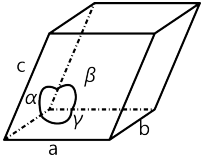
- If there are lattice points on each unit cell corners, and an additional lattice point on the centre of the top and bottom face of the unit cell, it is known as base centred, C.

This gives 14 fundamental unit cell types, known as the Bravais lattices, summarised in table 1.1. Given that the unit cells must stack completely without any excess space between them, generating 32 different point groups of the crystal is possible. Combining this with the 14 Bravais lattices, it is found that there are 230 3D space groups possible for crystals. Space groups can be used to quantify what lattice points there are in a crystalline material, and incorporates the symmetry of these lattice points when built up into a 3D structure.[19]

Crystals with the same chemical formula can sometimes also crystallise in different space groups or lattice types. This is known as polymorphism and is found in many different materials.[20] One such example is calcium carbonate, which can crystallise as one of three polymorphs in nature; calcite, which crystallises as a trigonal lattice; aragonite, which crystallises as an orthorhombic lattice; and vaterite, which crystallises as a hexagonal lattice. These polymorphs exhibit different physical properties, and indeed both aragonite and vaterite will transform into calcite in specific conditions by virtue of the increased stability of calcite.[21,22] A change in polymorph can alter many key properties of a crystal, such as solubility, colour and conductivity.[23,24] This is especially pertinent to consider when examining potential candidates of pharmaceutical ingredients, as a poorer solubility may mean that the ingredient would not be uptaken by the body and thus reduce the efficacy of the drug.[25] Ostwald postulated that unstable polymorphs are likely to form first when there is a competition between two forms crystallising from a melt, which has since been titled Ostwald's step rule.[26] This general rule originates from the postulation that the less stable phases are more likely to be closer in energy to the energy of the solution; therefore upon crystallisation, this is the phase that forms first. This proceeds with transformations to progressively more stable polymorphs until the most stable polymorph is reached.[27] Control of polymorph has previously been achieved through various methods, such as through applying high pressures, magnetic fields, or altering solvents of crystallisation.[28–30] Manipulation of which polymorph forms is can be important for tailoring the physical properties of a material, and can therefore be an important variable to consider when designing novel crystalline materials.

Often, substitution of one or more elements with another in a crystalline material can still result in the formation of the same polymorph, forming entire families of material with the same crystal structure. In these cases, the crystal structure usually becomes known by a specific name, often derived from the original mineral with this crystal structure. This is the case for some technologically significant crystal structures such as delafossites and perovskites.

Table 1.1: The seven different crystal systems, along with the possible lattice types for those crystal systems.

Crystal system	Cell lengths	Cell angles	Diagram	Lattice types
Cubic	$a = b = c$	$\alpha = \beta = \gamma = 90°$		P, I, F
Hexagonal	$a = b \neq c$	$\alpha = \beta = 90°, \gamma = 120°$		P
Trigonal	$a = b = c$	$\alpha = \beta = \gamma \neq 90°$		P
Tetragonal	$a = b \neq c$	$\alpha = \beta = \gamma = 90°$		P, I
Orthorhombic	$a \neq b \neq c$	$\alpha = \beta = \gamma = 90°$		P, I, F, C
Monoclinic	$a \neq b \neq c$	$\alpha = \gamma = 90°, \beta \neq 90°$		P, C
Triclinic	$a \neq b \neq c$	$\alpha \neq \beta \neq \gamma \neq 90°$		P

1.1.2.1 Perovskites

Perovskites are metal oxides that are isostructural to the mineral perovskite, $CaTiO_3$ - a mineral discovered in 1839 by Gustav Rose.[31] These ABO_3 crystal structures consist of six-coordinate B octahedra and twelve-coordinate A ions in the centre (Figure 1.2). The ideal perovskite structure consists of a cubic unit cell but depending on the relative sizes of the cations, there can be some strain in the structure which results in the twisting of the octahedra, displacement of the A ions,

or distortions in the octahedra and thus yielding different space groups.[32,33] This strain can result in exciting properties, such as with $BaTiO_3$ which owes its ferroelectricity and piezoelectricity to the slight strain found within the structure in several of its polymorphs.[34] Whether a material is able to crystallise as a perovskite structure can be calculated using the Goldschmidt tolerance factor. This tolerance factor attempts to quantify the level of structural strain that will form based on the relative sizes of the ions within the structure.[35] While it was initially just used for perovskite structures, additions to the Goldschmidt tolerance factor have been included to enable quantification of strain in other structures, such as the ilmenite structure and other metal oxide structures.[35,36] Perovskites exhibit many properties and have been explored for applications in laser materials and photovoltaic materials. Additionally, several high-temperature superconductors exhibit perovskite-like structures, as will be discussed in Section 1.2.2.1.[37] Recent research into perovskites has also examined the potential of perovskite nanomaterials, such as nanostructured perovskite solar cells and high-temperature superconductors.[38,39]
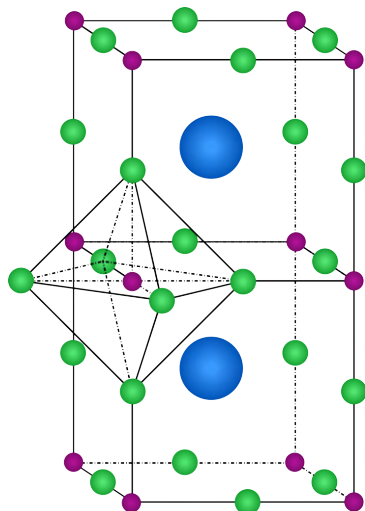
Figure 1.2: A depiction of a perovskite unit cell, for example $CaTiO_3$, where the blue atom represents calcium, the pink atoms represent titanium and the green atoms represent oxygen. To enable visualisation of the BO_6 octahedra formed, two unit cells have been illustrated with an octahedron shown.

1.1.3 Nanomaterials

A nanomaterial exhibits features on the order of a nanoscale, which means that it consists of features with sizes on the order 1×10^{-9} nm.[40] Confining a material's dimensions to the nanoscale can yield interesting phenomena due to quantum effects due in part to this being a point where quantum phenomena transition to macroscopic phenomena.[41] This enables access to several strange phenomena, such as the interesting optical properties of quantum dots, which occur due to their size.[42] Additionally, the use of nanoparticles of gold have been used historically to create red-coloured glasses, often with colour-shifting properties.[43] A further consequence of the

nanoscale is that the ratio of atoms on a nanomaterial's surface compared to the bulk is much larger than in ordinary macroscopic materials. This has consequences for the reactivity of these particles, as well as the trade-off between maximising the lattice enthalpy and simultaneously minimising the surface energy of the particles.[19]

Nanomaterials are extremely prevalent in nature, where they often exhibit phenomena that directly result from their nanostructures. For example, the nanotextured surface of lotus leaves is responsible for their super-hydrophobicity, and the nanostructures that cover the wings of a morpho butterfly result in its beautiful blue iridescent colour.[44,45] In a similar vein, the arrangement of silica microspheres in a hexagonal close-packed array results in the striking 'play of light' of opals.[46] This 'play of light' is the result of the formation of a 3D photonic crystal from the change in the dielectric constant or refractive index of the material in all three key directions, which leads to the direction-dependant propagation of light within the crystal.[47] Photonic crystals such as opals (or indeed inverse-opals, where the voids between spheres are filled and then the spheres removed) are being actively researched for various applications, such as photocatalytic applications or in display technology.[47,48]

The nanostructure of a material is essential to consider for various reasons; a type of nanostructured steel has enabled the manufacture of extremely strong steel with potential applications in railway infrastructure; and semiconducting nanoparticles have potential in photocatalysis.[49,50] Magnetic nanomaterials have also gained interest for drug delivery and water treatment applications. Additionally, the unique effect of confining magnetic behaviour to the nanoscale can give rise to new magnetic phenomena such as superparamagnetism.[51]

1.1.4 Magnetic materials

All materials react to a magnetic field in some way, but the direction and magnitude of this reaction partitions them into various types. All materials exhibit diamagnetism, which is the weakest of the magnetic states. When paired electrons are exposed to a magnetic field, a current is produced which opposes the applied field; therefore, a diamagnetic material is repelled by a magnetic field.[1] Paramagnetism is expressed when a material consists of unpaired electrons. These unpaired electrons lead to an attraction to an applied magnetic field. This interaction is much stronger than the natural repulsion from diamagnetism, and is often called Curie-Weiss paramagnetism. At higher temperatures, the spins exist in a disordered state and are orientated randomly, which is known as a paramagnet. Paramagnetism is temperature dependant and follows the Curie Weiss law, equation 1.1.[52] A ferromagnetic material is similar to a paramagnetic material, consisting of unpaired electrons. However, a ferromagnetic material can also condense into a lower energy state where these spins are all aligned in the same direction due to spin-exchange interactions. This means that the spins for these materials are already aligned, even in the absence of an external field, such that a ferromagnetic material has a residual magnetic moment.[19] Ferromagnets exhibit an ordering temperature known as the Curie Temperature,

T_C, above which thermal fluctuations overcome the spin-exchange interaction, thus yielding a paramagnet. Finally, another type of magnetic ordering is that of an antiferromagnetic material. The spin-exchange interactions in these materials are such that they naturally align so that adjacent spins are in opposite directions. This means that there is no net magnetic moment to an antiferromagnetic material. Antiferromagnets exhibit a characteristic ordering temperature known as the Néel temperature, T_N. Similarly to ferromagnets, above T_N, thermal fluctuations overcome the spin ordering, resulting in paramagnets with no long-range order. [53]

$$(1.1) \qquad\qquad \chi - \chi_0 = \frac{C}{T - \theta_{CW}}$$

The behaviour of a material within a magnetic field is known as its susceptibility, χ, where the sign of the susceptibility indicates whether it is attracted to (positive) or repelled by (negative) a magnetic field. The equation for volume susceptibility is given in equation 1.2, where M is the magnetisation of a material, ρ is its density, m is its mass and H is the applied magnetic field. [52]

$$(1.2) \qquad\qquad \chi = \frac{M\rho}{mH}$$

Depending on the type of magnetic material, there are common features observed on a plot of magnetic susceptibility against temperature; a paramagnetic material will exhibit a gradual increase of susceptibility as the temperature tends towards zero, a ferromagnetic material will exhibit a rapid increase of susceptibility at a specific temperature, the Curie temperature, and an antiferromagnetic material exhibits a peak in magnetic susceptibility at the Néel temperature. [52] These plots can be used to further characterise the material with equation 1.1, known as the Curie Weiss equation. In this case, χ is the magnetic susceptibility, χ_0 is a correction factor that can compensate for extraneous factors from the measurement, C is the Curie constant and θ_{CW} is the Curie-Weiss temperature.

1.1.4.1 Frustrated antiferromagnetism

When placing atoms or ions with unpaired electrons onto a net, the shape of the net is also important to consider for its properties. When these atoms or ions are placed onto a square net, the spins can be placed in such an arrangement to result in net zero total spin, with two spin-up atoms/ions and two spin-down atoms/ions. However, when placing spins onto a triangular net, the direction of the third spin to be placed is not facile to consider, as both spin-up or spin-down are valid options for the orientation of the last atom (denoted by the question mark in Figure 1.3). This ambiguity leads to so-called geometric frustration in the lattice and many possible degenerate ground states of spin orientation. These materials are therefore called 'frustrated antiferromagnets' and often exhibit low T_N. [54] Frustrated magnetism has been demonstrated in many different material morphologies, such as in Kagome lattices. [55] It is also important to note

that there are also possible sources of magnetic frustration, such as local-site disorder, found in spin glasses.[54]
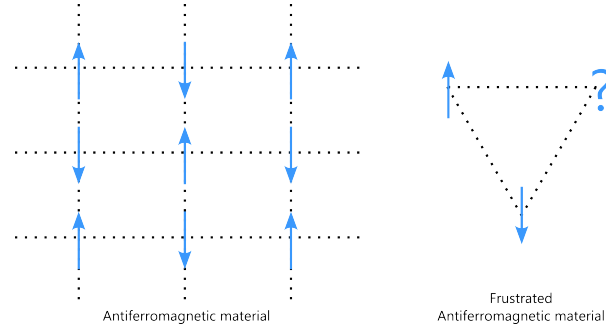
Figure 1.3: Representation of spin-active atoms placed on a net in an antiferromagnetic system and in a frustrated antiferromagnetic system.

1.2 Superconductivity

In 1908, Heike Kamerlingh Onnes liquified helium for the first time. This unlocked many new opportunities in cold-temperature research and allowed Onnes to begin investigations into conductivity at these temperatures.[56] At the time, there was much debate as to what would happen to the resistivity of metals as temperatures tended towards zero. Some theorists believed that the electrons would become 'frozen in place', leading to the resistivity tending towards infinity as temperatures decreased. In reality, the result was far stranger: in 1911, Onnes observed a sharp drop in the resistance of mercury at 4.2 K to below measurable values. Onnes later named this phenomenon 'superconductivity'.[57,58] It has since been determined that two important phenomena can characterise superconductivity: the lack of D.C. resistance and the complete expulsion of an external magnetic field. The latter effect is known as the Meissner effect and was first observed in 1933 by Meissner and Ochsenfeld.[59] Both effects occur below a specific temperature, known as the critical temperature (T_c). In the more than hundred years since their discovery, superconductors have been responsible for several Nobel Prizes, including one that was awarded in a record time of only a year after the initial discovery.[58] It has since been found that superconductivity is not a rare event - in fact, many materials can superconduct. Key developments in the timeline of superconductivity include: the discovery that superconductors exclude all magnetic flux from within them in 1933, the development of a theory of superconductivity in 1950, the discovery of high-temperature superconductivity in cuprate oxides in 1986, and the discovery of superconductivity in H_2S at high pressures in 2015.[17,59–61] A graph depicting the T_c of some key superconductive materials against the date they were discovered is given in Figure 1.4.
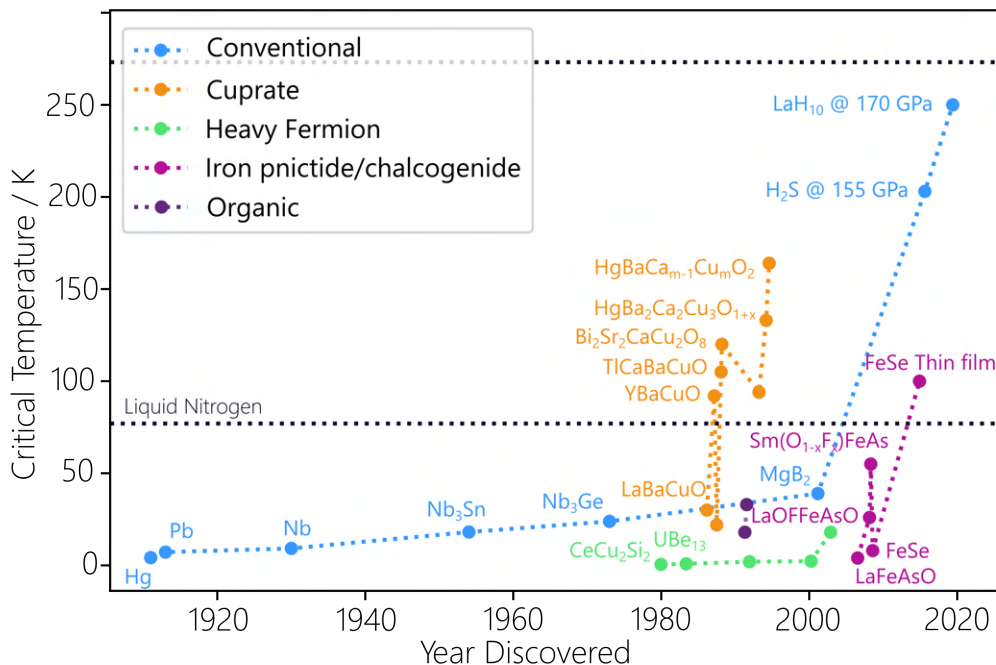
Figure 1.4: Graph showing some key discoveries of superconductors over time with their critical temperatures. Information for each datapoint are given in Appendix A.1.

1.2.1 Characteristics of superconductivity

As mentioned in Section 1.2, for a superconductor to be classified as such, it must exhibit two features: the disappearance of observable D.C. resistance below a specific temperature known as the critical temperature, T_c; and the exclusion of all magnetic flux from within the superconductive material, which is known as the Meissner effect. The way superconductors behave under an applied magnetic field partitions them further into two different types: type-I and type-II. Type-I superconductors are characterised by having a critical magnetic field strength, H_c. If a type-I superconductor is subject to a stronger field than its critical field its superconductivity is quenched. Type-II superconductors have an upper critical field, H_{c2}, and a lower critical field, H_{c1}. Between H_{c1} and H_{c2}, the material enters a mixed superconducting state where the magnetic field penetrates the superconductor at discrete points, forming tubes that are not superconducting among the bulk superconductor. The supercurrent flows around these tubes, causing a vortex of current around these centres, thus resulting in so-called flux vortices. This phenomenon provides the basis for something known as 'flux pinning', which enables the levitation of a superconductor over a magnet (or magnet over a type-II superconductor). As the applied field approaches the upper field limit, H_{c2}, these flux vortices grow in size and eventually grow to encompass the whole of the superconductor thus leading to the destruction of

the superconductivity in the material.[62]

1.2.1.1 BCS Theory of Superconductivity

The emergence of the Meissner effect for these superconductive materials indicated some form of correlated movement of electrons in superconductors.[63] This created some difficulty in understanding the material, as it indicated that the electrons must have condensed into a state where it was not forbidden for them to exist within the same electronic energy state as each other. Due to their non-integer value of spin, electrons follow Fermi-Dirac statistics and thus the Pauli Exclusion principle. Leon Cooper proposed that these materials condense into a paired state, yielding an integer value of spin and thus allowing the electron pairs (known as Cooper pairs) to condense into Boson quasiparticles.[62] Another clue to the mechanism of superconductivity was the isotope effect - it was discovered that the critical temperature was inversely proportional to the square root of the isotopic mass. It was proposed, therefore, that superconductivity was related to the vibrational frequencies of the lattice.[60,64] It was from these initial observations that the Bardeen-Cooper-Schrieffer Theory (BCS-theory) theory of superconductivity was developed.

BCS-theory theory was originally proposed in 1957 by John Bardeen, Leon Cooper and Robert Schrieffer.[65] It remains the most universally accepted theory behind the mechanism of superconductivity and resulted in all three authors being awarded the Nobel Prize in 1972.[66] BCS-theory theory shows that there is an inherent attractive force between electrons in a metal. This attractive force arises indirectly as a result of phonon interactions. A phonon is a lattice vibration which behaves somewhat like a particle and is thus a quasiparticle. As an electron travels through a metal, it distorts the cations around it, resulting in a pocket of positive charge around it. A second electron will then be attracted to this pocket of positive charge, thus resulting in an indirect attraction between the two electrons (Figure 1.5). This attractive force is relatively small, so the pairing between electrons can be disturbed by the phonons from thermal motion. When the temperature drops low enough that the thermal motion of the atoms is smaller than the attractive force between the electrons, they will condense into a paired state or macroscopic wave function.[62] This pair of electrons will thus be able to conduct electricity without resistance, as the attraction between them will prevent them from being scattered by lattice vibrations and collisions. Equation 1.3, developed by Bardeen *et al.*, shows how the T_c is related to the Debye temperature θ_D, the electron density of states at E_F, $N(0)$, and the electron-phonon coupling constant, V.[65] Therefore, to maximise T_c, it is necessary to maximise the parameters in this equation. However, the three parameters are not independent of each other, and thus by maximising one, another will be minimised.[37] From this, it can be extrapolated that the maximum T_c for electron-phonon mediated superconductivity is around 30 K due to the trade-off between the electron-phonon coupling constant, V, and the Debye temperature, θ_D.[67]

$$(1.3) \qquad\qquad T_c = \theta_D \quad \exp\left[\frac{-1}{N(0)V}\right]$$
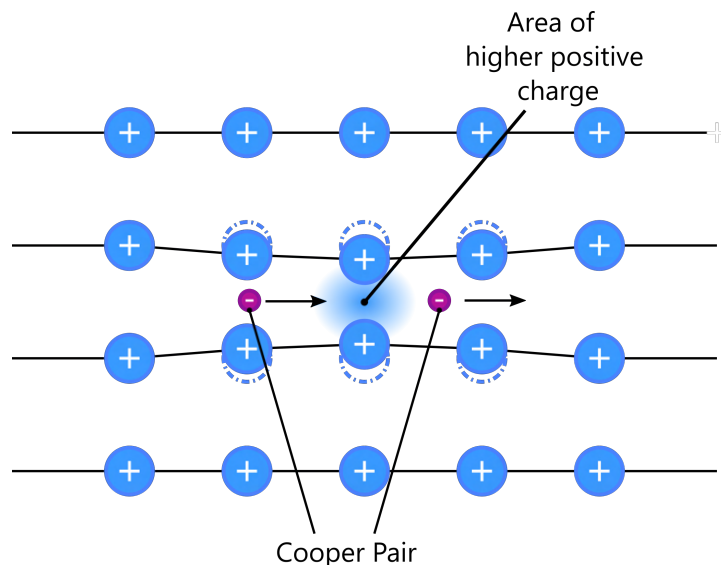
Figure 1.5: A representation of the source of the attractive force between electrons. When an electron passes through the lattice, it distorts the lattice, creating an area with a slight positive charge, thus yielding a slight attractive force between the electrons.

The other important variable that arises from considering Cooper pairs and BCS-theory theory is that of the coherence length, ξ. The coherence length represents the Cooper pair's size, and its size differs depending on the superconductor.[68] Therefore, it is necessary to consider the coherence length when designing superconductive materials. For example, a coherence length smaller than the size of a grain boundary would necessitate a highly pure crystal of a superconductor without grain boundaries to lead to a material that can carry the supercurrent.

BCS-theory does not apply to all known superconductors, and superconductors to which this theory does not apply shall be referred to as unconventional superconductors in this thesis. What makes these materials 'unconventional' is that the pairing of the superconductive electrons does not come from the electron-phonon interactions, but some other interaction entirely.[69] In fact, several different types of unconventional superconductors are classified by their proposed mechanisms, such as heavy fermion superconductors, which superconduct due to heavily correlated 4f electrons within their structure.

1.2.1.2 The Josephson Effect

In normal metallic materials, there is a phenomenon known as quantum-mechanical tunnelling, where an electron can cross an insulating gap, or classically forbidden region, between two conductive materials. This is because there is a non-zero probability that the electron can exist across this barrier due to an overlap of the wavefunction of the electron beyond the classically forbidden region.[70] This phenomenon has been successfully exploited in several applications such as Scanning Tunnelling Microscopy. In this case, an atomically thin tip is rastered across the

surface of a material without touching it. The current for the material can be monitored, as the tunnelling probability is a function of the distance between the gap.[71] This type of phenomenon is also possible with superconductive materials and manifests as the Josephson effect.

As the Cooper pairs approach a non-superconducting region or so-called 'weak-link', there is a non-zero probability that these Cooper pairs can tunnel across the gap, thus crossing the non-superconducting barrier.[62] These superconducting-nonsuperconducting-superconducting junctions are known as a Josephson-junction (JJ), named after Brian D. Josephson who predicted them in 1962.[72] The phenomenon of superconducting pairs of electrons tunnelling across the gap is known as the Josephson Effect. This gap is called often called a 'weak link'. The gap size traversable by the Cooper pairs is related directly to the coherence length of the superconductor - the shorter the coherence length, the smaller the gap has to be in order for the electrons to be able to tunnel across the gap.

There is also another important consequence of the Josephson effect, which occurs if a potential difference is applied across the JJ. In this case, the phase difference between the wavefunctions of the two superconductive sections gains a dependency with time. This results in an alternating current (A.C.) across the gap, which means that JJs are able to behave as perfect voltage-to-frequency converters.[73] The frequency of this radiation is related to the potential difference that is applied to the gap.[62]

JJ are essential in many applications of superconductors, such as in devices which can generate electromagnetic (EM) radiation (discussed in more detail in Section 4.1.2.1) and in SQUID which will be discussed in more detail in Section 1.4.3.

1.2.2 Cuprate superconductors

By the early 1980s, several superconductive materials had been discovered - generally in elemental or metallic materials. It was at this time that experimental physicist Bernd T. Matthias determined several empirical rules for discovering novel superconducting materials, such as avoiding highly oxygenated species, magnetic materials and insulating materials; while ensuring that the materials exhibit high symmetry.[74] For most superconductors discovered at the time, these rules were excellent guidelines - after all, the magnetic elements copper and iron do not exhibit any superconductivity. However, in 1986, Bednorz and Müller discovered superconductivity at 30 K in a copper-based compound, La-Ba-Cu-O (LaBCO).[17] This was an extremely exciting discovery at the time, as metallicity was thought to be required for superconductivity, yet the LaBCO compound was not only an insulator at room temperature, but its T_c was a record at the time at 30 K. This compound appeared to disobey many of Matthias' rules and spurred a new frenzy of experimentation.[37] Many new superconductors based on these cuprate materials were discovered in a short time. Cuprate superconductors are unconventional; thus, the mechanism behind the superconductivity is not yet fully understood.[69] However, it is known that the CuO_2-planes present in the crystal structure of these materials are where superconductivity

is facilitated.[75] All cuprate superconductors exhibit these layered structures with copper-oxygen planes and follow the same phase diagram with regard to hole or electron doping (shown in Figure 1.6). LaBCO is a double-layered perovskite structure with an orthorhombic unit cell. If the La ion within the structure is replaced with a rare-earth element, other superconductors can be synthesised. These are known as Rare Earth-Ba-Cu-O (ReBCO) superconductors.

The cuprate superconductors are sometimes nicknamed 'high-temperature superconductors' because of their high T_cs and were the first superconductive materials to exhibit T_cs that were achievable through cooling with liquid nitrogen. After the discovery of La-Ba-Cu-O with its T_c of 30 K, Y-Ba-Cu-O was discovered the following year and had an incredible T_c of 92 K.[76] This was technologically significant, as it was the first time the superconductive state was accessible by cooling with liquid nitrogen, a much more readily available cryogen than the previously used liquid helium. This advantage is especially pertinent in modern times, where helium supply and prices can be a potential snagging point in many research cases.[77] Cuprate superconductors with steadily increasing T_cs have since been discovered, culminating with the highest T_c for a cuprate superconductor of 134 K in Hg-Ba-Ca-Cu-O, which increases to 153 K when under 150 kbar of pressure.[78,79]

Cuprate superconductors are not superconductive in their parent state but rather must be electron or hole-doped to yield a superconductive transition. They exhibit a so-called "superconducting-dome" in their phase diagram (Figure 1.6), where there is a level of doping which is optimum, beyond which the T_c begins to fall. They are officially classified as Mott insulators, which are materials that should be conductive based on band theory but are insulating in reality due to electron-electron repulsion within the material.[80] An example of hole doping can be found with the La^{3+} ion in parent compound La_2CuO_4, which can be substituted with Sr^{+2} to form the compound $La_{2-x}Sr_xCuO_4$. A general phase diagram for cuprate superconductors can be found in figure 1.6. As can be seen, a wider range of dopant concentrations yields a superconductive phase in the hole-doped superconductors than in the electron-doped superconductors. Hole-doped superconductors have a range of different dopant concentrations that yield superconductivity, with an optimum dopant concentration that yields the maximum possible T_c for that material. Below this concentration, the superconductor is termed 'underdoped'; above they are termed 'overdoped'.

1.2.2.1 The ReBCO family

This family of superconductors all have a similar double layered perovskite-like crystal structure with an orthorhombic crystal lattice. LaBCO and YBCO are both members of this family. Indeed, La can be substituted for any rare-Earth element to result in a superconductive material, with the exception of Ce and Tb.[81] Despite initial observations of no superconductivity in Pr-Ba-Cu-O, it has since been found to be superconductive.[82] Of these ReBCO superconductors, one of the most
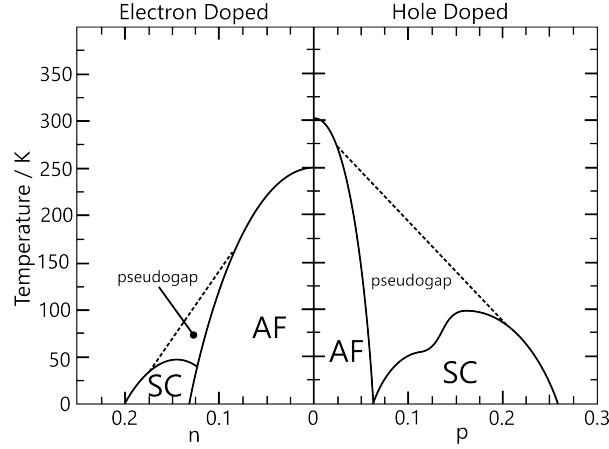
Figure 1.6: The phase diagram of the cuprate superconductors. To the left is the electron doped regime, with an antiferromagnetic (AF) section and a superconductive (SC). Similarly in the hole-doped regime, there is a 'superconductive dome' and an antiferromagnetic section.

prevalent in terms of applications is $YBa_2Cu_3O_{7-\delta}$. This phase is responsible for the observation of the T_c of 93 K observed by Wu *et al.* in 1987.[76] Materials in the YBCO family are often referred to by Y-abc, where a, b and c represent the stoichiometry of the yttrium, barium and copper, respectively. Some important YBCO phases presented within this thesis are given in Table 1.2. The phases consist of different reported T_cs, from exhibiting no superconductivity to the reported T_c of 93 K in Y-123. The structure of Y-123 is presented in Figure 1.7. The level of oxygen doping in Y-123 is important in tuning the T_c and ensuring a sharp transition. Additionally, when $\delta > 0.5$, an alternative crystal structure forms of tetragonal symmetry, which exhibits no superconductivity.[83] A notable phase of YBCO is Y-211, which is not superconductive and is often nicknamed the 'green phase' of YBCO by virtue of its green colour.[84] Y-211 can be converted to Y-123 through a peritectic melt reaction, which has been used to synthesise sponge-like structures of Y-123 previously.[85]

Table 1.2: Four significant stoichiometries of YBCO and their associated T_c. Data obtained from references 76 and 84.

Phase	Abbreviation	Critical Temperature / K
$YBa_2Cu_3O_{7-\delta}$	Y-123	92
$YBa_2Cu_4O_y$	Y-124	81
$Y_2Ba_4Cu_7O_y$	Y-247	94
Y_2BaCuO_5	Y-211	None

Figure 1.7 gives the structure of Y-123, where the 2-dimensional (2D) CuO_2 planes can be seen along the *a-b* axis. Y-123 can exhibit some problems due to its short coherence length of $\backsim 2$ nm along the *a-b*-axis, often resulting in the destruction of superconductivity at grain boundaries.[86] In an attempt to avoid this, thin films of Y-123 are grown epitaxially on a highly

15
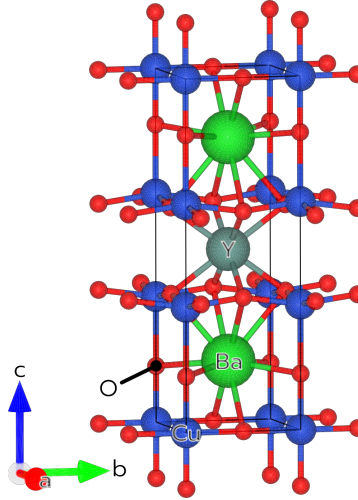
Figure 1.7: Crystal structure of Y-123, with teal, green, blue and red representing yttrium, barium, copper and oxygen respectively.

aligned nickel substrate separated by some other buffer layers.[68] Additionally, Y-123 is a brittle ceramic, meaning that it cannot be drawn into flexible wires for its applications. Processing Y-123 and other ReBCO superconductors are, therefore, difficult and a limitation for their applicability. More recently, new methods have been developed to synthesise tapes with high-current density capability, with the view to utilise them in fusion generators.[87]

1.2.2.2 The BSCCO family

The BSCCO family of superconductors are another cuprate superconducting family with interesting technological and historical significance. This family consists of three members with the formula $Bi_2Sr_2Ca_{n-1}Cu_nO_{2n+4}$, where n = 1, 2 or 3. These materials are often referred to as Bi-abcd, where a b c and d represent the stoichiometric amount of Bi, Sr, Ca, and Cu respectively. The first of this family discovered was Bi-2201, but its discovery did not garner much attention at the time due to the low T_c of only 10 K.[37,88] It was not until 1988 that this family became a subject of substantial research interest, as the high T_c of 105 K was coupled with the fact that the material didn't contain any rare-earth elements - which was interesting at the time.[89] The three different stoichiometries exhibit different characteristic T_c, where Bi-2201 is 22 K, Bi-2212 is 85 K and Bi-2223 is 110 K.[37] The crystal structures of these phases are presented in Figure 1.8

As mentioned, Bi-2201 was the first superconductor of this family to be discovered. However, further research into this phase determined that it was a complex material and exhibited an incommensurately modulated crystal structure. Indeed, all of the phases in the BSCCO family exhibit similar uncertainties in the crystal structure, which has been attributed to a lattice mismatch between the double Bi_2O_2 rock salt layers, and the $SrO-CuO_2-SrO$ perovskite layers.[90] In the case of Bi-2201, it has been found that there are several polymorphs and a complex phase
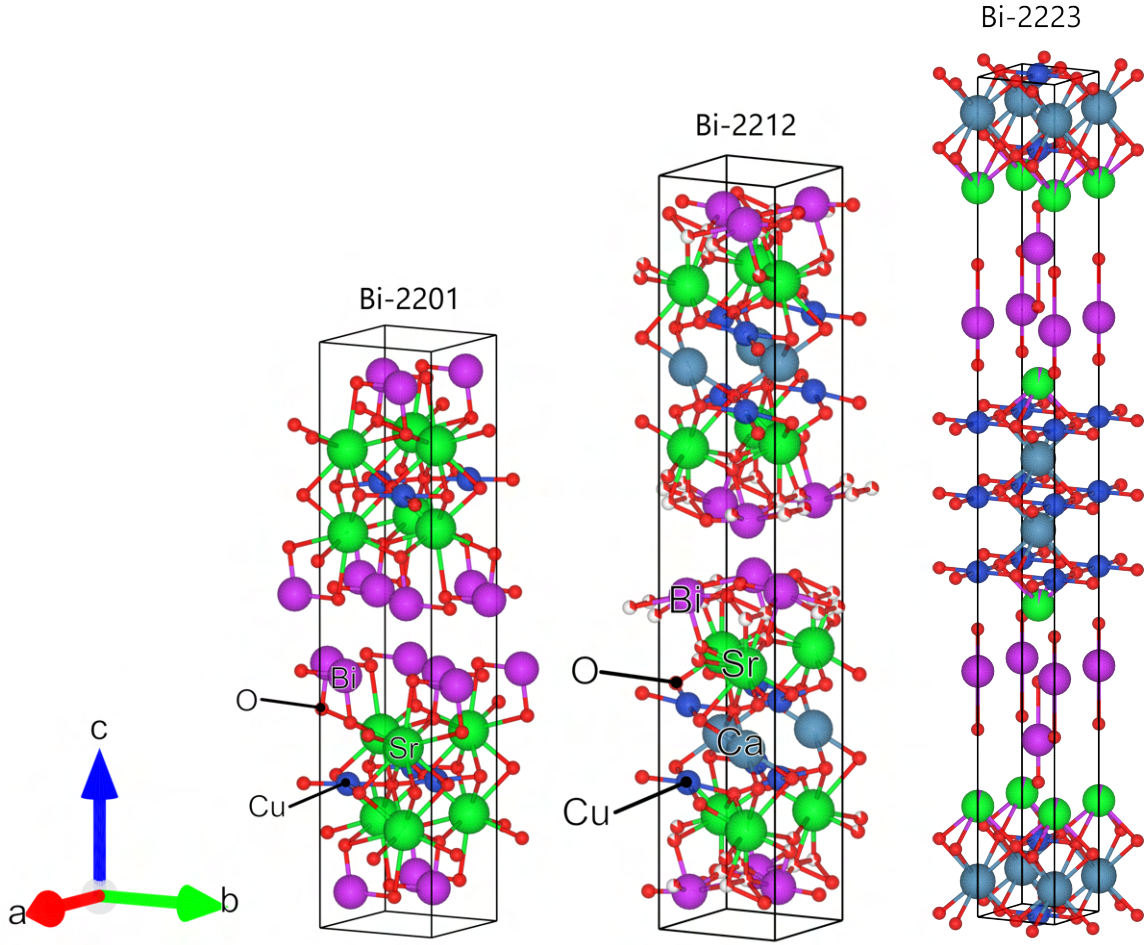
Figure 1.8: Crystal structure of Bi-2201 (left) and Bi-2212, with purple, green, grey, blue and red representing bismuth, strontium, calcium, copper and oxygen respectively.

Table 1.3: Table with the four main stoichiometries of BSCCO and their associated T_c. Abbreviations are how these phases will be referred to in this thesis. Data obtained from references 88 and 89.

Phase	Abbreviation	Critical Temperature / K
$Bi_2Sr_2CuO_6$	Bi-2201	22
$Bi_2Sr_2CaCu_2O_{8+x}$	Bi-2212	85
$Bi_2Sr_2Ca_3Cu_4O_{10+x}$	Bi-2223	110

diagram for its synthesis. In particular, the superconducting phase with orthorhombic symmetry was found to be in competition with a non-superconducting phase with monoclinic symmetry. The monoclinic phase was first reported by Bendersky *et al.*, but the crystal structure of this phase was unable to be fully resolved due to the aforementioned incommensurate structure.[91] The crystal structure to this monoclinic phase was finally resolved in 1993, and it was found that

there was a periodic crystallographic shear plane in the structure, which resulted in there being a β angle different to 90°, leading to a monoclinic crystal phase.[92]

The T_c of Bi-2212 being so close to the boiling point of liquid nitrogen somewhat limits its applications concerning using nitrogen as a cooling agent. However, despite this, it has garnered much research attention.[68] It has the potential to be a terahertz emitter due to its unique crystal structure, which will be discussed in more detail in Section 4.1.2.1. Additionally, Bi-2212 is much easier to synthesise than the other member of the BSCCO family, $Bi_2Sr_2Ca_2Cu_3O_{10+x}$ (Bi-2223). As well as this, Bi-2212 can be drawn into wires with a circular cross-section instead of tapes, which makes their use in magnets much more desirable, as the cross-section of the wire is uniform in all directions.[68]

1.2.3 Applications of superconductivity

The most common applications of superconductivity are as strong permanent magnets.[93] As a coil of normal wire generates a magnetic field, so too does a superconductive coil. Once a current is established within a superconductive coil, the magnet will remain at full field as long as the superconductive state is maintained without losing energy through resistance. In contrast, the equivalent magnet from a copper coil would need to be actively cooled to ensure that the magnet does not overheat, and power would need to be maintained throughout the copper coil.[62] Perhaps the most influential use of permanent superconducting magnets is in MRI or NMR imaging.[57] This has revolutionised both medical imaging and chemical analysis since its inception. Superconducting cables are also used in the Large Hadron Collider to generate strong magnetic fields.[94] Another specialist device that exploits superconductivity is the SQUID magnetometer. These devices exploit the Josephson Effect to measure magnetic fields precisely. They can be used to determine the magnetic nature of materials as a function of temperature. As such, these devices can determine if a substance is superconductive, paramagnetic, or antiferromagnetic.[95] There is also research on various other superconductors applications, such as their use in quantum computers or as terahertz emitters.[96,97]

Due to their ability to conduct electricity without resistance, superconductors could positively impact the environment. A report in 2021 estimated that the power lost through transformers and transmission in powerlines was about 10 %.[98] While this is a small percentage, when considered in the context of the amount of energy transported daily, it is a large day-to-day loss of power as heat. To conduct electricity without resistance would eliminate this. Of course, there are implications of the amount of cryogen required to cool these powerlines, and there are also practical limitations of the cuprate superconductors that mean that superconducting powerlines worldwide are yet to be realised. In 2012, a project in Essen, Germany, began named AmpaCity.[99] This project utilised 1 km of cryogenically-cooled superconducting cables to supply energy between two power stations. The company Nexans made the power cables, and were reported in 2018 to have continued to work successfully throughout the experiment.[100,101] More recently, the

potential of using gaseous helium to cool superconducting cables has been examined.[102]

1.3 Synthesis of solid materials

1.3.1 Solid-state syntheses

Solid-state reactions have been utilised since the first examples of ceramics and pottery, though the first scientifically documented alloying reactions between metals was in 1820.[103] The first syntheses of the cuprate superconductors were through solid-state methods, where they were synthesised *via* a coprecipitation and subsequent annealing method.[17] The synthesis of nano-materials through solid state reactions is also possible, with the advent of techniques such as mechanochemistry, spray pyrolysis and molten salt syntheses.[104–106]

The solid-state synthesis method is a highly robust method to synthesise crystalline and ceramic materials. Often named 'the ceramic method', this technique consists of combining solid precursors, often metal oxides or metal carbonates, grinding, pressing into pellets and subsequent calcination in a furnace.[19] Solid-state reactions are inherently limited by the fact that solids are slow to react with each other. Due to this slow mass transport, the resulting particles are often made from a core of starting material combined with an outer shell of the product material. As a result, these synthesis methods usually require additional grinding and heating steps to mitigate this effect and ensure the reaction proceeds to completion. However, some methods can be used to overcome these diffusion pathway limitations by reducing the particle size of the precursors.

1.3.1.1 The use of flux

In an attempt to overcome common shortcomings of conventional solid-state syntheses, much consideration has gone into finding methods to emulate the solution state for the solid synthesis. One such potential method is flux-mediated syntheses, also known as molten salt syntheses.[107] These synthetic techniques use inorganic salts with high melting points to solubilise the precursor material, thus providing a solution phase within which reactions can occur, and product material crystallise. The molten salts used in these reactions often exhibit relatively low melting points compared to typical inorganic materials, or consist of mixes of inorganic salts which form lower melting point eutectic solutions.[108] The flux behaves as a catalyst; becoming a solvent for the reaction to proceed through without participating in the reaction. Therefore, the flux must be carefully considered to ensure no by-products or undesirable phases are formed. Molten salt syntheses can yield products with a controlled particle morphology. It is often the case that heating the product for longer results in Ostwald ripening of the product material, thus yielding larger crystals of the target phase.[107] There are also examples of utilising a flux which evaporates during the synthesis, depositing crystals of the target phase at the end. This is the case for a common method of synthesising synthetic rubies, where Al_2O_3 and a chromium dopant

are dissolved in MoO_3, which eventually evaporates and deposits larger crystals of synthetic rubies.[109]

1.3.2 Sol-gel syntheses

Sol-gel syntheses provide an alternative route to the solid-state syntheses of metal-oxide materials. These methods synthesise metal oxides *via* a solution state and then a gel state. By exploiting the solution state, the precursors in this synthesis can achieve the uniform mixing of the liquid phase, and thus avoid the difficulties with incomplete mixing often found with solid-state syntheses.[110] In maintaining the homogeneity of the starting material, limitations to mass transport are avoided, thus resulting in some compelling benefits to these methods over solid-state methods. This often comes in the form of higher purity product and reduced calcination and sintering times. These methods traditionally exploit the hydrolysis and subsequent condensation of metal alkoxides, forming gels which can be further processed to yield the desired phase.[111] However, the field has also developed substantially since its inception, with alternative gels and precursors available.

The name sol-gel originates from the fact that there are essentially two driving phases of the reaction; the first is the formation of a 'sol' or colloidal solution, which is then followed by the condensation of this sol into a gel, or non-fluid 3D network that is extended through a fluid phase.[112] This gel can be subsequently dried, which can lead to shrinkage and collapse due to capillary forces, resulting in a xerogel. Alternatively, the gel can be dried with supercritical drying, which enables the removal of the fluid without the collapse of the gel, resulting in an aerogel. A schematic of the sol-gel process is given in Figure 1.9. In general, there are five different types of gel featured in sol-gel chemistry, as defined by Kakihana in 1996, such as colloidal or metal-oxane gels.[110] The first example of sol-gel chemistry was in 1846 when $SiCl_4$ formed a gel when exposed to air.[113] Since this time, it has been found that many factors can be carefully tuned to finely control the properties of the sol and the gel involved. For example, this method can be controlled by altering the pH of the solution, the silicon alkoxide to water ratio, and the processing of the resultant gel. This method has since been applied to alternative metals besides silicon, although the reactivity of these metals (for example Ti and Zr) can be much higher than that of Si. As such, it is often the case that additives are added to these solutions to slow down the hydrolysis and condensation steps.[114] As many metal alkoxides are unstable in water, the method was changed so that metal salts were used instead with small molecules that can form gels.[115] For example, this can be successfully carried out with citric acid as a sequestering agent. Douy and Odier first attempted this method with the successful synthesis of YBCO in 1989.[116] This study utilised the polymerisation of acrylamide and N,N'-methylene-bis-acrylamide *in-situ* with the chelated sample of citric acid. This so-called 'small-molecule' method has since advanced to only require mixing of the small-molecule (such as citric acid) with the metal nitrates, and subsequent heating to form a gel.[117]
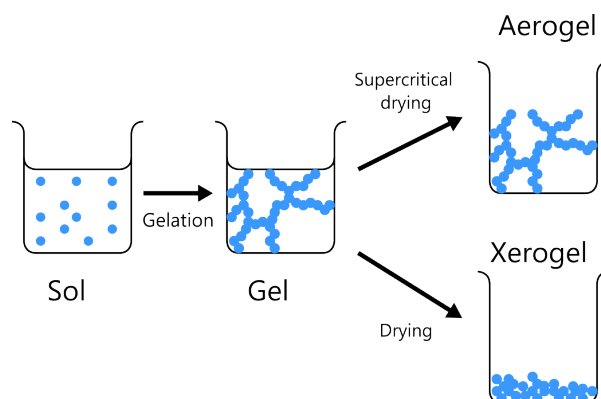
Figure 1.9: Schematic of a conventional sol-gel synthesis, where a sol undergoes polymerisation to form a gel. Subsequent drying can result in the collapse of the gel, forming a xerogel, or supercritical drying can result in the removal of fluid without the collapse of the gel, resulting in an aerogel.

In the synthesis of metal oxide materials, sol-gel methods have become invaluable as alternative pathways to solid-state syntheses. While solid-state methods are still a primary method for the synthesis of ceramic materials in industry, there are also examples of sol-gel techniques in industry, such as for the synthesis of coatings, films, laser materials and in the synthesis of thermally insulating aerogels.[118,119] Sol-gel syntheses can yield excellent quality thin films and coatings by simply dip casting a sol mixture onto a substrate and allowing the gelation reaction to occur. In simple condensation-based sol-gel syntheses, high temperatures are not required, meaning that substrates with poor tolerance to elevated temperatures are able to be coated in this method. One downside to this method is the fact that the film can undergo cracking as the water or alcohol evaporates from the gel, but this can be somewhat overcome by ensuring only thin coats are applied.[120] By changing the metal alkoxide involved in the synthesis, coatings and films can be synthesised with different chemical and optical properties; such as in the formation of waveguides for optical materials, and as antireflective coatings formed from antimony-doped tin oxide and silica.[121,122]

1.3.2.1 The Pechini Method

The Pechini method is named after the author of the original patent, Pechini.[123] Also referred to as the 'liquid-mix process', it was initially designed as a sol-gel method for niobates and titanates, which do not have favourable hydrolysis reactions.[124] It builds on the small molecule method discussed previously, with adjustments to enable it to apply to materials incompatible with an aqueous environment. This method utilises ethylene glycol as a solvent, combined with citric acid as a small molecule for gelation. In this case, the solvent participates in the gelation step, as citric acid and ethylene glycol can undergo a polyesterification reaction with each other. This polyesterification reaction results in a polymer network extending throughout the vessel,

a gel. The Pechini method involves mixing ethylene glycol and citric acid before the addition and dissolution of the metal salts in the correct stoichiometric ratios. The metal salts are able to chelate to the carbonyl groups on the citric acid, forming metal-citrate complexes. This mixture is then heated to induce the polyesterification reaction, as seen in figure 1.10, and then the material is calcined to form the metal oxide.[125]
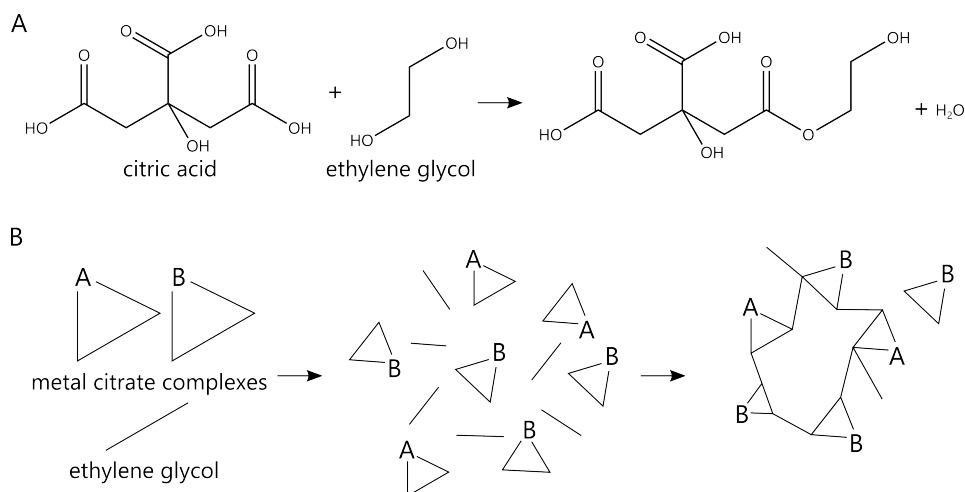
Figure 1.10: a) The polyesterification reaction between citric acid and ethylene glycol. b) A schematic to depict the way ethylene glycol and citric acid form a gel network with each other.

Part of what makes the Pechini method so desirable is the lack of need for water as a solvent, thus allowing access to syntheses with many reactive metals. Indeed, it is also valuable in cases where the metal salt is poorly soluble in water, for example in the case with bismuth nitrate. It has been used successfully in the synthesis of many metal oxides such as perovskites and ilmenites.[126,127] The method can also be modified somewhat, by still exploiting citric acid, but modifying the solvent to be simply ethanol.[127] The Pechini method is still being utilised in recent studies - for example, for applications in piezoelectronics.[128] Modifying the Pechini method can also be carried out to enable the fabrication of materials with controlled nanostructures.[129] The Pechini method has also been employed for the synthesis of the cuprate superconductors - for example, $Bi_2Sr_2CaCu_2O_{8+x}$ and $YBa_2Cu_3O_{7-\delta}$.[130,131]

1.3.2.2 Biopolymer-mediated syntheses

Biopolymers are naturally occurring polymeric materials, often polysaccharides such as starch or dextran. These biopolymers are usually extracted directly from biomass; for example, a common biopolymer, chitosan, is extracted from crab shells. While they do not fall into the conventional bracket of what constitutes a sol, the chains are still within 1 nm - 1 µm.[113] As well as providing the benefits of sol-gel, biopolymers can also be used as structure-directing agents.[132] In general, these syntheses involve mixing a biopolymer with a solution of metal salts, which is then allowed to gel. This is usually in the form of cross-linking by the metal ions to form a gel network. An

example is sodium alginate, which can be cross-linked to form a gel upon the addition of divalent cations. [133] This cross-linking of chains is also named the egg-box model of metal-ion chelation, first termed as such by Grant *et al.* [134]

The application of a biopolymer to synthesise a cuprate superconductor was first carried out in 2006. [135] In this study, a nanowire of YBCO was successfully synthesised with the biopolymer chitosan. Since this study, further experiments have been carried out with control of macro- and nanomorphology. [136,137] The type and amount of biopolymer can drastically change the phase of the product material, which can be due to the composition of the biopolymer, to what extent the biopolymer chelates to the metal cations and the amount of CO_2 given off during calcination. [138] There are also alternative ways to remove the biopolymer template when high-temperatures are not required for the formation of the target phase; for example dextran can be removed using the enzyme dextranase. [139]

Often these biopolymer-mediated syntheses enable access to control of nanostructures and macrostructures of the desired metal oxide. The extensive polymer chains can effectively hold the constituent metal ions in place for sufficiently long during calcination so that the resultant phase mimics the shape of the original biopolymer. Biopolymers can be quite resistant to thermal degradation, for example the gel formed between alginate and barium doesn't fully thermally degrade until temperatures as high as 498 °C. [140] This has enabled the replication of intricate macrostructures of materials - for example synthesising Y-123 that mimics the shape of a pasta template or that of a cuttlebone. [136,141] Various other biopolymers such as gelatin have enabled access to facile syntheses of nanoparticles of metal oxides, such as the synthesis of $Ca(OH)_2$ nanoparticles through stabilisation with gelatin. [142]

When deciding upon a biopolymer for the synthesis of metal oxides, the composition of the biopolymer must be considered, as side-reactions can occur during the synthesis which will result in the formation of unwanted impurity phases. In the case of Y-123, choice of a sulphur-containing biotemplate lead to difficulties avoiding the formation of highly-stable $Ba(SO_4)$. However, additional elements within the biopolymer can also aid in the formation of desired morphologies or composition - it was postulated that the sodium ion within the biopolymer sodium alginate was able to behave as a flux, which aided in the formation of nanowires of Y-123 through a mechanism known as the microcrucible mechanism, which will be discussed in more detail in Section 4.1.1.2. [143]

1.3.2.3   Ionic liquids and Deep Eutectic Solvents

Two types of solvents, ionic liquid (IL)s and deep eutectic solvent (DES) are fundamentally similar in make-up. Both involve solid constituent molecules which form a liquid close to room temperature when combined. For ILs, the constituent parts are ionically charged. It is usually stipulated that materials categorised as ILs have low melting points, below 100 °C, otherwise,

conventional molten salts such as liquid NaCl would also be considered to be ILs. To enable these materials to exhibit the low melting points required, ILs tend to consist of a large asymmetric cation and a bulky, charge diffuse anion.[144] There are many different potential salts that can form ionic liquids, indeed this customisability of constituent anions and cations enables the properties of these ILs to be tuned. Generally speaking, there are four common types of ILs based on the cation: alkylammonium, dialkyl imidazolium, phosphonium and N-alkyl pyridinium.[145] ILs have a lot of favourable characteristics, such as exhibiting low volatility, little to no flammability and promising electrochemical characteristics. Unfortunately, despite the limited risk of air pollution due to low vapour pressure, ILs are highly soluble in water which could lead to environmental contamination were they to be used commonly in industry in the future.[146] Additionally, there is some debate to their safety.[146,147] The synthesis of the constituent molecular components of ionic liquids can also be highly energy intensive and require the use of environmentally unfriendly organic solvents, which throws their status as a potential 'green' solvent into some contention.[148]

Deep eutectic solvents (DESs) are similar to ILs and usually contain an ionic component. Despite eutectic mixtures of solvents being well known, the term 'deep-eutectic solvent' was only coined by Abbott *et al.* in 2004. Molecular DESs form when two solid materials are mixed and form a liquid. A DES is usually formed by the complexation of a quaternary ammonium salt and a hydrogen bond donor or metal salt.[150] The delocalisation of charge between the two components results in a lower melting point of the combined material compared to the melting point of the separate molecules.[151] Despite the similarities between ILs and DESs, there are some advantages to DESs. For example, the preparation of eutectic mixtures in their purest form is achieved more quickly than for ILs, and so additional purification steps are not required for DESs.[152] As DESs are formed from extensive hydrogen-bonding throughout the liquid, they can also be thought of as supramolecular solvents - where the large bonding framework throughout the solvent is able to template metal salts and impart a nanostructure on resulting material.[153] This has been seen for the synthesis of zeolites using ILs and DESs as templating solvents.[154]

Both ILs and DESs have been used as solvents in synthesising functional ceramic materials. Due to their polar nature, these solvents are very good at solvating the metal ions in the solution phase of the sol-gel process to the point that dehydrated solutions of metal ions have become a facile process.[155] It was noted during this study by Green *et al.* however, that ILs are so strongly complexing, that they can preferentially bind with certain metal ions over others, thus in this study cellulose was added as a weakly coordinating non-specific chelating agent.[155] This method resulted in the synthesis of nearly phase-pure metal oxides for a wide range of applications, such as terbium-doped yttrium aluminium garnet, Bi-2212, and the ferromagnetic material, nickel-doped praesodynium cobalt oxide. ILs have garnered attention for the synthesis of nanomaterials due to their ability to behave as reaction media, templating agents and their ability to provide steric stabilisation for the resulting nanomaterial.[156] Zhang *et al.* described the use of ILs in

their synthesis of nanocrystals of lanthanide fluorides as an "all-in-one system", where the ionic liquids were not only the solvent for the reaction, but also the templating agent and resulting stabilisation media for the nanoparticles.[157] As well as this, the effect of ILs on the synthesis of YBCO has also been studied, and it was found that using 1-ethyl-3-methylimidazolium acetate as a solvent yielded a very pure sample of YBCO.[158]

DESs are also prevalent in the field of functional materials for the synthesis of complex systems of metal oxides. In fact, a so-called natural deep eutectic solvent has been used to successfully solvate bismuth nitrate in order to successfully synthesise Bi-2212.[159] NADES are the same as DESs, but with naturally occuring molecules, such as sugars, carboxylic acids, amino acids and amines.[160] It has been noted that many NADES based on glucose are excellent for solvating metal ions.[161] Therefore, the application of the NADES for the synthesis of Bi-2212 was especially valuable due to the excellent ability of the glucose-based DES to solvate the bismuth ions in solution, preventing the formation of insoluble bismuth subnitrate.[159] DESs have been used in similar ways to to ILs, where they can be used as both a solvent, template and stabilising agent. Indeed, they have been used for the generation of complex nanostructures of materials, such as monodisperse star-shaped gold nanoparticles.[153] This synthesis utilised the reduction of $HAuCl_4$ with L-ascorbic acid, combined with a choline chloride/urea DES as a solvent. In addition to not needing the addition of surfactant for the stabilisation of the gold nanoparticles, the water content of the DES could be tuned to access different morphologies of gold nanoparticle. DES usually exhibit more strong redox properties than conventional solvents such as water and other organic solvents. This can be especially useful in the synthesis of metal nanoparticles.[160] More recently, DESs have been used in the synthesis of high-entropy materials, which are compounds consisting of five or more metal species in a single-phase crystal structure. In a recent study, a glucose-urea DES was used to synthesise several high-entropy phases, such as $(Co, Ni, Cu, Zn, Mg)O$ with a rock-salt structure.[161]

1.4 Characterisation of solid materials

1.4.1 X-ray diffraction

For crystalline materials, the powerhouse of structure characterisation has been single crystal X-ray diffraction (scXRD) since its initial development in the 1910s-1920s. X-ray diffraction (XRD) exploits the periodic nature of crystals by utilising EM radiation in the form of X-rays, which have a wavelength which is on the order of the size of atoms. As such, when a crystal is illuminated by X-rays, the crystalline lattice is able to behave as a diffraction grating to the incident X-rays. A simplistic model of X-ray diffraction is that of the Bragg model, where a lattice can be represented as atoms on a net. When an incident X-ray hits one of these atoms, it is reflected. When there are multiple rows of atoms, the spacing between these rows can be calculated by understanding that X-rays diffracted from different rows of the lattice will travel different distances. If the

change in distance travelled is equal to an integer number of wavelengths, $n\lambda$, the X-rays will be able to interfere constructively, and thus the detector will read a signal from the sample. From trigonometry, it can be seen that this criterion is satisfied if the difference in distance travelled is equal to $2dsin\theta$ and a diagram of this can be seen in Figure 1.11. If the change in distance is not an integer number of wavelengths, the diffracted beam of X-rays will interfere destructively, and the detector will not register a signal. The resulting equation to determine the d-spacing of a crystal, the Bragg equation, is given as equation 1.4.
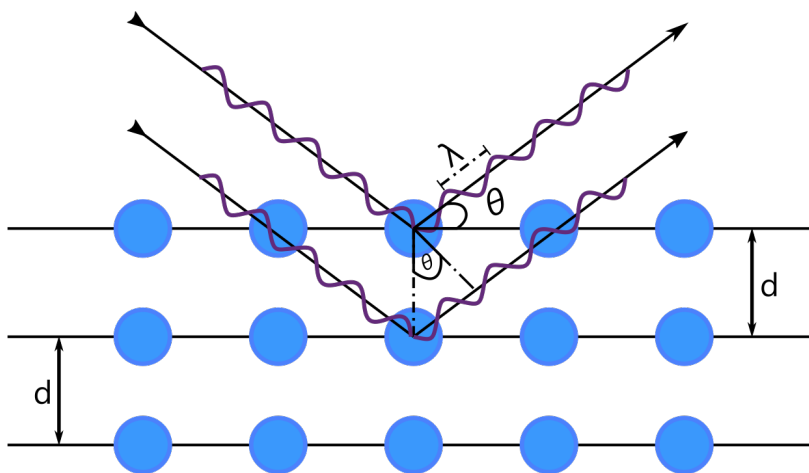
Figure 1.11: Diagram of the Bragg model, where an incident X-rays are diffracted by a crystalline lattice. If both diffracted X-rays reach the detector in phase, they will interfere constructively and a diffraction spot will be present.

$$(1.4) \qquad\qquad\qquad\qquad n\lambda = 2dsin\theta$$

scXRD has been used for many years and has remained one of the most reliable methods of crystal structure determination. However, it requires large, high-quality crystals for analysis which can limit its applicability in determining structures of materials where the crystals are difficult to grow - which is the case with membrane proteins, which are poorly soluble.[162] The intensity of the diffraction pattern from a crystal is proportional to the size of the crystal, which results in a requirement for larger crystals for good quality diffraction patterns. These high levels of radiation will cause damage to most substances, and thus smaller crystals are unable to be resolved with conventional scXRD.[163] Techniques are in place to attempt to overcome these issues, such as using X-ray free electron lasers or by using 3D electron diffraction.[164,165]

Instead of using single crystals of material, one can also examine the diffraction pattern that occurs when X-rays illuminate a microcrystalline powder. The analysis of the diffraction patterns that result from powders is called powder X-ray diffraction (pXRD), and is a vital tool

for determining the composition of crystalline powders and, indeed, whether they are crystalline at all.[166] The pXRD technique assumes that the powder is formed of many randomly orientated microcrystals, allowing for every crystallite orientation within the sample to be expressed. As all the crystallite orientations are present, the diffracted X-rays will be formed as cones and detected as rings instead of the spots observed in scXRD. This is because all planes of a d_{hkl}-spacing will be diffracted for a given 2θ, effectively rotationally averaging the diffracted X-rays, yielding diffraction cones instead of spots.[18,19] Indexing the rings to the correct Miller index can be challenging. Thus pXRD is often used as a fingerprint method for comparing the diffraction pattern to already-known materials.[19] There are examples of the *ab-initio* determination of crystal structure from pXRD spectra, but this is still challenging to carry out.[167]

Depending on how a crystalline or polycrystalline material is grown, there are sometimes features which can alter a resulting pXRD pattern, such as particle size, preferential orientation of crystal planes, and microstrain within the crystal structure. These phenomena have an affect on the average crystal structure of a material, and can thus alter peak position, peak shape and peak broadness. Small crystallites have the effect of broadening the peaks found in a pXRD pattern. This is because the destructive interference observed is a result of a summation of all diffracted beams; if there are fewer crystallite planes to diffract the beams there are not enough planes to produce complete destructive interference, and a broader peak will be observed.[19,168] Another common implication of the structure of the polycrystalline material is preferential orientation. This occurs when the crystals of one plane grow preferentially over others. In this case, the diffraction peak observed from this set of peaks will be over-represented, yielding a higher intensity signal than would be expected for a crystal where all planes are equally represented.[169] Strain within the crystal lattice can also result in peak broadening of the resulting pXRD patterns, which is due to displacement of the atoms within the lattice from their 'perfect' positions.[170] Features such as these can be used for analysis of the bulk properties of the material - for example through calculating the average size of the particulates.

1.4.1.1 Rietveld refinement

By itself, pXRD can only determine which phases are present within a powder diffraction pattern. To unlock more detailed analysis of a powder diffraction pattern such as the unit cell parameters and percentage quantities of individual phases, Rietveld analysis can be carried out. This utilises a least-squares fitting approach to compare a theoretical pXRD pattern with the experimental pattern, which is carried out using equation 1.5 and attempting to minimise the quantity R.[18]

$$(1.5) \qquad\qquad R = \sum_i w_i (Y_{io} - Y_{ic})^2$$

Here, Y_{io} is the observed intensity at i, Y_{ic} is the calculated intensity at i and w_i is a weighting factor. The larger the observed intensity, the larger the weighting factor, meaning

that less significance is placed upon lower intensity sections of the pXRD pattern.[18] Rietveld refinement can be adjusted to accommodate many deviations in the 'perfect' crystal structure, such as preferential orientation and micro-strain effects, which will alter peak size and shape in the pXRD pattern.

1.4.2 Electron microscopy

Compound light microscopes have existed since the 1600s; however, light can only resolve features that are on the order of ∽200 nm due to the diffraction limit (also known as Abbe's Limit).[171] While techniques have been developed that can be used to overcome this limit, there remain limitations to the maximum possible magnification that cannot be overcome with light microscopes.[172] Electrons have a much smaller wavelength than light, and thus microscopes based on an electron beam can view much smaller details.[173] As such when examining nanostructured materials, the electron microscope has become a vitally important instrument. There are two types of electron microscopy, scanning electron microscopy (SEM) and transmission electron microscopy (TEM). These two methods use an electron beam to examine the structure of a material but differ in how the beam interacts with the sample.[173]

SEM operates by rastering an electron beam over the surface of a sample and detecting electrons that are given off by the sample. Depending on the desired information about the sample, different types of electrons can be analysed to glean information about the sample.[174] For backscattered electron imaging, the electrons that are scattered by the sample are detected. Heavier atoms can deflect more electrons, resulting in a brighter image. As such, backscattered electron imaging can give compositional information about the surface of a sample.[175] In secondary electron imaging, the incident electron beam knocks out core electrons from the sample, which are then detected. Fewer electrons will escape from further down the sample, so secondary electron imaging can give topographical information about the surface of a sample.[176] An additional imaging mode for SEM is energy dispersive X-ray analysis (EDXA). When a secondary electron is ejected from an atom on the surface of a material, a higher energy electron can fall to the ejected electron's energy state. When this happens, the excess energy is released as a photon from the atom with a wavelength characteristic of the atom, which is in the X-ray region of the EM spectrum.[19] As such, the X-rays given off by the sample when the electron beam is rastered across the surface can be detected, creating an X-ray spectrum per pixel in the image. This allows maps to be built, containing compositional information about each area of the image.

TEM operates by shining an electron beam through a thin sample and detecting the electrons that pass through. This can result in very high-resolution images, with atomic resolution in some cases. When electrons interact with the sample, they can be scattered by varying amounts depending on the sample thickness or the mass of the atoms within the sample. A TEM utilises an aperture to stop all atoms which deviate by a certain angle, meaning that if more electrons are scattered, fewer will reach the detector. This leads to a black-and-white image with darker
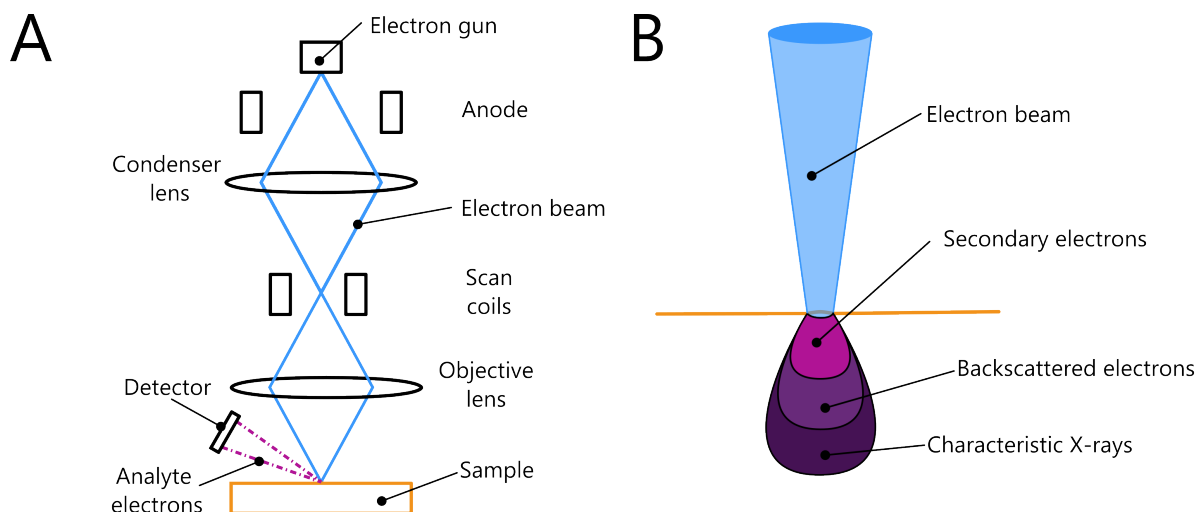
Figure 1.12: a) Diagram depicting a conventional SEM b) Diagram depicting the source of the electrons or X-rays from several imaging modes

regions representing a section of the sample that is either thicker or made of heavier atoms.[173]

Similarly to X-ray diffraction, electrons can also diffract when they encounter a regular lattice. TEM operates by passing a beam of electrons through a sample. Therefore, these electrons can also be diffracted by the analyte sample. Similarly to XRD the resulting diffraction spot pattern can be analysed to determine the crystal structure of the material being examined. A benefit of selected-area electron diffraction (SAED) over conventional scXRD is its ability to measure the crystal structure of small crystallites, though it is only recently that a more complicated technique, 3D electron diffraction has been accessible. This technique combines a tilting TEM stage with highly sophisticated electron detectors to fully determine crystal structures of small crystallites.[165] This has enabled the resolution of several crystal structures which could not be grown to large enough sizes for scXRD, for example with the regioisomer of paracetamol, orthocetamol.[177] Another consequence of the diffraction occurring on a TEM is that a larger amount of reciprocal space can be viewed than for XRD. This can be visualised using the Ewald sphere, a construction of the reciprocal lattice, and which lattice planes satisfy the Bragg diffraction condition. As the radius of this sphere is $1/\lambda$, if a incident beam of smaller wavelength is used, the Ewald sphere will be larger, thus allowing a larger region of the reciprocal space to be viewed (Figure 1.13b).[18] Therefore, depending on the accelerating voltage of the electron beam, a beam which exhibits a smaller wavelength than that of X-rays is possible.

1.4.3 Magnetometry

Superconducting Quantum Interference Device (SQUID) magnetometers are a highly sensitive devices for sensing the magnetic behaviour of materials. They exploit the Josephson effect, described in Section 1.2.1.2. Depending on the type of current pushed through the SQUID,
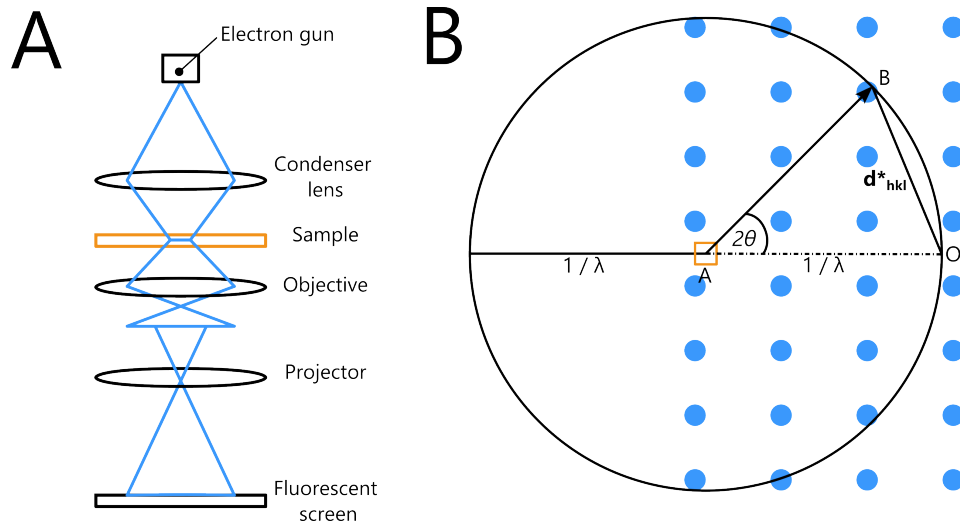
Figure 1.13: a) Diagram depicting a conventional TEM b) Diagram depicting the Ewald sphere.

they can be referred to as D.C.-SQUIDs or RF-SQUIDs for a D.C. and an A.C. respectively.[178] A conventional D.C. SQUID is formed from a ring of superconducting material with two non-superconducting junctions or JJs (Figure 1.14). A D.C. is applied across this loop, which leads to the supercurrent splitting evenly to flow down each branch of the loop, and crossing both JJs. If a magnetic field is applied within the loop, another current is induced in the loop, which will be in the same direction as the current through one of the JJs, but opposite in the other JJ. If the current through either JJ exceeds the critical current of the superconductor, a potential difference will be applied across the junction. This creates an alternating current which can interfere with the signal achieved by the other junction. As such, the frequency of this interference can be analysed to determine the amount of magnetic field that has caused the signal. The amount of flux that passes through a superconducting ring is quantised; therefore, a SQUID can detect perturbations on the order of a single flux quantum and is thus highly sensitive.[68]
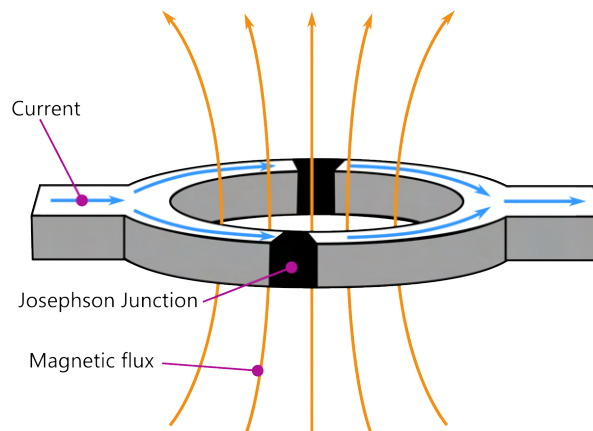
Figure 1.14: Diagram of a conventional D.C. SQUID, formed from a superconducting loop with two evenly spaced JJs on each branch of the loop.

1.5 Project aims and summary

This work focuses on the control of the nanostructures of functional metal oxides, with a particular focus on superconducting materials. To achieve this aim, syntheses were examined with increasing dimensionality; from designing a novel synthesis of materials predicted to be superconducting with no specific structural direction; to the synthesis of 1-dimensional and 2-dimensional nanowire structures; to synthesising 3-dimensional sponge nanostructures.

This begins with the synthesis of materials predicted to be superconductive, $Na_3Ni_2BiO_6$, $Na_3Ca_2BiO_6$ and $KBa_6Zn_4Ga_7O_{21}$. These materials have previously been synthesised through solid-state methods, necessitating long dwell times and, in the case of $Na_3Ni_2BiO_6$, requiring additional annealing steps. Therefore, alternative solution-based methods were sought, with a view to shorten the synthesis time while maintaining good purity. Following this, the aim was to test the materials for superconductivity through SQUID magnetometry.

The next aim was to synthesise nanowires of a well-studied superconductor, $Bi_2Sr_2CaCu_2O_{8+x}$. This is because nanowires of this material specifically are technologically significant due to their potential applications as terahertz emitters. Examination of potential synthesis methods were explored, with a view to emulate the microcrucible mechanism of nanowire growth in the absence of a biopolymer.[143] By achieving this, it would allow the microcrucible mechanism to be applicable to other systems that would be otherwise incompatible with a biopolymer. Additionally, the prospect of viewing nanowire growth with a high-temperature TEM was explored.

Finally, the prospect of using a new structure directing agent in the form of melamine formaldehyde was explored with a view to synthesise sponge-like morphologies of high-temperature superconductors. In addition to successfully synthesising porous $YBa_2Cu_3O_{7-\delta}$ (Y-123) and $Bi_2Sr_2CaCu_2O_{8+x}$ (Bi-2212), this set up a new way to control the 3-dimensional nanostructures of these superconductors.

CHAPTER

2

Materials and Methods

Parts of this chapter are published in Nanoscale Advances and Dalton Transactions. [179,180]

2.1 Materials

All materials were purchased from a supplier and used without further treatment with the exception of copper oxide, which was purchased as copper carbonate basic and heated to 500 °C to convert into copper oxide. All materials were purchased from Sigma-Aldrich or Fisher Scientific, with the exception of calcium acetate monohydrate (Honeywell), copper nitrate hemi(pentahydrate) (Alfa Aesar), betaine (Alfa Aesar) and, high fraction dextran (Acros Organics).

Table 2.1: The amounts of metal nitrates used in the synthesis of $Na_3Ni_2BiO_6$

Metal nitrate	Concentration / M	Mass / mg
$NaNO_3$	0.1545	131.3
$Ni(NO_3)_2 \cdot 6H_2O$	0.10	290.1
$Bi(NO_3)_3 \cdot 5H_2O$	0.05	121.5

2.2 Methods

2.2.1 Novel and rapid sol-gel syntheses of honeycomb-layered and orthorhombic metal oxides

2.2.1.1 Synthesis of the natural deep eutectic solvent (NADES)

To make 10 mL of NADES, 3 g of betaine and 1.8453 g D-(+)-glucose were added together, before 6.336 mL water was added to create a mixture with a final volume of 10 mL. The vial was shaken until all the powders were dissolved, thus forming the NADES stock solution.

2.2.1.2 Aqueous synthesis of $Na_3Ni_2BiO_6$

Sodium nitrate, nickel nitrate hexahydrate and bismuth nitrate pentahydrate in the ratios given in table 2.1 were added to 10 mL deionised water. To aid the dissolution of bismuth, 0.2 g of EDTA was added to the solution as a chelating agent. To overcome the volatility of the sodium, the sodium nitrate was added at a 3% excess, as was recommended by the original synthesis, leading to an concentration of $0.1545 \, \mathrm{mol \, dm^{-3}}$.[181] This was kept as a stock solution and used for multiple syntheses - 'NNB aq stock'. The whole system was heated to 80 °C and stirred for 30 minutes until dissolved. 300 mg high fraction dextran was added to a crucible, and 1 mL of the metal precursor solution added to this. The sample was stirred mechanically to form a viscous solution, before being placed in a box furnace for calcination. The sample was calcined between 500 - 1000 °C with a $5 \, \mathrm{°C \, min^{-1}}$ ramp rate and a 2 hour dwell time.

2.2.1.3 Natural deep eutectic solvent synthesis of $Na_3Ni_2BiO_6$

Sodium nitrate and nickel nitrate hexahydrate were added to a vial in the amounts given in table 2.1, along with 10 mL deionised water and shaken until all powder had dissolved. This solution was kept as a stock solution - 'NN aqueous stock'. The final stock solution involved adding bismuth nitrate pentahydrate in the amounts given in table 2.1 to 10 mL of NADES and stirring until dissolved, forming the Bi-NADES stock solution.

1 mL of Bi-NADES stock solution was added to a crucible, with 1 mL NN aqueous stock and 1.05 mL NADES. The material was stirred at 80 °C for 2 hours until dehydrated, before calcination at 800°C with a dwell time of 2 hours and ramp rate of 5 $\mathrm{°min^{-1}}$.

Table 2.2: The amounts of metal nitrates used in the synthesis of $Na_3Ca_2BiO_6$.

Metal nitrate	Concentration / M	Mass / mg
$NaNO_3$	0.1545	131.3
$Ca(NO_3)_2 \cdot 4H_2O$	0.10	232.6
$Bi(NO_3)_3 \cdot 5H_2O$	0.05	121.5

2.2.2 Syntheses of $Na_3Ca_2BiO_6$

2.2.2.1 Aqueous synthesis of $Na_3Ca_2BiO_6$

In the temperature study experiments, sodium nitrate and calcium nitrate tetrahydrate in the ratios given in table 2.2 were added to 10 mL deionised water and stirred until dissolved. Bismuth nitrate pentahydrate was added separately to 10 mL of deionised water, along with 0.2 g of ethylenediaminetetraacetic acid (EDTA) and then was stirred at 80 °C until all solid had dissolved. 1 mL of each aqueous precursor solution was added to 100 mg dextran in a crucible and stirred mechanically until a gel formed. This was then placed in a furnace and calcined at temperatures between 500 and 1100 °C with a dwell time of 2 hours. The ramp rate of the furnace was $5\,°C\,min^{-1}$.

2.2.2.2 Natural deep eutectic solvent synthesis of $Na_3Ca_2BiO_6$

Sodium nitrate and calcium nitrate tetrahydrate in the amounts given in table 2.2 were added to 10 mL deionised water and shaken until all had dissolved. This solution was kept as a stock solution - 'NC aqueous stock'. The final stock solution involved adding bismuth nitrate pentahydrate in the amount given in table 2.2 to 10 mL of NADES and stirring until dissolved, forming the Bi-NADES stock solution.

1 mL of Bi-NADES stock solution was added to a crucible, with 1 mL NC aqueous stock and 1.05 mL NADES. This solution was stirred at 80 °C to until the solution has fully dehydrated. The solution was then calcined at 800°C with a dwell time of 2 hours and a ramp rate of 5 °C min^{-1}. The resulting fluffy powder was a light orange colour.

For the temperature studies of this material, the calcination temperature was changed between 500 and 1000 °C in 100 °C intervals.

2.2.3 Brief attempts at the synthesis of $KBa_6Zn_4Ga_7O_{21}$

2.2.3.1 Aqueous synthesis of $KBa_6Zn_4Ga_7O_{21}$

Potassium chloride, barium nitrate, zinc nitrate hexahydrate and gallium nitrate hydrate in the amounts given in table 2.3 were added to 10 mL deionised water and stirred overnight until all metal salts had dissolved. a 1 mL aliquot of this solution was added to a crucible with dextran

Table 2.3: The amounts of metal nitrates used in the synthesis of $KBa_6Zn_4Ga_7O_{21}$

Metal nitrate	Concentration / M	Mass / mg
KCl	0.01	7.5
$Ba(NO_3)_2$	0.06	156.8
$Zn(NO_3)_2 \cdot 6\,H_2O$	0.04	119.0
$Ga(NO_3)_2 \cdot xH_2O$	0.07	305.2

(between 100 and 1000 mg), and stirred mechanically until a gel or paste formed. This was then placed in a furnace without further treatment and calcined between 700 and 900 °C with a 2 h dwell time and 5 °C min^{-1} ramp rate.

2.2.3.2   Natural deep eutectic solvent synthesis of $KBa_6Zn_4Ga_7O_{21}$

Potassium chloride, barium nitrate and zinc nitrate in the amounts in table 2.3 were added to 10 mL deionised water, and the solution stirred until all metal salts had dissolved - this formed the KBaZn-Aq stock solution. Gallium nitrate hydrate in the amount given in table 2.3 was added to 10 mL of the NADES, and the solution stirred until everything had dissolved. 1 mL of this Ga-NADES was added to 1 mL KBaZn-Aq stock, along with 1.05 mL NADES. This was then stirred at 80 °C until the water had completely evaporated, before calcination at 700 or 750 °C with a 2 h dwell time and 5 °C min^{-1} ramp rate..

2.2.4   Synthesis of nanowires of $Bi_2Sr_2CaCu_2O_{8+x}$

2.2.4.1   Synthesis of nanoparticles of $Sr_{1-x}Ca_x(CO_3)_2$

The nanoparticle synthesis follows a previously reported method.[182] Stock solutions of 0.05 M aqueous metal nitrates [$X(NO_3)_2$, X= Ca, Sr] and 0.025 M Na_2CO_3 were prepared. 50 ml of each $X(NO_3)_2$ solution was placed in a sonicator. Under sonication and vigorous stirring 200 ml of the 0.025 Molar solution was added drop-wise over 8 h. The resultant milky solution was dried at 110 °C before being calcined at 450 °C, yielding a white powder.

2.2.4.2   The synthesis of $CaCu(OCOOH)_4 \cdot 6\,H_2O$

Calcium acetate monohydrate (3.55 g, 2.0 mol dm^{-3}) was dissolved in deionised water (10 mL at approximately 70 °C). Separately, copper acetate monohydrate (1.00 g, 0.67 mol dm^{-3}) was dissolved in deionised water (7.5 mL at approximately 70 °C). To ensure complete dissolution of the salts, further water was added dropwise. The two solutions were subsequently mixed at 70 °C then filtered, covered and allowed to stand until dark blue crystals formed. The resulting crystals were ball-milled for 24 h to attain a fine powder.

An alternative synthesis method was additionally devised for this material. Calcium acetate (704.8 mg, 0.4 M, 2 mmol) was added to 10 mL deionised water along with (798.6 mg, 0.4 M, 2

Table 2.4: The amounts of metal nitrates used in the synthesis of $KBa_6Zn_4Ga_7O_{21}$

Metal nitrate	Concentration / M	Mass / mg
$Bi(NO_3)_3 \cdot 5\,H_2O$	0.1	485.1
$Sr(NO_3)_2$	0.1	211.6
$Cu(NO_3)_2 \cdot 2.5\,H_2O$	0.05	232.6

mmol). The solution is heated to $50\,°C$ to aid the dissolution of copper acetate. A $2.5\,mL$ aliquot of this solution was pipetted into a separate container, and then $15\,mL$ of acetone was added to this, forming a gel. The resulting gel was spread out in a petri dish, allowing the gel to collapse, depositing crystals of the target material.

2.2.4.3   Synthesis of $Bi_2Sr_2CuO_6$

Via. **a NADES synthesis**: A NADES between betaine and D-(+)-glucose was synthesised as described in Section 2.2.1.1. Bismuth nitrate pentahydrate in the amount given in table 2.4 was added to $5\,mL$ of this NADES and shaken until dissolved. A separate aqueous solution of strontium nitrate and copper nitrate hemi(pentahydrate) in the amounts given in table 2.4 was also made. $1\,mL$ of this solution was combined with $1\,mL$ of the Bi-NADES solution, and an additional $1.05\,mL$ of the NADES. This was then calcined at $850\,°C$ with a ramp rate of $5\,°C\,min^{-1}$ and a dwell time of $2\,h$.

Via. **a biopolymer-mediated synthesis**: Bismuth nitrate pentahydrate, strontium nitrate and copper nitrate hemi(pentahydrate) were added to $10\,mL$ deionised water in the amount given in table 2.4, along with ethylenediaminetetraacetic acid ($0.5\,g$) and ammonium hydroxide ($300\,µL$). The solution was covered and then heated to $80\,°C$ until all of the metal salts dissolved. This solution was subsequently transferred to a crucible, and dextran ($5\,g$) was added. The material was stirred mechanically with a spatula, allowing a thick gel to form. The crucible was left in an oven at $80\,°C$ overnight to allow all water to evaporate, before subsequent calcination at $850\,°C$ with a ramp rate of $5\,°C\,min^{-1}$ and a dwell time of $2\,h$.

2.2.4.4   Synthesis from Bi_2O_3 CuO and $Sr_{1-x}Ca_x(CO_3)_2$

Bismuth oxide (Mr = 465.96, 0.5 mmol, 232.98 mg) was added to copper oxide (Mr = 79.55, 1 mmol, 79.55 mg) and ground together with a pestle and mortar. Previously synthesised strontium calcium carbonate nanoparticles (Mr = 395.34, 0.5 mmol, 197.67 mg) were added, as well as an additional flux ($CaCl_2$, Na_2CO_3, $BiCl_3$ or $NaCl$) in the amounts given in table 2.5. The powders were mixed and ground together until a uniform powder was formed.

Table 2.5: The amount of flux required for different molar percentages.

	Mr	Moles / mmol	Mass / mg
$CaCl_2$ (10%)	110.98	0.025	2.8
$CaCl_2$ (15%)		0.0375	4.2
$CaCl_2$ (20%)		0.05	5.6
Na_2CO_3 (10%)	105.99	0.0125	1.3
Na_2CO_3 (15%)		0.01875	2.0
Na_2CO_3 (20%)		0.025	2.6
$BiCl_3$ (10%)	315.34	0.025	7.9
$BiCl_3$ (15%)		0.0375	11.8
$BiCl_3$ (20%)		0.05	15.8
NaCl (10%)	58.44	0.025	1.5
NaCl (15%)		0.0375	2.2
NaCl (20%)		0.05	2.9

The powder was pressed into pellets, and calcined at temperatures between 700 and 900 °C, with a ramp rate between 1-15 °C/min, and a dwell time between 1-5 hours. Sometimes an additional dispersion of the appropriate flux was scattered over the top of the sample prior to calcination.

2.2.4.5 Synthesis with $Bi_2Sr_2CuO_6$ and $CaCu(OAc)_4 \cdot 6H_2O$

Bi-2201 ($Bi_2Sr_2CuO_{6+x}$, 100 mg, synthesised either through a NADES method or the aqueous method) was crushed and mixed with 1 equivalent of $CuCa(CH_3COO)_4 \cdot 6H_2O$. Sodium flux was added in the form of NaCl to give 30 % mole of sodium relative to bismuth content. All materials were ground together with a pestle and mortar. The mixture was crushed into a pellet and lightly broken up again before being calcined at 850 °C for 2 hours.

2.2.5 Synthesis of sponge architectures of high-temperature superconductors

2.2.5.1 Aqueous precursor solution for $YBa_2Cu_3O_7$

Yttrium(III) nitrate hexahydrate (191.5 mg, 0.05 M, $Y(NO_3)_3 \cdot 6H_2O$), barium nitrate (261.3 mg, 0.1 M, $BaNO_3$) and copper(II) nitrate hemi(pentahydrate) (348.9 mg, 0.15 M, $Cu(NO_3)_2 \cdot 2.5H_2O$) were added to a vial with 10 mL deionised water. The solution was stirred overnight until all powders had dissolved, affording a blue solution.

2.2.5.2 Aqueous precursor solution for $Bi_2Sr_2CaCu_2O_8$

Bismuth nitrate pentahydrate (485.1 mg, 0.1 M, 1 mmol, $Bi(NO_3)_3 \cdot 5H_2O$), strontium nitrate (211.6 mg, 0.1 M, 1 mmol, $Sr(NO_3)_2$), calcium nitrate tetrahydrate (118.1 mg, 0.05 M, 0.5 mmol, $Ca(NO_3)_2 \cdot 4H_2O$) and copper(II) nitrate hemi(pentahydrate) (232.6 mg, 0.1 M, 1 mmol

$Cu(NO_3)_2 \cdot 2.5\,H_2O$) are added to a vial, along with 0.2 g ethylenediaminetetraacetic acid (EDTA). 10 mL deionised water was added, and the whole system was heated to 80 °C and stirred until the metal salts were fully dissolved, resulting in a blue solution.

2.2.6 Sponge architecture syntheses

2.2.6.1 Sponge-only synthesis

Sections of sponge were cut off from the Flash Magic Eraser and submerged in the YBCO and Bi-2212 aqueous precursor solutions, prepared using the methods in 2.2.5.1 and 2.2.5.2 respectively. The beakers containing the sponges were covered in parafilm, and left to soak overnight. The sponge was dried at 80 °C overnight, before being placed in alumina crucibles and caclined under the conditions outlined in table 2.6.

Table 2.6: The calcination parameters for $YBa_2Cu_3O_{7-\delta}$ and $Bi_2Sr_2CaCu_2O_{8+x}$

	Dwell temperature / °C	Ramp rate / °C min^{-1}	Dwell time / hours
YBCO	920	5	2
BSCCO	850	5	2

2.2.6.2 Sodium alginate and sponge synthesis

The synthesis method closely follows a previously reported method.[183] 0.1 g of sodium alginate was added to 50 mL of deionised water and stirred overnight until dissolved. For the concentrated alginate solution, 0.5 g of sodium alginate was added to 50 mL deionised water and likewise stirred overnight. Sections of sponge were then cut off the Flash Magic Eraser, and submerged in the respective alginate solutions in a beaker. The beakers were covered in parafilm and holes pierced in the film before the beakers were put under vacuum for 5 minutes. Following this, the sponges were dried at 80°C in an oven. The sponges were submerged in aqueous precursor solutions of YBCO and BSCCO (synthesis method reported in sections 2.2.5.1 and 2.2.5.2) before subsequent drying at 80°C. Following this, the sponges were placed in alumina crucibles and calcined under the conditions outlined in table 2.6.

2.2.6.3 Modified Pechini Method synthesis

This method follows the Pechini method, named after the original patent.[123] Citric acid (0.4306 g, 0.0224 mol, 1 eq) was added to ethylene glycol (10 mL, 0.179 mol, 8 eq) and heated to 90 °C with stirring to allow the citric acid to dissolve. For YBCO, metal nitrates in the concentration and masses in table 2.7 were added to the solution and then heated to 90 °C under stirring until all powders have dissolved.

39

Table 2.7: The necessary amounts required to synthesise YBCO and Bi-2212 in the correct stoichiometric ratios.

Target Phase	Metal salt	Concentration / M	Mass / g
YBCO	$Y(NO_3)_3 \cdot 6\,H_2O$	0.05	191.5
	$Ba(NO_3)_2$	0.1	0.2613
	$Cu(NO_3)_2 \cdot 2.5\,H_2O$	0.15	348.9
Bi-2212	$Bi(NO_3)_3 \cdot 5\,H_2O$	0.1	485.1
	$Sr(NO_3)_2$	0.1	211.6
	$Ca(NO_3)_2 \cdot 4\,H_2O$	0.05	118.1
	$Cu(NO_3)_2 \cdot 2.5\,H_2O$	0.1	232.6

A section of Melamine formaldehyde sponge was added to the solution, before gelation in a furnace at 140 °C with a dwell time of 2 hours. Following this, the samples were calcined according to the criteria in table 2.6.

2.3 Analysis

2.3.1 Powder X-ray Diffraction

Powder X-ray diffraction was carried out on a Bruker D8 Advance powder X-ray diffractometer with a $Cu-K\alpha$ (λ =1.5418 Å) source and a positron sensitive PSD LynxEye detector. PXRD patterns obtained after the initial COVID-19 lockdown were captured by Dr. Natalie Pridmore.

Multiphase Rietveld refinement was carried out using the software Profex (version 5.0.2) in order to determine phase quantities and unit cell parameters.[184] Profex provides a graphical user interface for the BGMN Rietveld refinement program. Crystal structures were mostly obtained from the Inorganic Crystal Structure Database (ICSD) as cif files and then imported into Profex to be converted into structure (str) files. ICSD numbers for phases used are included in the Appendix. Where an ICSD file was not able to be found, cif files were then either extracted from the Cambridge Crystallographic Data Centre, or found atomic information found from the initial discovery papers and then cif files created using the software VESTA.[185]

2.3.2 Microscopy

2.3.2.1 Scanning Electron Microscopy

Scanning electron microscopy (SEM) was carried out on a Jeol IT300 scanning electron microscope. In a typical analysis, a sticky carbon disk was adhered to an aluminium stub, before the sample was stuck to the disk. The samples were either left uncoated, sputtered in *ca.* 15 nm silver, or *ca.* 10 nm carbon. Energy dispersive X-ray analysis data were obtained using an X-max $80\,m^2$ EDX attachment from Oxford Instruments and analysed with the corresponding AZTec software.

2.3.2.2 Transmission Electron Microscopy

Transmission electron microscopy (TEM) was carried out on either a Jeol 1400 with a 120 kV accelerating voltage, or on a Jeol 2100 with a 200 kV accelerating voltage. Samples examined by the latter were run by Dr Jean-Charles Eloi. energy dispersive X-ray analysis (EDXA) were obtained with an X-Max 80T attachment and also analysed with the corresponding AZTec software. Samples were cast onto copper grids with either a full carbon film or a lacey carbon fillm. Samples were first suspended in ethanol, before brief sonication and then a drop of this was deposited onto the grid. selected-area electron diffraction patterns were obtained in diffraction mode on either TEM and analysed with the CrysTBox software.[186]

For the *in-situ* TEM, a single tilt heating holder (Gatan Model 628) was used. The sample grid was suspended between two tantalum spacers and mounted into the holder. The heating of the sample was controlled with a Gatan SmartSet Model 901 Hot Stage Controller, which allows the user to set a ramp rate and desired temperature automatically, or to control this manually by adjusting the current.

2.3.3 Resistance Measurements

For $YBa_2Cu_3O_{7-\delta}$ resistance measurements, the sample was etched with argon plasma for 15 seconds, before gold contacts were evaporated on top of the sample. Gold wires were contacted to the gold contacts with silver paint (Dupont N4929), before a 4-probe AC method was used to measure the resistance with an applied current of $10\,\mu A$. For $Bi_2Sr_2CaCu_2O_{8+x}$, the gold wires were attached directly to the sponge with silver paint (Dupont N4929) before the 4-probe AC method was used to measure the resistance. Images of the samples prior to resistance measurements for $YBa_2Cu_3O_{7-\delta}$ (Y-123) and $Bi_2Sr_2CaCu_2O_{8+x}$ (Bi-2212) can be found in Appendix A.5 and A.6 in the Appendix.

2.3.4 SQUID Magnetometry

Superconducting Quantum Interference Device (SQUID) magnetometry was carried out on an MPMS3 by Quantum Design. Samples were loaded into gel capsules, before being suspended in a straw. Samples were centred with a centering field between 500 and 1000 Oe. All samples were cooled under no field, before a field was applied and the moment measured on the increase in temperature. The data obtained for $Na_3Ni_2BiO_6$ (NNB) were obtained by the Henry Royce Institute on the same model of SQUID.

2.3.5 Porosity Analysis

2.3.5.1 BET Isotherm

Gas sorption isotherms were determined using nitrogen sorption at $77\,K$ with a Micromeritics 3-Flex volumetric gas sorption analysis system (nitrogen with purity of 99.9999% was purchased from Air Products). $100\,mg$ of samples were degassed under dynamic high vacuum ($10 \times 10^{-6}\,mbar$ mbar) at $120\,°C$ over 6 hours prior to analysis. Helium was used for free space determination following isothermal data collection.

2.3.5.2 Mercury Porosimetry

Hg-porosimetry was carried out by MCA Services on a MicroActive AutoPore V 9600.

NOVEL AND RAPID SOL-GEL SYNTHESES OF HONEYCOMB-LAYERED AND ORTHORHOMBIC METAL OXIDES

With regards to the synthesis of novel superconductive materials, their discovery is often based on the intuition of the researcher alone. There are superconductive families where the mechanism of superconductivity is still debated, and it is, therefore, difficult to determine which materials would be superconductive without resorting to 'carpet-bombing' type analyses, where large subsets of materials are sequentially tested. With the advent of high-throughput computing, materials chemistry is becoming able to predict novel superconductive materials and identify potential candidates without the necessity for testing each proposed material. This chapter presents a novel synthesis of two materials predicted to be superconductive by a machine learning algorithm, and the subsequent analysis of their magnetic behaviour.

3.1 Introduction

3.1.1 Data-driven discovery of materials

As computing power has become more powerful, predicting a material's properties prior to synthesis has become increasingly possible. This has been described as a 'new paradigm shift' in materials science. [187] Calculations using first principles, also known as *ab-initio* calculations, are now achievable within ever-shortening time-frames, enabling high-throughput calculations for

material property prediction. Many examples of *ab-initio* calculations are being exploited in the computation of novel materials, such as in protein-structure prediction and crystal structure prediction.[188,189] These *ab-initio* calculations have been used extensively in chemistry and materials science to predict reaction pathways, band structures and the shapes of the molecular orbitals. In the field of superconductivity, *ab-inito* techniques have been used previously to successfully predict novel superconductive and thermoelectric candidates, which were subsequently synthesised and tested.[190,191] Indeed, the recent discoveries of the hydride superconductors are due in part to the capability to calculate their properties through *ab-initio* calculations. This is the case for LaH_{10}, which was first predicted to be superconductive through computational calculations.[192] These calculations were later proven to be reasonably accurate upon the synthesis of the phase.[193] The calculation of key properties for these superconductors is possible as they can be described by the Bardeen-Cooper-Schrieffer Theory (BCS-theory) mechanism of superconductivity, so there is an understanding of what is required for a good superconductor in this case. When this is applied to the cuprate or iron based superconductors, it becomes a much more difficult problem to solve as the exact mechanism behind the superconductivity is not fully understood. As such, other techniques must be applied to predict novel cuprate materials, or indeed novel families of superconductors. However, there have been some recent breakthroughs in understanding cuprate superconductivity, so *ab-initio* calculations could soon become accessible for these materials.[194]

3.1.1.1 Machine learning

Machine learning is a process where a computer algorithm is used to learn patterns in data based on a training dataset, after which the new knowledge can be applied to a new dataset and thus predict results from these data patterns.[195] It is a type of artificial intelligence and is the technology behind many modern computational applications such as facial and voice recognition.[196] Machine learning can be ideal for delving into large amounts of data and subsequently using this data to predict new ideas based on patterns within this data. This has been successfully used for medical applications such as drug development.[197,198] Machine learning is best when using sufficiently large datasets for the resulting analysis, meaning that treating data before subjecting it to the machine learning algorithm is important to examine carefully. Nevertheless, machine learning has become a powerful tool for discovering novel materials through high-throughput calculations with large datasets.[199,200]

More recently, machine learning has also been used to predict completely novel superconductors without a prior understanding of their superconducting properties. In 2018, a machine learning algorithm was trained on the SuperCon database, a database full of all known superconductive materials. This algorithm was then applied to the Inorganic Crystal Structure Database (ICSD), and the machine learning pipeline identified several materials as potential superconductors.[201] 35 of these materials were identified as particularly interesting due to their lack of iron or copper in their crystal structure. This means that, should superconductivity be

Table 3.1: Table that summarises the 35 compounds identified by the machine learning algorithm to potentially exibit superconductivity. Figure reproduced from reference 201. An additional column has been added to provide the predicted T_C's identified by the pipeline.

Compound	Symmetry	ICSD Code	Predicted T_C / K
$CsBe(AsO_4)$	Orthorhombic	074027	24.57
$RbAsO_2$	Orthorhombic	413150	35.83
$KSbO_2$	Monoclinic	411214	34.13
$CsSbO_2$	Monoclinic	59329	31.83
$AgCrO_2$	Hexagonal	004149/025624	48.44
$K_{0.8}(Li_{0.2}Sn_{0.76})O_2$	Hexagonal	262638	26.84
$Cs(MoZn)(O_3F_3)$	Cubic	018082	33.78
$Na_3Cd_2(IrO_6)$	Monoclinic	404507	39.65
$Sr_3Cd(PtO_6)$	Hexagonal	280518	38.7
$Sr_3Zn(PtO_6)$	Hexagonal	280519	40.37
$(Ba_5Br_2)Ru_2O_9$	Hexagonal	245668	Below 5 K
$Ba_4(AgO_2)(AuO_4)$	Orthorhombic	072329	45.66
$Sr_5(AuO_4)_2$	Orthorhombic	071965	39.91
$RbSeO_2F$	Cubic	078399	28.57
$CsSeO_2F$	Cubic	078400	26.09
$KTeO_2F$	Monoclinic	411068	30.29
$Na_2K_4(Tl_2O_6)$	Monoclinic	074956	46.34
$Na_3Ni_2BiO_6$	Monoclinic	237391	41.23
$Na_3Ca_2BiO_6$	Orthorhombic	240975	43.74
$CsCd(BO_3)$	Cubic	189199	35.3
$K_2Cd(SiO_4)$	Orthorhombic	083229/086917	40.73
$Rb_2Cd(SiO_4)$	Orthorhombic	093879	43.13
$K_2Zn(SiO_4)$	Orthorhombic	083227	39.7
$K_2Zn(Si_2O_6)$	Orthorhombic	079705	36.26
$K_2Zn(Ge_2O_6)$	Orthorhombic	069018/085005/085007	50.88
$Na_6Ca_3(Ge_2O_6)_3$	Hexagonal	067315	30.06
$Cs_3(AlGe_2O_7)$	Monoclinic	412140	35.57
$K_4Ba(Ge_3O_9)$	Monoclinic	100203	44.74
$K_{16}Sr_4(Ge_3O_6)_4$	Cubic	100202	44.23
$K_3Tb[Ge_3O_8(OH)_2]$	Orthorhombic	193585	32.53
$K_3Eu[Ge_3O_8(OH)_2]$	Orthorhombic	262677	35.08
$KBa_6Zn_7(Ga_7O_{21})$	Trigonal	040856	30.13

found in any of these materials, it would indicate an entirely new family of superconductive materials. The initially reported table is reproduced in Table 3.1, but an extra column is added to indicate the predicted critical temperature (T_c) as determined by AFLOW and the initial algorithm.

Many of these compounds have been reported on only a few times, with no prior conductivity

or magnetic susceptibility data, except for $AgCrO_2$ and $Na_3Ni_2BiO_6$ (NNB), which were found to be antiferromagnetic.[181,202] Despite this, it was decided that NNB and $Na_3Ca_2BiO_6$ (NCB) were good candidates to attempt to synthesise due to the ease of availability of the metal nitrates of the constituent elements and due to their similar crystal structures. A further material chosen to be synthesised in this thesis was $KBa_6Zn_4Ga_7O_{21}$ (KBZGO), again due to ease of access of the metal nitrates. As discussed in Section 1.3.2.2, all of the metal nitrate salts used would be compatible with biopolymer-mediated syntheses where water is a solvent. It is possible that $AgCrO_2$ and NNB were identified as potential candidates by the pipeline *because* of their antiferromagnetic behaviour. This is because the cuprates, iron-pnictides, and iron-chalcogenides are antiferromagnetic in their parent states, requiring doping to induce the superconductive state.[203] Thus, the machine learning algorithm could have identified this as a potential marker for superconductivity.

3.1.2 $Na_3Ni_2BiO_6$ and $Na_3Ca_2BiO_6$

NCB and NNB are both layered metal oxides with crystal structures based on α-$NaFeO_2$.[181,204] α-$NaFeO_2$ and the Delafossite structure AMO_2 are common layered crystal structures, with many potential elemental compositions. α-$NaFeO_2$ in itself is an interesting material, as the iron ions are magnetically active but form a frustrated net, forming a frustrated antiferromagnetic material, as discussed in Section 1.1.4. Na_xCoO_2 is also a frustrated antiferromagnetic material, but it can form two hydrated compounds that exhibit superconductivity.[205] Typically in the α-$NaFeO_2$ structure, the alkali metal is octahedrally coordinated between layers of MO_6 octahedra. If 1/3 of the M ions are substituted for another element, $A_3M_2M'O_6$ is formed, though the exact crystal structure depends on the oxidation state and size of the constituent ions. If A and M' are similarly sized but very different in oxidation state - for example +1 to +5, the M and M' ions are crystallised in the same layer, with the M ions forming a hexagonal array around the M' ions, and is often referred to as a honeycomb layered oxide. This is the case for NNB and other members of the family such as $Na_3Ni_2SbO_6$, $Li_3Ni_2BiO_6$ and $Na_3Mn_2SbO_6$. Alternatively, a competing rock-salt like phase can form with a *Fddd* space group, which is often referred to as the orthorhombic phase - this is the case for NCB.[204,206] These two polymorphs can be in close competition with each other, and it has been shown that the synthesis method can be key in directing the eventual structure; this was seen with $Li_3Co_2SbO_6$, where varying the synthesis conditions altered the primary phase formed in the synthesis.[206] A graphical representation of the two crystal structures can be found in Figure 3.1

NCB has not been studied much following its initial synthesis, and thus its electronic and magnetic properties are yet unknown. The Material's project, a computational project with the aim of predicting many properties of materials computationally, has calculated a potential bandgap for this material of $1.564\,\text{eV}$, though notes that DFT calculations can underestimate this value.[207] The seminal synthesis of NCB involved a solid-state process, where the constituent
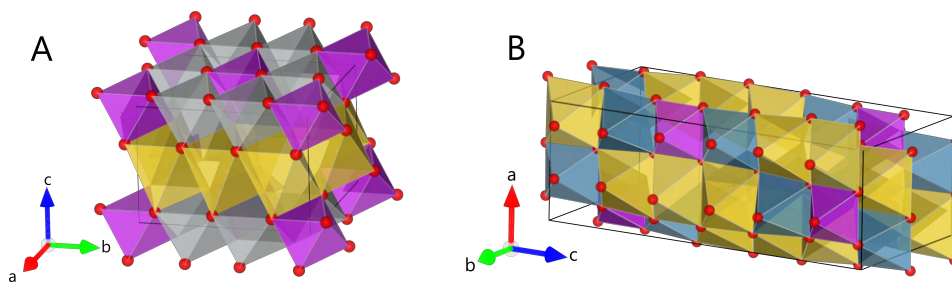
Figure 3.1: Figure depicting the crystal structures with a polyhedral representation of the octahedra in (A) NNB, where yellow represents sodium, silver represents nickel, purple represents bismuth, and red represents oxygen. (B) NCB where yellow represents sodium, blue represents calcium, purple represents bismuth and red represents oxygen.

elements were combined as solid powders and heated within a tube furnace. The calcination required a heat to $1100\,^{\circ}$C and holding there for $24\,$h. It was then cooled slowly to $800\,^{\circ}$C and held for an hour, before allowing to cool to room temperature naturally.[204] NCB is isostructural with $Na_3Ca_2TaO_6$, which is intriguing as $Na_3Ca_2TaO_6$ was found to exhibit some conductivity at high temperatures, indicating that there could be some interesting properties to NCB.[208]

An interesting magnetic structure is formed when a spin-active ion is present in the honeycomb-layered oxide, as is the case for NNB. Strictly speaking, this antiferromagnetic structure is not traditionally considered to be frustrated. Still, it must be acknowledged that magnetic ions on a hexagonal net can often experience some form of frustration that leads to a depression of ordering temperature. This can be seen when considering the next-nearest neighbour interactions of the magnetic ions. This manifests as a low magnetic ordering (Néel) temperature of 12 K.[181]

The seminal synthesis of NNB utilised a two-step synthesis, where metal oxide and carbonate powders consisting of the constituent elements were combined as powders and pressed into pellets and calcined in a furnace under flowing oxygen at $700\,^{\circ}$C for $8\,$h with a ramp rate of $2\,^{\circ}$C/min. This was followed by a regrinding step and reheating to $750\,^{\circ}$C for $12\,$h. Most further studies on NNB utilise this synthesis, though a top-down method has also been carried out, using electrospinning to create a fibre that is then calcined.[209]

3.1.3 Na-ion batteries

Li-ion batteries (LIBs) have revolutionised electronics and enabled high-power, portable electronics to become a regular feature of everyday life. The invention of LIBs was such a feat that the inventors Goodenough, Whittingham and Yoshino were awarded the Nobel Prize in chemistry in 2019.[210] However, despite their excellent energy density and rechargeability, these batteries have several downsides. LIBs commonly used in laptops and mobile phones are usually lithium-polymer batteries and consist of a polymer gel as an electrolyte. While gas generation occurs as a normal by-product of the reactions inside the cell, sometimes manufacturing errors

47
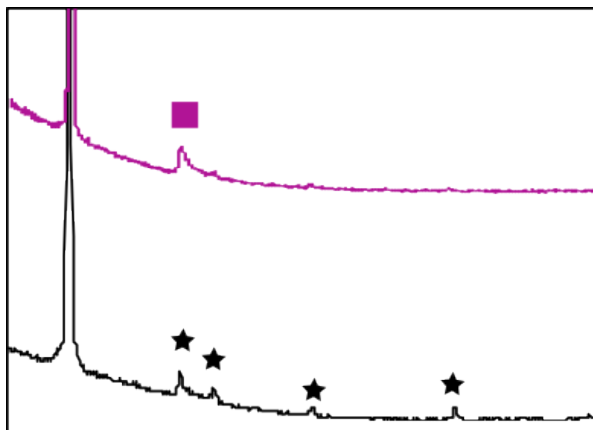
Figure 3.2: Figure depicting a slice from a powder X-ray diffraction (pXRD) pattern of NNB, where the black line depicts a sample that exhibited the hexagonal superlattice peaks (labelled with a star) indicative of the ordered structure, and the pink line represents a sample that exhibited stacking defects and thus consisted of only a Warren peak (labelled with a square).

can lead to excess gas production and the battery packs can swell and rupture, leading to the release of harmful and often flammable gases.[211] Additionally, there are several other factors that can lead to runaway reactions inside LIBs, resulting in excess heat production and often fires or explosions.[212,213] Indeed, a fault with the battery supplier caused Samsung to recall their Note7 phones after several reported fires.[214] This instability, combined with the fact that lithium is a finite resource in high demand, has led to the desire for alternative materials for a cathode, for example Na-ion batteries (NIBs).[215,216] NIBs are a favourable potential alternative to LIBs, due to the similarity in chemistry between sodium and lithium, combined with sodium's much higher abundance and increased relative safety.[217]

NNB has been explored for its potential as a cathode in NIBs due to the mobility of the sodium ions in the crystal structure.[218] The nickel ions in its crystal lattice are in a reduced-valence state, and are thus able to access a full redox chemistry. A similar material, $Na_3Ni_2SbO_6$ has also been shown to exhibit good cycling stability and theoretical discharge capacity.[219,220] However, there are often stacking defects along the c-axis in these materials, which can limit the battery capacity, resulting in poor performance.[221] These stacking defects manifest as characteristically shaped x-ray peaks known as Warren Peaks.[222] These peaks appear with a sharp increase in intensity at the low-angle end with a gradual decrease in intensity at the high-angle end, resulting in asymmetrical peaks.[223] For NNB, the stacking defects can be somewhat resolved by performing an additional annealing step. Figure 3.2 shows an example of what a Warren peak looks like in comparison to the peaks arising due to the hexagonal superlattice.

Warren peaks were first observed from the diffraction pattern of carbon black, which prompted Warren to analyse these anisotropic peaks mathematically to determine how they arose. He determined that it was a mixture of random-layer stacking, combined with broadening from small particle sizes that resulted in these distinct asymmetrical peaks.[223] The stacking features

that give rise to a Warren peak are due to random shifts between layers of unit cells. This can be imagined to be similar to a stack of cards which are not stacked uniformly on top of each other, but instead the occasional group of cards are shifted out of alignment. There is therefore a probability function for the likelihood of the planes to be shifted out of alignment, and the intensity of the diffracted peak is inversely related to this probability - if the stacks are aligned perfectly, the Bragg condition will be satisfied and therefore the diffracted peak will be registered by the detector.[224] Similarly to the broadening observed for small crystallites in pXRD, there is peak broadening in the case of disordered stacking due to too few planes being sufficiently aligned to destructively interfere fully.[168] These two effects behaving in tandem give rise to the Warren peaks in place of the distinct hexagonal superlattice peaks expected for NNB.

3.2 Results and discussion

This work aimed to explore novel syntheses of these metal oxides and subsequently test the magnetic behaviour with Superconducting Quantum Interference Device (SQUID) magnetometry. It was also decided that the synthesis techniques used should be facile, without the necessity for many solid-state heating steps with a view to create a more 'green synthesis'. Therefore, two methods were devised for this, one aqueous biopolymer-mediated synthesis, and one utilising a natural deep eutectic solvent (NADES) formed between betaine and glucose. The biopolymer-mediated synthesis was decided upon due to its previously proven robustness at synthesising metal oxide materials such as $YBa_2Cu_3O_{7-\delta}$, $Bi_2Sr_2CaCu_2O_{8+x}$ and metal oxide sponges and nanoparticles.[138,225,226] The method utilising the NADES between betaine and glucose was chosen due to its suitability for the synthesis of $Bi_2Sr_2CaCu_2O_{8+x}$, due to the ability of the NADES to solubilise the Bi^{3+} ions.[159] Due to its success with $Bi_2Sr_2CaCu_2O_{8+x}$, it was thought that this synthesis would be similarly compatible with NNB and NCB. Both of these methods are aqueous, thus the metal salts utilised in the synthesis were also important to consider, and where possible metal nitrates were chosen. The constituent elements for NNB, NCB and KBZGO are all available as metal nitrate salts, so these were chosen to be synthesised first from the list of interesting candidates by the machine learning algorithm given in Table 3.1. Of these metal nitrate salts, all are relatively benign, with only nickel being hazardous due to its status as a carcinogen. In comparison to other candidates identified by the machine learning algorithm, such as those containing hazardous elements such as arsenic, or those containing prohibitively expensive elements such as platinum, it was thought that beginning these studies with NNB, NCB and KBZGO would be interesting, to determine if superconductivity can be identified in these materials. Additionally, the lack of previous research on NCB and KBZGO was interesting, as these could be interesting materials for other applications besides superconductivity. NNB is an interesting compound in its own right, due to its potential as a cathode in NIBs.

3.2.1 The synthesis of $Na_3Ni_2BiO_6$

3.2.1.1 Aqueous synthesis method

The first synthesis attempted utilised an aqueous solvent with the addition of the biopolymer dextran as a chelating agent. To aid the dissolution of $BiNO_3 \cdot 5\,H_2O$, ethylenediaminetetraacetic acid (EDTA) was added to the initial solution. Bismuth has previously been shown to form insoluble hydrate salts such as bismuth subnitrate, which prevent it from dissolving into the aqueous solution.[227] The seminal synthesis of NNB used the sodium precursor in excess of 3 % to overcome its natural volatility.[181] Therefore, an excess of 3 % $NaNO_3$ was used in all syntheses.

A synthesis with 300 mg of dextran per 1 mL of aqueous precursor solution was attempted. This yielded the target phase of NNB when a dwell temperature of 700 °C was used, but it was also successful with 800 °C. This is unsurprising as the seminal synthesis required a temperature of 700 °C with a subsequent anneal at 750 °C. Interestingly, despite the prevalence of the target phase, the peaks that should arise due to the hexagonal superlattice were not present, and instead a Warren peak was observed, where there was a sharp peak at the low angle which tapers off in intensity at higher angles. This is shown in Figure 3.3, and indicated that the target phase exhibited stacking defects. Annealing the sample at 750 °C for 6 h yielded a sample with peaks attributable to the hexagonal superlattice, however this experiment was not reproducible, and annealing attempts with subsequent samples did not appear to work. Due to the high oxygenation of NNB, its first synthesis required an atmosphere of flowing oxygen for all steps of the synthesis. When dextran burns, it forms carbon dioxide and carbon monoxide, which result in a reducing atmosphere within the furnace. As the furnaces used in this work are chamber furnaces, there is very little airflow for the sample, thus resulting in a reducing atmosphere which is not ideal for the formation of NNB.

Therefore, to examine the effect of the amount of dextran on this synthesis, a few different amounts of dextran were utilised; 0, 100, 300 and 1000 mg. The resulting pXRD patterns are given in Figure Figure 3.3. The dextran used in this synthesis was labelled as 'high fraction', which corresponded to an average molecular weight of $M_r \backsim 250\,000\,Da$. The target phase was found to form only when 100 or 300 mg of dextran was used. The sample with only 100 mg exhibited the peaks that can be attributed to the hexagonal superlattice, thus indicating that the sample was ordered and didn't exhibit stacking defects. In contrast, the sample with 300 mg dextran exhibited a Warren peak instead of the characteristic peaks arising due to the hexagonal superlattice. In the absence of any dextran, the target phase did not form, indicating that the EDTA alone is not sufficient for the chelation of the metal ions in solution to result in the desired phase. It appears that there is a requirement for some biopolymer, as is the case with the 100 mg sample, but too much and the desired phase is no longer able to form, as is the case with the 1000 mg sample. Another interesting feature of the synthesis with 100 mg of dextran is the fact that when dwelled at 700 °C, the sample was less pure, and far less of the target phase formed. This indicates that the addition of less dextran has resulted in the requirement for a higher

dwell-time before the desired phase is formed.

In the pXRD patterns given in Figure 3.3, and those that appear later on in this chapter, two phases reported are $NaNO_2$ and $NaNO_3$ (sodium nitrite and sodium nitrate, respectively). Sodium nitrate is known to begin to decompose into sodium nitrite at temperatures above 450 °C, which would ordinarily rule it out as a potential products during this synthesis.[228] However, both sodium nitrate and sodium nitrite are also known to form molten salt mixtures, such as the equimolar mixture between potassium nitrate and sodium nitrate, which are much more stable and able to persist up to temperatures as high as 650 °C.[229]. It is therefore possible that the bismuth or the nickel nitrate is forming a molten salt with the sodium nitrate, and thus stabilising this component at much higher temperatures and resulting in the precipitation of the original salt after the furnace has cooled. Indeed, ternary molten metal salts have also been observed from mixtures of calcium, sodium and lithium nitrates, which are stable up to 600 °C.[230] To determine if this is the case, a future study could be to mix the sodium nitrate with bismuth and/or nickel nitrate individually, to determine if sodium nitrate is sill a product in this case. An alternative phase that could also match these pXRD peaks is $NaBiO_3$, which was first observed in 2020 through a hydrothermal synthesis.[231] However, this phase was also found to degrade at temperatures above 400 °C, which would mean it was also an unlikely product in this synthesis. Due to previous observations of molten salt formation for sodium nitrate and sodium nitrite, it was reasoned that these phases are possible to have formed in this synthesis and was therefore used for the refinements in the pXRD patterns in this chapter.

To further understand the phase evolution of this synthesis, dwell temperatures at 100 °C intervals between 500 and 1000 °C with 2 h dwell times were carried out. The resulting pXRD patterns and Rietveld analysis are given in Figure 3.4. As these samples were not examined *in-situ*, the phases present likely represent a thermodynamic product, rather than representing what was happening during calcination. To fully probe this, variable temperature pXRD would need to be utilised so that the phase evolution during the calcination can be analysed. Interestingly, a significant phase of the synthesis at 600 °C, and indeed the syntheses with no dextran and 1000 mg, seemed to match a polymorph of Bi_2O_3 which has only been observed from a high-pressure synthesis previously.[28] The phase observed is not the high-pressure polymorph reported during that work, but rather a decomposition product of the high pressure polymorph, denoted as $R-Bi_2O_3$. The high-pressure polymorph is metastable, and relaxes into $R-Bi_2O_3$, before a final transformation to the most commonly occurring polymorph of Bi_2O_3, α-Bi_2O_3. Additional evidence for the presence of this material came from energy dispersive X-ray analysis (EDXA) performed by Dr. Iryna Andrusenko on the material in a TEM. It was observed that there were two main morphologies of material, a rod-like material the consisted mostly of bismuth and oxygen and the bulk material which consisted mostly of nickel and oxygen. These data are presented in Appendix A.1. After roughly a year, this sample was re-examined with pXRD, and it was found that the crystal structure had transformed, at least partially to $Bi_2O_2CO_3$. While this
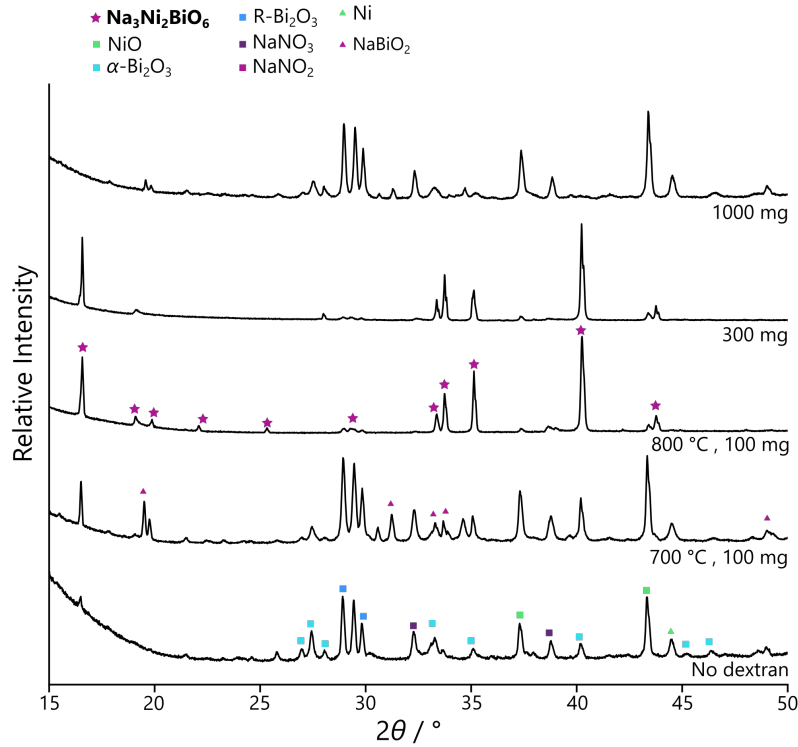
Figure 3.3: pXRD data showing the results of changing the amount of dextran on the product material. The dextran used in this synthesis had a molecular weight of $\sim 250\,000\,\mathrm{Da}$.

is not the expected α-$\mathrm{Bi_2O_3}$ phase, it is still a possible decomposition product of the $\mathrm{R-Bi_2O_3}$ phase. These data are also found in Appendix A.1. A full breakdown of the phase quantities as determined by Rietveld refinement can be found in Table 3.4.

Finally, the synthesis was reattempted with a different molecular weight of dextran to explore the effect of chain length on the synthesis. Therefore the synthesis was performed with with $\mathrm{M}_r \sim$ $70\,000\,\mathrm{Da}$ dextran instead of the higher molecular weight dextran used in the previous tests. The results from this synthesis at $800\,^{\circ}\mathrm{C}$ are examined in Figure 3.5, where it can be seen that the peaks due to the hexagonal superlattice are highly prevalent. The first hexagonal superlattice peak does exhibit a small amount of anisotropy, indicating that there could be some disorder to the structure. Rietveld refinement determined this sample to consist of 82 % of the target phase, $\mathrm{Na_3Ni_2BiO_6}$, 2 % $\mathrm{R-Bi_2O_3}$, 6 % NiO and 9 % $\mathrm{NaNO_3}$. The $\mathrm{R_{wp}}$ of this sample was 5.61 %, resulting in a χ^2 of 4.16. Despite being the lowest χ^2 observed thus far, it is still not within the general acceptance limit of $\chi^2 = 1.5$. The higher χ^2 in this case could be due in part to the anisotropic peak observed for the first hexagonal superlattice peak. As the disordered polymorph does not have a crystal information file (CIF), Profex is not able to accurately refine these data. scanning electron microscopy (SEM) of the sample indicated that it was mostly formed of a blocky structure, without much porosity or direction of structure. It is possible that attempting to

Figure 3.4: (a) pXRD data depicting the phases present in the product material calcined at various different temperatures. These syntheses utilised 100 mg of the $M_r \backsim 250\,000\,\mathrm{Da}$ dextran. The target phase, NNB was observed at 700 and 800 °C. (b) Plot depicting the phase evolution of the different constituent phases present during the aqueous synthesis at different temperatures.
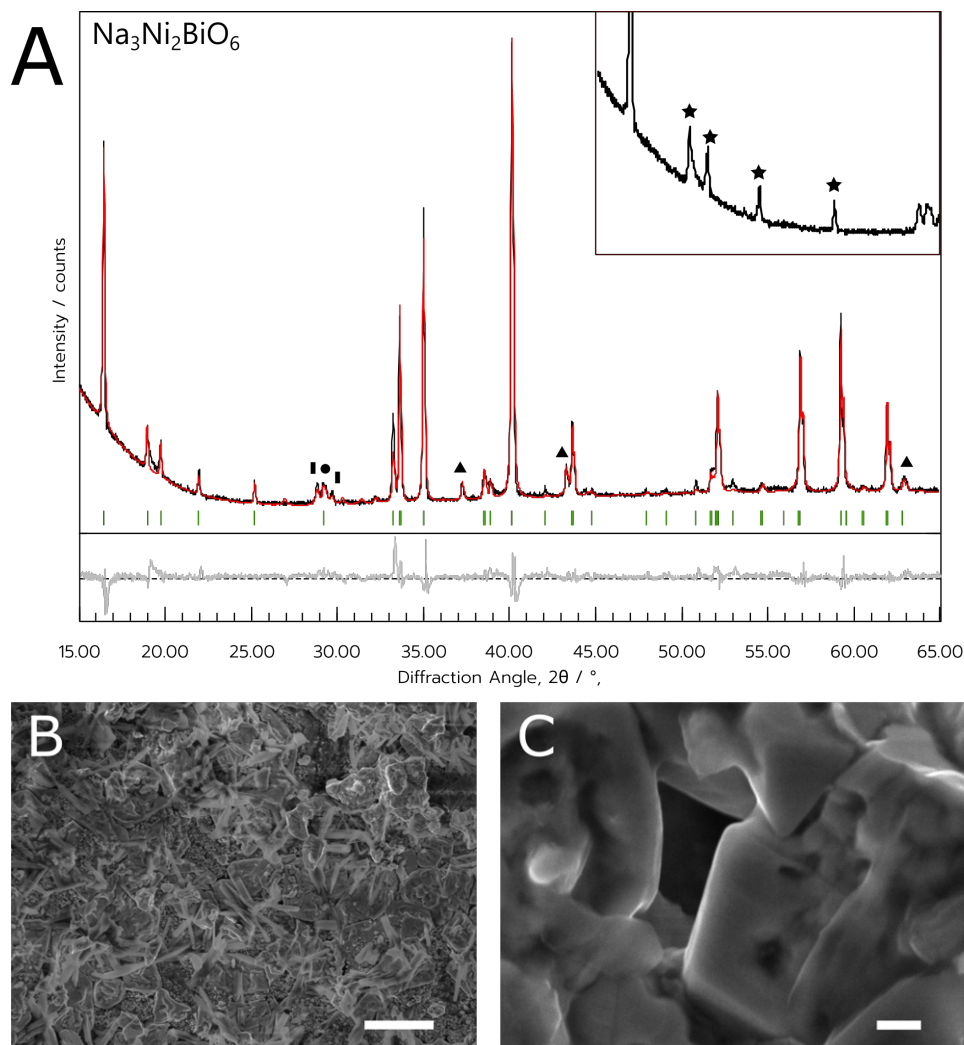
Figure 3.5: a) pXRD data of the NNB sample synthesised using 100 mg dextran as the chelating agent. Green indices are attributed to the Bragg reflections of the target $Na_3Ni_2BiO_6$ phase. Impurities of NiO and $NaNO_3$ are indicated by the triangle and circle symbols, respectively. Inset shows a magnified section of the experimental data between 15°and 27°2θ with stars denoting the peaks arising from the hexagonal superlattice. b) and c) SEM images of the NNB sample, depicting a clear difference in morphology of the sample. Scale bar in (b) indicates a length of 20 μm, (c) indicates a length of 1 μm.

manipulate

some deliberate control of the structure.[225] The gel formed in this synthesis is likely not viscous enough, however, to be able to draw it into strands.

From these syntheses, it has been found that it is possible to synthesise NNB through a biopolymer-mediated synthesis. The most promising example is an 800 °C synthesis with a 2 h dwell time and the dextran with a $M_r \sim 70\,000$ Da.

3.2.1.2 Synthesis by a natural deep eutectic solvent

This synthesis is based on a method that was first devised by Rojas *et al.* for the synthesis of $Bi_2Sr_2CaCu_2O_{8+x}$ (Bi-2212). The advantage of this method was the excellent ability of the NADES to solubilise the bismuth nitrate pentahydrate and there was therefore no need to add additional chelating agents such as EDTA. As such, this synthesis was adapted for the synthesis of NNB. Similarly to the aqueous syntheses, a phase evolution study was carried out, where multiple samples were calcined at different temperatures between 500 and 1000 °C to gain a broad understanding of which phases formed during the syntheses. The pXRD patterns and Rietveld phase evolution information are found in Figure 3.6 and a full breakdown of this information as determined by Rietveld refinement can be found in Table 3.3. As with the aqueous synthesis, common impurities were NiO and $NaNO_3$. Again, the metastable phase $R-Bi_2O_3$ was observed at various temperatures throughout the synthesis. The target phase formed at 800 and 900 °C, with an optimum temperature of 800 °C. While this is a higher temperature than the seminal synthesis, the overall dwell time is greatly reduced, and it forgoes the necessity for flowing oxygen throughout and a subsequent annealing step.

Further analysis of this sample synthesised at 800 °C indicated that there was a prevalence of hexagonal superlattice peaks (Figure 3.7a). This indicated that the sample was an ordered polymorph without stacking defects in the crystal structure. From SEM, it was found that the material's structure was predominantly porous, but there was also evidence of micro- and nanowires spread sporadically throughout the porous network, as seen in Figure 3.7. These were not confirmed to be due to the target phase and indeed it is likely that they are due to an impurity phase such as $NaNO_3$ or $R-Bi_2O_3$. The pores could be due to the decomposition of the NADES into CO_2 during the heating cycle, which forms bubbles within the remaining metal oxide. The porous nature of this material could be a beneficial architecture of electrodes; it has been shown that a porous material for an electrode could be ideal, as the larger surface area could allow ample contact between the electrolyte and the electrode surface.[232]

Rietveld refinement determined that the powder consisted of 76 % of the target phase, 17 % of the $NaNO_3$ and 7 % NiO. The goodness of fit of this refinement was 4.02, which corresponds to a χ^2 of 16.20. This worse fit appears to arise due to an intensity mismatch between the (001) and (002) peaks in the pattern. The (002) peak is relatively higher intensity than the (001) peak. Often in Rietveld refinement, the parameters of each structure must be adjusted in order to account for things such as preferential orientation or microstrain within the structure. However, in the case of the (001) and (002) peaks, accounting preferential orientation would not overcome the intensity mismatch as they arise from the same direction of the crystal lattice. It is possible that this mismatch is due to the uncertainty of the site occupancy for the Ni and Bi ions given in the CIF; in the originally reported structure, the first Bi/Ni site is 63.8 % likely to contain Bi and 36.2 % likely to contain Ni, whereas the second site is more likely to be occupied by Ni over Bi (81.8 % for Ni and 18.1 % Bi). Nickel and bismuth scatter X-rays differently; nickel has a much

55
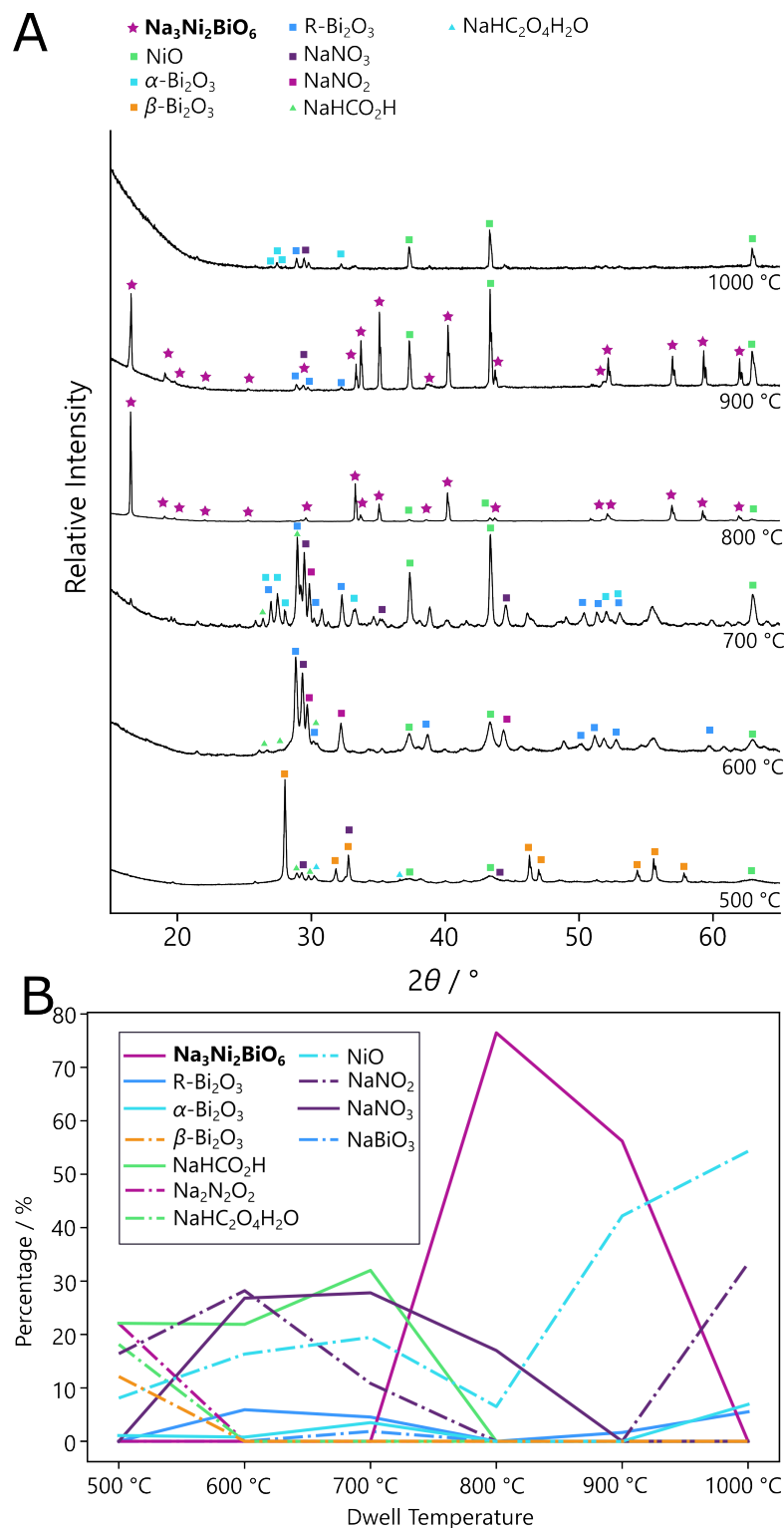
Figure 3.6: (a) pXRD data depicting the phases present in the product material calcined at various different temperatures synthesised with the NADES method. The target phase, NNB was observed at 800 and 900 °C. (b) Plot depicting the phase evolution of the different constituent phases present during the NADES synthesis at different temperatures.

lower scattering factor than bismuth. Therefore, if the occupancy of this site is different to what is expected, the relative intensities of the (001) and (002) peaks could be affected. Another reason for the intensity mismatch could be due to the stacking defects that reduce the intensity of the hexagonal superlattice peaks. These stacking defects are along the c-axis, meaning that if the unit cells are not stacking correctly, there could be a lower-than-expected signal from the (001) plane. As the (002) plane is within the unit cell, if the stacking slip is between unit cells, the intensity of the (002) plane should be relatively unaffected, thus yielding the (002) being higher in intensity than expected when compared to the (001) reflection.

Upon repeat experiments, it was also found that the disordered polymorph of NNB occasionally formed. The cause for this is likely due to the slight changes in the atmosphere within the furnace yielding a reducing environment and thus resulting in stacking defects in the product material. This synthesis, along with the aqueous synthesis, is incompatible with utilising flowing oxygen due to the combustible precursor materials. However, subsequent annealing steps could be utilised to attempt to produce an ordered polymorph. Additionally, performing this reaction in an open tube furnace to allow for the carbon dioxide produced by the reaction to escape, yielded the ordered polymorph.

3.2.1.3 Magnetic susceptibility measurements

The sample synthesised by the aqueous method with $100 \, \text{mg}$ of $M_r \backsim 70\,000 \, \text{Da}$ dextran was analysed by SQUID due to the prevalence of hexagonal superlattice peaks. The volume susceptibility of the samples was calculated using Equation 1.2, where the density used was the literature-reported crystal density. For these samples, a susceptibility against temperature plot which was characteristic of an antiferromagnetic material was observed, shown in Figure 3.8 which is consistent with what has been observed for this material previously.[181] The magnetic ordering temperature, or Néel temperature, was observed to be $11.9 \, \text{K}$. Additional analysis of this sample was also possible, in order to calculate additional physical properties using equations 1.1 and 3.1.

The Curie-Weiss temperature of the material could be calculated by plotting a graph of $\frac{1}{\chi}$ against T. In this way, the gradient of such a plot represents $\frac{1}{C}$, where C is the Curie constant and the intercept of this graph represents $\frac{\theta_{CW}}{C}$ where θ_{CW} is the Curie Weiss temperature. In some cases, a temperature-independent correction factor, χ_0, is utilised to accommodate unaccounted for interactions, such as diamagnetism of the sample holder or additional magnetic effects of the sample.[52] In this case, however, it appears that the extra correction factor was unnecessary, as the resulting $\frac{1}{\chi}$ against T showed a good straight line relationship. Using this plot of $\frac{1}{\chi}$ against T, a line of best fit between 40 and $130 \, \text{K}$ was extrapolated. This lead to a gradient of 2.07, with an intercept of 1.16, which leads to C equalling $0.484 \, \text{K}^{-1}$ and a Curie-Weiss, θ_{CW}, temperature of $0.79 \, \text{K}$. A positive value of the Curie-Weiss temperature when considering an antiferromagnetic material is indicative of a frustrated system. The small magnitude of θ_{CW} in this case, however,
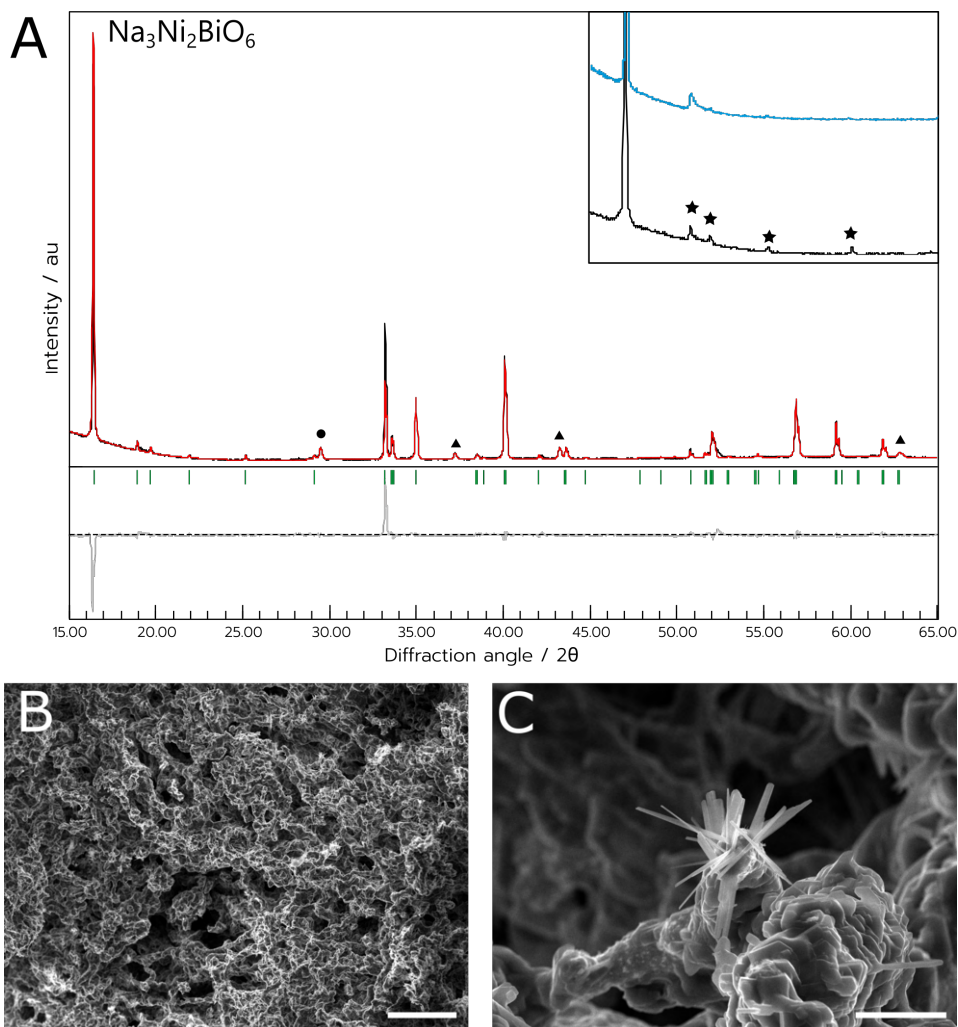
Figure 3.7: a) PXRD data of the NADES sample synthesised at 800 °C. Green indices are attributed to the Bragg reflections of the target $Na_3Ni_2BiO_6$ phase. Impurities of NiO and $NaNO_3$ are indicated by the triangle and circle symbols, respectively. Inset shows a magnified section of the experimental data between 15°and 27°2θ, with stars denoting the peaks arising from the hexagonal superlattice. In blue is an example of an experiment that resulted in the Warren peak instead of peaks belonging to the hexagonal superlattice. b) Scanning electron micrograph depicting the as-synthesised material. c) Scanning electron micrograph depicting the as-synthesied material, focusing on the nanowire-like growths that occurred throughout. Scale bar in (b) indicates a length of 100 µm, (c) indicates a length of 10 µm.
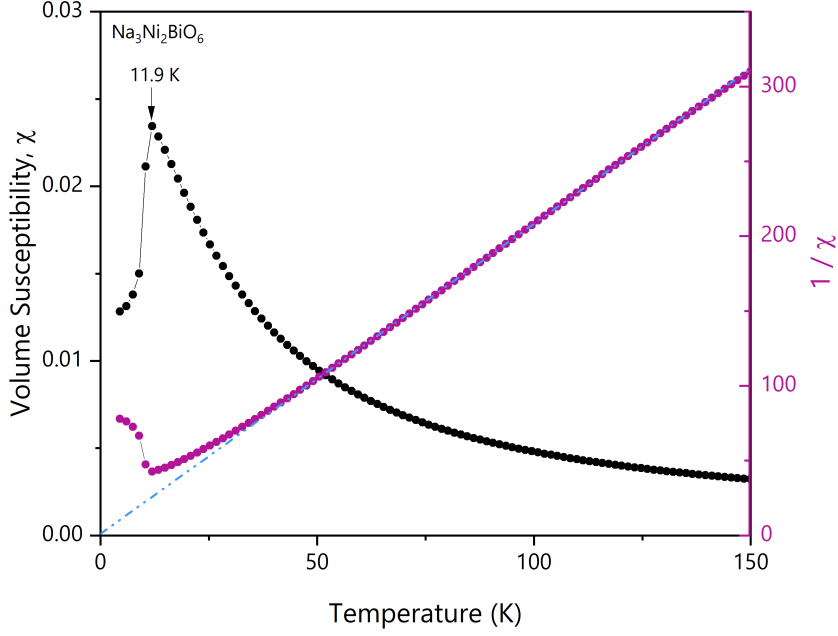
Figure 3.8: Zero-field cooled SQUID magnetometry data of the NNB sample synthesised with the biopolymer-mediated synthesis with $100\,$mg of dextran with $M_r \backsim 70000$. In purple is the plot of inverse susceptibility against temperature. This SQUID data was obtained by the Henry Royce institute at Sheffield.

indicates that the degree of frustration is low, and that it behaves as a paramagnetic material at room temperature.

$$(3.1) \qquad\qquad C = \frac{n\mu_0\mu_{eff}^2}{3K_B}$$

From these data, it is possible to also calculate the effective moment of the nickel ions within the sample. Using the volume of the unit cell to be the literature-reported value of $271.9\,$Å and the fact that there are 6 nickel ions per unit cell, the volume density of nickel, n, in this case was $2.2 \times 10^{28}\,\mathrm{m}^{-3}$. Rearranging equation 3.1 gives equation 3.2

$$(3.2) \qquad\qquad \mu_{eff} = \sqrt{\frac{3k_B C}{n\mu_0}}$$

Using the calculated value of C, $0.484\,\mathrm{K}^{-1}$, and the calculated value of n, it follows that the effective moment, μ_{eff} was calculated to be $2.90\,\mu_B$, where μ_B is the Bohr magneton, with a value of $9.274 \times 10^{-24}\,\mathrm{J\,T}^{-1}$. This is consistent with a divalent nickel ion in an octahedral environment, and indicates that the magnetic behaviour of the crystal is, indeed, arising from the nickel ions within the lattice.[52]

59

3.2.2 The synthesis of $Na_3Ca_2BiO_6$

3.2.2.1 Aqueous synthesis method

This synthesis method was initially unsuccessful due to the metal nitrate salts dropping out of solution frequently, even with the addition of EDTA. Following several attempts, the synthesis was subsequently carried out by creating two separate aqueous solutions: one with $Bi(NO_3)_3 \cdot 5H_2O$ only, and one with $NaNO_3$ and $Ca(NO_3)_2 \cdot 4H_2O$. Using the knowledge from the syntheses of NNB, the synthesis utilised 100 mg of dextran. Initially, it was believed that this method was incompatible with NCB, as the target phase was not formed when synthesised at 1000 °C, which was thought to be the temperature necessary for this phase based on its seminal synthesis. However, further temperature studies, where dwell temperatures between 500 and 1000 °C were used, determined that the target phase formed between 700 and 900 °C, after only a 2 h dwell time. A plot of this data can be found in Appendix A.2. A control experiment was also carried out with no addition of dextran, in order to determine if the dextran was necessary for the formation of the target phase. As can be seen from Figure 3.9, the target phase did form, however there were also several impurity phases such as $Ca_4Bi_6O_{13}$, $Ca_6Bi_6O_{15}$ and CaO which lowered the overall purity of the sample. Comparing the two syntheses, both samples were very similar, with a significant percentage of the sample consisting of CaO. For both samples. the percentage of the sample that formed the target phase was around 50 %, indicating that there is some change needed to the synthetic method to yield a more pure sample.

Based on the data for NNB, it was considered that using dextran with $M_r \backsim 70,000$ could result in the synthesis of a purer sample of NCB. As such, it was decided that the use of 100 mg dextran with $M_r \backsim 70\,000$ Da should also be examined. Dwell temperatures between 600 and 1000 °C were carried out with this molecular weight of dextran, and the results of this can be found in Figure 3.10. It appears that this method is very successful at synthesising the target phase, and it was successfully synthesised between temperatures of 700 - 900 °C. The optimum temperature for the synthesis of NCB using this method was found to be 800 °C with it found to consist of 79 % of the target phase, though the synthesis at 700 °C was also excellent, with a phase purity of 70 %. It is important to note that these phase evolution data are not taken *in-situ*, and instead likely represent a thermodynamic product from each synthesis. Additionally, to keep the samples consistent with each other, the furnace was dwelled at each temperature for 2 h, further ensuring that the product consisted of the thermodynamic product. It appears as though with this method, the target phase begins to break down into CaO and $Ca_6Bi_6O_{13}$ and, presumably, some volatile Na-phases above 900 °C, as evidenced by the data observed for the 900 and 1000 °C dwell times. This is interesting when considering the seminal synthesis of NCB, as the maximum dwell temperatue in that synthesis was 1000 °C. Another common impurity phase was $Na(NO_3)$ which was also observed with the synthesis of NNB. A full breakdown of this phase information can be found in Table 3.4.

It is interesting that there is such a marked difference between the syntheses with 'High-
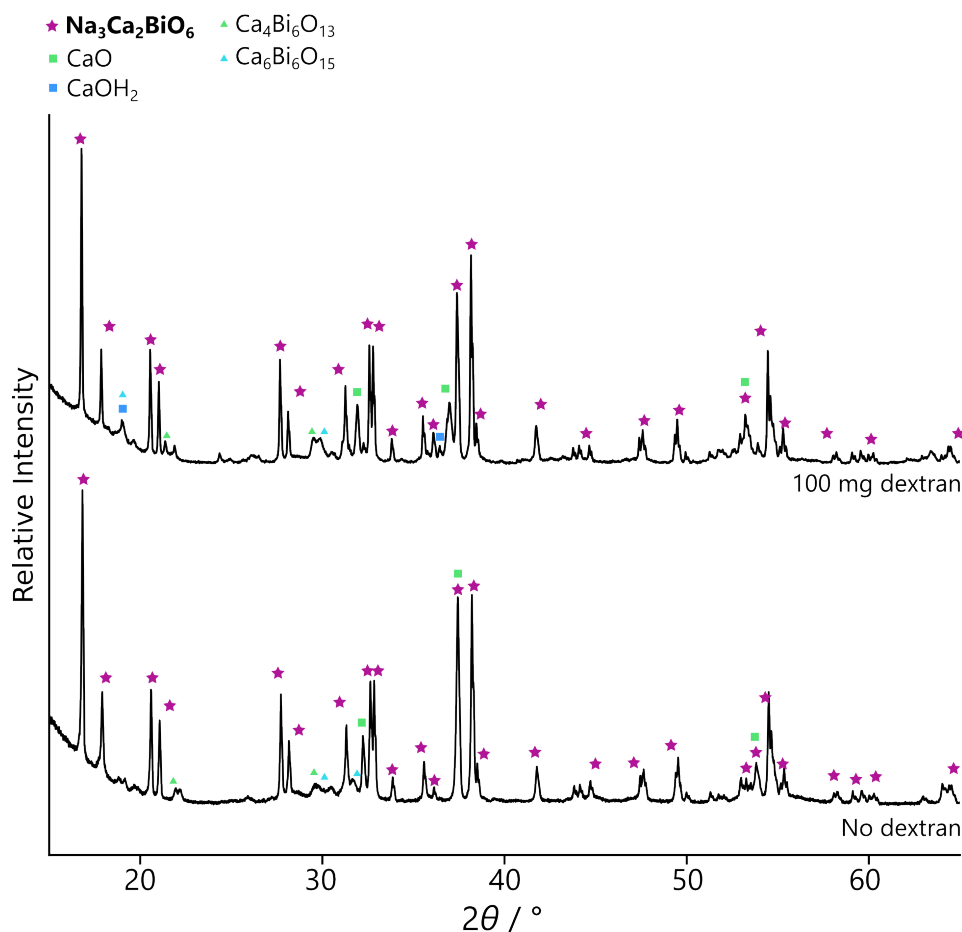
Figure 3.9: pXRD data for (top) NCB synthesised using 100 mg dextran and (bottom) synthesised without any dextran.

fraction' dextran as compared to dextran with a $M_r \backsim 70\,000$ Da. Changing the molecular weight of dextran has been shown previously to affect red blood cell aggregation and on its phase separation properties with protein/dextran aggregations.[233,234] The difference between the samples in this case could be due to the lack of movement of the longer chains of dextran, resulting in poorer mixing of the metal cations in solution, thus preventing a good random mixing of the metal ions and thus yielding a poorer quality product.
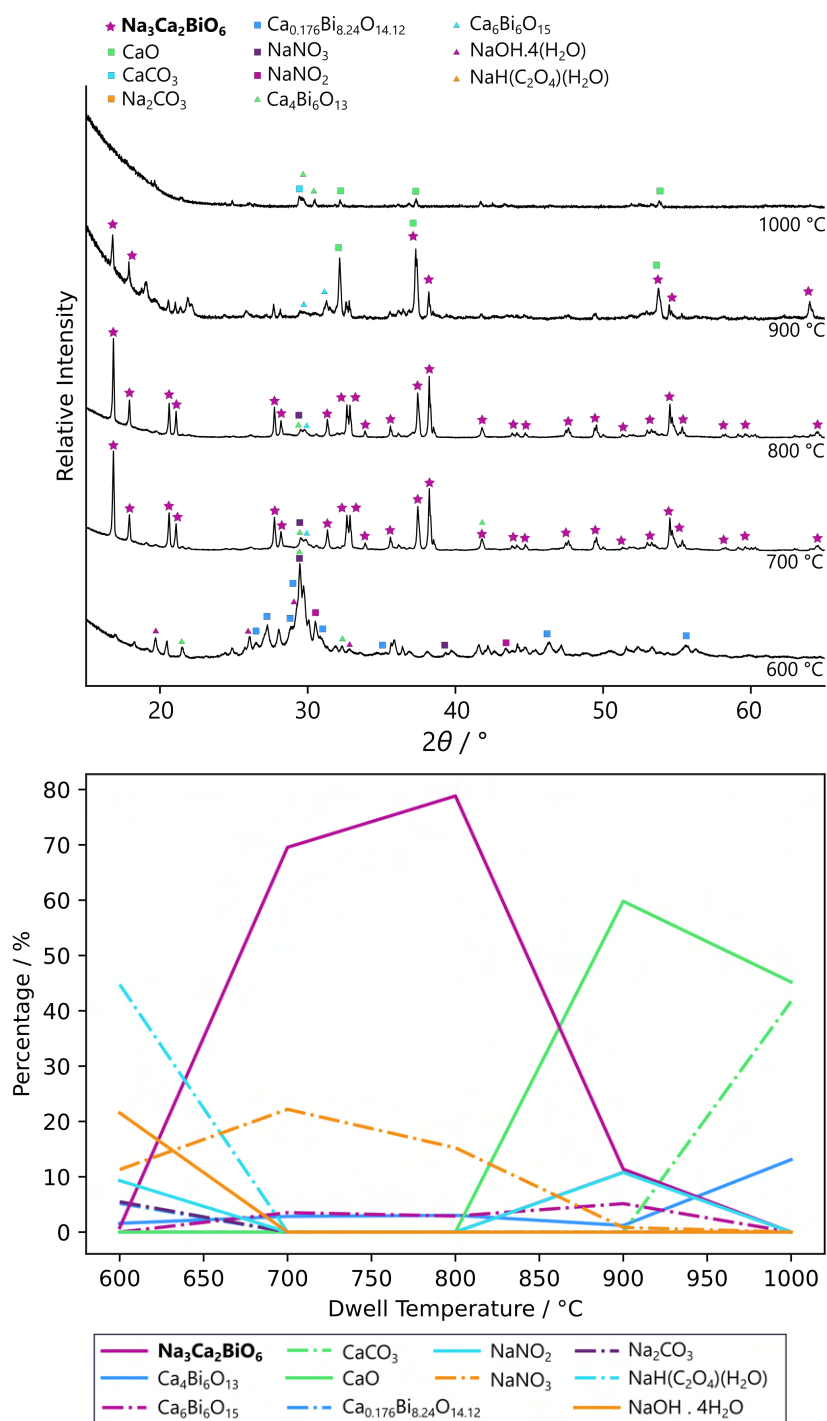
Figure 3.10: a) pXRD data depicting the phases present in the product material calcined at various different temperatures *via.* the biopolymer-mediated synthesis with $M_r \backsim 70\,000\,\text{Da}$ dextran. The target phase, NCB was observed between 700 and 900 °C. (b) Plot depicting the phase evolution of the different constituent phases present during the NADES synthesis at different temperatures.
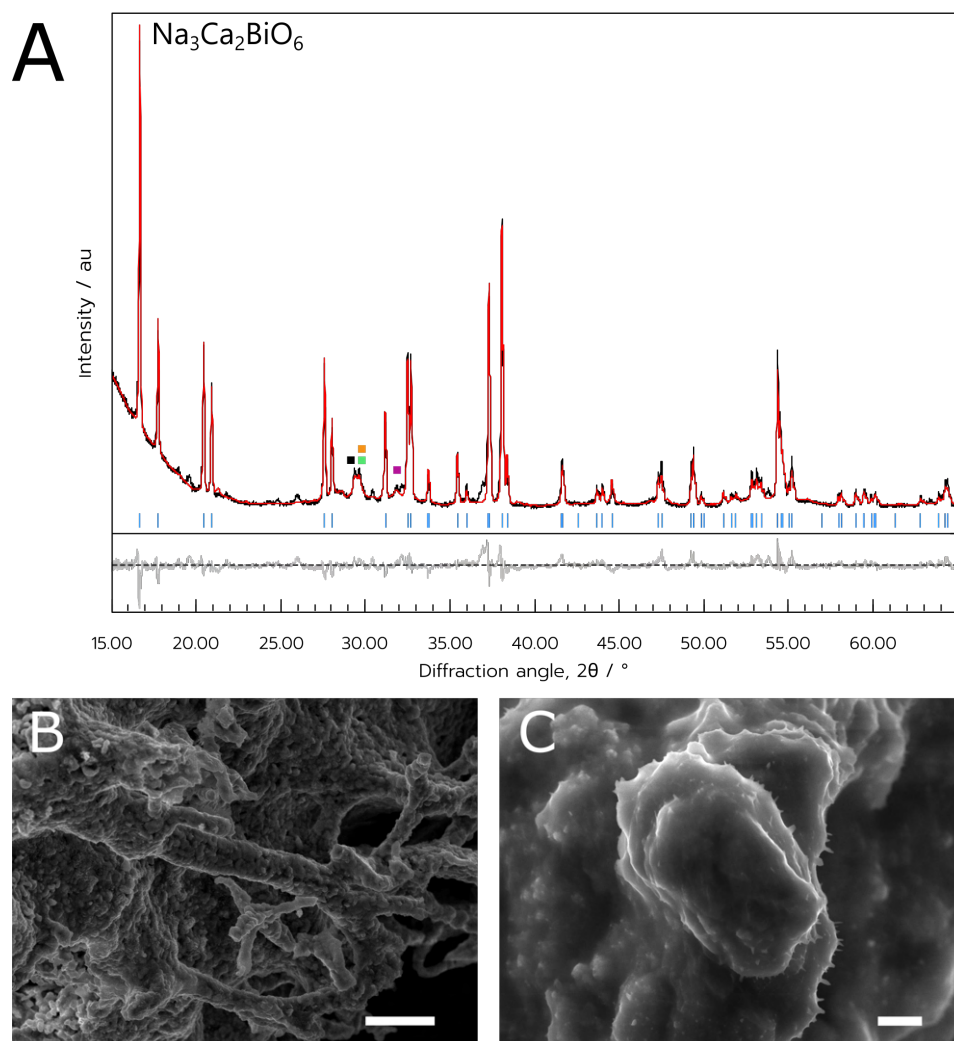
Figure 3.11: a) pXRD data of the NCB sample synthesised through the aqueous method. Blue indices are attributed to the Bragg reflections of the target phase, $Na_3Ca_2BiO_6$. Impurity peaks belonging to $Ca_4Bi_6O_{13}$, $Bi_6Ca_6O_{15}$, and β-Bi_2O_3, $NaNO_3$ are denoted by green, orange, purple and black squares respectively. b) and c) SEM images of the NCB-aqueous sample. Scale bars indicate a length of (b) 10 μm and (c) 2 μm.

3.2.2.2 Synthesis via a natural deep eutectic solvent

This synthesis followed the same process as what was carried out for NNB. The bismuth nitrate readily dissolved into the NADES, and no precipitation was observed when the NADES solution was combined with the NaCa-aqueous stock solution (the same as what was used for the aqueous synthesis). After heating for two hours at 80 °C, the solution was viscous and dark brown, indicating that the water had completely evaporated from the solution. The target phase was detected at 700, 800 and 900 °C, but syntheses were also carried out at 500, 600 and 1000 °C. Unlike the synthesis of NNB, the metastable polymorph of Bi_2O_3 was not observed after these syntheses. Common impurity phases discovered were $Ca_4Bi_6O_{13}$ and $Ca_6Bi_6O_{15}$, though it is

63

possible that the true phases present were actually an off-stoichiometry of these, as there are a
wide-range of possible Ca-Bi-O stoichiometries that are able to form. Interestingly, in comparison
to the syntheses with NNB, the only Bi_2O_3 polymorph that was found to form a majority phase at
any point was β-Bi_2O_3, which was the major product for the synthesis at 500 °C. Instead, at higher
temperatures, β-Bi_2O_3 seemed to convert to $Ca_4Bi_6O_{13}$ and $Ca_6Bi_6O_{15}$. It appeared that Bi-Ca-O
phases were more likely to form over Bi-O phases. Additionally, the metastable $R-Bi_2O_3$ phase
was not observed in any of these syntheses, indicating that it is energetically more favourable for
the formation of Bi-Ca-O phases than for the metastable $R-Bi_2O_3$. Additionally, very few mixed
Ni-Bi-O phases were observed in the syntheses of NNB. This indicates that Bi-Ni-O phases are
much less energetically favourable than Bi-Ca-O phases, possibly due to the differing Shannon
radii of Ca^{+2} versus Ni^{+2}.[235] Full Rietveld refinement details can be found in Table 3.5

As with the aqueous synthesis method, the optimum dwell temperature was determined to be
800 °C, with 91 % of the sample consisting of the target phase, $Na_3Ca_2BiO_6$. The data given in
figure 3.13a shows the as-refined pXRD data. In 3.13b and c, the morphology of the sample as
analysed by SEM is shown. It appears that, as is consistent with the equivalent NNB sample,
this NADES-synthesised material is porous with small crystallites. The target phase made up
91 % of the sample, with other impurity phases of $Ca_4Bi_6O_{13}$ (3 %), $Ca_6Bi_6O_{15}$ (3 %) and Bi_4O_7
(3 %), The refinement had a goodness of fit value of 2.77. This data was very promising, and it
was therefore clear that the target phase, $Na_3Ca_2BiO_6$ had been successfully synthesised by this
method. This method was also repeatable, though the exact percentage of the target phase would
fluctuate between 80 - 90 %, with differing quantities of the impurity phases.

Overall, it appears that for optimal synthesis of NCB *via.* a NADES, the dwell temperature
should be 800 °C. This temperature appears to be the most viable temperature, as syntheses
at 700 or 900 °C resulted in poor purity of the target phase. It is possible that adjusting these
parameters by dwelling at temperature for longer could improve syntheses at these temperatures.
However, it remains the case that this synthetic technique allowed the production of the target
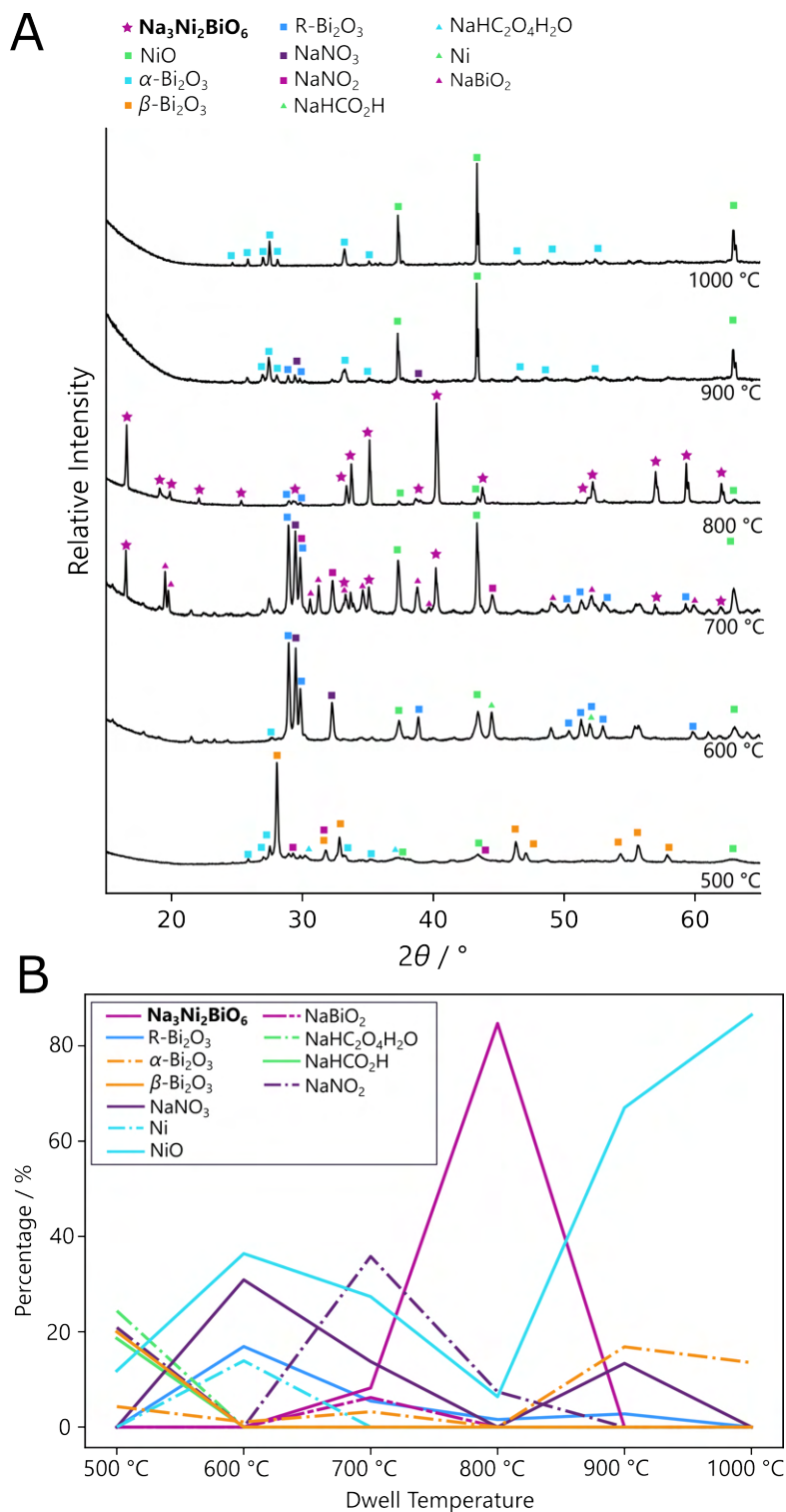phase at a much reduced dwell temperature and dwell time than the seminal synthesis.
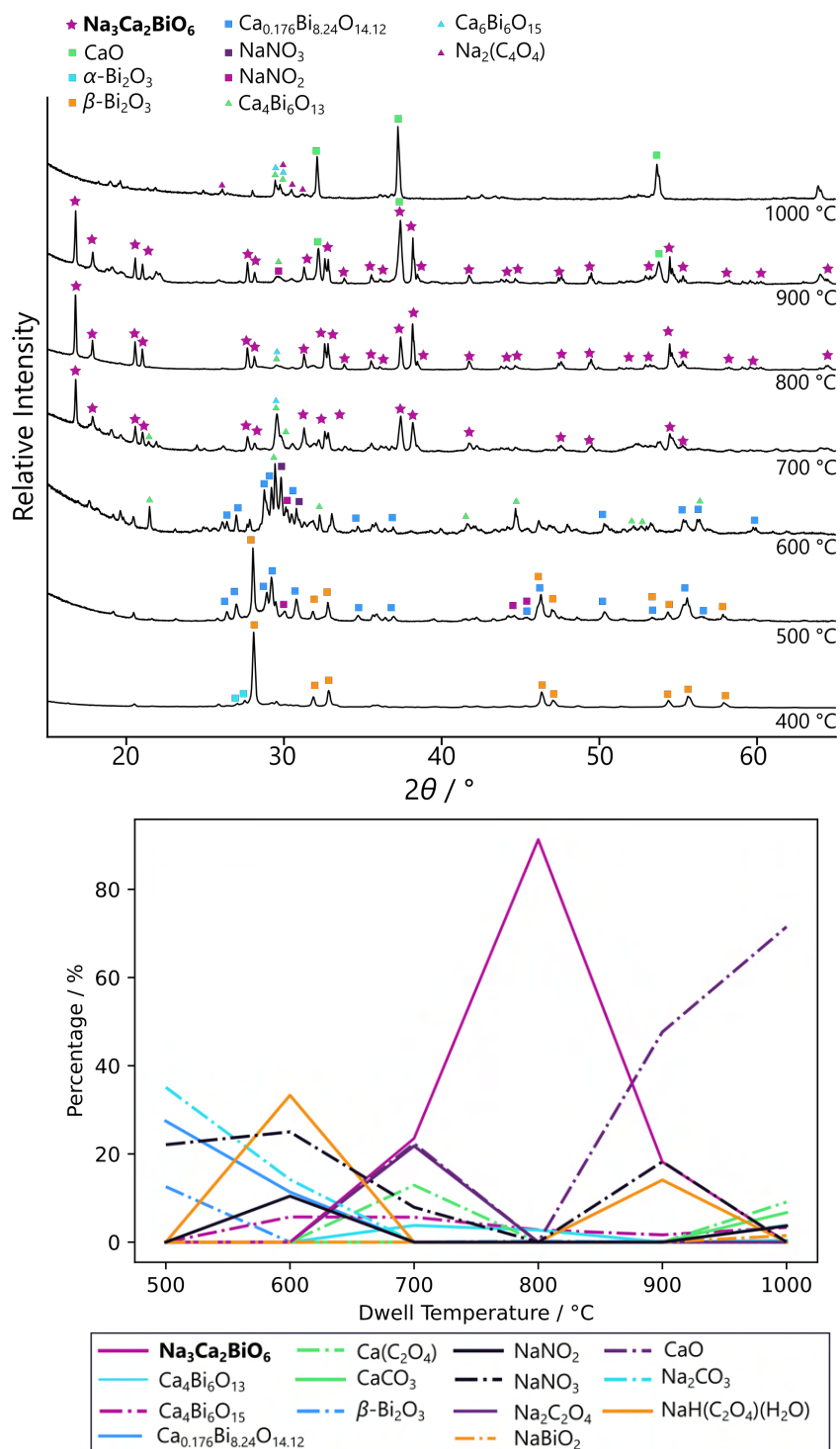
Figure 3.12: (a) pXRD data depicting the phases present in the product material calcined at various different temperatures. The target phase, NCB was observed at 700, 800 and 900 °C. (b) Plot depicting the phase evolution of the different constituent phases present during the NADES synthesis at different temperatures.
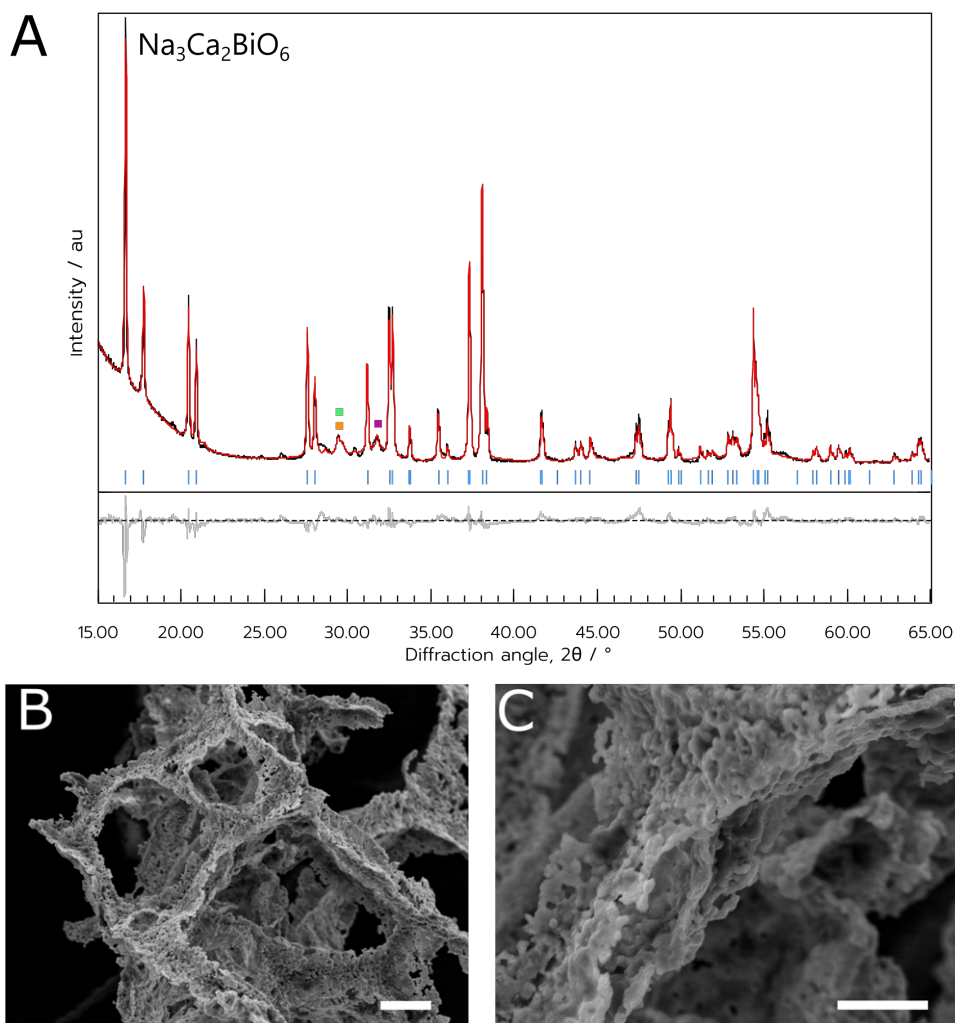
Figure 3.13: a) pXRD data of the NCB NADES sample. Blue indices are attributed to the Bragg reflections of the target $Na_3Ca_2BiO_6$ phase. Impurity peaks belonging to $Ca_4Bi_6O_{13}$, $Bi_6Ca_6O_{15}$, and β-Bi_2O_3 are denoted by green, orange and purple squares respectively. b) and c) SEM images of the NCB NADES sample. Scale bars indicate a length of (b) $20\,\mu m$ and (c) $10\,\mu m$.

3.2.2.3 Magnetic susceptibility measurements

For the NCB samples, SQUID magnetometry was carried out on the NADES sample calcined at $800\,°C$. A zero-field cooled measurement was carried out from 2 to $150\,K$ with an applied field of 100 Oe. As was the case with the NNB magnetic measuments discussed in Section 3.2.1.3, the volume susceptibility of the sample was calculated using the crystal density as reported in the literature and the mass of the sample loaded in the gel capsule.[204] The measured data show a characteristic upturn of magnetic susceptibilty at low temperatures, which is indicative of a paramagnetic material. However, the magnitude of the signal is very small, at a volume susceptibility on the order of 1×10^{-4}. As such, it is possible that the signal arises from impurities within the material that are not detectable by pXRD. By performing a fit to the data with equation
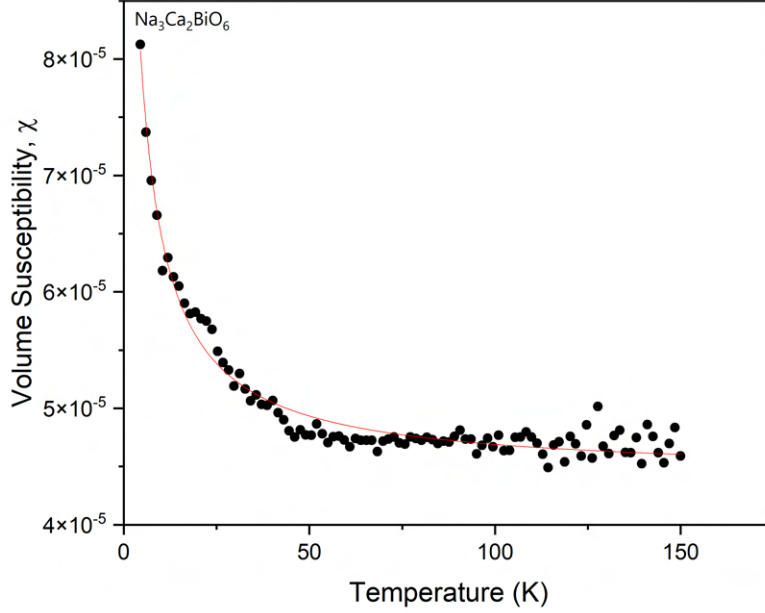
Figure 3.14: Zero-field cooled SQUID magnetometry data of the NCB sample synthesised with the NADES method. The red line is fitted to the data with equation 1.2.

1.1, the Curie constant and the Curie-Weiss constant could be extracted. With this sample, an additional correction factor, χ_0 was applied as it resulted in the best fit to the data. From these data, a value for the Curie constant of $2.65 \times 10^{-4} \, K^{-1}$ was obtained. The Curie Weiss temperature, θ_{CW}, was determined to be $-2.79 \, K$, which indicates a slight antiferromagnetic behaviour.

To estimate the percentage of the sample that is giving rise to the signal, equation 3.1 can be used. If one were to assume a μ_{eff} of $1 \, \mu_B$, an estimate for n can be subsequently calculated, and thus an estimate of the number of atoms giving rise to the magnetic signal can be determined. Following this calculation using the Curie constant as extracted from the data, it was found that only 0.18 % of the atoms within the sample were giving rise to the magnetic signal. This indicates that the magnetic behaviour of the sample is arising from some kind of impurity rather than from NCB itself. This could be from the starting chemicals, for example if they were to contain iron or copper ions as impurities. Alternatively, there could be metal ions that have been leached into the crucibles that were used for previous syntheses of other materials. Therefore, it can be concluded that this material exhibits very little to no magnetic behaviour.

3.2.3 Initial attempts at synthesising $KBa_6Zn_4Ga_7O_{21}$

Another material predicted to be superconductive by Stanev *et al.* was KBZGO. Like NCB this material is relatively unexplored. It was originally synthesised by Scheikowski and Müller-
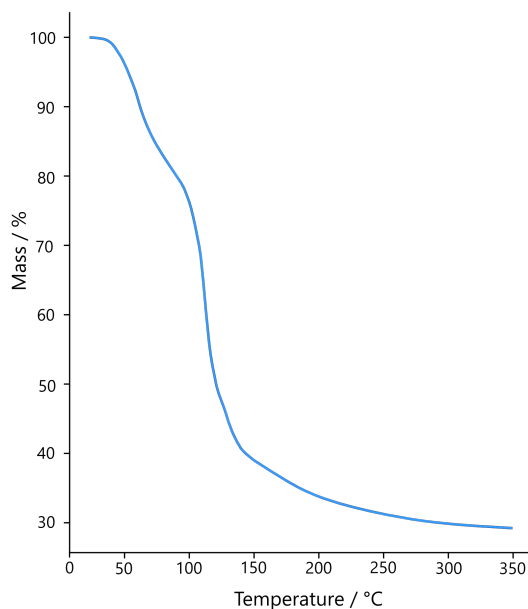
Figure 3.15: TGA data depicting the decomposition of $Ga(NO_3)_3 \cdot xH_2O$ under an atmosphere of N_2.

Buschbaum in 1994, however this material has remained unexplored in terms of applications.[236] The discovery paper has only been cited four times since the discovery, and none of these papers are related to the applications of KBZGO specifically. The Material's project predicts the band gap for this material to be 2.459 eV, though, again, this can be an overestimate.[207] The first synthesis of KBZGO was carried out using the metal oxides of the component elements; KO_3, BaO, Ga_2O_3 and ZnO. The reactants were sealed in a silver ampoule before calcination at 750 °C with a dwell time of a week, before slow cooling to room temperature.

Attempts at synthesising KBZGO first required the determination of the numbers of waters of hydration in the $Ga(NO_3)_3 \cdot xH_2O$, which was done by performing thermogravimetric analysis (TGA) on the powder from the bottle. The resulting TGA data showed an interesting shape, which did align with a previously reported result (Figure 3.15).[237] Aqueous syntheses with the biopolymer dextran were attempted first, as the metal nitrates of all the metal salts are readily available and soluble in water.

Previous work in the group determined that an aqueous synthesis method with KNO_3 resulted in little to no potassium crystalline phases in the product material.[238] It was thought that this was due to the low decomposition temperature of KNO_3, so KCl was used instead. After the dissolution of the salts, the biopolymer dextran was added in several different amounts, with different calcination temperatures. Figure 3.16 shows the resulting pXRD data from these studies. Initial studies were carried out with two different amounts of dextran, 500 mg and 1000 mg, and
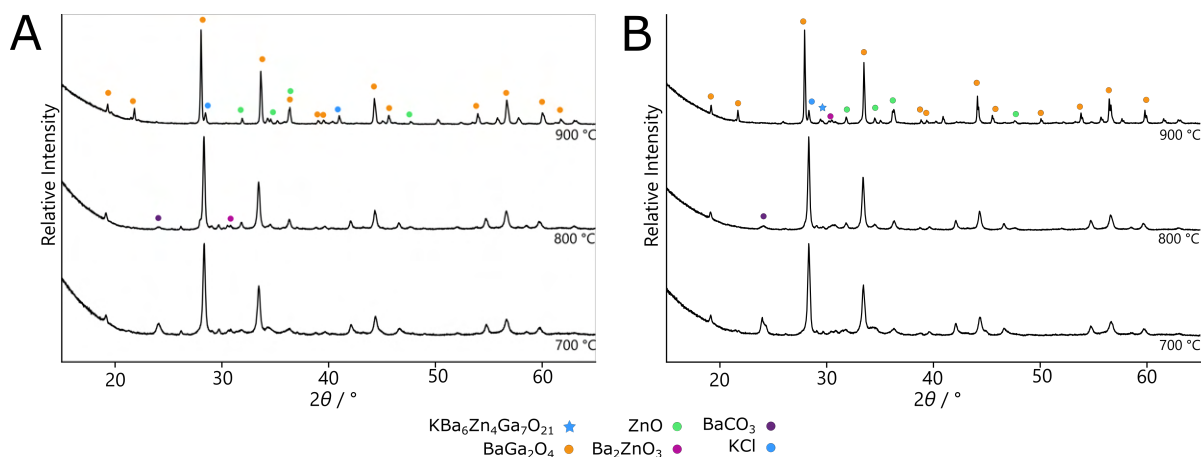
Figure 3.16: a) Results from the attempts at synthesising KBZGO with 500 mg dextran. b) Results from the attempts at synthesising KBZGO with 1000 mg dextran.

combined with three different dwell temperatures: 700, 800 and 900 °C. Unfortunately it can be seen that the target phase did not form in the sample for any of the parameters used. Indeed, the phases present for these syntheses did not vary much between samples, indicating that the phases formed were very stable, and unlikely to be available to react further. The majority phase in all of these attempted syntheses was $BaGa_2O_4$, which is an exciting compound in its own right, owing to its photoluminescent properties, though it exists in several polymorphs.[239,240]

Attempts were also made to synthesise the material from a NADES synthesis. As the $Ga(NO_3) \cdot xH_2O$ was the least soluble in water, it was dissolved in the NADES instead of the aqueous precursor solution. The first experiment at 700 °C was unsuccessful, and only produced a white powder that mostly consisted of barium carbonate (Figure 3.17). A subsequent synthesis utilised a dwell temperature of 750 °C, and instead resulted in a majority product of $BaGa_2O_4$. It seems that this phase is a desirable phase to form, and will likely form with these component materials.

Two further experiments were carried out in an attempt to reduce the amount of barium carbonate in the product material when a dwell temperature of 700 °C is used. The first was to utilise a boat-type crucible instead of the high-form crucibles used previously. It was thought that having a thin layer of material instead of a pool within a smaller footprint, would allow more of the reaction mixture to contact the air. This higher surface area of contact with air would prevent the reaction mixture from smothering itself with the carbon dioxide given off during the synthesis. Unfortunately the result from this synthesis was much the same as the synthesis with 750 °C, with the formation of $BaGa_2O_4$ as a majority phase. The other attempt carried out to reduce the amount of carbonate formation, was to use a smaller amount of the NADES solution. Instead of adding 2.05 mL of the solution, only 1 mL was added. However, this method was also unsuccessful at forming the target phase of $KBa_6Zn_4Ga_7O_{21}$.
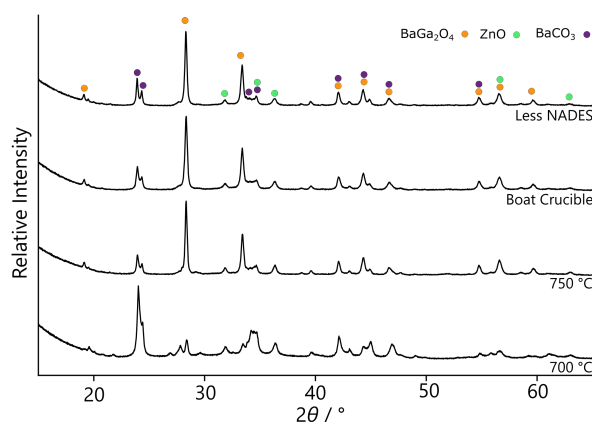
Figure 3.17: a) Results from synthesis attempts with the NADES synthesis method.

3.2.4 Summary

In summary, two different synthetic methods were utilised to produce two α-NaFeO$_2$ compounds, Na$_3$Ni$_2$BiO$_6$ and Na$_3$Ca$_2$BiO$_6$. These syntheses were performed at either lower temperatures or with shorter dwell times than the solid-state syntheses where they were originally reported.

For NNB, it was found that both the aqueous, biopolymer-mediated synthesis and the NADES method were able to synthesise the target phase. For both synthetic methods, the target phase was obtained when calcined at 800 °C. When synthesised with 300 mg dextran, the sample appeared to form the disordered polymorph, indicating that the amount of biopolymer is a crucial factor to control in this synthesis. However, when no biopolymer was included at all, the target phase also did not form, indicating that some chelation is necessary in the synthesis. The NADES synthesis also yielded the target phase at 800 °C, with a good purity of the target phase. It was found, however, that this method could be inconsistent, occasionally resulting in the synthesis of the disordered polymorph of NNB, characterised by a Warren peak in place of the peaks that ordinarily arise from the hexagonal superlattice.

Table 3.2: The results from the NNB phase evolution studies, when carried out with the aqueous biopolymer-mediated synthesis technique.

Phase	Synthesis Temperature / °C					
	500	600	700	800	900	1000
$Na_3Ni_2BiO_6$	0	0	8	85	0	0
$R-Bi_2O_3$	0	17	5	2	3	0
α-Bi_2O_3	4	1	3	0	16	14
β-Bi_2O_3	20	0	0	0	0	0
$NaHC_2O_4H_2O$	24	0	0	0	0	0
$NaHHCOO_2$	18	0	0	0	0	0
$NaNO_2$	21	0	36	7	0	0
$NaNO_3$	0	31	14	0	13	0
$NaBiO_3$	0	0	6	0	0	0
NiO	12	36	27	6	67	86
Ni	0	13	0	0	0	0
R_{wp}	4.9	13.6	7.9	6.4	4.9	4.8

Table 3.3: The results from the NNB phase evolution studies, when carried out with the NADES synthesis technique.

Phase	Synthesis Temperature / °C					
	500	600	700	800	900	1000
$Na_3Ni_2BiO_6$	0	0	0	76	56	0
$R-Bi_2O_3$	0	6	5	0	2	5
α-Bi_2O_3	1	1	3	0	0	7
β-Bi_2O_3	12	0	0	0	0	0
$Na_2N_2O_2$	22	0	0	0	0	0
$NaNO_2$	16	28	11	0	0	33
$NaNO_3$	0	27	28	17	0	0
$NaBiO_3$	0	0	2	0	0	0
NiO	8	16	19	7	42	54
R_{wp}	6.2	10.3	12.1	9.8	4.7	5.8

The syntheses of NCB were also successful, with the formation of the target phase being possible for both synthesis methods. The optimal temperature for all of the synthetic methods was 800 °C, but it was found that NCB also formed between 700 and 900 °C. From the syntheses attempted, it was found that the ideal synthetic technique was a NADES synthesis. This allowed the target phase to be rapidly formed with a good purity of 91 %. Interestingly, for both synthesis techniques, it did not appear that the metastable polymorph of Bi_2O_3, $R-Bi_2O_3$, formed. This indicates that the nickel ions in the synthesis either catalyse its formation, or that the phase present is actually some kind of mixed phase of Bi-Ni-O. This would align with the data observed for the syntheses of NCB, as the impurity phases present in this case were often Ca-Bi-O phases. As well as this, it was found that when using 100 mg of 'High-Fraction' dextran, that its presence did not affect the synthesis at 800 °C significantly compared to not using any dextran at all. As

Table 3.4: The results from the NCB phase evolution studies, when carried out with the aqueous biopolymer-mediated synthesis technique with $M_r \backsim 70\,000$ Da dextran.

Phase	Synthesis temperature / °C				
	600	700	800	900	1000
$Na_3Ca_2BiO_6$	0	69.55	78.8	12.5	0
Na_2CO_3	5.5	0	0	0	0
$Ca_{0.176}Bi_{8.24}O_{14}$	5.19	0	0	0	0
$NaNO_2$	9.31	0	0	12.5	0
$Ca_4Bi_6O_{13}$	1.59	2.8	3.03	1.4	13.1
$Ca_6Bi_6O_{15}$	0	3.5	2.9	5.5	0
$NaNO_3$	11.3	22.19	15.24	0	0
$NaHC_2O_4H_2O$	44.8	0	0	0	0
$NaOH(H_2O)_4$	21.5	0	0	0	0
Bi_4O_7	0	1.6	0	0	0
CaO	0	0	0	68	45.2
$CaCO_3$	0	0	0	0	41.7
R_{wp}	12.8	8.93	9.16	12.05	7.50

Table 3.5: The results from the NCB phase evolution studies, when carried out with the NADES synthesis technique.

Phase	Synthesis temperature / °C					
	500	600	700	800	900	1000
$Na_3Ca_2BiO_6$	0	0	23	91	18	0
Na_2CO_3	35	14	0	0	0	4
$Ca_{0.176}Bi_{8.24}O_{14}$	27	11	0	0	0	0
$NaNO_2$	22	25	8	0	18	0
$NaNO_3$	0	10	0	0	0	4
$Ca_4Bi_6O_{13}$		6	6	3	2	3
$Ca_6Bi_6O_{15}$	0	0	4	3	0	0
$NaHC_2O_4 \cdot H_2O$	0	33	0	0	14	0
Bi_4O_7	0	0	0	3	0	0
CaO	0	0	22	0	48	72
$CaCO_3$	0	0	0	0	0	7
CaC_2O_4	0	0	13	0	0	9
β-Bi_2O_3	13	0	0	0	0	0
R_{wp}	11.7	13.1	14.8	7.79	13.9	10.8

such, $M_r \backsim 70\,000$ Da dextran was found to be much more valuable in the synthesis of the NCB and indeed NNB.

Unfortunately, KBZGO was not successfully synthesised in this work. With all syntheses, it was found that the majority phase which formed was either $BaCO_3$ or $BaGa_2O_4$. For the samples with majority $BaCO_3$ phases, attempts to reduce the amount of carbonate formation were successful but only formed $BaGa_2O_4$ instead. Many of the syntheses resulted in very little potassium-containing phases within them, indicating that there is a necessity for an excess of potassium salt in the synthetic protocol. There are a large number of variables for the synthesis,

however, such as dwell time, dwell temperature, ratio of metal salts in solution, solvent and the metal salts themselves. For example, adding the potassium source as K_2CO_3 instead of KCl could be something that would assist in the generation of the target phase. When potassium-containing phases were observed in the synthesis, they were often unreacted KCl, indicating that it is not able to engage in the reaction, or that it is too stable to react. Furthermore, the synthesis could be reattempted with a vast excess to overcome any potential volatility of the potassium salts.

THE SYNTHESIS OF NANOWIRES OF HIGH-TEMPERATURE SUPERCONDUCTORS

Some experiments within this chapter were undertaken by my outstanding master's students, Hector Christodoulou and Sorrel Haughton. Where data from them has been used, it has been noted in the text.[241,242] All microscopy was carried out by me, except for the high-resolution TEM, which Dr Jean-Charles Eloi carried out. Parts of this chapter are published in Small Structures.[243]

As devices become increasingly miniaturised, so too is there a greater necessity to develop more reliable methods for synthesising nano-sized materials. This coincides with the fact that Moore's law, the observation that the number of transistors in an integrated circuit doubles every two years, has begun to slow down since 2010.[244] To keep up with the demand for ever-shrinking components in computers, engineering nanostructures has become increasingly important in manufacturing. This chapter presents a solid-state method for synthesising nanowires of high-temperature superconductors by emulating the conditions necessary for the microcrucible nanowire growth mechanism.

4.1 Introduction

4.1.1 Nanowires and their synthesis

As discussed in Section 1.1.3, nanomaterials are defined as having at least one dimension on the order of the nanoscale, or 1×10^{-9} m. By this definition, nanowires are long, anisotropic materials with a width on the order of a nanometre but an unconstrained length. When a material is confined to the nanoscale, it often results in emergent properties that differ from those in the bulk.[245] As such, many nanomaterials exhibit exciting properties compared to the same material formed on

the macroscale. Nanostructures have begun to be extensively utilised in microelectronics, where their synthesis has enabled the steady miniaturisation of electrical components for use in many different devices.[246] There has been much focus in the literature on silicon nanowires. However, there are other potential applications for other inorganic materials, such as with ZnO nanowires for biosensing applications and as piezoelectric generators.[15,247] Additionally, nanowires of superconductors could potentially be utilised as single-photon detectors or as THz emitters, as discussed in Section 4.1.2.1.[248] More recently, superconductor-semiconductor nanowires have been synthesised with the hope for them to be applied to quantum computing.[249]

Syntheses of nanowires can generally be partitioned into two types: 'top-down' or 'bottom-up'. Top-down syntheses generally rely on a slab of material being made before lithographic or etching techniques are employed to remove material and form the desired shape.[250] Many robust top-down techniques are utilised in synthesising silicon-based nanostructures for use in everyday electronics.[251] However, these techniques are becoming limited as the necessity for ever-smaller devices has required nanostructures of increasingly smaller sizes. While these dimensions are achievable through top-down techniques, their demand calls for ever more complex and expensive syntheses.[252] Bottom-up techniques employ natural forces during the synthesis, where a building block forms itself into a nanowire by virtue of the forces operating on it - often resulting in the self-assembly of the material into the desired shape.[253] This results in the formation of nanowires without the necessity for direct manipulation or waste material. Most processing nanomaterials for use in electronics is by utilising top-down techniques, but some examples of bottom-up approaches are becoming more common in everyday manufacturing processes. Indeed silicon nanowires have been successfully grown through bottom-up techniques at widths down to singular nanometres, which is not normally achievable through top-down methods.[254]

4.1.1.1 Nanowire growth mechanisms

Many simple metal-oxides can be grown through bottom-up methods, such as ZnO and silicon-based nanowires. CuO is very good at growing as a nanowire, as was found when copper TEM grids were heated in air, yielding large arrays of CuO nanowires.[255] Mechanisms of nanowire growth have often been speculated upon and have been found to influence the morphology of the resultant wires.[256] One frequently observed mechanism, vapour-liquid-solid (VLS), was first proposed by Wagner and Ellis in 1964.[257] This mechanism claims that a nanoparticle impurity behaves as a seed for the nanowire by forming an alloy with the substrate. The vapour of the substrate reacts with this alloy, depositing the pure substrate underneath the droplet.[257] Nanowires formed from this mechanism are characterised by a droplet of the catalytic material at the tip of the wire. This VLS mechanism is one of many mechanisms that utilise a catalytic material to confine growth to a single dimension, with other mechanisms also being named after the phases involved in the synthesis; such as vapour-solid-solid, solution-liquid solid and vapour-solid growth.[258–260] While VLS is well-understood, there are limitations to the wires formed from

this method, in that they taper to one end and contain a droplet with a different composition on the end. Other mechanisms that operate without a catalytic material also exist, for example, those that exploit natural defects found in crystalline materials, such as screw-dislocation which forms cylindrical nanowires.[261] There are also techniques that exploit templates to confine a material to the nanoscale, such as utilising anodised aluminium oxide templates. In the case of anodised aluminium oxide in particular, despite their ability to template and form nanostructured materials, these are often polycrystalline, which can limit their potential applications.[258]

4.1.1.2 The microcrucible mechanism

Nanowires of $YBa_2Cu_3O_{7-\delta}$ (Y-123) have been grown previously using a sol-gel method with the biopolymer sodium alginate. The synthesised wires were interesting as they did not exhibit the telltale signs of other growth mechanisms such as VLS.[262] Instead, the wires observed in this work were not tapered at all, and there was no evidence of the catalytic droplet from the tip of the material. These features of the wires were indicative of the so-called microcrucible mechanism. Some preliminary studies into this synthesis observed that, after an initial calcination step at 500 °Celsius, there were barium carbonate particles suspended in an amorphous matrix.[262] The microcrucible mechanism was observed directly in 2014 by Boston *et al.*[143] This work showed evidence of barium-rich nanoparticles moving through the matrix of yttrium and copper oxides, reaching the surface of the matrix, and then a nanowire growing from this nanoparticle. It should be noted that, due to the vacuum of the TEM, the composition of the resulting wire was under-oxygenated, and was thus Y_2BaCuO_5 (Y-211). Figure 4.1 presents a graphical representation of this. From these observations, it was concluded that for a microcrucible mechanism to be induced, there are three necessary criteria: a solid matrix consisting of one or more of the constituent elements of the target phase; nanoparticles consisting of the other elements of the target phase which are embedded in the matrix; and a flux that can melt the nanoparticle and induce growth of the nanowires. This mechanism of growth of anisotropic features has been theorised to be one of the mechanisms by which whiskers of $Bi_2Sr_2CaCu_2O_{8+x}$ (Bi-2212) grow.[263]

It has been found that sodium alginate is not compatible with Bi-2212, as it instead forms $Na_3Ca_2BiO_6$, which will be discussed in more detail in Chapter 5.[179] Therefore, to synthesise nanowires of Bi-2212 with the microcrucible mechanism, it would be necessary to induce this mechanism through a different method that does not require sodium alginate as a biopolymer. Previous work in the group has attempted to utilise a solid-state method which recreates the conditions required for the microcrucible mechanism but avoids the necessity for a biopolymer.[264] This was successful at synthesising nanowires of Y-123. So it was thought that using the same principle for Bi-2212 could be a viable route to the successful synthesis of nanowires. The solid-state microcrucible mechanism works by emulating what was observed for the Y-123 study by Boston *et al.* Y_2O_3 was mixed with CuO and combined with nanoparticles of $BaCO_3$. Finally, a flux was added in the form of a sodium salt - in this case NaCl or $NaCO_3$, and the sample was
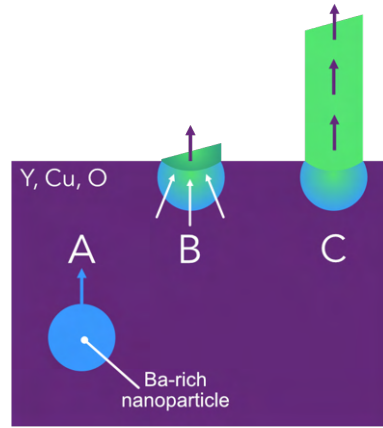
Figure 4.1: Graphical representation of the microcrucible mechanism for the formation of Y-Ba-Cu-O (YBCO) nanowires. It depicts (A) a barium-rich nanoparticle migrating through a matrix of yttrium and copper oxides, (B) it reaching the surface of the oxide matrix and reacting with the flux and the matrix around it and a wire beginning to grow from the base (C) the continued growth of the resulting wire. In this case, the wire is a Y-211 wire.

compressed into a pellet before calcination. This reaction requires that three key phases are present simultaneously along with the flux, so compressing the sample into a pellet increased the likelihood that the phases would be close together and thus able to react.

4.1.2 Terahertz emission

As technology has advanced, it has become necessary to be able to exploit all frequencies of the electromagnetic (EM) spectrum. For solid-state sources of EM radiation, this has historically been carried out by two primary sources: for low-energy EM radiation below 0.2 THz, the radiation is generated by alternating currents in transistors. For higher-energy EM radiation, the radiation is generated by electronic transitions in lasers.[265] However, there is a limitation to both of these generation methods, as the frequencies accessible by them do not overlap in the middle. This yields a section of the EM spectrum between roughly 0.1 and 10 THz that cannot be generated by either method, yielding a gap in generatable frequencies, often called the 'terahertz gap'.[97] Terahertz radiation has been envisioned as the next step in wireless communication, with a potential application as 6th generation or 6G wireless.[266] Additionally, Terahertz radiation is non-ionising and is safe for use around humans, meaning that it is ideal for future applications such as in medical imaging.[267,268] However, to fully realise applications of these EM frequencies, more reliable generation mechanisms must be developed to create novel devices using this technology.

Several attempts have been made to overcome the terahertz gap through alternative solid-

state generation sources, such as resonant tunnelling diodes and quantum cascade lasers. [269,270] These make up the majority of current THz emission devices. However, the manufacturing process still needs to be simplified for consumer applications, and the range of frequencies these devices can access does not encompass the lower THz frequencies. [269,271] An alternative method of generating THz radiation is through exploiting the Josephson effect in superconductors. As was discussed in Section 1.2.1.2, when a potential difference is applied across a Josephson-junction (JJ), there will be an alternating current (A.C.) that is induced across the junction at the Josephson frequency. These JJs are formed when two superconducting sections of material are separated by a small insulating gap, where the superconducting pairs of electrons, or Cooper pairs, are able to tunnel across the gap. These JJs are also referred to as 'weak links', where the weak link is a break in the bulk superconductive material. This weak link can be a section of insulator material, a normal conductor, or a physical interruption of the bulk material - such as a grain boundary. The generation of frequencies from a potential difference means that JJs can convert this potential difference to a high-frequency current, and the frequency of this current can be within the range of the THz gap. [272] A limitation is that the emission from a single junction can be very low-powered, meaning that many JJs must simultaneously emit radiation in phase with each other to yield an appreciable THz signal.

4.1.2.1 $Bi_2Sr_2CaCu_2O_{8+x}$ as a THz emitter

Bi-2212 has been shown to exhibit some potential as a candidate in the fabrication of THz emission devices. [273] The crystal structure of Bi-2212 has superconducting copper oxide planes, which are separated by an insulating Bi-Sr-O layer. Unlike many other members of the cuprate family of superconductors, the copper oxide planes in Bi-2212 are uncoupled, leading to superconducting sections separated by insulating material. [272] This structure means that, within Bi-2212's crystal structure, intrinsic JJs are formed. As discussed in Section 1.2.1.2, this means that, if a potential difference is applied across the junction, an alternating current can be obtained. The frequency of this current is dependant on the Josephson frequency (equation 4.1), where U is the applied voltage and Φ_0 is the flux quantum, providing the applied voltage is constant. [271]

$$(4.1) \qquad\qquad f_j = \frac{U}{\Phi_0}$$

This relates to a frequency of 1 THz with an applied voltage of about 2.1 mV. Ordinarily, the emission from a single junction is weak, and thus results in low-power emission of radiation. However, in Bi-2212, the packing density of these JJs is substantial, as each superconducting copper oxide plane is separated by only $\smallfrown$ 3.06 nm. [274] Thus if each JJ within the crystal structure of Bi-2212 were to emit radiation in phase, there is potential for the generation of a sizeable THz signal. Therefore, if nanowires of Bi-2212 were produced, there would be a large number of intrinsic-JJs within the structure with the potential to emit coherent THz radiation. Currently,

much research is being carried out into Bi-2212 mesas, which are flat rectangular structures with
a certain height. These can emit THz radiation in phase, generating an appreciable radiation
signal. However, these mesas can only be built up to a certain height due to heat generation within
the mesas, causing the destruction of the superconducting state in the Bi-2212.[272] Therefore,
these mesas have been limited to an output of $100\,\mu\text{W}$ of power.[271] As such, alternative formats
of devices should be proposed for the development of superconducting THz emitters. One such
alternative morphology of the device is that of a nanowire. If a nanowire were to be grown such
that the c-axis aligned with the length of the wire, the wire would contain many JJs along its
width with the bonus of being a thin wire to allow for heat dissipation along its surface. Bi-2212
has been observed to form whiskers through a variety of experimental methods, such as through
rapid cooling of a melted precursor when coated with Al_2O_3, but achieving a nano-sized wire of
Bi-2212 is yet to be observed.[263]

4.2 Results and discussion

As Bi-2212 is a quinternary metal oxide, it was anticipated that emulating the microcrucible
mechanism for this material could be challenging due to the large number of elements that
must be present in the same place for a nanowire consisting of all elements to be successfully
synthesised. As such, two different synthesis methods were devised with mixed-metal phases
to reduce the necessity for five different components to come together at precisely the correct
place for the microcrucible reaction to occur. One method involved combining two metal oxides
with a mixed-metal carbonate nanoparticle, in this case, Bi_2O_3, CuO and $Sr_xCa_{1-x}(CO_3)$. The
other method followed recommendations from a study carried out by Green $et\ al.$, where they
analysed the phase evolution of Bi-2212 during a typical biopolymer-mediated synthesis.[138]
In this study, quench studies were performed, where the calcination was stopped at 100 °C
increments and powder X-ray diffraction (pXRD) on the reaction mixture was carried out. In this,
they observed a potential reaction pathway for the synthesis of Bi-2212, and determined that
some key phases of importance were mixed-metal carbonates. In this proposed mechanism, they
observed the formation of $Bi_2Sr_2CuO_6$ (Bi-2201), followed by its reaction with $Bi_2(Ca_{1+x}Sr_{3-x})O_7$
to form Bi-2212. This indicated that Bi-2201 could be a precursor material for the target Bi-2212
phase. As such, it was considered that synthesising Bi-2201 and then combining this product with
a mixed calcium-copper phase and additional flux could be a route to the synthesis of Bi-2212
nanowires. For this work, the calcium-copper salt chosen was $CaCu(OCOOH)_4 \cdot 6H_2O$. Another
note from the study by Green $et\ al.$, was that the mixed metal carbonate $Sr_xCa_{1-x}(CO_3)$ was also
of key importance in the formation of Bi-2212.[138]

When deciding upon the flux used for the microcrucible mechanism, a few criteria were
considered for the following experiments. Firstly, in the seminal observation of the microcrucible

mechanism, the biopolymer used was sodium alginate. It was noted in another study that when the sodium alginate was swapped with ammonium alginate, no nanowire growth was observed.[133] During this study, it was also found that if the sodium alginate was changed to sodium ascorbate, there was also no evidence of nanowire growth. From this, it seemed that the sodium ion and the extensive cross-linking from the alginate biopolymer were important for the microcrucible mechanism. A key difference between the products of the synthesis of sodium alginate and sodium ascorbate were the crystalline phases which were produced as part of the synthesis. As was noted in an additional study, the appearance of barium carbonate nanoparticles with an amorphous matrix was observed with the synthesis of Y-123 nanowires. Therefore, the proposed solid-state method sought to emulate this so-called 'currant-bun' motif by embedding nanoparticles within a matrix of the other metal ions. The other thing to consider therefore was the role of sodium, which is likely that of a flux - lowering the melting point of the barium carbonate nanoparticles and allowing them to react with the matrix around them, forming a nanowire. In the present solid-state method, sodium-based salts were therefore chosen as a starting point for the flux necessary for the synthesis. The two salts chosen initially were $NaCl$ and Na_2CO_3, as they have melting points close to the dwell temperature required for Bi-2212, with 801 and 851 °C respectively.[107] Additionally, during the work within this chapter, it was observed that some nanowires produced were deficient in calcium. As such, the use of $CaCl_2$ as a flux was also explored during this chapter. It has also been noted previously that calcium carbonate could play a role in the solid state reactions during the synthesis of Bi-2212, where it could form eutectic mixtures with the strontium carbonate in the reaction.[275] It is also possible that other phases during the synthesis could be behaving as fluxes, such as Bi_2O_3, which has previously been used as a flux in molten salt syntheses.[107]

4.2.1 Synthesis using Bi_2O_3, CuO and $SrCa(CO_3)$ nanoparticles

The first method attempted was to combine the metal oxides of Bi_2O_3 and CuO with mixed strontium-calcium carbonate nanopaticles. This method was chosen, as it has been shown previously that mixed metal carbonates, in particular $Sr_xCa_{1-x}CO_3$, are key in the phase evolution of Bi-2212.[138] Dr. Jason Potticary synthesised the nanoparticles used in this chapter through a gas-combustion method, described in section 2.2.4.1. The fine powder was then used without further treatment in the synthesis. To ensure that the correct ratio of metals was present for the desired target phase, a mixed phase of $Sr_{0.67}Ca_{0.33}CO_3$ would be necessary. This is possible, as there is a polymorph of $CaCO_3$ (aragonite) that is isomorphous with $SrCO_3$, so the Sr^{2+} ions can be be substituted by Ca^{2+} ions. $CaCO_3$ is found naturally as one of three different polymorphs in nature; the hexagonal polymorph calcite, the orthorhombic polymorph aragonite and the more rare polymorph known as vaterite. Due to its larger ionic radius, $SrCO_3$ only crystallises as an isomorph of the aragonite structure, also known as strontianite.[276] In order to confirm whether the sample was indeed a mixed phase of $CaCO_3$ and $SrCO_3$, the d-spacing of the (111) reflection

was compared to that of the pure $CaCO_3$ and $SrCO_3$ as well as some mixed phases that were
obtained from the Inorganic Crystal Structure Database (ICSD). As the ionic radius of Sr^{2+} is
larger than Ca^{+2}, the unit cells of these crystals are slightly different sizes, which is reflected in
the d-spacing from the (111) reflection.[235] From these data, it was determined that the ratio of
Sr : Ca in the nanoparticles used in this work is 0.873 : 0.127. While this is not the target ratio,
the synthesis did result in nanoparticulate material as determined by transmission electron
microscopy (TEM) (Figure 4.2a). As can be seen from the micrograph, the material is made from
smaller crystallites, which have aggregated together in this case. These crystallites tended to be
oval-shaped, generally exhibiting one longer axis. As such, when determining the diameter of
the nanoparticles, the larger diameter was measured and an estimate for the particle size was
determined from the TEM to be 160 nm with a lognormal distribution such that the standard
deviation, $ln\sigma = 0.444$. It can also be seen from the pXRD that the diffraction peaks are broad,
indicating that the particles are nano-sized.

4.2.1.1   NaCl Flux

Initially, experiments were attempted with sodium chloride as the flux for the synthesis of the
materials based on the success of previous experiments carried out by Hector Christodoulou.
Many parameters can be altered in order to change the reaction conditions: the dwell temperature,
the dwell time, the ramp rate, the amount of flux within the sample, and whether an additional
dispersion of the flux is added to the surface of the pellet. The first parameters tested for this
method were the use of 10 % NaCl flux and two different dwell temperatures (830 and 850 °C)
for 2 hours. Additionally, for each temperature, a sample was also placed in the furnace with
an additional dispersion of NaCl over the top of the pellet. scanning electron microscopy (SEM)
of the samples (Figure 4.3) showed that very few wires were observed. All samples consisted of
anisotropic, flakey crystallites, a commonly observed morphology of Bi-2212. A few anisotropic
wire-like features were observed for the sample synthesised at 850 °C, but this was not consistent
throughout the sample.

Previous observations of Y-123 by Dr. Jason Potticary indicated that wires of the target phase
form at much lower temperatures than the conventional dwell temperature of 920 °C, possibly
owing to the NaCl flux.[264] Therefore, dwell temperatures of 750 and 800 °C were also carried
out to examine if this was also the case for Bi-2212. The dwell time, ramp rate and percentage
amount of NaCl were kept the same from the previous experiments. Furthermore, the additional
dispersion of NaCl over the pellet of sample was still carried out on these samples. For the sample
without an additional dispersion of NaCl over the top, there was a clear difference in morphology
between sections of samples synthesised at 750 °C, (Figure 4.4a and b), which was exemplified
when imaging the sample with backscattered electron imaging. It was clear that some sections of
material were formed from lighter elements and thus appeared darker in the electron micrograph.
When an additional dispersion of NaCl was applied to the top of the pellet, bundles of nanowires
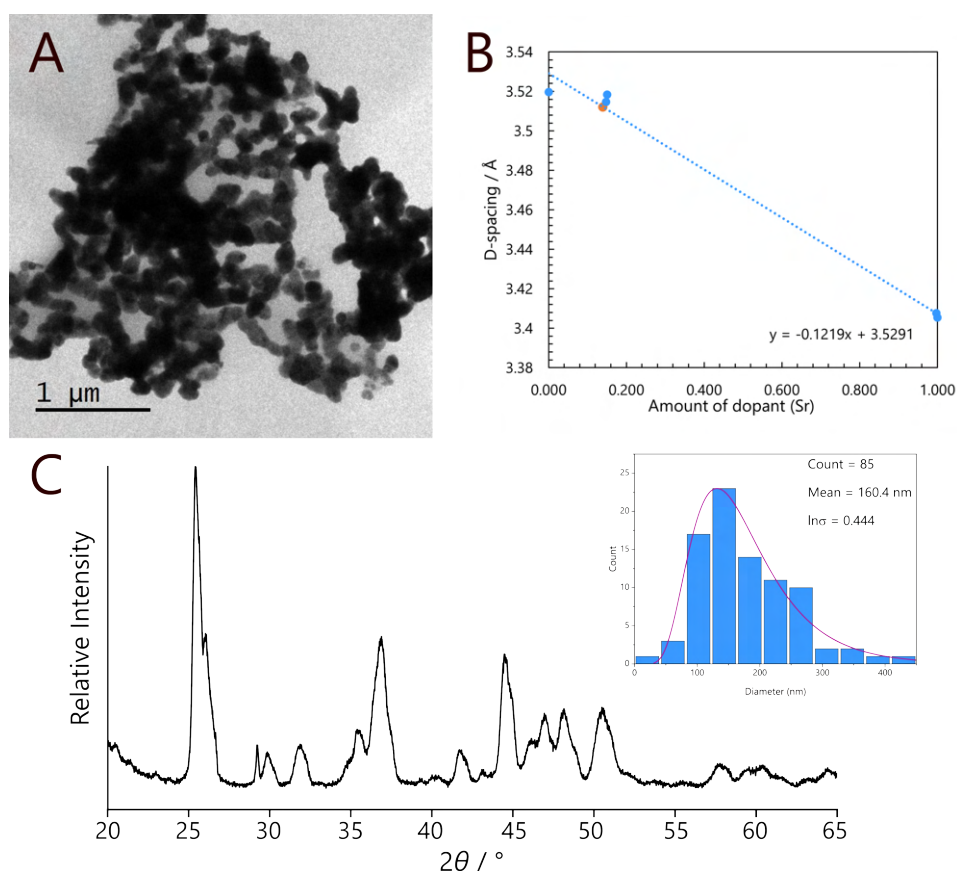
Figure 4.2: a) TEM of the as-synthesised nanoparticles from the micrograph, it can be seen that the sample is formed of small crystallites that are around 160 nm in size. b) Graph depicting the d-spacings of the (111) reflection for $Sr(CO_3)$, $Ca(CO_3)$ and $Sr_{0.85}Ca_{0.15}(CO_3)$ in blue, and the corresponding d-spacing determined from pXRD of the as-synthesised nanoparticles determined by Rietveld refinement in orange. c) The corresponding pXRD data from this sample. Inset shows a histogram of the size distribution of particles as determined by measuring from TEM images. Nanoparticles synthesised by Dr. Jason Potticary

growing from the surface of the sample were observed (Figure 4.4c and d). Again, when imaging the backscattered electron image, these nanowire growths appeared to consist of mostly lighter elements. Further analysis by energy dispersive X-ray analysis (EDXA) (Figure 4.4e) determined that these growths of wires were clearly formed from a mix of sodium and oxygen. Additionally, there appeared to be sections of copper-rich phases around the rest of the bismuth, strontium and calcium matrix. pXRD determined that these samples did not consist of the target phase Bi-2212, and were instead formed of incomplete reaction products (Figure 4.6).

When examining the sample at 800 °C there was no evidence of any nanowire-like growths in the sample, though there were some very small growths found in Figure 4.5b. When additional NaCl was dispersed on the top of the sample, the texture of the crystallites on the sample was very rough (Figure 4.5d). There was no evidence of the nanowire growths found in the samples
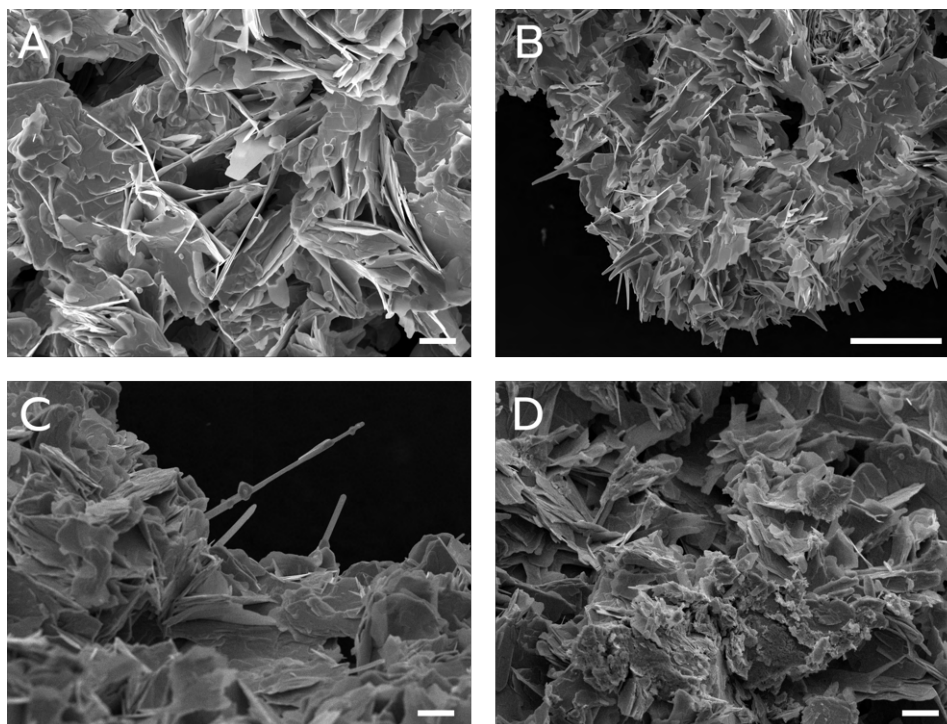
Figure 4.3: Scanning electron micrographs of different Bi-2212 nanowire synthesis attempts with
a 10 % NaCl flux. (a and b) Indicate samples with a dwell temperature of 830 °C and 2 hour dwell
time. (c and d) Indicate samples with a dwell temperature of 850 °C and dwell time of 2 hours. (b
and d) had an additional dispersion of NaCl on top of the pellet prior to calcination. Scale bars in
(a), (c) and (d) indicate a length of 10 μm and in (B) indicate a length of 50 μm.

synthesised at 750 °C, indicating that these phases had melted and reacted.

pXRD of these samples can be found in Figure 4.6. These data show that the samples
synthesised at 750 °C did consist of a significant amount of unreacted copper oxide. Additionally,
the extra NaCl in the form of a dispersion on top of the pellet also changed the material phase
quantities within all of the samples. It appears that the samples with an excess of NaCl could
generate the target phase at a lower temperature than without it. This is likely due to the NaCl
behaving as a flux, forming a eutectic mixture with the reactant materials and thus enabling
reactions to proceed through alternative pathways or enable better mixing of the sample when
compared to the bulk.
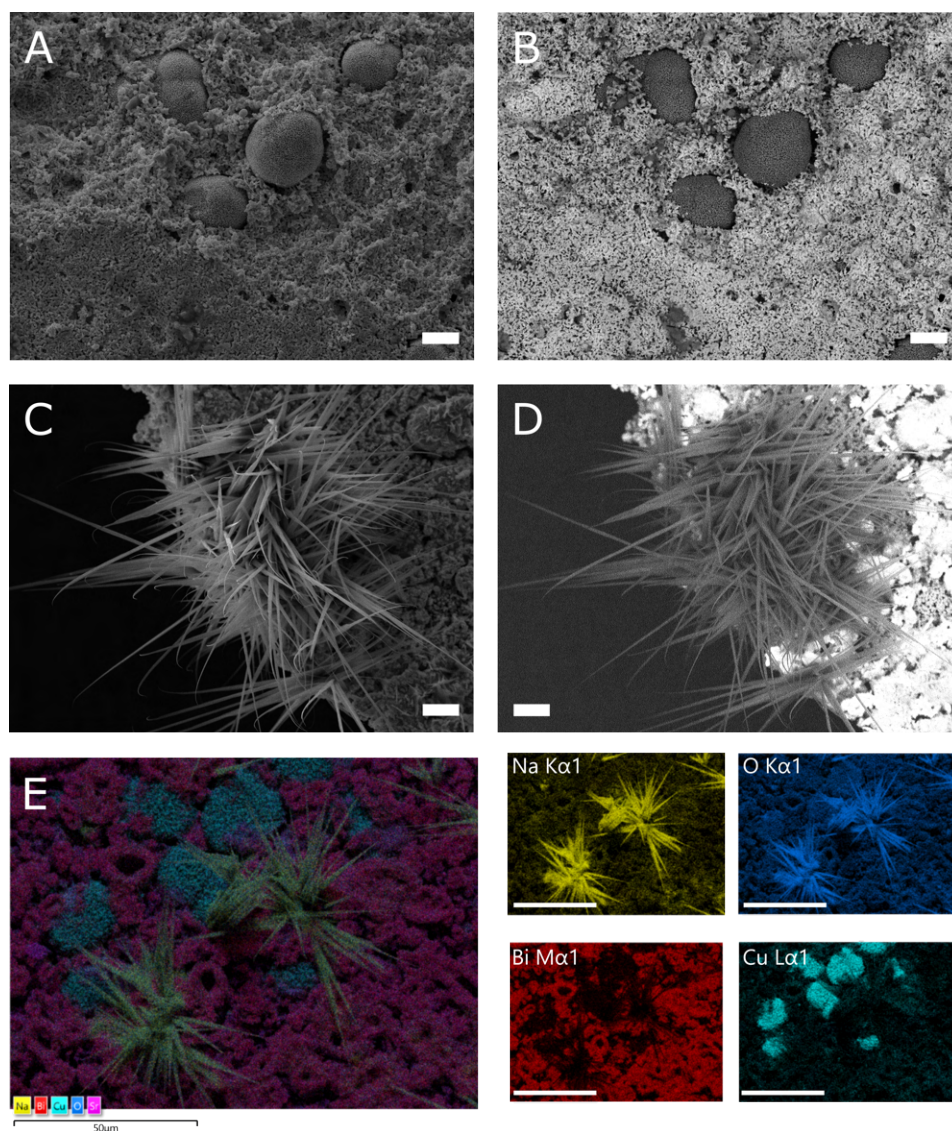
Figure 4.4: Scanning electron micrographs of the Bi-2212 synthesis attempts at 750 °C. (a and b) are samples with 10 % NaCl. (c and d) have an additional dispersion of NaCl on top of the pellet. Micrographs (a and c) were imaged using secondary electron imaging and (b and c) were imaged using backscattered electron imaging. e) is an EDXA map of the sample in (c and d). Scale bars in (a-d) represent a length of 10 μm. Scale bars in the EDXA images represents a length of 50 μm.
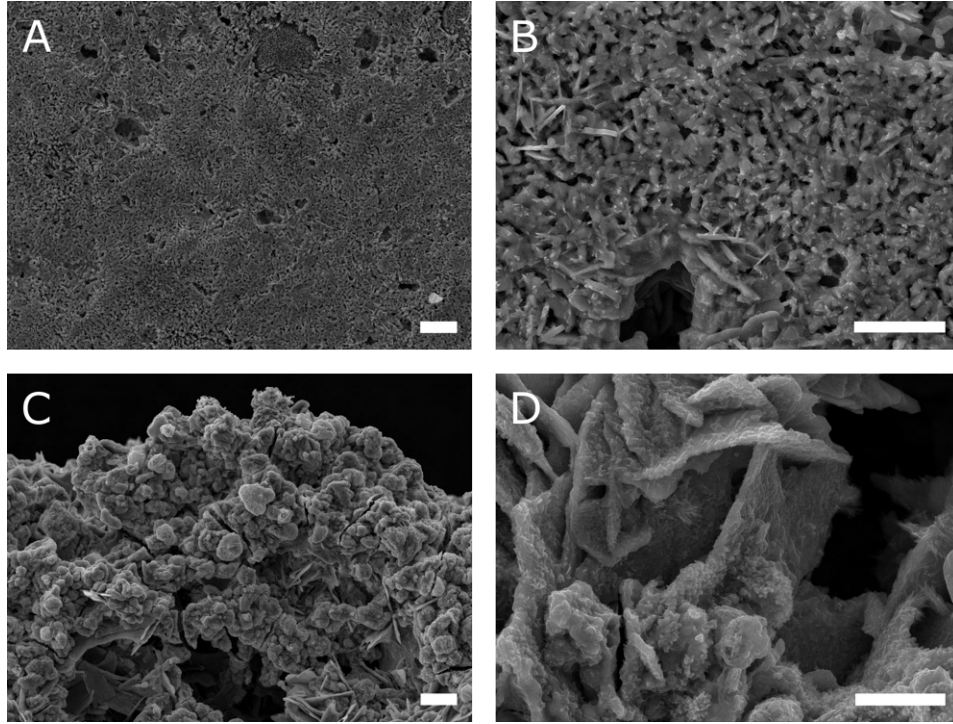
Figure 4.5: Scanning electron micrographs of the Bi-2212 synthesis attempts at 750 °C. (a and b) are samples with 10 % NaCl. (c and d) have an additional dispersion of NaCl on top of the pellet. Micrographs (a and c) were imaged using secondary electron imaging and (b and c) were imaged using backscattered electron imaging. e) is an EDXA map of the sample in (c and d). Scale bars in (a-d) represent a length of 10 μm.
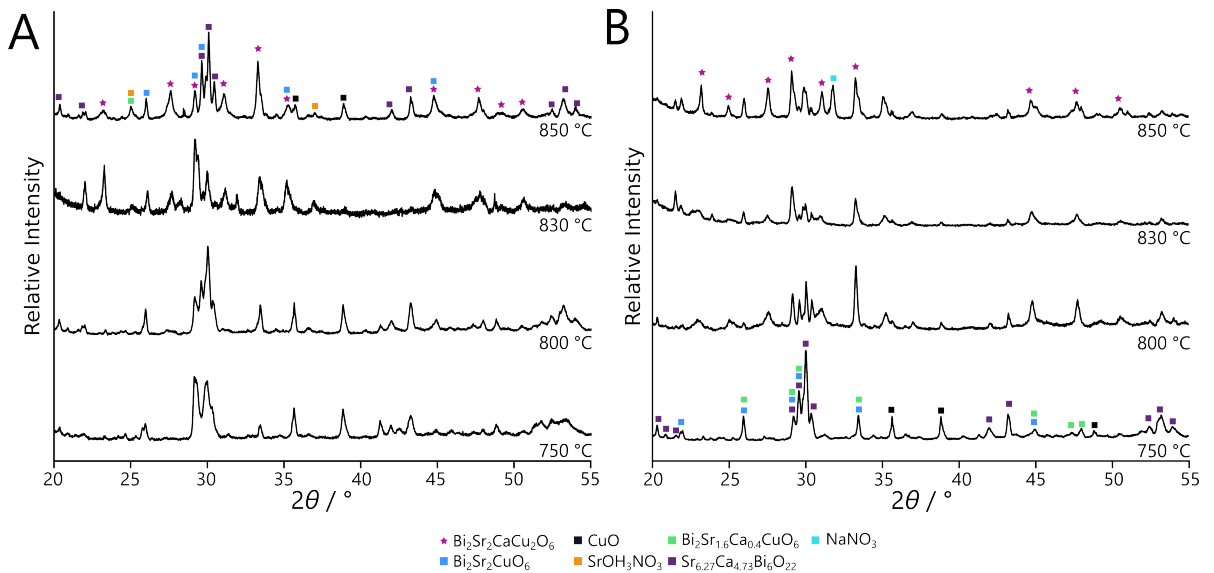
Figure 4.6: a) pXRD of the bulk material from the samples synthesised with 10 % NaCl at various temperatures which are labelled in the plot. b) pXRD of the bulk material from the samples synthesised with 10 % NaCl with an additional dispersion of NaCl over the top of the pellet.

4.2.1.2 Na_2CO_3 Flux

Another flux attempted was Na_2CO_3, as it was attempted previously for the synthesis of YBCO nanowires in Dr. Jason Potticary's previous work.[264] The melting point of Na_2CO_3 is 851 °C, so it is possible that any behaviour as a flux would be limited for the synthesis of Bi-2212, where the typical dwell temperature is 850 °C.[277] It is possible, however, that the flux could form a eutectic mixture with the other reactants within the furnace, depressing the melting point of the Na_2CO_3, and thereby allowing the microcrucible mechanism to occur.

As can be seen in Figure 4.7, nanowires were successfully synthesised using this method. The wires shown were found scattered periodically throughout the sample at all dwell times and temperatures, though more consistently when dwelled at 850 °C. The wires observed exhibited a high-aspect ratio and were only observed at the edges of the material. Additionally, many of the wires were observed to have bent during growth. For a wire to become bent during synthesis, there must be some sort of imbalance of forces placed on it during growth, causing strain on the growing crystal and thus resulting in a wire that bends as it grows. This has been artificially induced in the past through the growth of nanowires from core-shell heterostructures, which grew into u-shaped wires.[278] Another reason for the bending of the wires can be inferred from the SEM. The wires are extremely thin with a high aspect ratio. The wires may be too thin to support the length as they grow, resulting in strain as they grow and leading to their bending. These wires appear to exhibit no tapering towards the end, nor evidence of a catalytic droplet at the end; which implies that the wires have not grown *via* the VLS mechanism of growth.

For these samples, adding a dispersion of Na_2CO_3 over the top of the sample, thereby increasing the relative amount of flux on the sample, also seems to increase the likeliness for nanowires to form. This is seen by examining the difference between the SEM on the left column of Figure 4.7, compared to those on the right column. Especially when comparing those that were synthesised at 830 °C in Figure 4.7a-d. For both dwell times, the samples that contained an extra surface dispersion of Na_2CO_3 exhibited some nanowire growth, particularly when examining the edge of the pellet. However, these nanowire growths were rare in the sample, and thus it is unlikely that they would be isolatable from the sample for further examination by TEM. Indeed, attempts to carry this out were unsuccessful; thus, additional analysis of the wires through selected-area electron diffraction (SAED) was not achieved. For the samples grown at a higher dwell temperature of 850 °C, nanowires were observed more frequently, with evidence of their growth from the bulk of the pellet observed in all four different experiments (Figure 4.7). Again, in this case the wires were infrequently observed, thus unable to be examined by TEM.

When analysed by pXRD, the samples were found to consist of the same phases as each other, but in differing relative quantities. For the samples synthesised at 830 °C with a 1 h dwell time, the quantity of the target phase, was low at around 7 % of the sample. Overall the phase purity of all of these samples was poor, with no single phase making up more than 50 % of any of the samples. This indicates that the reaction cannot proceed to completion with the parameters used,
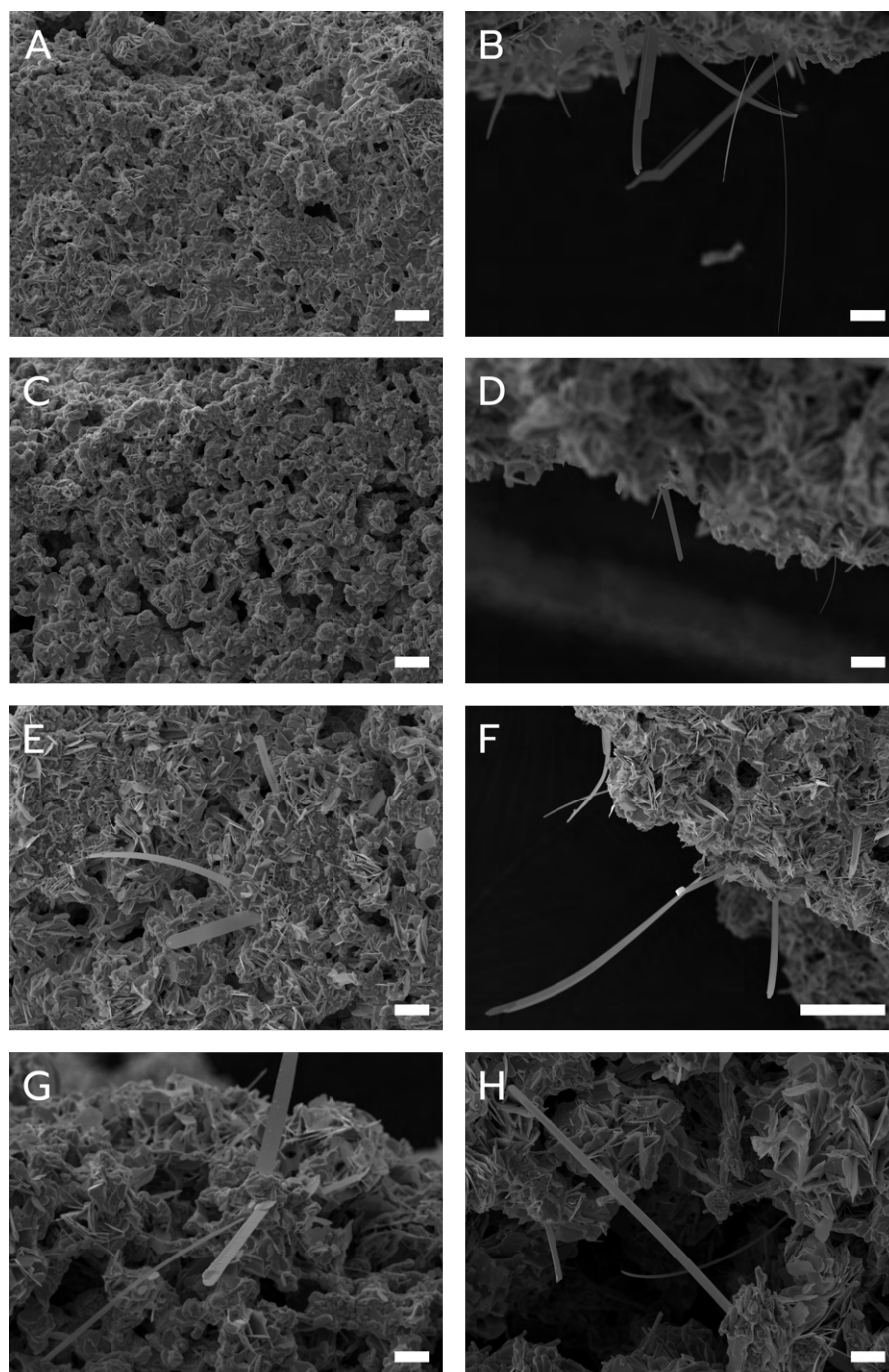
Figure 4.7: Scanning electron micrographs depicting the results from synthesis attempts of
Bi-2212 qusing a Na_2CO_3 flux. (a-d) were dwelled at 830 °C, with a-b being dwelled for 1 hour
and c-d being dwelled for 2 hours. (e-h) were dwelled at 850 °C, with e-f being dwelled for 1 hour,
and g-h being dwelled for 2 hours. (b, d, f and h) had an additional dispersion of Na_2CO_3 over the
surface of the pellet prior to calcination. Scale bars in (a-e and g-h) indicate a length of 10 μm
and (f) indcates a length of 50 μm.

which is unsurprising in the case of a solid-state reaction, where the reaction is limited by mass transport of the solid state, thus resulting in incomplete calcination.
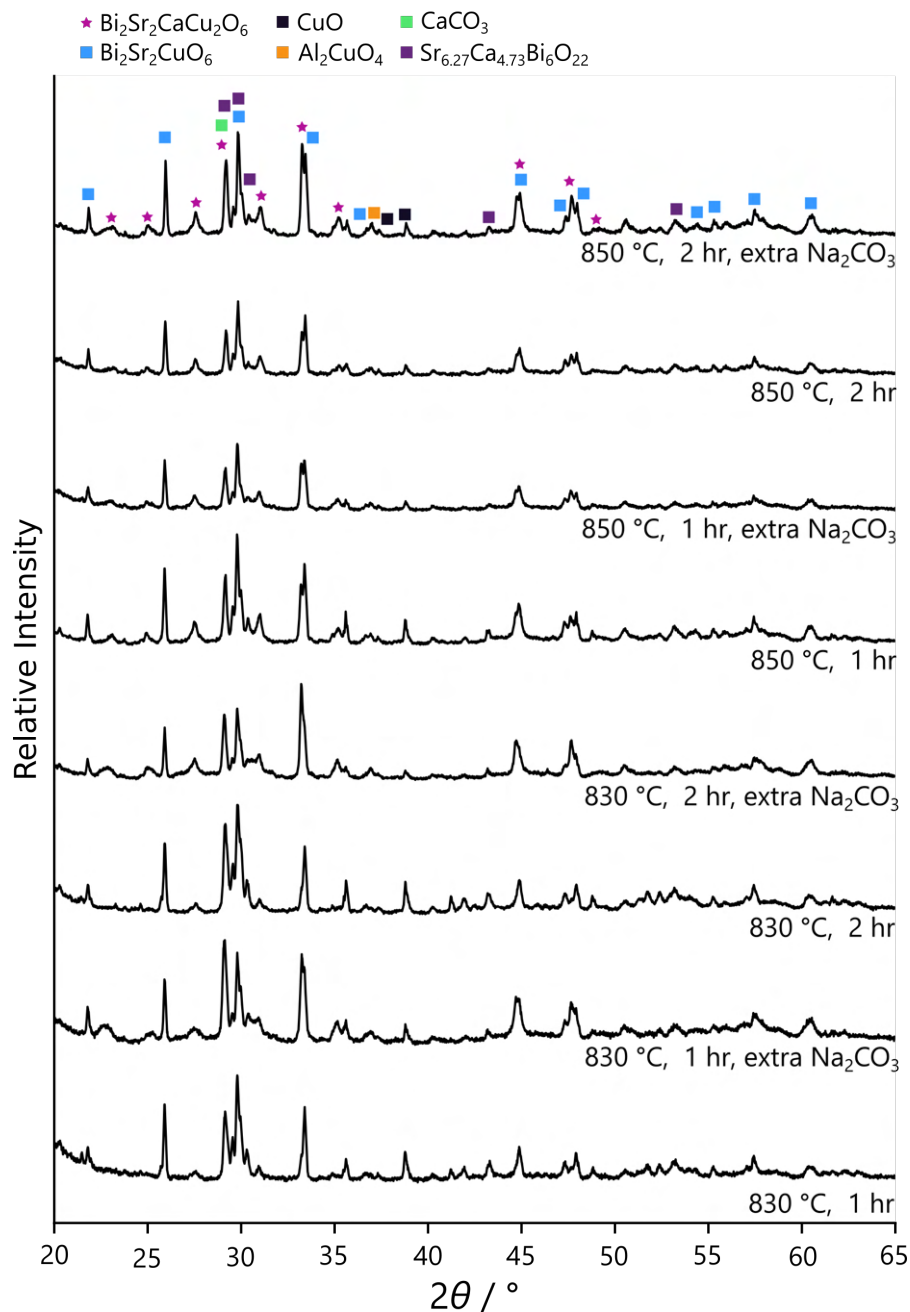
Figure 4.8: pXRD data corresponding to the samples in Figure 4.7. In general, there was very little difference in the phases that were present between samples, but rather just a change in the relative quantities of each phase.

4.2.1.3 CaCl$_2$ Flux

Some results in Hector Christodoulou's work determined that the nanowires were deficient in calcium; it was considered that using a calcium-based flux could yield nanowires, with an excess of calcium providing the necessary stock solution for Bi-2212 nanowires.[241] In this case, several different temperatures and dwell times were attempted. It was found that with a dwell temperature of 850 °C and dwell time of 2 hours, there was evidence of some nanowire growth which had then merged and melted. There was no evidence of nanowire growth with a dwell time of 1 hour, so progressively longer dwell times were explored. All of these samples consisted of 10 % CaCl$_2$ with respect to bismuth. However, only the samples coated in an additional dispersion of CaCl$_2$ over the pellet showed any evidence of nanowires. Figure 4.9 shows the progression of nanowire growth at these different dwell times and a plot of several EDXA spectra of one of the wire samples. From the SEM shown, it appears that the nanowire growth occurs within a very small window of about 20 minutes, though it should be noted that these SEM are not carried out *in-situ* so the sample has been allowed to cool to room temperature as well. This cycle of wire formation and subsequent melting means that the nanowire growth may have been missed when analysing other samples. From figure 4.9b, it appears that when nanowire growth begins, the surface of the pellet becomes coated in a bumpy texture before subsequent nanowire growth. Figures 4.9e and 4.9f appear to show the standard texture of Bi-2212 and exhibit no evidence of nanowires, despite Figure 4.9g exhibiting evidence of nanowires that have grown and melted together again. This could be indicative of the nanowire growth not occurring over the entire sample, and so any evidence of the wire growth has been missed during these samples. The shape of the wires indicates the microcrucible mechanism of nanowire growth, as they do not taper towards one end, nor is there any evidence of a catalytic droplet indicative of VLS.

Table 4.1: EDXA data determining the relative atomic percentage amounts of different atoms within the sample at several sites over the SEM depicted in Figure 4.9h.

	Site 1 At %	Site 2 At %	Site 3 At %	Site 4 At %	Site 5 At %
Bi	0.5	0.6	0.7	1.0	0.1
Sr	2.3	2.7	2.7	2.5	2.6
Ca	17.7	20.4	23.7	18.1	19.5
Cu	13.1	12.9	12.6	8.3	14.2
O	39.4	36.5	38.1	29.3	40.8
C	26.4	26.9	22.2	40.3	22.7

Unfortunately, from EDXA data, it is clear that the samples are extremely bismuth and strontium deficient, with an atomic percent of 1.2 % and 3.6 %, respectively, compared to that of calcium and copper, with atomic percentages of 30.1 % and 16.3% respectively. It is possible that the extra equivalent of the chloride ion, from the divalent calcium chloride, is reacting
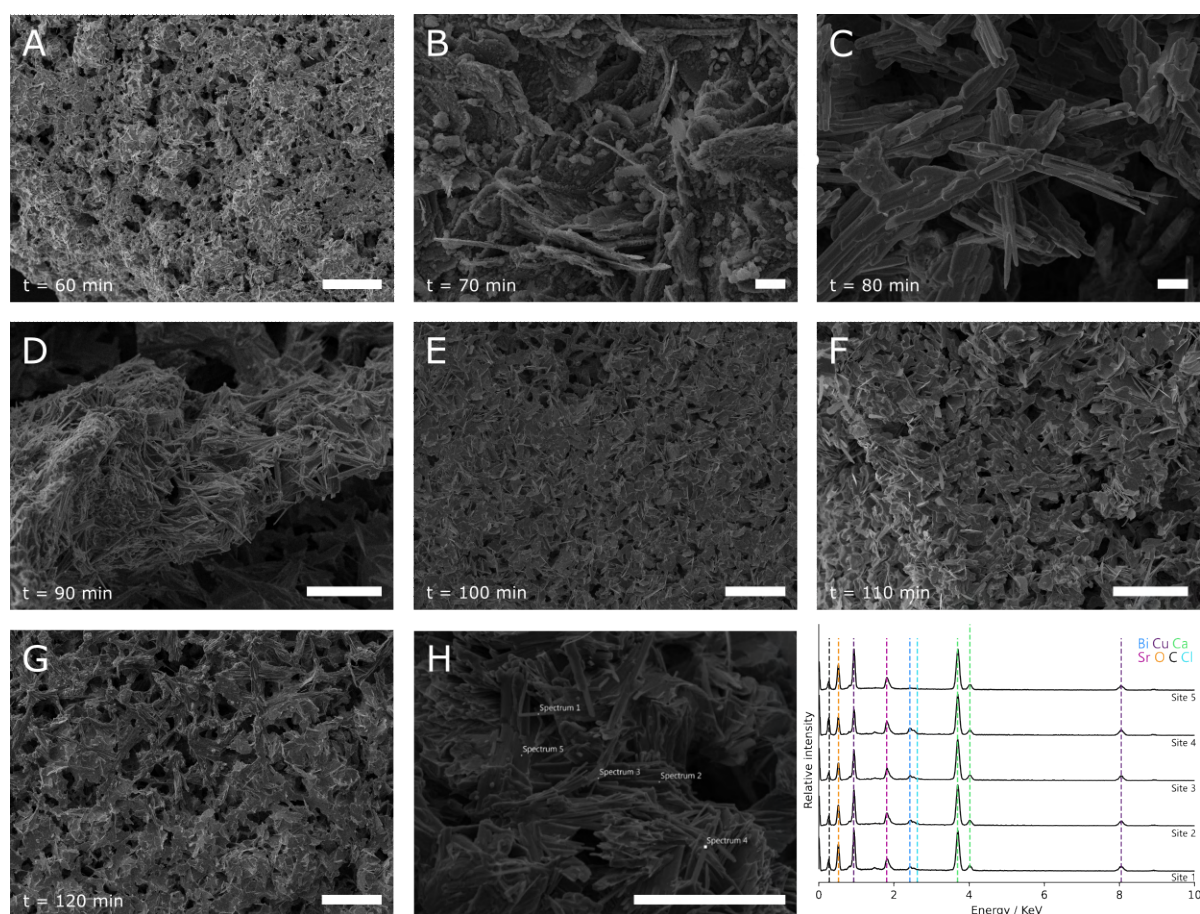
Figure 4.9: a-g) Scanning electron micrographs of samples of Bi-2212 synthesised from metal oxides and with a CaCl$_2$ flux. (h) A closer section of figure d, with annotations of where the EDXA spectra in (i) were taken. (i) EDX spectrum obtained from a point on the nanowires in figure (H). Scale bars in (a, e, g) indicate a length of 100 μm, in (d, f, h) indicate a length of 50 μm, and in (b, c) indicate a length of 10 μm.

with the bismuth to form bismuth oxychloride. This evaporates at around 450 °C, thus resulting in a deficiency of bismuth. A potential experiment using thermogravimetric analysis could be conducted to determine if this was the case. If there is a significant mass loss detected at 450 °C it could be indicative of this transformation and then loss. Indeed, the thermogravimetric analysis (TGA) in Figure 4.10 does show a loss of mass which begins at 470 °C, which could indicate some form of degradation of the material. However, this does not fully confirm that the mass loss is indeed due to the formation of a specific bismuth phase, but rather that volatile phases are formed during the synthesis. It should also be noted that the SEM data are not necessarily indicative of the phases and morphology of the samples within the furnace at the synthesis time. This is because all samples were required to be cooled before analysis, so additional phase evolution and nanowire growth could occur while this cooling is happening. To fully quantify what is occurring inside the furnace, in-situ techniques such as environmental SEM and a powder

X-ray diffractometer with a heating stage would be required.
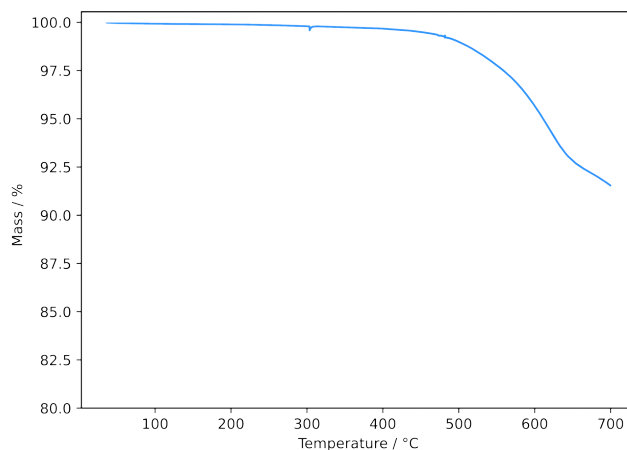
Figure 4.10: TGA data of the precursor powders with a $CaCl_2$ flux. The TGA was performed with an atmosphere of air.

The samples were examined with pXRD to analyse the phase evolution further. Interestingly, as the nanowires form, the phase quantity of the target phase, Bi-2212, falls. Nanowires were observed at dwell times of 80 and 90 min. This observation is consistent with a fall in percentage quantity of the target phase, which begins at 70 min, and a rise in $Sr_2CuO_{3.24}$, CuO and $Bi_4Sr_{7.86}Cu_5O_{19.1}$. The percentage of Bi-2212 reaches a minimum at 100 min, which coincides with the observation of the wires melting together. The percentage quantity of the target phase rises again after this point. These data appear to correspond with the observation from the EDXA data, where the wires are not found to be the target phase.
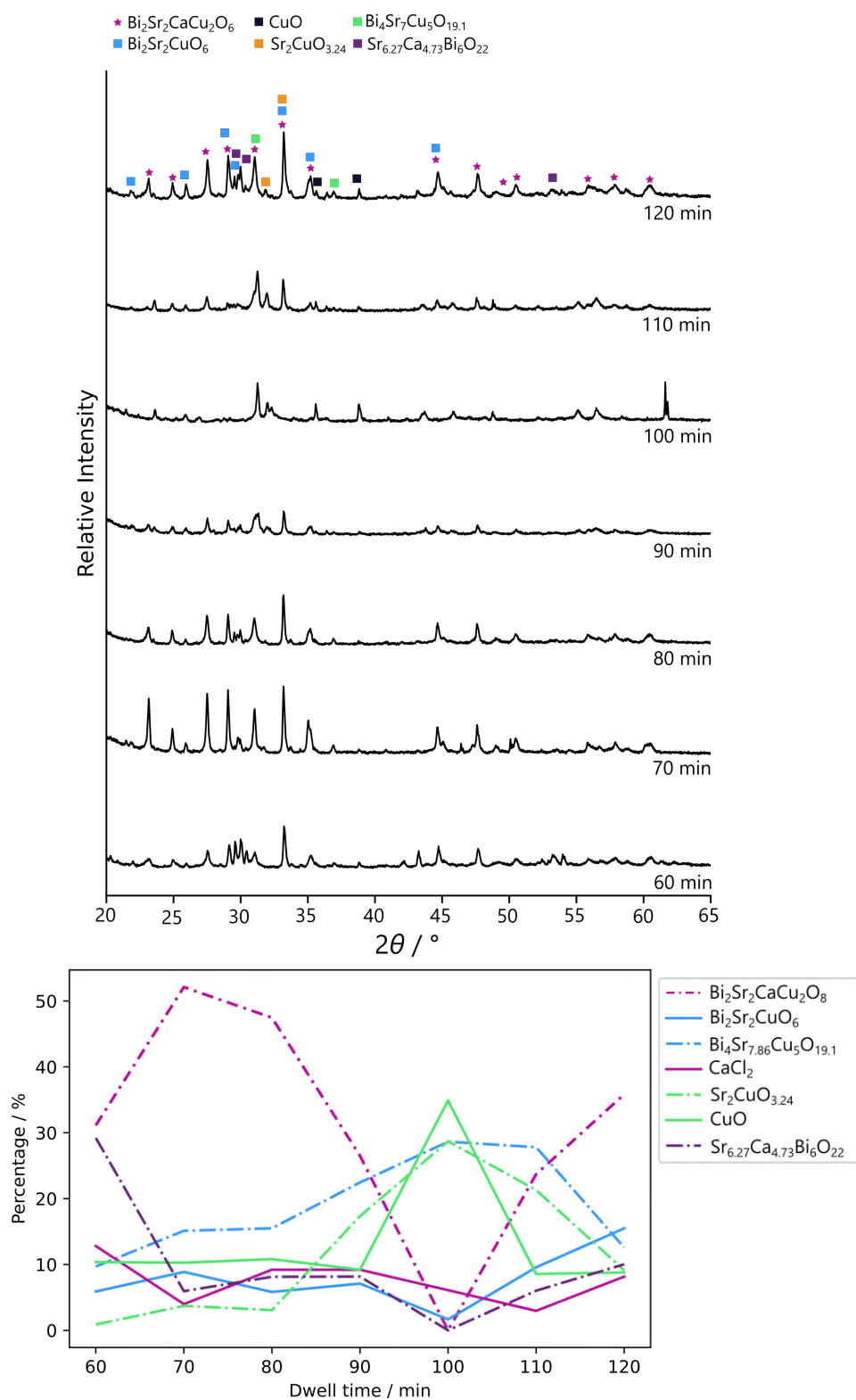
Figure 4.11: pXRD data of the samples corresponding to the images in Figure 4.9.

4.2.2 Synthesis using $Bi_2Sr_2CuO_6$ and $CaCu(OCOOH)_4 \cdot 6H_2O$

As was discussed previously, Bi-2201 was also observed to be a key component in the synthesis
of Bi-2212 from a previous study by Green *et al.* As such, an alternative synthesis method was
devised utilising Bi-2201 as a key starting material. To convert Bi-2201 into Bi-2212, a 1:1
stoichiometric ratio of Ca:Cu must be added. Additionally, during the in-situ observation of the
growth of Y-123 nanowires, it was observed that $BaCO_3$ was a crucial component in the synthesis.
Therefore, a carbonaceous salt of calcium and copper with a 1:1 stoichiometric ratio was desired.
From this, the salt $CaCu(OCOOH)_4 \cdot 6H_2O$ (the OCOOH ion is referred to as OAc hereafter) was
therefore chosen.

It was decided that the Bi-2201 would be combined with $CaCu(OAc)_4 \cdot 6H_2O$ and a flux in an
attempt to manufacture the conditions necessary for the microcrucible mechanism. The Bi-2201
would first be synthesised with a sol-gel method to reduce the necessity for long reaction times;
then this synthesised material would be subsequently ground together with $CaCu(OAc)_4 \cdot 6H_2O$
and the flux, pressed into a pellet and calcined in the furnace. This method would therefore be a
hybrid method which combines a sol-gel synthesis of the starting material and a subsequent solid-
state synthesis. It was hoped that this method would only require three separate components to
combine to result in the growth of nanowires, thus creating the conditions for a ternary reaction
instead of a quinternary reaction as would be required if all the constituent elements and flux
were separate.

4.2.2.1 The synthesis of $CaCu(OAc)_4 \cdot 6H_2O$

Calcium copper acetate hexahydrate ($CaCu(OAc)_4 \cdot 6H_2O$) was first observed in the 1960s through
non-congruent crystallisation between copper acetate and calcium acetate. Its crystal structure,
and that of its isomorph of calcium cadmium acetate hexahydrate, were refined in 1967 and
further developed in 1983.[279,280] $CaCu(OAc)_4 \cdot 6H_2O$ was initially thought to be only a synthetic
compound, but it was also found to naturally occur in the Potosi mine, along with copper ac-
etate.[281] The mineral $CaCu(OAc)_4 \cdot 6H_2O$ was named paceite from then onwards. Recently a
mechanochemical synthesis was carried out to examine the mechanism by which this salt crys-
tallises in nature.[282]

By virtue of the higher solubility of calcium acetate compared to copper acetate, conventional
syntheses require a non-congruent crystallisation. A typical synthesis of $CaCu(OAc)_4 \cdot 6H_2O$
involves mixing two supersaturated solutions of calcium acetate and copper acetate and waiting
for the $CaCu(OAc)_4 \cdot 6H_2O$ crystallites to form. Depending on the desired crystallite size, this can
take several days to weeks. There is also a risk of forming calcium acetate deposits on the crystal-
lites should the solution be left for too long due to the abundance of calcium acetate required.
This synthesis is incompatible with the nanoparticle syntheses carried out for the $Sr_xCa_{1-x}(CO_3)$
particles synthesised previously, so the non-congruent crystallisation was attempted in this case.

Following non-congruent crystallisation, the crystals were subsequently crushed with ball-milling or hand grinding. From the SEM in Figure 4.12, particles were of a wide range of sizes with most of the particles on the order of a micron. However, when examined with TEM (Figure 4.12b), it could be seen that there were smaller crystallites, with sizes around 541 nm. This TEM is not representative of the whole sample, but it does indicate that there are particles present that are nanosized. Despite not providing only nanosized particles, it was reasoned that experiments with this material would yield a sufficient proof-of-concept test to determine whether this method was viable to synthesise anisotropic wire-like growths of Bi-2212. Should the method be successful, alternative methods could be devised to produce nanosized particles of $CaCu(OAc)_4 \cdot 6H_2O$ or produce an alternative CaCu co-crystal which can be synthesised as nanoparticles. SEM and pXRD data for the $CaCu(OAc)_4 \cdot 6H_2O$ is found in Figure 4.12. It can be seen from the SEM that some sections of particles are nanosized, while the rest are larger clumps of material. Should this method successfully synthesise nanowires, the resulting wires would likely exhibit a wide range of widths. All peaks observed in the pXRD could be attributed to the target phase.
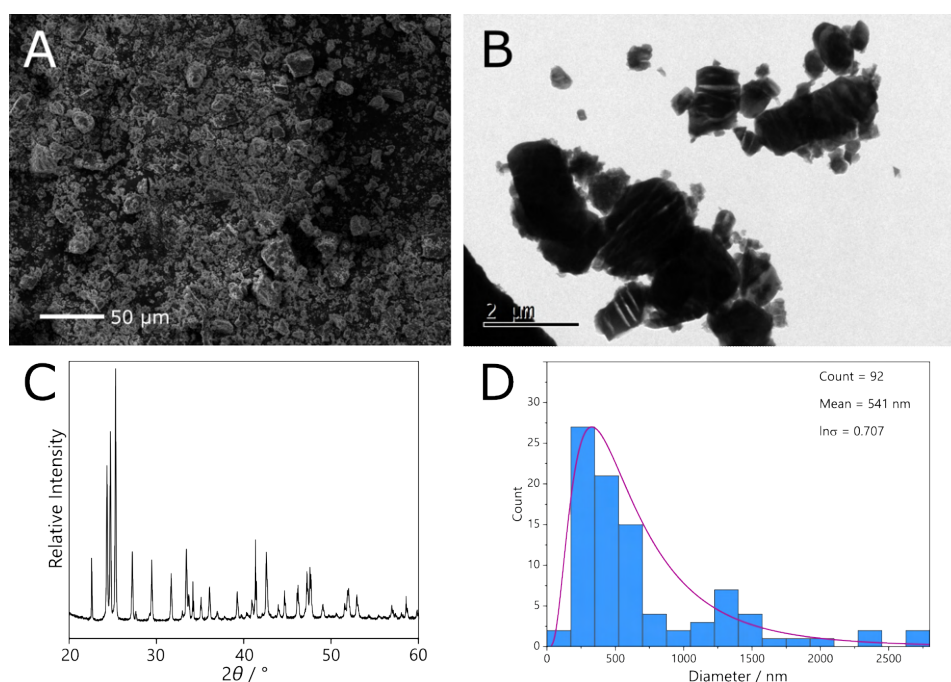
Figure 4.12: a) SEM of the $CaCu(OAc)_4 \cdot 6H_2O$ after ball milling. Scale bar represents a length of 50 μm. b) TEM of the same sample c) pXRD of the as-synthesised $CaCu(OAc)_4 \cdot 6H_2O$. All peaks can be attributed to the target phase, $CaCu(OAc)_4 \cdot 6H_2O$. d) histogram distribution of measured diameters of the particles. Sample was synthesised by Sorrel Haughton.

Interestingly, in an attempt to speed up the synthesis of the $CaCu(OAc)_4 \cdot 6H_2O$ by utilising a potential antisolvent to force the target phase to crystallise quicker, it was found that the addition of acetone to an aqueous solution of $Ca(OAc)_2 \cdot H_2O$ and $Cu(OAc)_2 \cdot H_2O$ resulted in the formation of a gel. This gel subsequently underwent syneresis and collapsed, resulting in the crystallisation

of the target phase. Some examples of this synthesis method can be found in Figure 4.13 - it
can be seen that as the gel undergoes syneresis and collapses, blue crystals are deposited along
the outside of the gel. While these samples were not used in the following syntheses of Bi-2212
nanowires, it was an interesting result that indicated a potential rapid route to the synthesis
of $CaCu(OAc)_4 \cdot 6H_2O$ in the future. The formation of gels from $Ca(OAc)_2 \cdot H_2O$ is well known to
occur when combined with ethanol, but it has not been observed for its formation with acetone.[283]
Indeed, the formation of a solid gel from ethanol and $Ca(OAc)_2 \cdot H_2O$ is the basis behind 'solid
ethanol' and has been used in the food service industry as a solid source of fuel for keeping food
warm as the brand Sterno previously.[284,285]
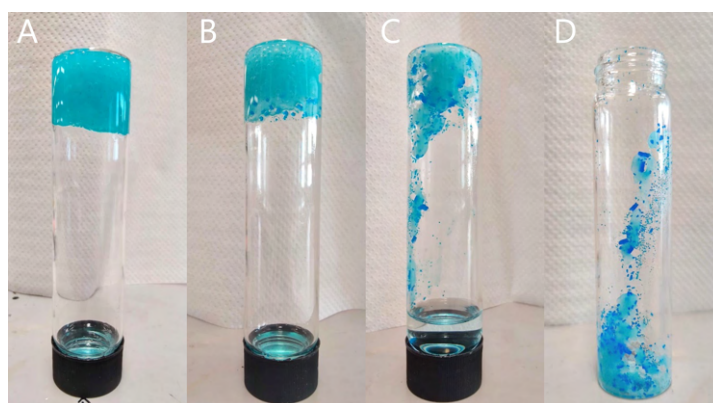
Figure 4.13: Photos of the gel formed between an aqueous solution of $Ca(OAc)_2 \cdot H_2O$ and
$Cu(OAc)_2 \cdot H_2O$ and acetone and its degradation. a) is as it was made, b) is 1 day after its
synthesis, c) is 1 week after its synthesis, d) is a day after the lid was removed and excess solution
had been removed.

4.2.2.2   The synthesis of Bi-2201

To synthesise Bi-2201, two methods were devised: through a biopolymer-mediated synthesis
utilising dextran, and using a natural deep eutectic solvent (NADES) between betaine and
glucose as a solvent. These two syntheses follow methods discussed in Chapter 4, and were used
for similar reasons as discussed there. As discussed, Bi-2212 has been successfully synthesised
through both methods previously, so it was reasoned that Bi-2201 could be similarly synthesised
by adjusting the ratio of metal salts within the precursor solutions.[138,159] Both syntheses were
carried out, as they would likely yield different morphologies, which could affect subsequent
nanowire synthesis attempts. From SEM, it is clear that there is a marked difference between
the morphologies of these materials when synthesised by these methods. The sample synthesised
through the NADES was observed to consist of a flakey sample with small combined crystallites.
The sample is also porous, with large chunks of material with voids between them (4.14a).
In contrast, the results from the synthesis with dextran showed no real structural direction,
appearing to show randomly sized chunks of material (Figure 4.14b).
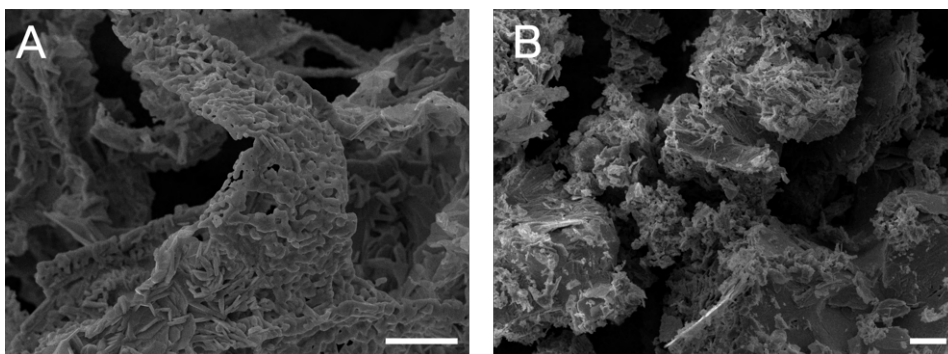
Figure 4.14: SEM depicting the materials when synthesised by (a) a method utilising NADES as a solvent, and (b) a biopolymer-mediated method with dextran as the biopolymer. (b) was synthesised by Sorrel Haughton. Scale bars in both images represent a length of $10\,\mu m$.

When considering the pXRD of the samples, the NADES synthesis also appeared to show that when synthesised *via.* a NADES, the sample was much purer than what was synthesised with dextran as a biopolymer. It could be that synthesising the material with a lower molecular weight dextran, as was carried out in Chapter 3 could alter the purity, though this was not carried out in the present thesis.

4.2.2.3 Bi-2201 and sodium flux nanowire synthesis

As a control experiment, a pellet was made from the Bi-2201 and NaCl with no $CaCu(OAc)_4 \cdot 6H_2O$. Incredibly, the result from this synthesis showed a pellet seemingly made from wires when examined by SEM (Figure 4.15). The appearance of these wires corresponds to what would be expected from wires grown with the microcrucible mechanism; a consistent width along the wire and flat ends. This is intriguing as there should be no reaction during the synthesis as it is merely Bi-2201 and NaCl being heated together. Therefore, the NaCl may be forming a eutectic mixture with parts of the Bi-2201 pellet, forming sections of molten material which become supersaturated, followed by wires growing from these molten beds. Alternatively, as the Bi-2201 is not pure, the impurity phases within the bulk of the material could behave as the microcrucible from which the Bi-2201 is growing. Whether this mechanism is applicable to other systems is yet unknown, though the pellet was somewhat reminiscent of the observations of Bi-2212 whiskers that have been previously reported.[263] This would have to be affirmed through an environmental experiment such as an SEM or TEM with a heating stage.

The pXRD pattern (Figure 4.16) from this sample did not appear to match any of the Bi-2201 phases in the ICSD, but instead, the peaks matched those reported by Bendersky *et al.* which has an entry in the International Centre for Diffraction Data (ICDD).[91] Unfortunately, this paper does not report atomic positions, so making a crystal information file (CIF) for the material to be converted later to a Profex-compatible str file was impossible.[91,184] However, Darriet *et al.* were able to resolve the specific monoclinic phase by using a combination of electron diffraction,
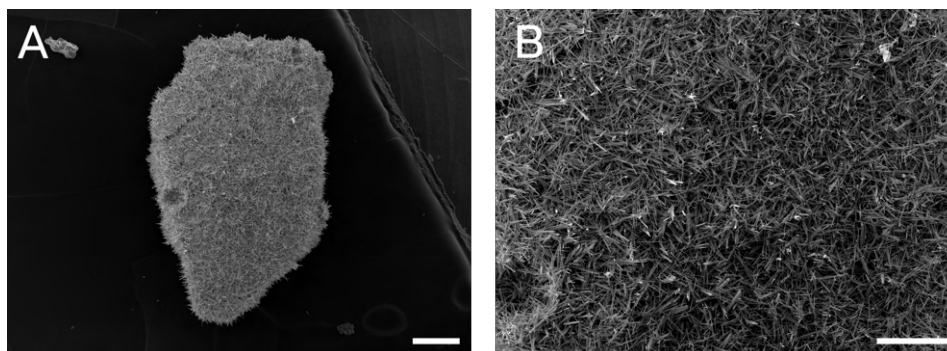
Figure 4.15: SEM depicting the results of combining Bi-2201 with NaCl. Scale bars in (a) represent 200 μm, in (b) represent 100 μm.

X-ray diffraction and neutron diffraction. While this phase is not present on the ICSD, a CIF was able to be made using the program VESTA, which could then be imported into Profex for analysis by Rietveld refinement.[185] The resulting pXRD pattern (Figure 4.16) appears to show that the sample primarily consists of the monoclinic polymorph of Bi-2201. Interestingly, this synthesis often yielded wires that looked melted together when the Bi-2201 had been synthesised from NADES instead of the dextran. Both the morphology and the purity of the starting material were different when synthesising the sample from dextran over NADES, indicating that something about the morphology and ratio of impurity phases of the Bi-2201 phases was promoting the growth of nanowires in this case.
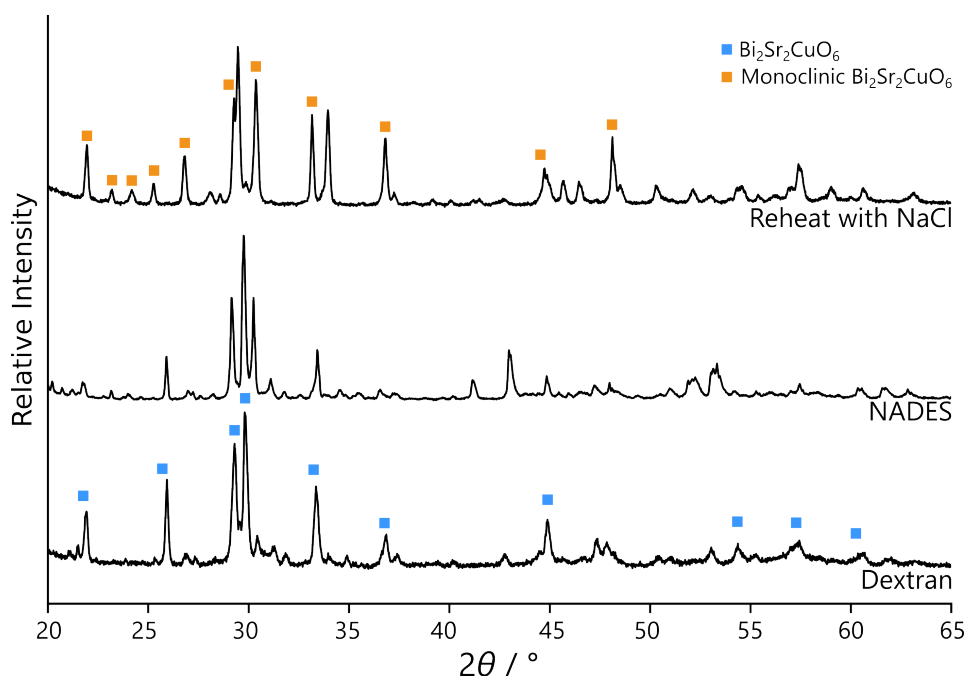
Figure 4.16: pXRD of the Bi-2201 synthesised by dextran, NADES, and the synthesis with the NaCl.

4.2.2.4   The synthesis of Bi-2212 wires with a NaCl flux

Even though wires formed when Bi-2201 was combined with a flux and subsequently calcined, the proposed synthesis utilising $CaCu(OAc)_4 \cdot 6H_2O$ was still carried out. It was thought that adding the Ca-Cu phase in combination with the previous synthesis could allow for the combination of these phases during the calcination, resulting in Bi-2212 wires. Interestingly, there was a difference in the product material depending on the synthesis method of the Bi-2201. When Bi-2201 was synthesised from a NADES sol-gel method, nanowires were not frequently observed. In contrast, when the samples were synthesised through a dextran-mediated method, wires were consistently found in abundance throughout the surface of the sample (Figure 4.17). The wires were measured to consist of an average diameter of 570 ± 1.57 nm, the distribution of nanowire diameters can be found in Figure 4.17e.

It can be seen that dextran-based synthesis results in the formation of wires. When synthesised with 30 mol % NaCl with respect to bismuth, many wires were observed throughout the sample. As shown in Figure 4.17, the wires were found throughout the pellet's surface, appearing to have grown from within the pellet rather than just being localised to its edges. The wires ranged in size between 200 nm and 2 µm, with a lognormal distribution and mean wire width of 570 nm. Interestingly, this coincides with the size distribution of the smaller $CaCu(OAc)_4 \cdot 6H_2O$ particles examined by TEM previously. This agreement in size distribution agrees with the assessment that the $CaCu(OAc)_4 \cdot 6H_2O$ could behave as a microcrucible in this reaction. To further confirm the crystal structure of the nanowires, the wires were cast onto a TEM grid by sonicating them in ethanol for *ca.* 10 s and then dropcasting the material onto a copper grid. From the SAED in Figure 4.18d, it can be seen that the diffraction patterns consists of bright spots and surrounding satellite spots which are lower in intensity. This occurrence of satellite spots is characteristic of Bi-2212 because it consists of bismuth-rich and bismuth-poor zones, creating an incommensurately modulated structure that results in additional diffraction spots on the SAED.[286,287] However, these satellite spots are consistent for all members of the BSCCO family, and as such their appearance is not proof of the formation of the target phase.

Analysis of the diffraction spot pattern for this sample determined that it was indexable to the target Bi-2212 phase with a zone axis of [001]. However, when examined with the software CrysTBox, it was also found to be indexable to Bi-2201 with the same zone axis.[186] Upon direct comparison of the analysis of these two data, it was found that when indexed to Bi-2212, the standard deviation of the calculation was 0.0014, compared to 0.0016 when indexed to Bi-2201. It is possible that the sample was an off-stoichiometry sample with a lower amount of calcium than expected. To further analyse this, EDXA was performed on this sample (Figure 4.19). The sample was cast on a copper grid, so the data for copper is unreliable in this case. Despite this, it can be seen that there is a higher concentration of calcium ions on the wire than in the surrounding area. Analysis of the spectrum in terms of atomic percent (excluding the data for copper, as it could not be separated from background data from the grid) determined that the sample consisted of 5 %
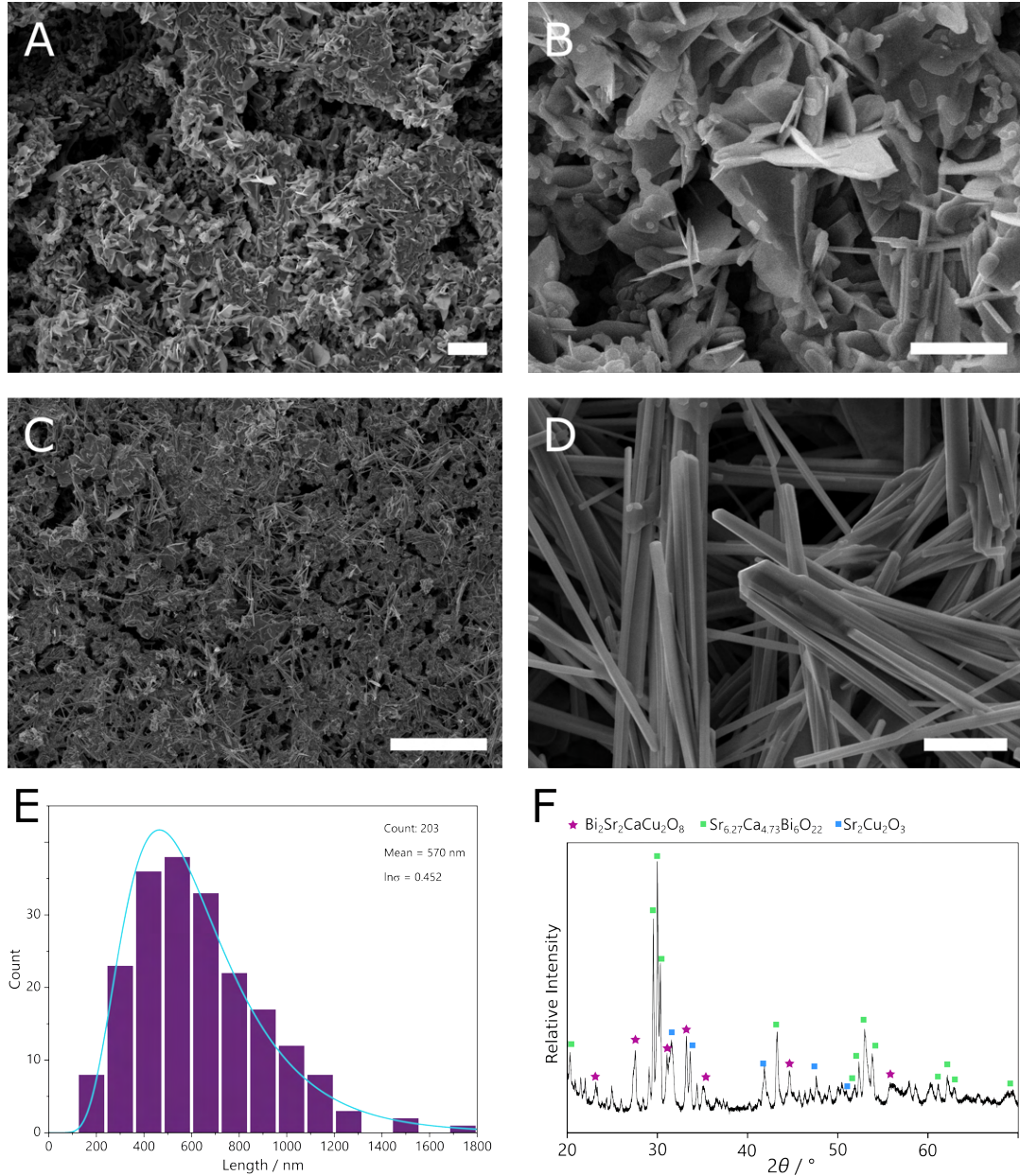
Figure 4.17: a and b) SEM of a sample synthesised with Bi-2201 synthesised from a NADES, compared to (c and d) SEM of a sample synthesised with Bi-2201 synthesised *via* the biopolymer dextran. Scale bars in (a) represents 10 °C (c) represent 100 µm in (b and d) represent 5 µm. e) histogram distribution of the widths of the wires, along with the logaritmic mean of the plot. Mean wire width was calculated to be 570 nm with a standard deviation of 1.57 nm. f) pXRD data from the same sample. Sample displayed in (c - f) was synthesised by Sorrel Haughton

calcium compared to 56.4 % strontium and 38.6 % bismuth. Therefore, this material appears to be abundant in strontium and sparse in calcium. It is likely that neither Bi-2201 nor Bi-2212 are the exact phase present and that the sample is an off-stoichiometry material.
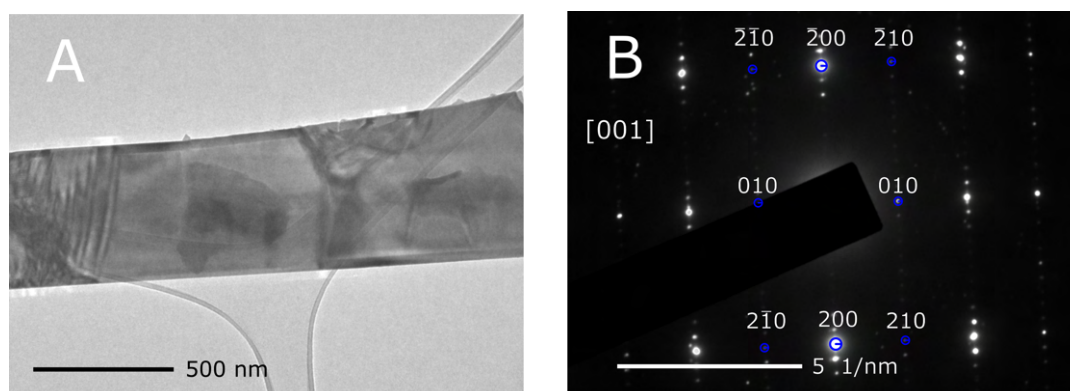
Figure 4.18: a) TEM of a wire from the same sample, with b) the corresponding SAED. Spots are indexed to Bi-2212 with a zone axis of [001].
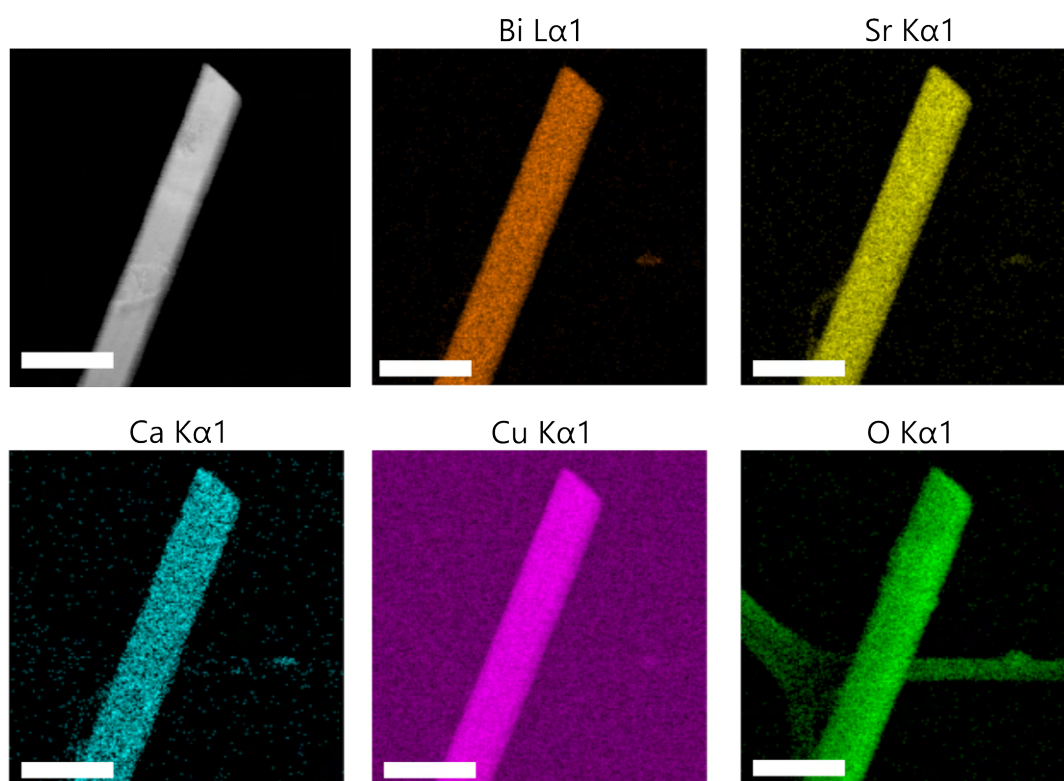
Figure 4.19: Scanning TEM image of the same grid as in 4.18. Corresponding EDXA maps of specific energy transitions are shown. The feature behind the wire shown in the O Kα_1 energy map is from the lacey carbon film upon which the wire is suspended. Scale bars indicate a length of 500 nm.

Additional diffraction data were taken from other wires found within the sample, and a summarisation of the SAED analysis are given in Table 4.2, which is paired with the SAED data given in the Appendix (Figure A.3). As can be seen, the vast majority of the diffraction patterns obtained from this sample consistently obtain a zone axis of [001] and a low standard deviation.

101

Table 4.2: Data as obtained from the software CrysTBox when examining the SAED observed for various wires examined by TEM. Corresponding images are found in Figure A.3.

Image	Bi-2212		Bi-2201	
	Zone axis	Stdev	Zone Axis	Stdev
a	[001]	0.0014	[001]	0.0016
b	[001]	0.0019	[001]	0.0021
c	[001]	0.0006	[001]	0.0004
d	[001]	0.0057	[001]	0.006
e	[$\bar{1}$01]	0.0058	[011]	0.0025
f	[001]	0.0013	[001]	0.0008

Furthermore, when applied to both Bi-2212 and Bi-2201, there was very little difference between the calculated standard deviations, indicating that the diffraction pattern was a good fit for both crystal structures. This, again, indicates that the wires are likely an off-stoichiometry of BSCCO.

If these wires were Bi-2212, the calculated zone axis of [001] indicates that the wire is growing along the a or b-axis. This indicates that this material's intrinsic JJs are actually along the length of the wire instead of perpendicular to the wire. Of course, this is not ideal for forming the high-density of intrinsic JJ as desired, but these wires could still find applications in other superconductor-based microelectronics.

4.2.3 In-situ TEM studies

A heating stage was utilised to attempt to reproduce the observations by Boston *et al.* for the Bi-2201 system and fully elucidate the mechanism of nanowire growth. A grid was prepared by touching a gold grid with a carbon film to a powder made of Bi-2201 and NaCl. The grid was then loaded into a Jeol 2100. The sample was heated quickly to 500 °C and then slowly ramped up to 850 °C while a video was captured. The heating was paused at *ca.* every 100 °C to allow for videos to be saved and to pan around the sample to determine if any observations had been missed. Unfortunately, as shown in Figure 4.20, there was no observation of nanowire growth from this sample. The heating stage used had no way to control the cooling rate and would rapidly cool without control if a lower temperature was set - regardless of which temperature was set. Therefore, this attempt likely resulted in rapid quenching of the material, essentially freezing the sample in place. Despite an attempt to reheat this sample later, nothing happened. Some data from this attempt is promising, however, as it appears that the lighter NaCl crystallites can be seen to be melting. The application of a current to the grid, thus enabling it to heat, resulted in the image drifting throughout the analysis. Therefore, the image had shifted significantly between the two images given in 4.20; as such, an arrow has been added to the image, which indicates the same position in both frames.

Some proof-of-concept heating attempts were subsequently made to rule out that the vacuum
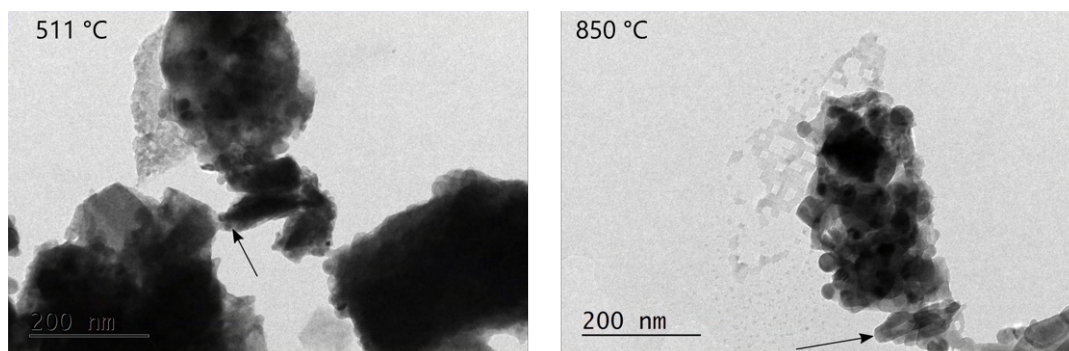
Figure 4.20: Bi-2201 and NaCl sample at 511 °C and 850 °C. Arrows in both micrographs are pointing to the same feature to accommodate the drift that occurs due to the heating.

was affecting the synthesis. These utilised the solid-state synthesis of Y-123 as initially reported by Dr. Jason Potticary.[264] This involved mixing Y_2O_3, $BaCO_3$ and CuO combined with 10 wt % NaCl, which was then added to a carbon-film gold grid by touching it to the powder as with the Bi-2201/NaCl sample. As this is the same system examined by Boston *et al.* but with a solid-state synthesis, it was determined that the vacuum would likely not affect this sample. This time, the heating rate was controlled by manually adjusting the heating current of the stage. This experiment was also used as calibration for future experiments, enabling a correlation between heating current and temperature to be developed. A plot of these data can be found in the Appendix (Figure A.4). The ramp rate of this experiment was much faster than would take place during a routine experiment, and no real change was observed during the synthesis. Unfortunately, the carbon film decomposed during this experiment at about 860 °C, which meant that a complete comparison of the material before and after the synthesis was impossible. Some areas of material left after the heat and cool appeared to show some small nodules of material that could indicate wires beginning to grow (Figure 4.21). As such, it was decided that the experiment would be repeated with a slower ramp rate.
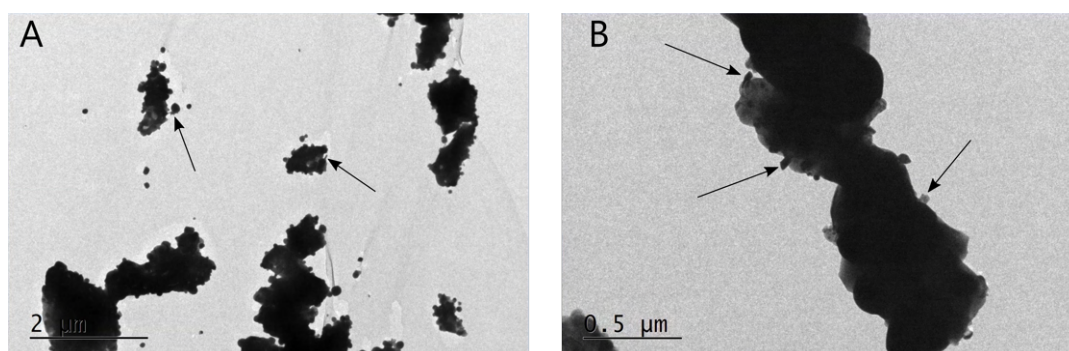
Figure 4.21: Y_2O_3, CuO, $BaCO_3$ and NaCl sample after the heating run. Arrows in a) and b) are pointing to sections of material that could be indicative of the beginning of nanowire growth.

The next attempt exploited the knowledge obtained from the previous run to control the

heating rate to be much slower manually. This was again carried out by manually controlling the current of the heating stage throughout the attempt. As before, videos were captured at 10 min intervals, and the heating was paused between each video. Overall, this equated to a heating rate of $4.9\,°\text{C}\,\text{min}^{-1}$ from 515 to 884 °C, including the pauses to save each video. The individual heating stretches were operated at a ramp rate of $5\,°\text{C}\,\text{min}^{-1}$. A gold grid without a carbon film was used to avoid the risk of the decomposition of the carbon film. Therefore, the material was observed hanging off the grid's edge instead of suspended on a film. In this attempt, several transitions were observed throughout the synthesis. The first of note occurred between the temperatures of 773 - 780 °C, which was after the sample had been heating for 61 min, which is presented in Figure 4.22. This appeared to be some form of melting event, where several sections of material were observed to disappear quickly, while other sections were observed to grow. For this figure, t = 0 represents 61 min. Interestingly, it appeared as though a wire was attempting to grow at t = 17 s, and it continued to grow until it rapidly appeared to melt into the bulk material at t = 46 s. Unfortunately, the scale bar shown is inaccurate due to a software glitch.
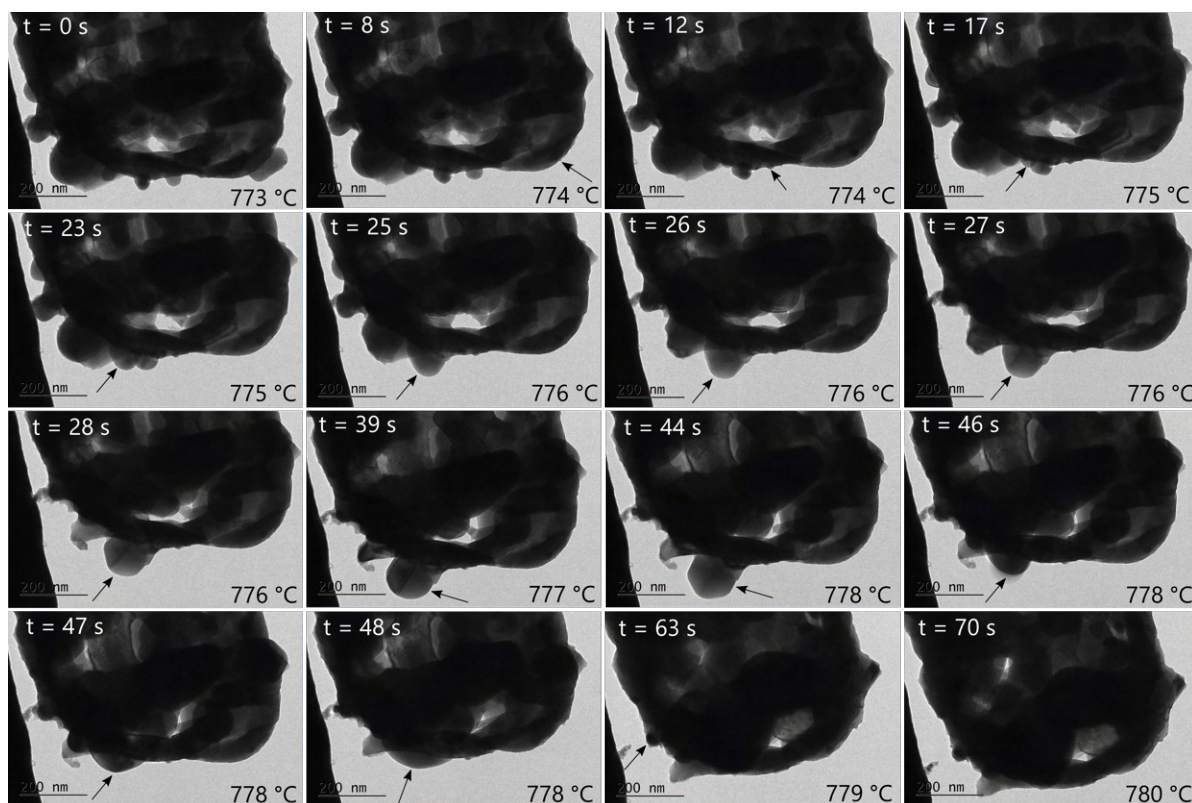
Figure 4.22: Figure depicting still frames from a video taken during the heating from 710 to 810 °C. The images in this figure are a subset from the video between 773 and 780 °C. t=0 represents 61 min since the heating of the sample began. Arrows in figure are pointing to sections of material that have changed between the previous image.

Another significant event that was observed is displayed in Figure 4.23. Again, the scale bar in these images is incorrect due to a software glitch. The t = 0 in Figure 4.23 represents 79 min since the heating began. The clump of material appears to begin to break down at t = 37 s, and the material around it appears to melt together. There was no evidence of any nanowire growth observed in the rest of the heating of the sample. Due to the better control of the temperature throughout this synthesis, it was possible to control the cooling rate of the sample, which had not been carried out in the previous samples. This was undertaken at a similar rate to the heating rate ($5\,^{\circ}\mathrm{C\,min}^{-1}$), but no further transitions for this sample were observed.
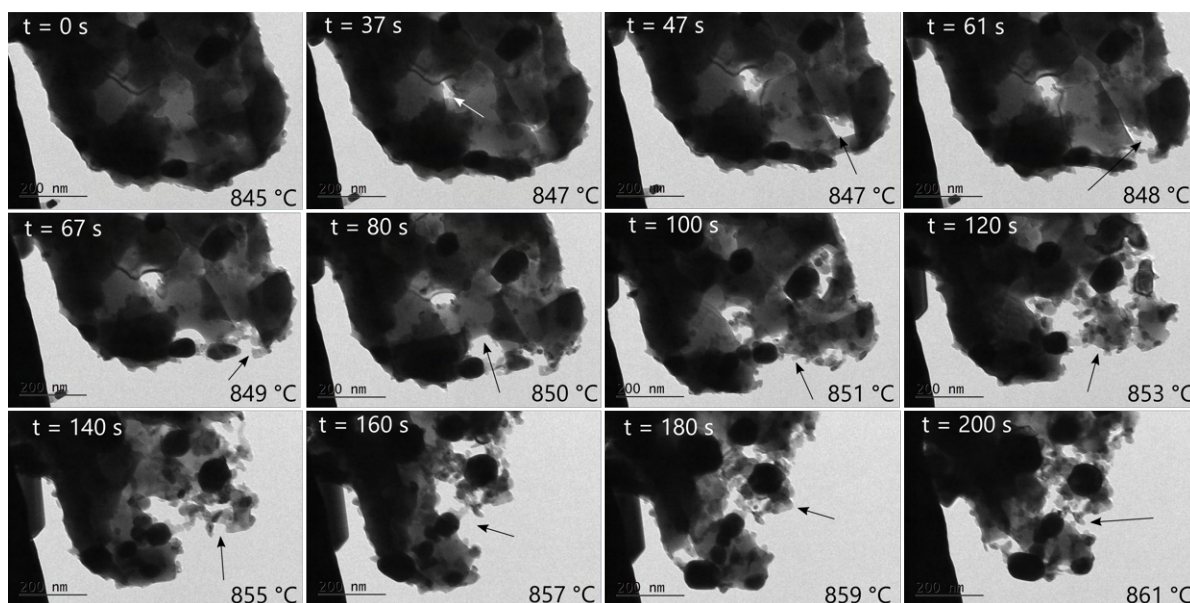
Figure 4.23: Still frames from a video taken during the heating of the sample from 845 to $861\,^{\circ}\mathrm{C}$. The images in this figure are a subset from the video between 845 and $887\,^{\circ}\mathrm{C}$. t=0 represents 79 min since the heating of the sample began. Arrows in figure are pointing to sections of material that have changed between the previous image.

Due to the promising observations from this synthesis, the same experiment was repeated. The lack of observed nanowire growth in the previous experiment could be due to the fact that all four constituent particles had not been simultaneously present on the grid. Unfortunately, due to the heating stage holder, the grid was not in an optimum position for EDXA, so it was difficult to determine if the phases were all present *in-situ*;. At the same time, although this would be possible from SAED; it was challenging to solve these patterns before the experiment. The sample was, therefore, re-run with the same ramp rate but a much faster cooling rate of $26\,^{\circ}\mathrm{C\,min}^{-1}$. It was thought that this increased cooling rate would better emulate the conditions within the furnace, as there is no control of the cooling rate with those experiments. During the heating cycle, there were occasional observations of transformations and features which appeared to be growing into wires - much like what was observed in the previous synthesis (Figure 4.24). However, these features consistently degraded and appeared to re-melt back into the bulk material.
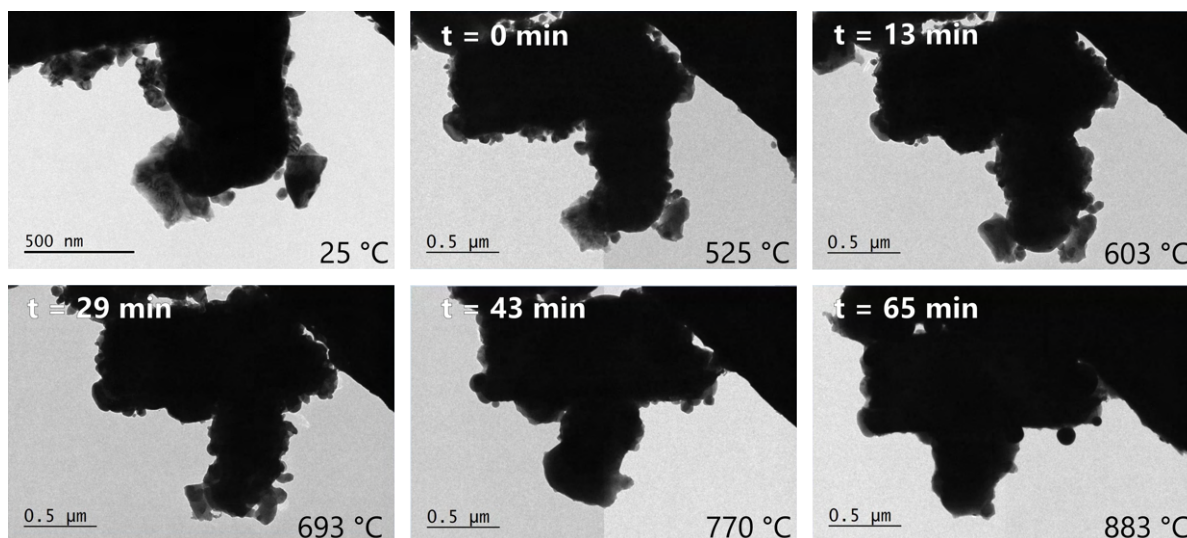
Figure 4.24: Still frames from videos taken during the heating of the sample from room temperature to 883 °C, t = 0 represents the beginning of the controlled heating of the sample from 525 °C.

After this heating, the sample was cooled at $27\,°\text{C}\,\text{min}^{-1}$. Several wires were observed to grow from the bulk material during this cooling period. The speed of this growth appeared arbitrary, as some wires grew throughout the entire cooling period, and others grew very quickly. Details of this are given in Figure 4.25. For Figure 4.25, t= 0 represents the beginning of the cooling period. In particular the wire shown at t=13 min grew to a length of 620 nm with a width of 12 nm, giving it an aspect ratio of 52. This wire was shown to be very flexible during its growth and was seen to bend significantly before it either folded up out of view or broke off completely.

After the cooling, high-resolution TEM could be carried out. From Figure 4.26b, it can be seen that the base of one of the wires is highly crystalline, with a clear change of direction of the lattice fringes at the base of the wire. The d-spacing found in the bulk of this growth was $3.1\,\text{Å}$ which could be associated with the d-spacing for the (220) plane in Y-211, which has a d-spacing of $3.07\,\text{Å}$. SAED from a different section of the material was indexable to Y-211 (Figure 4.26c and d). While this is not the target phase, Y-123, it is not unexpected that Y-211 formed instead, as the vacuum of the electron microscope led to an under-oxygenated phase forming. This was also observed in the initial study by Boston *et al*.

The sample within its holder was then examined with SEM, as more wires may have grown vertically out of the grid. However, when the same feature that had been observed from TEM was found, it appeared as though the wires had disappeared in the transport between the TEM and the SEM. Additionally, these wires were small enough that they were approaching the limit of what is observable by SEM. The backscattered electron imaging shows that some sections of the sample are made of a heavier element than the surrounding material, shown by its lighter colour. Further examination with EDXA (Figure 4.27) showed that some of these sections gave rise to a signal from gold. A signal from gold is to be expected due to the grid upon which the sample
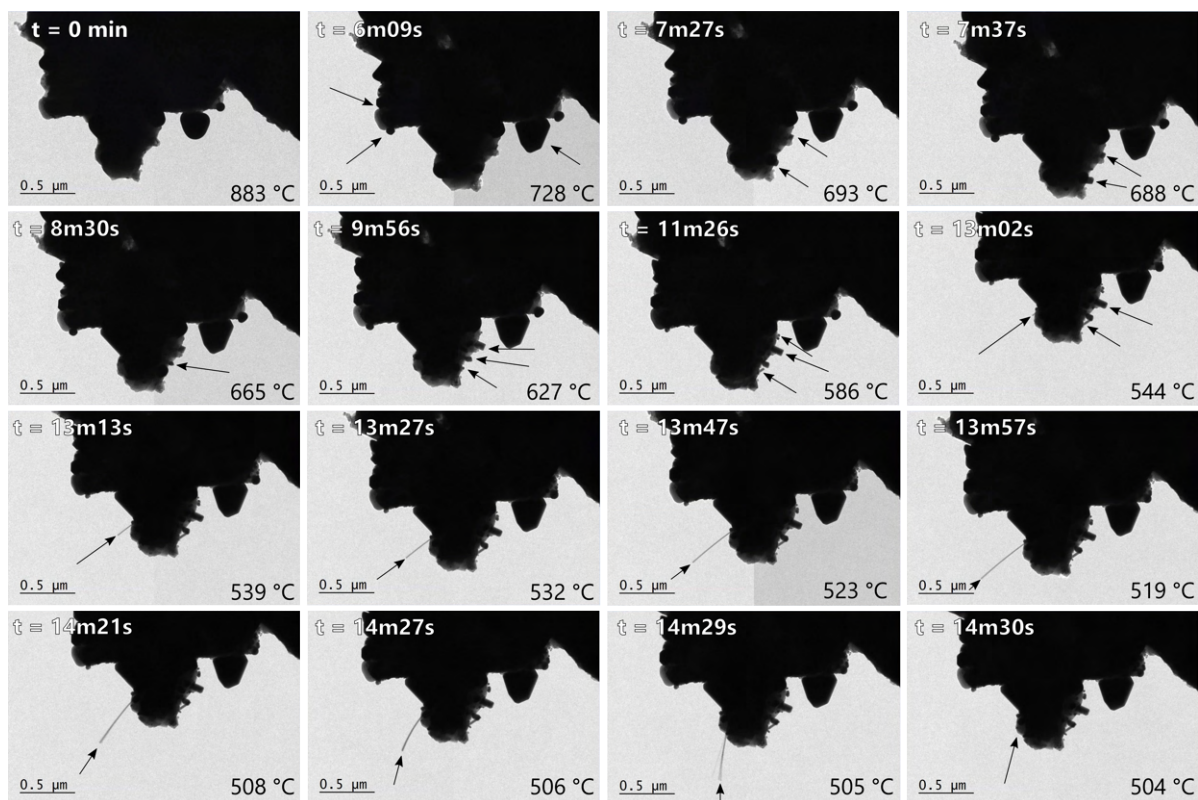
Figure 4.25: Still frames from a video taken during the heating of the sample from 883 to 338 °C. The images in this figure are a subset from the video between 883 and 504 °C. t=0 represents the point at which the cool-down of the sample began. Arrows in figure are pointing to sections of material that have changed between the previous image.

was mounted; however, it appears that some of the sections from which the nanowire growth had occurred also contain some signal from gold. While it is possible that this signal is arising from further within the sample, it is also possible that the grid was degrading during the synthesis of the sample. It has been shown that *in-situ* experiments with a TEM can result in the degradation of the grid, where the heated grid begins to shed nanoparticles upon heating.[288] In this work by Zhang and Su, gold was the most resistant to this effect and no nanoparticles were observed when the grid had been heated to 850 °C. However, in the present work, the sample had been heated to 883 °C, and it is possible that the grid could have shed nanoparticles in this situation. If nanoparticles had been shed from the grid, the nanoparticles produced could have behaved as nucleation points during the cooling, upon which the nanowires could have subsequently grown. Further examinations of the grids *in-situ* would have to be carried out to determine if this is the case.
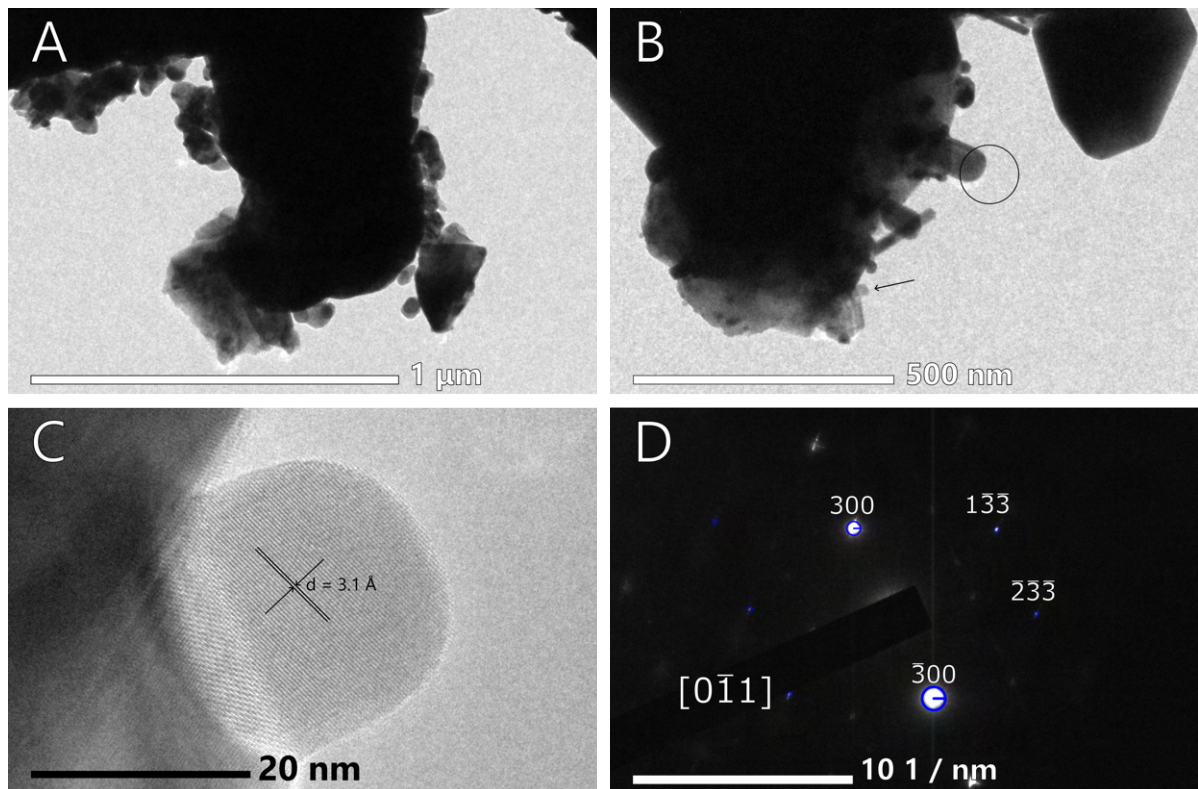
Figure 4.26: a) The area that was examined prior to any heat had been applied. b) The same area after both the heat-up and cool-down of the sample. c) A close-up of one of the areas that had grown during the cool down of the sample. Labelled with an arrow in (b). d) SAED of the section of (b) which is labelled by a circle.
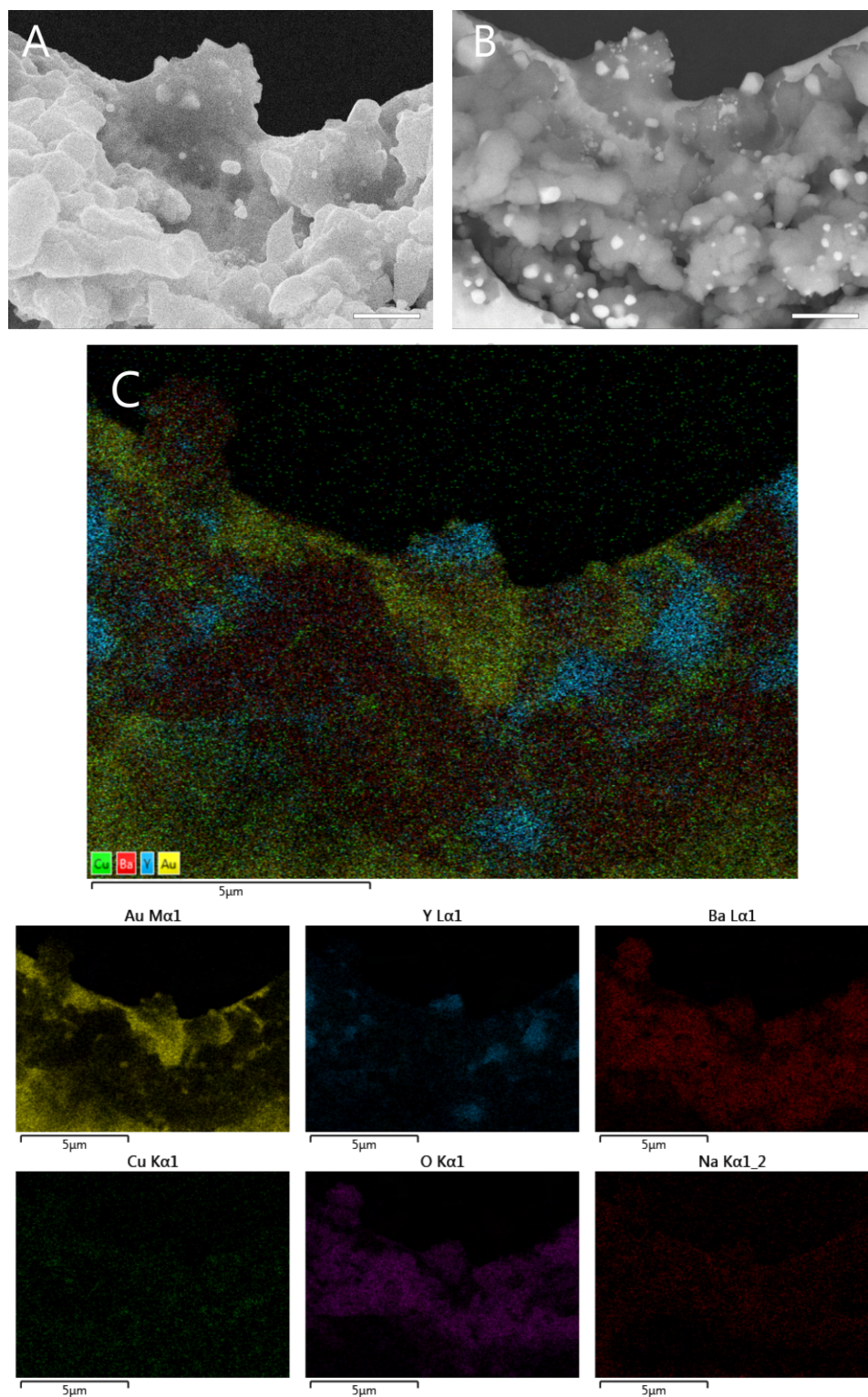
Figure 4.27: a) SEM of the the feature observed in Figure 4.26, imaged with secondary electron imaging b) SEM of the same area but imaged with backscattered electron imaging c) EDXA of the same area. Scale bars in (a), (b) indicate a length of 1 μm.

4.2.4 Summary

Two different methods were used to manufacture the microcrucible mechanism for synthesising nanowires of Bi-2212. The first method combined the component metal oxide with a mixed carbonate nanoparticle with a flux; the second method combined Bi-2201 with $CaCu(OAc)_4 \cdot 6H_2O$ and a NaCl flux.

For the first method, the fluxes examined in this were NaCl, Na_2CO_3 and $CaCl_2$. With all three of these fluxes, nanowires of an ideal composition were not observed. The least consistent method was with a NaCl flux, where only a few wires were observed through a range of samples at four different dwell temperatures. Wires were observed for the samples which utilised a Na_CO_3 flux. Interestingly, these wires were often observed to be bending during growth. This indicated some strain on the wires during growth or potentially that the wires were so thin that they could not support themselves. Despite the observations of wires, the samples synthesised with a $CaCl_2$ flux were highly deficient in bismuth. This indicated that they were formed of a different phase to $Bi_2Sr_2CaCu_2O_{8+x}$. In addition, wires were observed for this sample within a very narrow dwell time, indicating that the wires can form and subsequently melt together. It was realised that this could occur for all of the synthesised samples.

For the second synthetic technique, a large number of wires spread over the surface of the sample was observed. These wires exhibited an average width of 570 nm. However, upon investigation into their composition on the TEM, it was found that they could be indexed to both Bi-2212 and Bi-2201. Further examination of these wires with EDXA indicated that they were highly deficient in calcium and abundant in strontium, indicating that these wires were likely a phase that was somewhere between Bi-2212 and Bi-2201. Further experimentation could be carried out to examine potential solutions to this deficiency in calcium; for example, by utilising alternative fluxes or adding excess calcium into the precursor materials.

Finally, *in-situ* TEM was carried out on the samples to determine if the growth of nanowires could be observed directly. This would have enabled direct confirmation of the microcrucible mechanism. Of particular interest was the examination of the Bi-2201 sample when heated with NaCl, as this would help elucidate the mechanism by which the wires formed. Unfortunately, the preliminary study with this method was unsuccessful, and no nanowire growth was observed. As this experiment was completely new, the heating stage was tested with a system where nanowire growth had already been observed *in-situ*, that of YBCO. The first test with this system was utilised to calibrate the current required to reach specific temperatures. However, unfortunately, no nanowire growth was observed - in part due to the decomposition of the carbon film during the synthesis. For the next two syntheses, the ramp rate of the heating stage was able to be controlled to a rate of $\sim 5\,°C\,m^{-1}$ as would be observed in the syntheses within the furnace. Nanowire growth was observed in the second of these syntheses during the cooling period of the sample. SAED of one of these wires could be indexed to Y-211, which is promising for future studies.

5

SYNTHESIS OF SPONGE ARCHITECTURES OF HIGH-TEMPERATURE SUPERCONDUCTORS

Parts of this chapter are published in Nanoscale Advances. *All data presented within this chapter were obtained by me, with the exception of the Brunauer–Emmett–Teller (BET) isotherm data obtained by Lui R. Skytree and Huan V. Doan and the mercury porosimetry data, which was obtained by MCA services on behalf of Huan V. Doan. The morphology of the original sponge analysed by scanning electron microscopy (SEM) was carried out by Jason Potticary.*[179]

When designing novel functional materials, it is essential to consider the nanostructure of the material along with its chemistry. Nanoscaled features often result in macroscopic emergent properties, such as structural colour. Indeed, it is often the case that a propety of a material is due to the nanostructure of the material and not its chemical makeup.[289] Emergent behaviour resulting from nanostructures is very prevalent in natural materials; for example, the nanotextured surface of a lotus leaf is responsible for its super-hydrophobicity.[44] The capability to reliably replicate and synthesise nanostructures of materials is, therefore, important in the development of novel functional materials. In this chapter, the use of a melamine formaldehyde sponge as a templating agent for the synthesis of sponge-like architectures of high-temperature superconductors is explored.

5.1 Introduction

5.1.1 Porous materials

Porous materials can be characterised as materials that contain voids, where the voids can be filled with a liquid or gas. The International Union of Pure and Applied Chemistry (IUPAC)

has defined a porous solid as 'a solid with pores, i.e. cavities, channels or interstices, which are deeper than they are wide', and the pores within the materials can be randomly orientated or ordered.[290] The different pore diameters, d, of pores within a porous solid have also been partitioned into three types by IUPAC: micropores with $d < 2\,nm$, mesopores with $2 < d < 50\,nm$, and macropores with $d > 50\,nm$. Porous materials have found applications in catalysis, filtration and in lightweight materials by virtue of their often high surface areas and permeability.[291] Additionally, the chemical nature of the pores can drastically alter the applications of the material. For example, molecular sieves based on silica are hydrophobic and can filter organic molecules from water; in contrast, molecular sieves based on aluminosilicates are hydrophilic and can scavenge ions from organic solutions.[292,293]

The pores in a porous material can be highly ordered, such as those in metal-organic frameworks (MOFs), and zeolites.[294] Alternatively, the pores can be randomly orientated with a wide range of sizes within the same material, such as those in sea sponges. There are also naturally occurring porous materials, such as sea sponges. Sea sponges are ocean-dwelling organisms that have channels and pores throughout their bodies and can be thus considered to be a porous material. Originally, the sponges used for cleaning were made from sea sponges, but these have been mostly replaced by synthetic plastic alternatives. These materials exhibit large open frameworks of solid material with large voids, and can be referred to as three-dimensional reticulated foams.[291] For the purposes of this thesis, porous materials with this structure shall be referred to as sponge-like or foam-like.

5.1.1.1 Synthesis of porous materials

Porous materials can be synthesised in various ways depending on the desired morphology of the material. For example, MOFs are self-assembled structures between a metal-ion or cluster and a multidentate organic linker.[295] These individual components chelate to each other in a 3-dimensional (3D) network, with pore sizes dictated by the size of the individual components. MOFs are typically synthesised through a various methods, from simply mixing the precursor molecules together to utilising solvothermal techniques.[296]. In the case of randomly-distributed or closed pores, they can be induced by ensuring that gas bubbles are given off during the synthesis. For example, many polyurethane foams are synthesised in this way, where a gelling reaction is followed by a so-called 'blowing' reaction, where carbamic acid is formed and subsequently decomposes into carbon dioxide bubbles.[297] Porous materials can also be synthesised by exploiting natural self-assembly motifs, for example, by the self-assembly of polymer chains and then the formation of covalent bonds to lock the polymer in place.[298] A similar method to this is to combine polymerisation with a template. This is the method by which mesoporous silica is synthesised, where micelles are self-assembled into the desired shape, and a silica source is allowed to polymerise around this micellar template. The micellar template can subsequently be washed away, resulting in silica with a well-controlled mesoporous structure.[299]

5.1.1.2 Porous superconductors

Controlling the nanostructure of high-temperature superconductors is vital in ensuring that they have optimal superconductive properties. At grain boundaries, high-temperature superconductors can exhibit Joule heating, where a section of conducting material heats up due to the resistance in that section of material. This can create hotspots within the superconductor, resulting in the destruction of superconductivity in these regions.[300] To ensure optimal stability, the formation of these hotspots is undesirable, as it results in the quenching of the superconductive state. One route to overcoming the Joule heating arising from grain boundaries would be to create a porous superconductor that can be fully submerged into the cryogen to allow ample heat dissipation.[301] Additionally, cuprate superconductors often require additional heating steps to ensure optimal oxygenation of the material. These oxygenation steps usually yield higher critical temperature (T_c)'s and narrower transitions to the superconducting state. The oxygenation steps are material-dependent - for example, $YBa_2Cu_3O_{7-\delta}$ (Y-123) is annealed at 500 °C under an atmosphere of 100 % oxygen, but for $Bi_2Sr_2CaCu_2O_{8+x}$ (Bi-2212) the oxygenation step can be at 850 °C in an atmosphere of air or 20 % oxygen and 80 % argon.[302,303] Porous superconductors could reduce the necessity for these oxygenation steps as they are diffusion-based, so the higher surface area can shorten these diffusion pathways and thus result in shorter reaction times.[304]

There are several examples of the synthesis of porous Y-Ba-Cu-O (YBCO); for example, Reddy and Schmitz synthesised sponges of YBCO by first synthesising a sponge of Y_2BaCuO_5 (Y-211) and then providing a Y-123 seed in order to convert the Y-211.[85] This is possible due to the fact that Y-211 can be converted to Y-123 through a peritectic melt crystallisation. Additionally, foam-like structures of Y-123 have also been synthesised using the biopolymer dextran.[225] Bi-2212, on the other hand, has not previously been synthesised in a porous morphology, though nanofabrics of Bi-2212 have been made successfully.

5.1.2 Melamine formaldehyde

Melamine formaldehyde, MF, is a resin formed between melamine, a trimer of cyanamide, and formaldehyde (structure shown in 5.1a). These two constituents can undergo a condensation reaction and form a tough polymer, which has been frequently used as laminates, coatings or adhesives.[305] Melamine by itself is very flame resistant because of its propensity to undergo condensation reactions which release the flame-diluent gas ammonia. When melamine burns, it forms melam, melem and melon, which are thermally stable and form a char-layer on top of the melamine (structures shown in figure 5.1b).[306] Similarly, with melamine formaldehyde (MF), its combustion yields many nitrogen-containing gases, disrupting the atmospheric oxygen around the burning material and putting out the fire.[307] MF has also been shown to form thermally resistant char layers, similar to melamine, and can also self-extinguish when the source of flame has been cut off.[308] Additional applications of MF includes the formation of so-called aminoplasts,
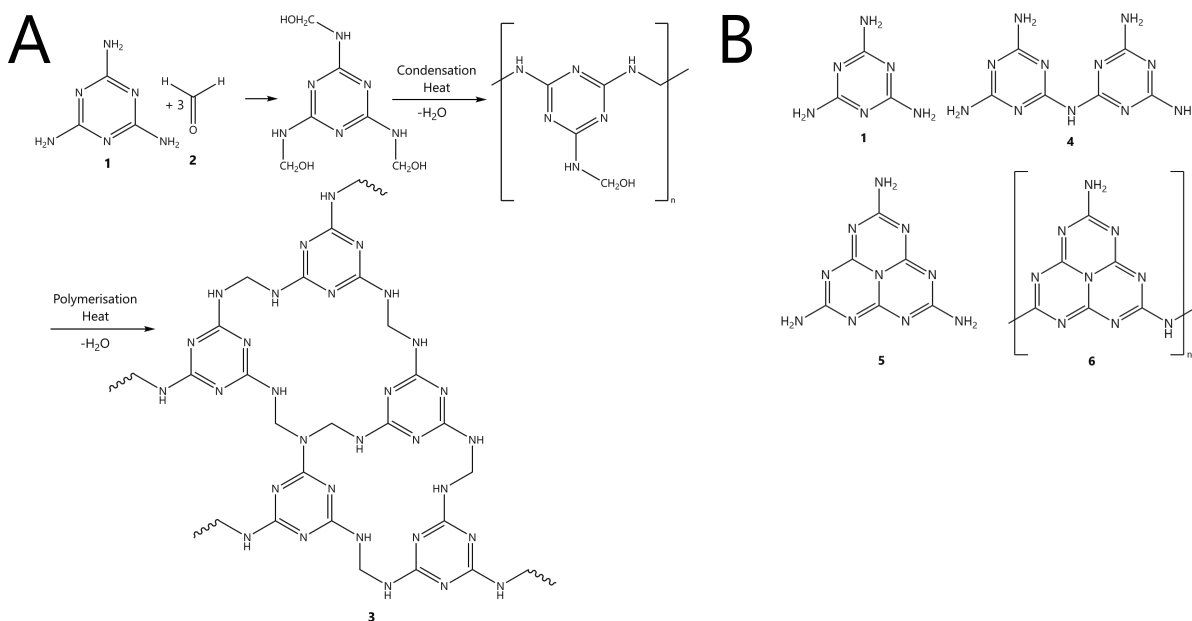
Figure 5.1: (A) Schematic showing the condensation reaction between **1** melamine and **2** formalde-
hyde, to eventually form the **3** melamine formaldehyde crosslinked polymer. Initial reaction
scheme for the material reported in reference 309. (B) Schematic showing the structure of **1**
melamine, **4** melam, **5** melem, and **6** melon.

which are microcapsules of MF.[309] MF can also be formed into a foam, allowing it to be used
for other applications such as soundproofing and fire retardant materials. A commercial form of
this foam is known as the 'Magic Eraser' by Flash in the United Kingdom or Mr Clean in the
United States of America. They are useful as abrasive materials for cleaning and are chemically
very similar to the resin melamine formaldehyde but are also a co-polymer with sodium bisulfite.
These sponges are highly porous, with reported porosities of 99% and 100 nm pore sizes.[310] MF
sponges have been explored in the scientific community for their capability as flame retardant
materials and as materials for separating oil from water.[311,312] A fascinating study explored
the potential of these sponges as filters of uranium ions from seawater.[183] In this study by
Wang *et al.*, a MF sponge was coated in sodium alginate so that additional polymers could be
attached to the sodium alginate and thus form a highly porous material that had a high affinity
for uranium ions in solution. This particular study was interesting with respect to the synthesi
of porous superconductors, as sodium alginate has been used priorly to successfully synthesise
YBCO.[262] As such, it was thought this could be used as a starting point for synthesising porous
superconductors using MF as a sacrificial template.

To test the viability of melamine formaldehyde as a sacrificial template for complex metal
oxides, three different synthesis methods were devised: using the MF sponge as a templating
agent to the solution of metal nitrates by themselves before calcination; first coating the MF
sponge in sodium alginate, which is then soaked in a solution of metal nitrate salts before

calcination; or using a modified Pechini method, where the metal nitrates are first dissolved in a solution of ethylene glycol and citric acid before the sponge is soaked in this solution and then the sample is gelled before the calcination. By so doing, the templating ability of the sponge by itself, the effect of combining the sponge with additional biopolymers, and the effect of changing the solvent of the synthesis were able to be examined.

5.2   Results and discussion

For this work, the commercial form of the sponges as the Flash Magic Eraser were purchased and used without further treatment. SEM of the sponge (Figure 5.2a) showed that it was a very open and porous structure, consisting of many thin wires that connect in a reticulated structure. Interestingly, thermogravimetric analysis (TGA) of the sponge showed that some mass remained after heating it to 700°C (Figure 5.2b). As was discussed in Section 5.1.2, MF is a very flame-resistant material, so it is not surprising that there was still some carbonaceous material left after subjecting it to TGA. However, it was decided that the percentage of product material that contained carbon would be small in the synthesis of the resultant superconductor, due to its literature-reported porosity of 99 %. Therefore, the overall percentage of the mass belonging to the sponge was considered to be insignificant - particularly as the synthesis temperatures for YBCO and Bi-Sr-Ca-Cu-O (BSCCO) are 900-920 °C and 830-850 °C respectively, which is higher than what was tested by TGA. It was also thought the structure being so thermally resistant may allow it to persist in the furnace for longer, providing a scaffold for the metal oxide to grow around.

(a)

(b)
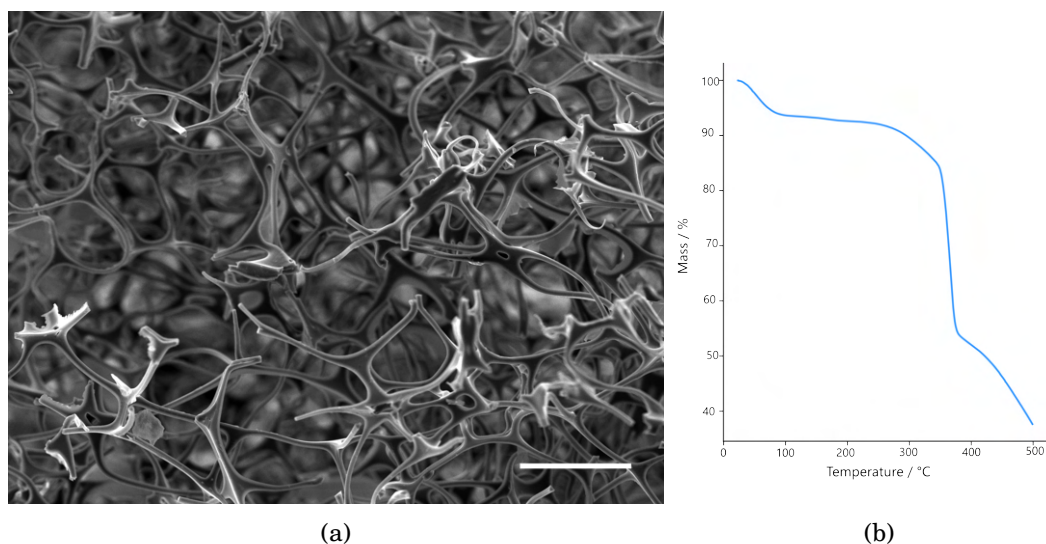
Figure 5.2: (a) SEM of the original MF sponge as purchased. Scale bar indicates a length of 100 μm. (b) TGA of the as-purchased sponge, indicating a sharp drop in mass at 400 °C. There is still some mass present after heating it to 500 °C.

115

5.2.1 YBa$_2$Cu$_3$O$_{7-\delta}$ and Bi$_2$Sr$_2$CaCu$_2$O$_{8+x}$ from the melamine formaldehyde sponge only

Initial attempts at synthesising sponge architectures of Y-123 and Bi-2212 were carried out by simply soaking the sponge in an aqueous solution of the constituent metal nitrate salts in their stoichiometric ratios. It was thought that the MF sponge could behave as a chelating agent to the metal nitrates, similarly to the biopolymer-mediated syntheses discussed in Section 1.3.2.2. This was attempted for Y-123 and Bi-2212. Due to the poor solubility of Bi(NO$_3$)$_3 \cdot$5 H$_2$O, an additional chelating agent of ethylenediaminetetraacetic acid (EDTA) was added. This addition has been shown previously to prevent the formation of bismuth subnitrate, which is poorly soluble.[227] The sponges were cut into *ca.* 2 x 2 cm sections, submerged in the aqueous solutions and subjected to a vacuum for roughly 5-10 minutes. After soaking, the sample was allowed to dry. The sponge did appear to successfully uptake the metal nitrates, as it became blue after soaking and drying, which was indicative of the blue colour of the solution arising from the copper nitrate hemi(pentahydrate). The sponges were then calcined without further treatment at 900 °C for Y-123 and 830 °C for Bi-2212 with a ramp rate of 5 °C min^{-1} and a 2 h dwell time.

By way of a control experiment to determine whether the sponge was acting as a good chelating agent, the aqueous solutions were also pipetted into a crucible, allowed to dry and subsequently calcined. The powder X-ray diffraction (pXRD) data in Figure 5.3 show that both samples do not consist of a majority of the target phase, with 32 % of the Y-123 aqueous control consisting of the target phase, and 2 % of the Bi-2212 target phase. A full breakdown of the results of Rietveld refinement from these samples is given in table 5.1 and 5.2.

116

A
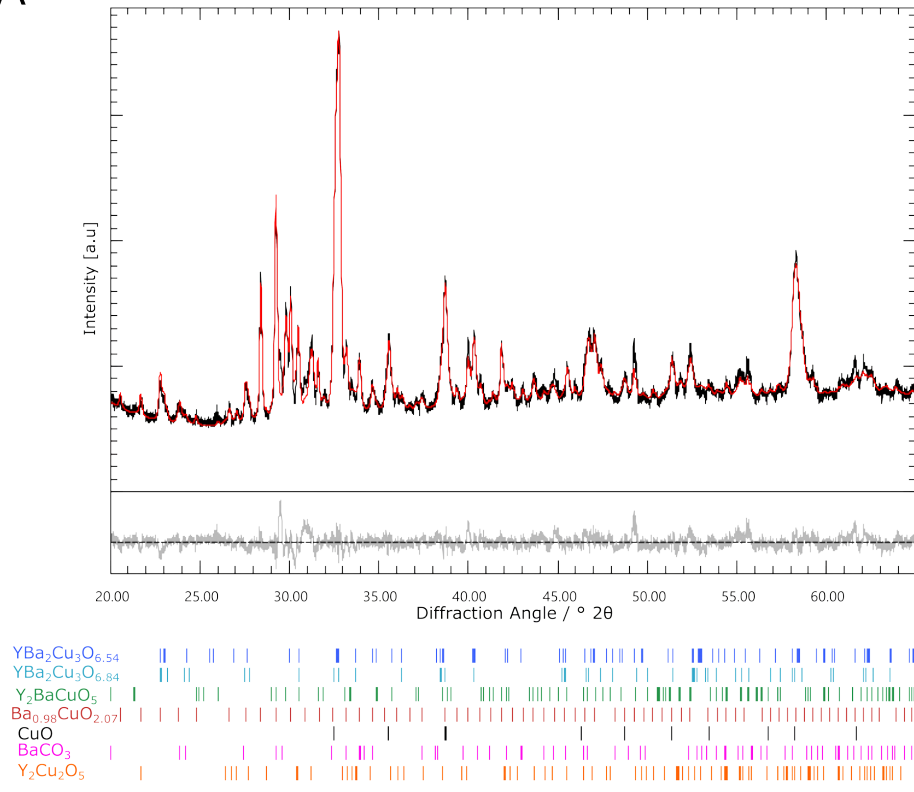
B
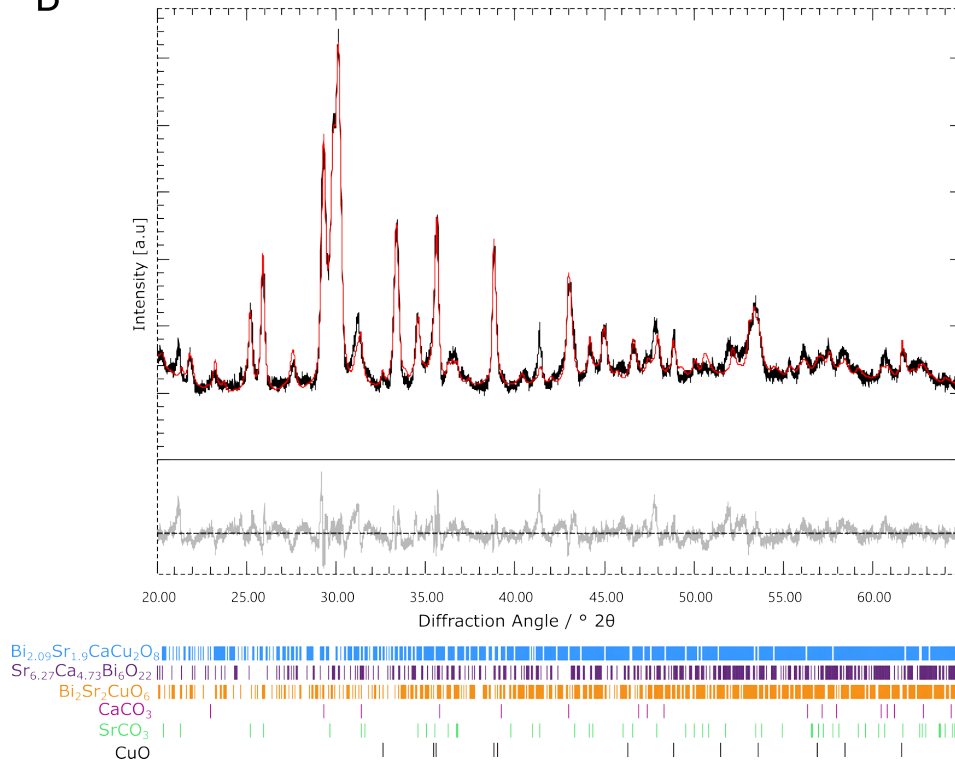
Figure 5.3: (a) pXRD data of the calcined aqueous control experiments (a) for the Y-123 sample, (b) for the Bi-2212.

5.2.1.1 $YBa_2Cu_3O_{7-\delta}$

After calcination, the MF only templated synthesis YBCO sample (MF-YBCO) had crumbled slightly. Additionally, the sample exhibited regions that were green in colour, visibly indicating the presence of Y-211. Y-211 is often nicknamed the 'green phase' of YBCO and is not super-conductive.[84] The presence of Y-211 was confirmed later by pXRD, and is shown in figure 5.4. MF-YBCO did appear to exhibit some sponge-like morphology as shown in the SEM in figure 5.4 b and c. However, the purity of this sample was poor, as can be seen in the pXRD data given in Figure 5.4. Multiphase Rietveld refinement affirmed this observation, calculating that only 37 % of the sample consisted of the target Y-123 phase. Other YBCO phases detected were the aforementioned Y-211 phase with 17 % of the sample and another non-superconductive phase, $YBa_4Cu_3O_9$, at 9 %.[84,313] Additional impurity phases were $Ba_{0.98}CuO_{2.07}$ representing 18 % of the sample, $Y_2Cu_2O_5$ representing 4 % of the sample, $BaCO_3$ representing 4 % of the sample, and CuO representing 12 % of the sample. The goodness of fit for the refinement was higher than would be desired, at an R_{wp} of 6.93 %, yielding a χ^2 value of 6.44. R_{wp} and χ^2 are indicators of how well the calculated pattern matches to the experimental pattern. For an exemplary fit, one would expect χ^2 to be between 1 and 1.5, but this can sometimes be difficult to reach. As it stands, the noise and slight mismatch of the peak intensities for the sample does raise the χ^2 value, but all the peaks in the pXRD pattern are accounted for with some slight mismatches in intensity between the calculated and the experimental data. These slight deviations between the calculated and experimental data likely stem from slight parameters that could be changed in the refinement to account for features such as microstrain in the crystal structure or preferential orientation of the material. This has been accounted for in the target Y-123 phase but not for all of the phases within the refinement, as there can be issues with over-fitting the data, and the fact that the calculation becomes more expensive. While the χ^2 of 6.44 is not perfect in this case, it is enough to gain some qualitative information about the relative abundances of each phase within the sample. To account for the higher error of the refinement, the phase quantities have been rounded to the nearest percent for the purposes of discussion. The phase quantities as calculated are provided in Table 5.1.

Overall, it appears that for Y-123, using the MF sponge as a templating agent alone is insufficient for optimal purity. It is interesting that the poor purity is combined with a good replication of nanostructure, as this implies that there is good chelation of the metal ions to the sponge to enable the nanostructure replication. However, the lack of purity implies that, despite the good chelation, the target phase is not the most favourable phase to form. In the case of MF, its high thermal resistance and fire retardancy allows it to persist until the late stages of the synthesis. This is shown by the fact that when a MF sponge was subject to TGA up to 500 °C in a nitrogen atmosphere, a significant portion of the mass of the sponge remained (Figure 5.2b). This flame resistance could be enabling a scaffold for the metal oxide phases to

Figure 5.4: (a) pXRD data of MF-YBCO as given by Rietveld refinement. The tick marks under the plot indicate the Bravais reflections of the associated phase, also labelled under the plot. The red line indicates the calculated pattern from the refinement. $R_{wp} = 6.91\%$ (b)-(c) SEM of the sponge after calcination. Scale bars in both indicate a length of 200 µm.

form around throughout the synthesis, but the actual chemical make-up of the MF sponge could
be inappropriate for ideal chelation for Y-123. It is likely that the lack of carbonyl groups in the
MF sponge for metal chelation could be leading to this lack of product purity.

5.2.1.2 $Bi_2Sr_2CaCu_2O_{8+x}$

When synthesised *via* this method, the resulting MF templated synthesis BSCCO sample (MF-
BSCCO) did not appear to replicate the original sponge morphology. While some sections of
material appeared to be sponge-like in appearance, as shown in Figure 5.5b, the majority of the
material appeared to show no direction of structure, and instead consisted of amorphous lumps of
material as shown in Figure 5.5c. Despite the lack of replication of structure, the sample consisted
of predominantly the target phase, Bi-2212. Multi-phase Rietveld refinement calculated that 86
% of the sample consisted of this target phase, with some additional impurities of $Bi_2Sr_2CuO_6$
(Bi-2201), 6 %, $Sr_{6.27}Ca_{4.73}Bi_6O_{22}$, 6 %, and $CaCO_3$, 2 %. For the multi-phase Rietveld refinement
in the BSCCO phases in this chapter, structures of $Bi_{2.09}Sr_{1.9}CaCu_2O_{8.22}$ and $Bi_{10}Sr_{10}Cu_5O_{29}$
were used for the refinement for Bi-2212 and Bi-2201 respectively. These provided a better
refinement fit and represent a modulated structure of Bi-2212 and a superlattice of Bi-2201,
respectively.[314,315] Both materials are still reported to be superconducting and are instead a
slight off-stoichiometry of the target phase or disordered structure. This sample, with the lack
of adoption of the sponge morphology but good purity, appears to contradict what was observed
for the MF-YBCO sample. The calculated R_{wp} of this sample was 8.93 %, with a χ^2 of 10.39.
MF-BSCCO was combined with an additional chelating agent of EDTA, which contains carbonyl
groups for chelation to the metal ions in solution. That several sections of material did exhibit a
slight sponge-like morphology does indicate that there was some templating to the MF sponge. As
with MF-YBCO, the thermal resistance of the sponge could be aiding in the resulting morphology,
yielding the occasional examples of porous-like material that were observed. It is likely that the
Bi-2212 metal ions are chelating preferentially with the EDTA and resulting in the amorphous
lumps of material.
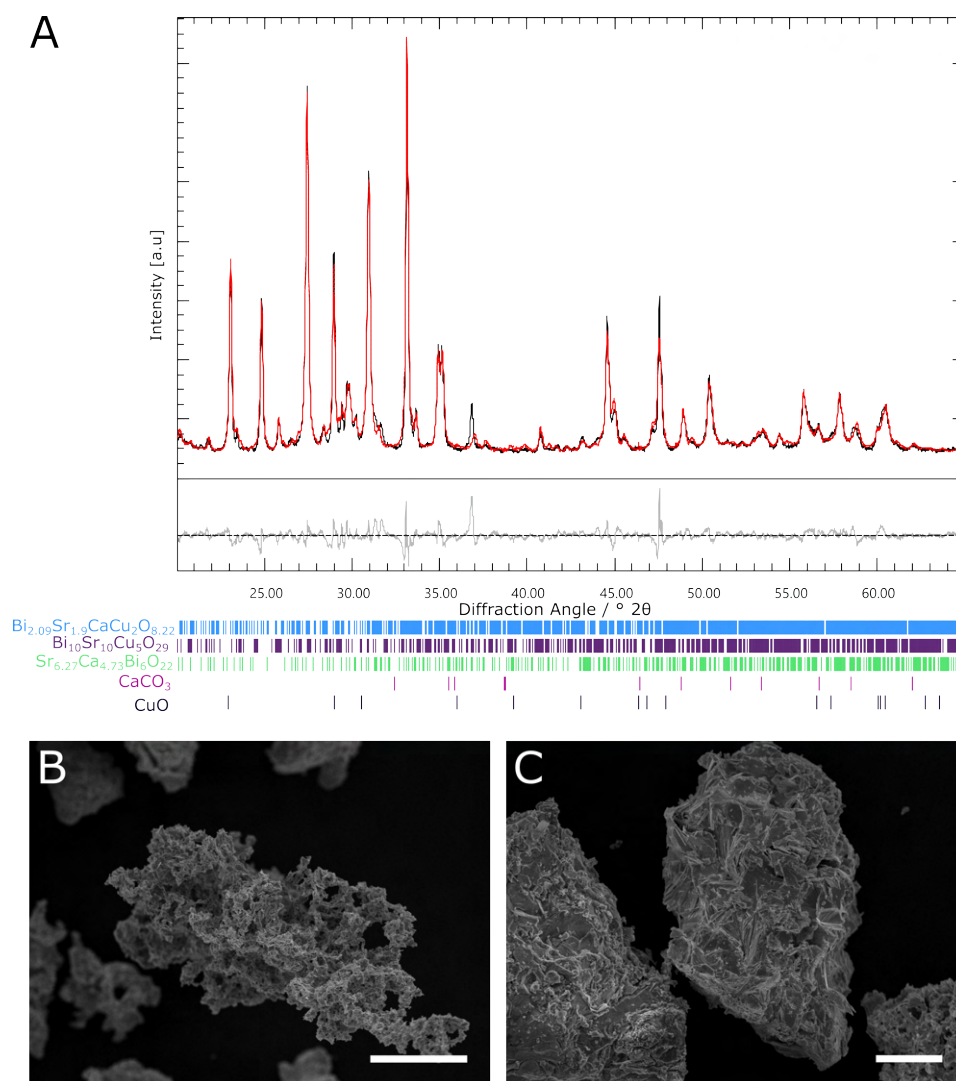
Figure 5.5: (a) pXRD data of MF-BSCCO as given by Rietveld refinement. The tick marks under the plot indicate the Bravais reflections of the associated phase, also labelled under the plot. The red line indicates the calculated pattern from the refinement. $R_{wp} = 8.93\%$ (b)-(c) SEM of the sponge after calcination. Scale bars indicate a length of a) $100\,\mu m$ and b) $50\,\mu m$.

5.2.2 $YBa_2Cu_3O_{7-\delta}$ and $Bi_2Sr_2CaCu_2O_{8+x}$ from sodium alginate coated sponges

This method closely follows the method previously reported by Wang *et al.*, where the sponge was coated with sodium alginate prior to additional coating steps to tailor the material to capture uranium ions. Sodium alginate has been used for the synthesis of YBCO previously, so it was thought that the addition of the MF template may yield some control of structure after the synthesis.[183] It has not been used for Bi-2212 previously, so a control experiment, where the same procedure as the Y-123 was carried out, but with the Bi-2212 aqueous precursor solution instead (pXRD data is given in Figure 5.6). In this case, it was found that $Na_3Ca_2BiO_6$ formed over the desired Bi-2212 phase. It is likely therefore, that BSCCO is incompatible with sodium alginate as a biopolymer. An attempt at coating the MF sponge with sodium alginate and subsequent chelation to the constituent salts of Bi-2212 was attempted regardless, as it was considered that the small amount of sodium alginate would likely not impact the generation of the target Bi-2212 phase.

5.2.2.1 $YBa_2Cu_3O_{7-\delta}$

The MF and sodium alginate-templated synthesis YBCO sample (MFA-YBCO) sample did appear to show a good porosity and much improved purity. The target phase represented a much higher percentage of this sample, with 65 % of the sample consisting of the target phase. It should be noted that the refinement was carried out with two separate Y-123 phases in the same calculation. The difference between the two phases was a slight difference in oxygen stoichiometry. It's possible that regions of the sample consist of a higher-oxygentated Y-123, perhaps due to the decomposition of the MF sponge releasing gases such as NH_4 and thus smothering the sample from oxygen. As the calcination was undertaken in a chamber furnace, there was no active flow of air within the furnace. This could have lead to a poorly oxygenated atmosphere within the furnace, thus resulting in insufficient oxygen to form the ideal phase of Y-123. Annealing of YBCO is a common practice, whereby the sample is heated to 500 °C under flowing oxygen.[302] As this is a diffusion-based process, it is also possible that the 2-hour calcination time was insufficient for the full diffusion though the sample. The increased purity of the sample compared to that of MF-YBCO, is consistent with what has been observed for both materials so far - the addition of an additional chelating agent to the MF sponge has enabled a much purer sample to be synthesised. Other phases present were Y-211 with 13 %, $Ba_{0.98}CuO_{2.07}$ with 8 %, $Y_2Cu_2O_5$ with 1 %, CuO with 9 % and $BaCO_3$ with 4 %. The R_{wp} of the refinement was 4.01 %, yielding a χ^2 of 2.45. A breakdown of the multiphase refinement results can be found in 5.1.

The morphology of the sample was similarly sponge-like to MF-YBCO (Figure 5.7b and c), but in this case the sample was much more mechanically fragile. This was qualitatively confirmed, as the sample tended to collapse upon sputter treatment prior to analysis by SEM. The reasoning for this increased fragility of sample can be inferred from the SEM, as it can be seen that there

Figure 5.6: (a) pXRD data of the calcined alginate control experiments (a) for the Y-123 sample, (b) for the Bi-2212.

Figure 5.7: (a) pXRD data of MFA-YBCO as given by Rietveld refinement. The tick marks under the plot indicate the Bravais reflections of the associated phase, also labelled under the plot. The red line indicates the calculated pattern from the refinement. $R_{wp} = 4.01\,\%$ (b)-(c) SEM of the sponge after calcination. Scale bars in (b) indicates a length of $100\,\mu$m, (c) indicates a length of $50\,\mu$m.
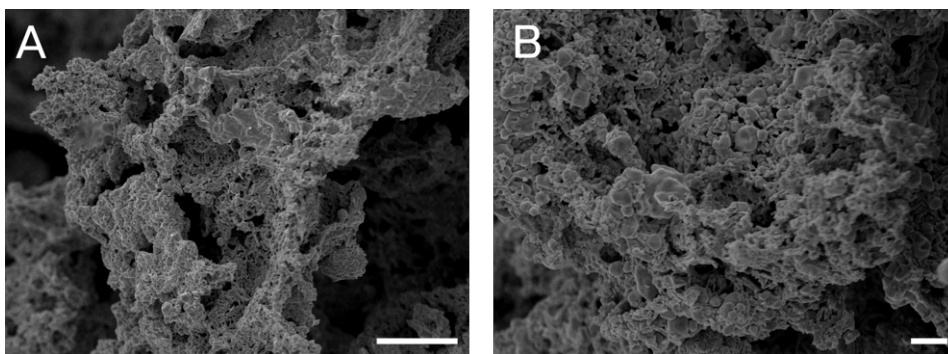
Figure 5.8: SEM of the Y-123 samples synthesised with a more concentrated solution of sodium alginate. These samples appeared to consist of largely no structure direction and are not as porous as would be expected of a direct template from the MF sponge. Scale bars in (a) indicate length of 50 µm, (b) indicates a length of 10 µm.

are thin sections of material connected by thin wires or struts of material. This is likely due to the MF only being coated by a very thin layer of sodium alginate, resulting in only thin sections are chelated to the metal ions, thus forming only thin sections of product material. The fact that the sample appears to be thinner than the MF-YBCO could indicate that, by coating the MF sponge in sodium alginate, there is little structure direction from the sponge itself. Rather, it is likely that the thin layer of sodium-alginate on top of the sponge is what is behaving as a structure-directing agent.

In an attempt to overcome this fragility, a higher concentration of sodium alginate solution was used for coating the sponge. However, the higher viscosity of the solution likely resulted in poor coating of the sponge and possibly just filled some of the voids between the struts of the MF material. The SEM of these higher concentration samples showed a lack of sponge-like structure, and are found in Figure 5.8.

5.2.2.2 $Bi_2Sr_2CaCu_2O_{8+x}$

After the synthesis of MF and sodium alginate-templated synthesis BSCCO sample (MFA-BSCCO), the target phase of Bi-2212 was sucessfully synthesised, but at a lower purity than MF-BSCCO. pXRD data are given in Figure 5.9. Interestingly, the $Na_3Ca_2BiO_6$ phase was not detectable from this synthesis. The sample was found instead to consist of 65 % of the target Bi-2212 phase, along with impurities of Bi-2201 which made up 17 %, $Sr_{6.27}Ca_{4.73}Bi_6O_{22}$ which made up 5 % and $CaCO_3$ which made up 14 %. The R_{wp} of the refinement was 7.72 %, which gave a χ^2 of 5.89. A common impurity phase that forms alongside the BSCCO phases is $Bi_2(Ca_{1+x}Sr_{3-x})O_7$.[138] For multiphase Rietveld refinement using the software Profex, an exact stoichiometry is required, so $Sr_{6.27}Ca_{4.73}Bi_6O_{22}$ was used for the refinements. This phase was a good fit for the observed peaks that corresponded to this phase, though it did not exactly match the stoichiometry of $Bi_2(Ca_{1+x}Sr_{3-x})O_7$ ($Sr_{6.27}Ca_{4.73}Bi_6O_{22}$ actually corresponds to $Bi_2Ca_{1.58}Sr_{2.09}O_{7.3}$). To overcome
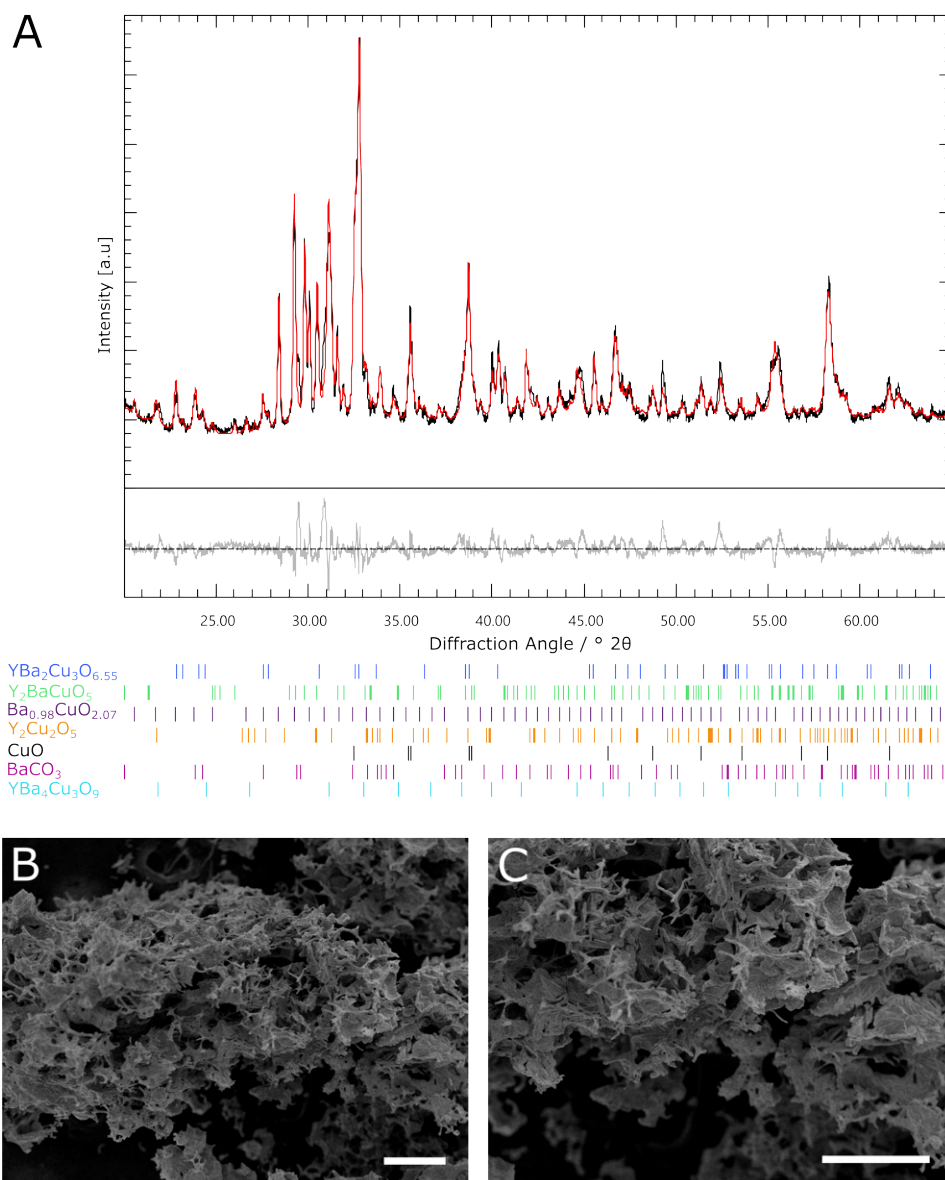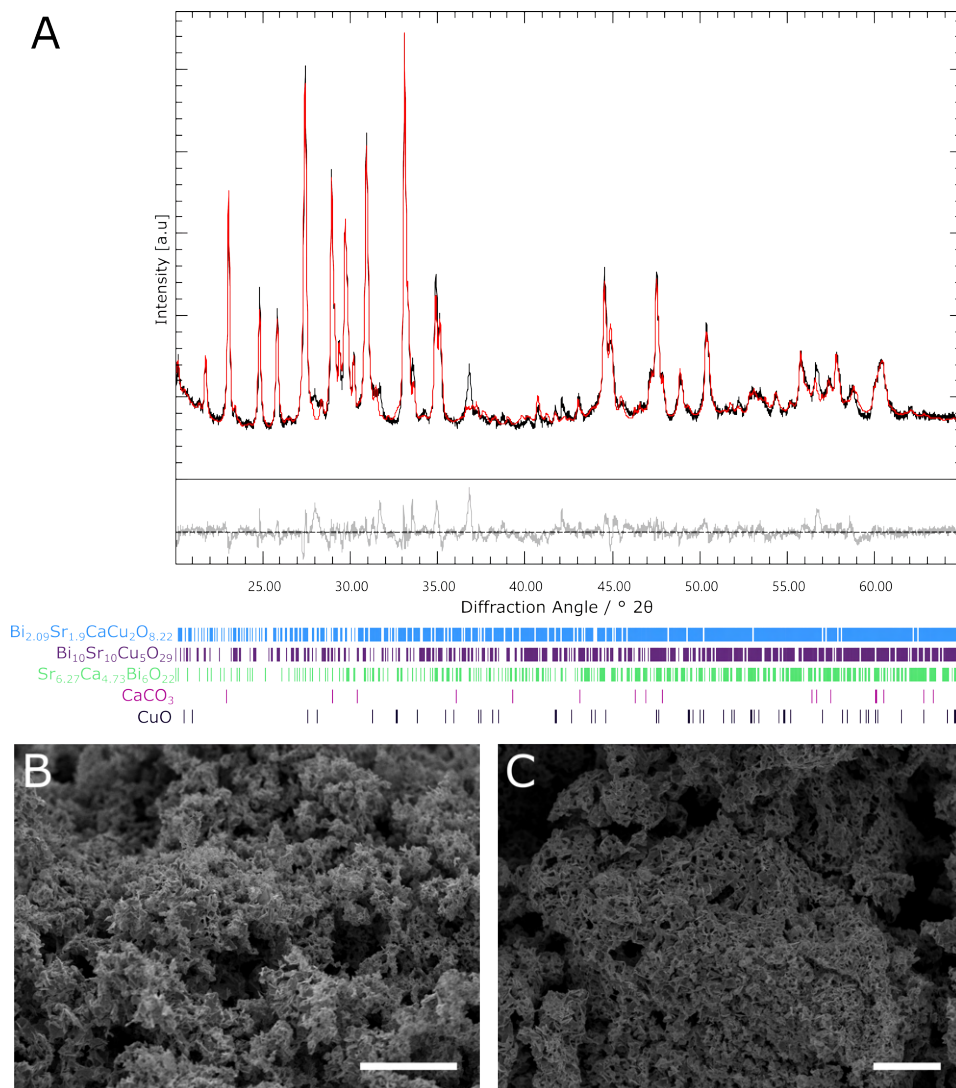
Figure 5.9: (a)pXRD data of MFA-YBCO as given by Rietveld refinement. The tick marks under the plot indicate the Bravais reflections of the associated phase, also labelled under the plot. The red line indicates the calculated pattern from the refinement. $R_{wp} = 7.72\%$ (b)-(c) SEM of the sponge after calcination. Scanning electron micrographs of the sponge after calcination. Scale bars indicate a length of b) $100\,\mu$m and c) $50\,\mu$m.

this slight mismatch, the refinement program was allowed slightly more leniency in calculating the unit cell dimensions for this phase - enabling it to adjust the unit cell parameters more to correspond the represented phase.

The SEM from this sample appears to show a porous structure, but not as open as would be expected if the MF sponge had been a good chelating agent. Rather, the sample exhibited highly anisotropic crystallites with slight pores throughout, shown in Figure 5.9b and c. Despite the overall lack of complete replication of structure, the sample did exhibit some good porosity. However the replication of the structure was, overall not as clear as would be expected for a
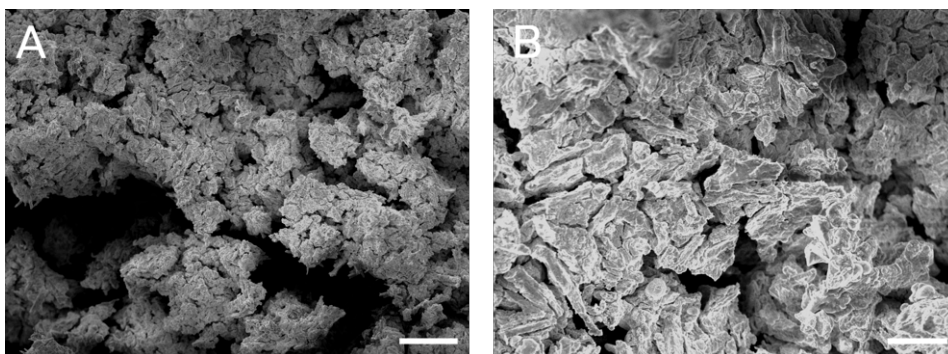
Figure 5.10: SEM of the Bi-2212 samples synthesised with a more concentrated solution of sodium alginate. These samples appeared to consist of largely no structure direction and are not as porous as would be expected of a direct template from the MF sponge. Scale bars in (a) indicates a length of 50 μm, (b) indicates a length of 10 μm.

good templated synthesis. This, combined with the lower purity of the sample meant that further examination of this sample was not carried out. As with the MFA-YBCO, an additional synthesis with a more-concentrated solution of sodium alginate was carried out. The resulting sample was also found not to be porous by SEM, and instead appeared to consist of a largely amorphous sample. The SEM are found in Figure 5.10

5.2.3 YBa$_2$Cu$_3$O$_{7-\delta}$ and Bi$_2$Sr$_2$CaCu$_2$O$_{8+x}$ synthesis from melamine formaldehyde sponges with a modified Pechini method

5.2.3.1 Optimisation of the ratio of ethylene glycol : citric acid

Initial studies with this method at the conventional ratio of ethylene glycol : citric acid often lead to the complete dissolution of the sponge, forming a thick gel instead. This meant that any resulting porous structure could not be attributed to the templating power of the sponge, but was rather likely caused by the decomposition of the gel forming air bubbles and resulting in a porous structure. To examine what was happening to cause the dissolution of the sponge, fourier transform infra-red spectroscopy (FTIR) was carried out. Importantly, when comparing the three separate components of ethylene glycol, citric acid and the MF sponge to that of them combined together, the -OH stretching peak was broadened by the addition of citric acid. When metal ions were added - in this case the metal ions for Bi-2212, the peak was similarly broadened, which indicated some chelation of the metal ions to the -OH groups. Interestingly, it was difficult to find a difference between the samples besides that. It is possible that this is due to the sponge being such a small percentage of both samples, that the peaks arising from its stretching frequencies are so small that they are obscured by the peaks arising from ethylene glycol and citric acid. It is likely, however, that the melamine formaldehyde is undergoing a hydrolysis reaction, which is breaking apart the sponge and resulting in the destruction of its macrostructure.

It was also found that when the sponge was not submerged in excess solution, the sponge
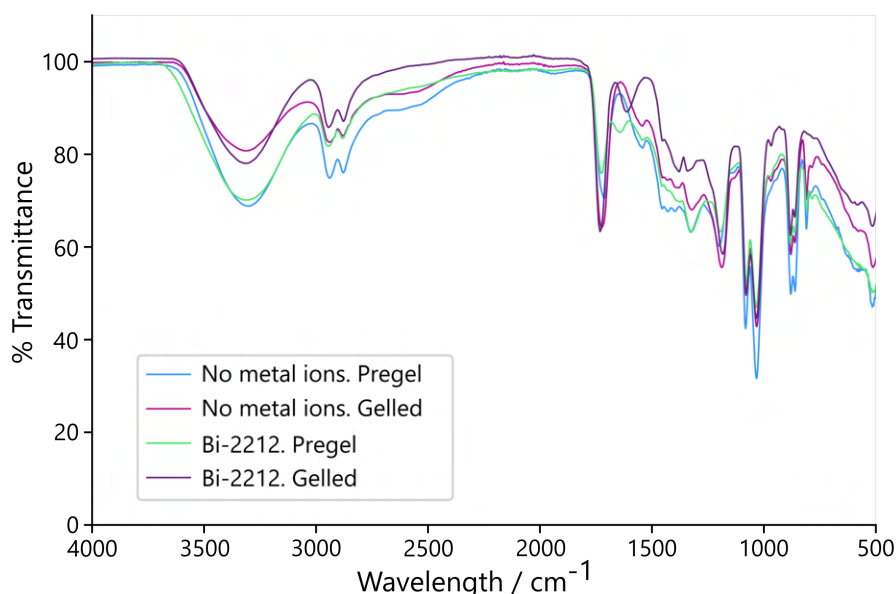
Figure 5.11: Figure depicting the FTIR data of the sponges containing a 1:8 ratio of ethylene glycol to citric acid before and after gelling with no metal ions or the metal ions required for Bi-2212.

did not dissolve. Additionally, without the metal nitrates in the solution, the sponges also did not dissolve. This indicated that the solution needed to be in excess for the dissolution to occur, and that if the solution was particularly acidic, the sponge would be dissolved. This would likely be due to the acidic environment allowing a hydrolysis reaction to occur, thus breaking the covalent bonds between the formaldehyde and cyanimide units. To prevent accidental dissolution of the sponge, this synthesis was carried out with 10 % of the literature quantities of citric acid compared to ethylene glycol, resulting in a ratio of 1 : 80. Control experiments with this ratio were carried out in the absence of a MF sponge, and the data are shown in Figure 5.12.

5.2.3.2 YBa$_2$Cu$_3$O$_{7-\delta}$

Interestingly, MF and Pechini method-templated synthesis YBCO sample (MFP-YBCO) exhibited good replication of the macromorphology of the initial sponge, which was evidenced by the replication of the decorative branding of the original sponge. As can be seen in Figure 5.13f, the cross-shaped decorative branding of the sample from the MF sponge is present both before and after calcination of the sample. The sample also shrunk in size by a factor of 4 after the calcination. SEM and pXRD was carried out to determine the purity of the resultant sample and its morphology, and these data are given in Figure 5.13. It can be seen from the SEM that the sample is highly porous, with an open network of thin wires connecting larger sections of material. These connecting struts appear to be formed of small crystallites, in a reticulated structure.

MFP-YBCO also exhibited good purity, with 69 % of the sample consisting of the target
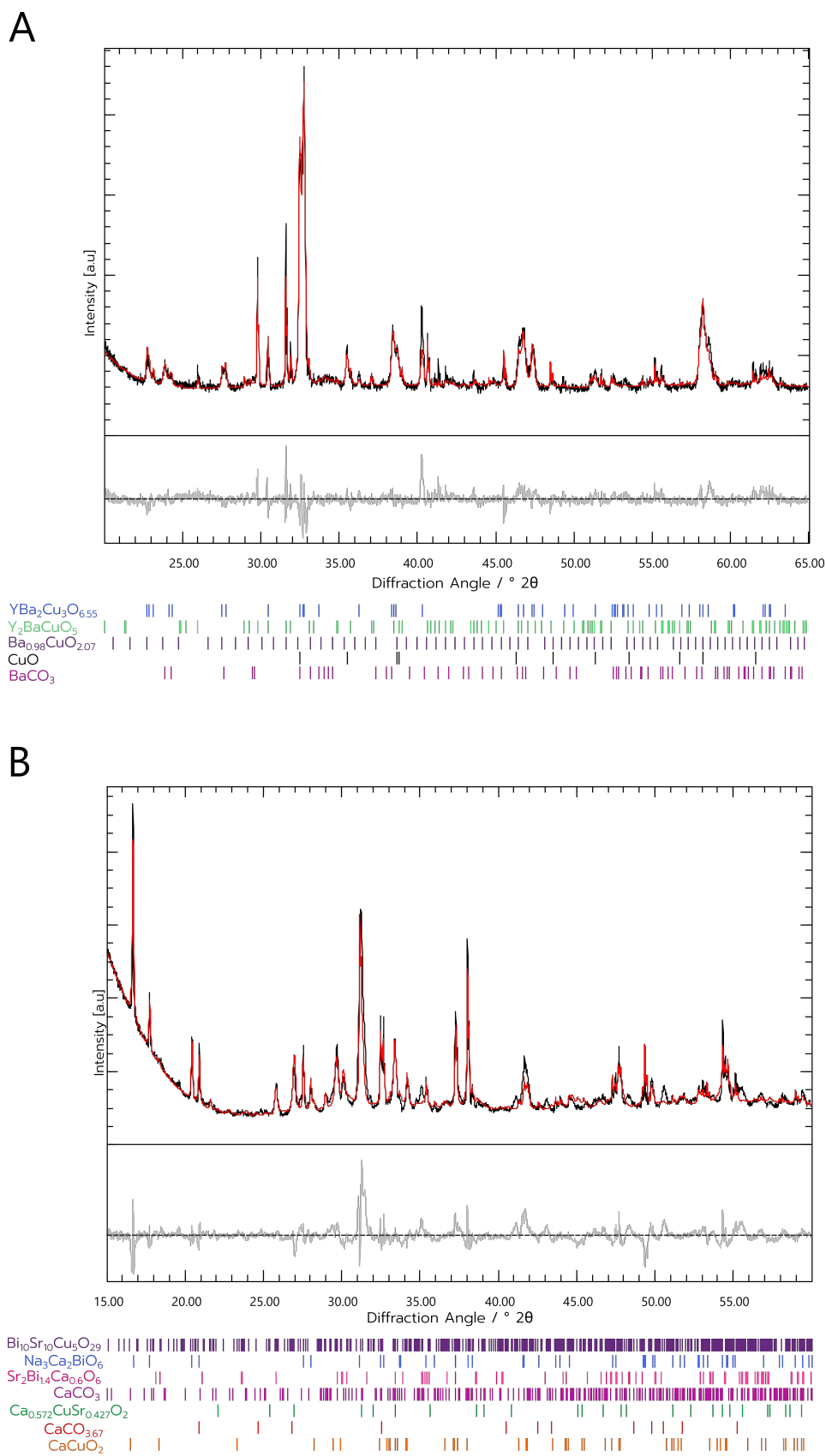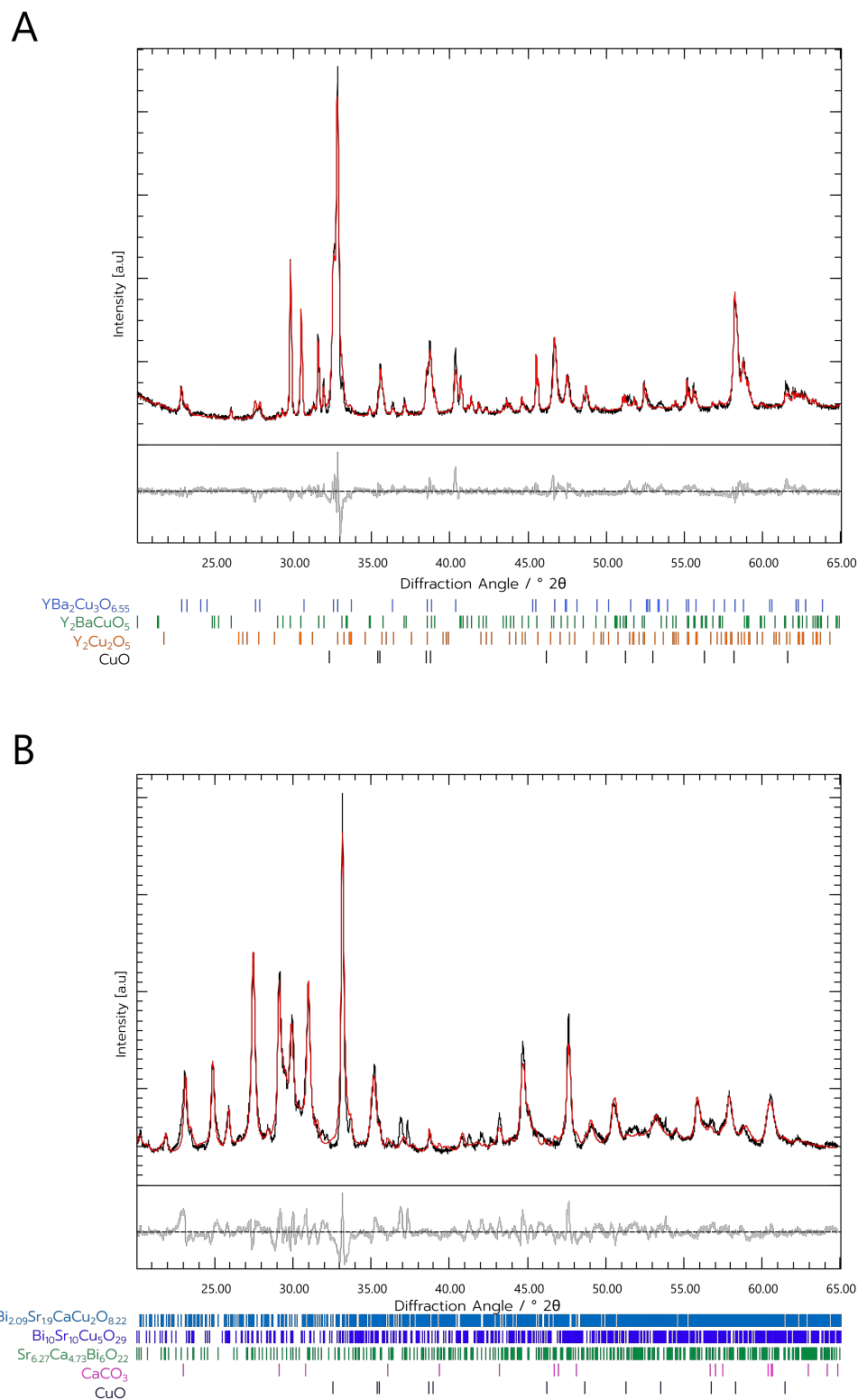
Figure 5.12: (a) pXRD data of the calcined Pechini control experiments (a) for the Y-123 sample, (b) for the Bi-2212.
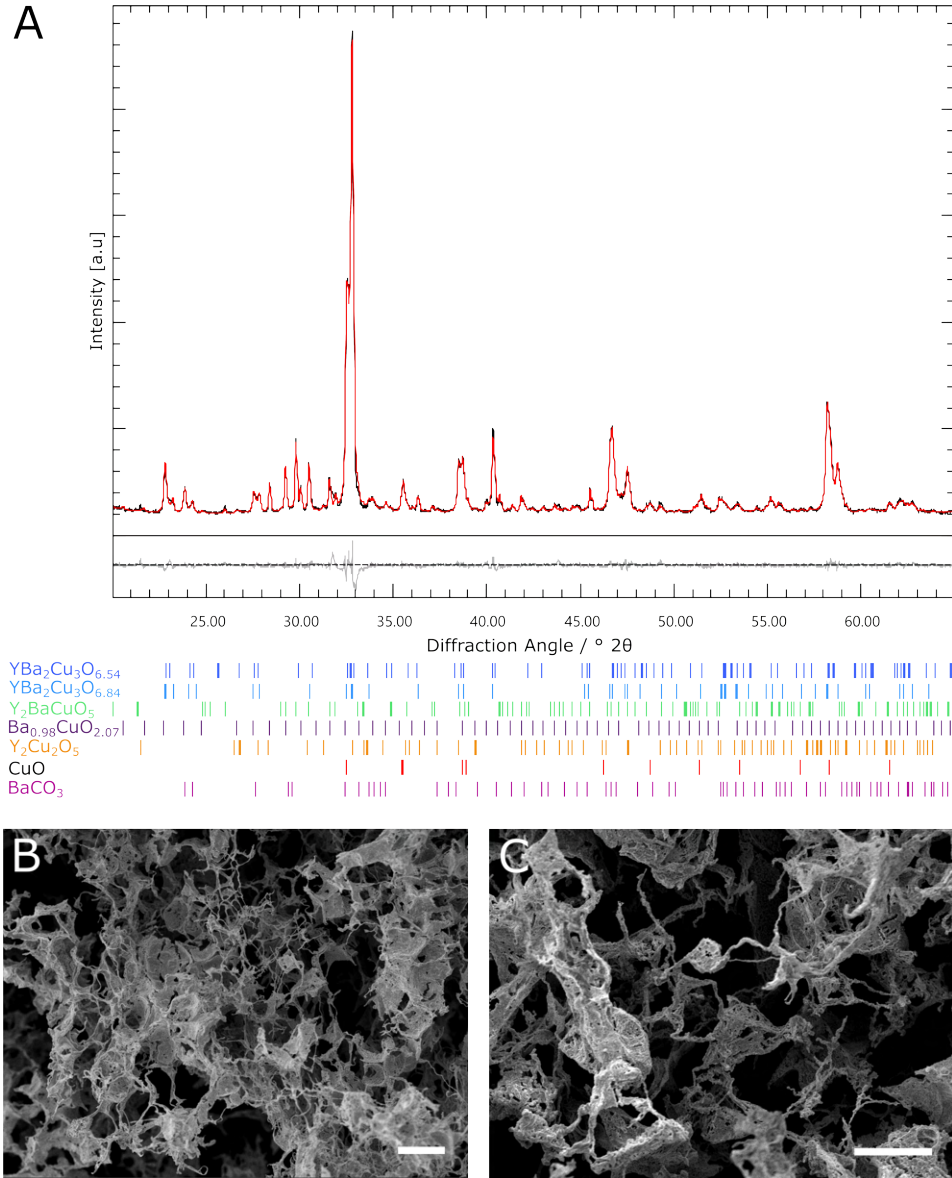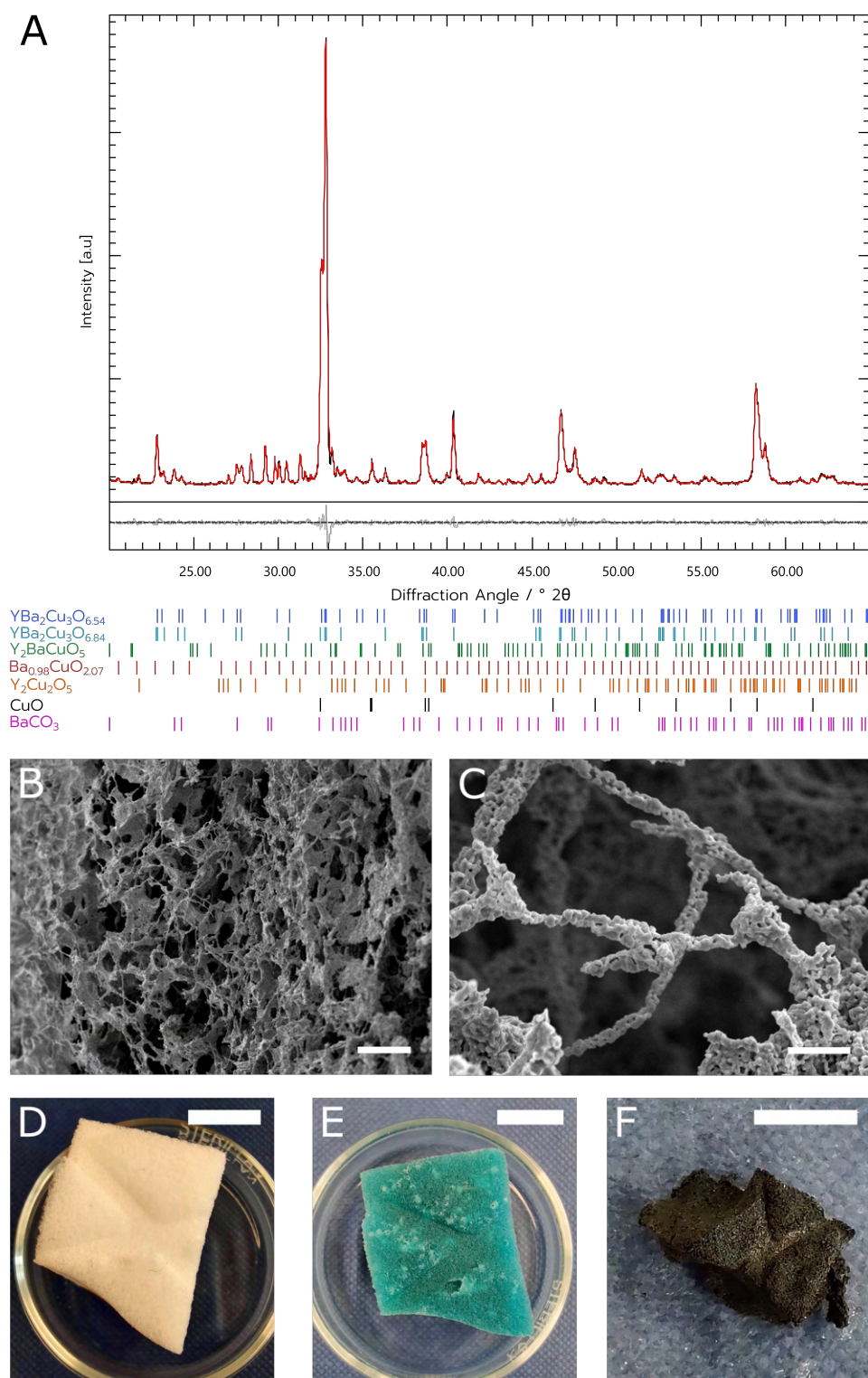
Figure 5.13: (a) pXRD data of MFP-YBCO as given by Rietveld refinement. The tick marks under the plot indicate the Bravais reflections of the associated phase, also labelled under the plot. The red line indicates the calculated pattern from the refinement. $R_{wp} = 3.37\%$ (b)-(c) SEM of the sponge after calcination. Photographs of the sponge (d) before and (e) after the calcination step of the sponge synthesis. Scale bars in (b) indicates a length of $100\,\mu m$, (c) indicates a length of $10\,\mu m$, (d and e) indicates a length of $1\,mm$, (f) indicates a length of $0.5\,mm$.

phase. As with MFA-YBCO, two Y-123 phases were input into the refinement. This provided a much better refinement fit and indicated that two Y-123 phases at different levels of doping were present. It is possible that there are a wide range of doping levels of the Y-123 within the sample. As the crystal structures of different doping levels are very similar to each other, with minor differences in lattice parameters, it is difficult to determine exactly which stoichiometries are present, as the amount of flexibility that the refinement allows the unit cell to adjust by masks the exact unit cell. If single crystal X-ray diffraction (scXRD) or selected-area electron diffraction (SAED) was carried out on a crystal of the sample, the exact level of doping could possibly be measured. Unfortunately, the polycrystalline nature of the product is unsuitable for scXRD, and the crystallites for this sample were too thick to be analysed effectively with transmission electron microscopy (TEM). Other phases present in the sample were Y-211 with 4 %, $Ba_{0.98}CuO_{2.07}$ with 9 %, $Y_2Cu_2O_5$ with 8 %, CuO with 7 % and $BaCO_3$ with 3 %. The R_{wp} of the refinement was 3.37 %, yielding a χ^2 of 2.22. A breakdown of the multiphase refinement results can be found in 5.1.

5.2.3.3 $Bi_2Sr_2CaCu_2O_{8-x}$

The MF and Pechini method-templated synthesis BSCCO sample (MFP-BSCCO) was found to be the least pure of the three samples tested in this chapter, but it appeared to show excellent replication of both the macrostructure and nanostructure of the original sponge, shown in Figure 5.14. The pXRD data given in Figure 5.14 indicates that the sample consisted of 56 % of the target phase, with the rest of the material consisting of 3.8 % Bi-2201. 8.6 % $Sr_6 \cdot 27 Ca_4 \cdot 73 Bi_6 O_{22}$, 8.4 % CuO and 7.3 % $CaCO_3$ as determined by Rietveld refinement. The refinement had a R_{wp} value of 7.57 %, which corresponded to a χ^2 value of 11.02.

The fact that increasing the amount of citric acid in the synthesis results in the dissolution of the sponge indicates that the solution is interacting with the chemical makeup of the sponge, disrupting the covalent bonds in the polymer and chemically breaking it down. This is potentially a reason for why this Pechini-like synthesis is better at replicating the nanostructure of the sponge itself, as the metal ions are able to chelate directly to the sponge instead of just to a biopolymer shell around the sponge.
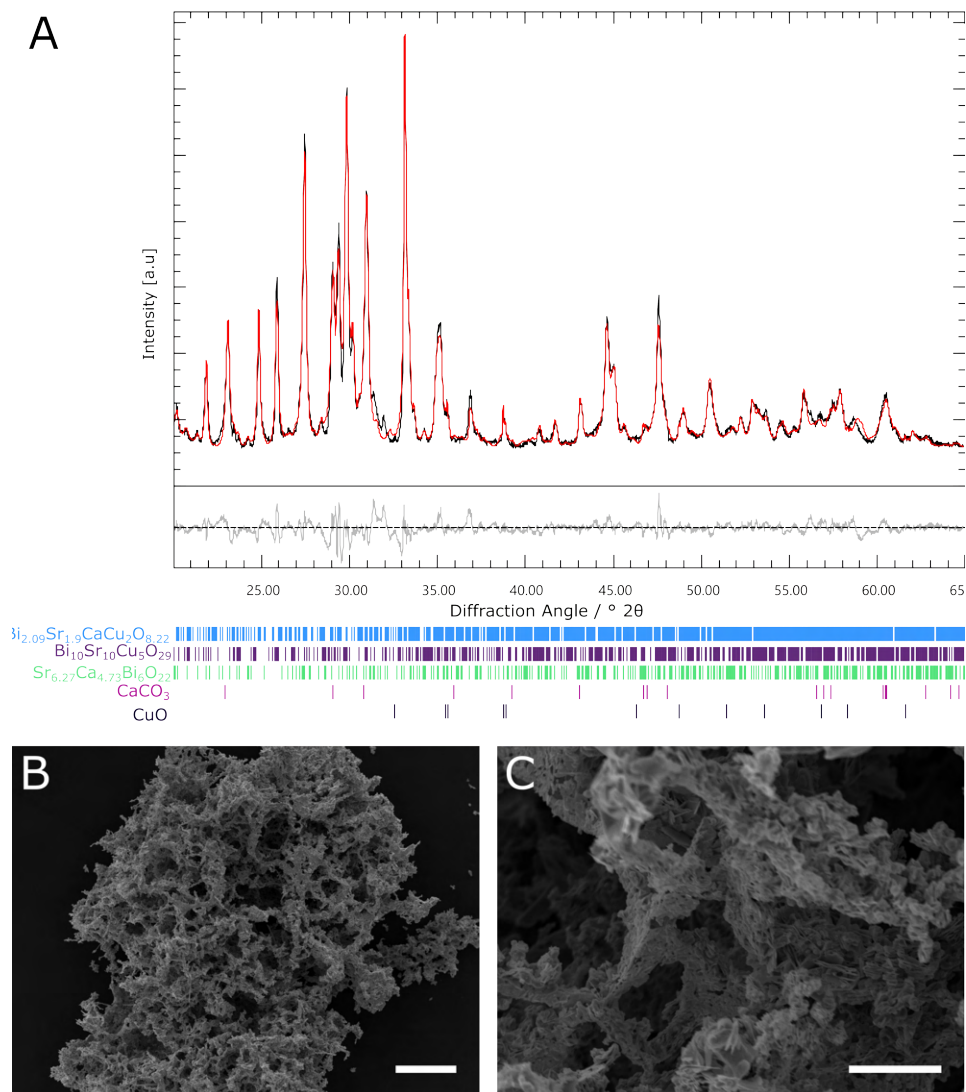
Figure 5.14: (a) pXRD data of MFP-BSCCO as given by Rietveld refinement. The tick marks under the plot indicate the Bravais reflections of the associated phase, also labelled under the plot. The red line indicates the calculated pattern from the refinement. $R_{wp} = 7.57\%$ (b)-(c) SEM of the sponge after calcination. Scale bars in (b) indicates a length of $200\,\mu$m, (c) indicates a length of $20\,\mu$m

5.2.3.4 Further analysis of the MFP samples

As the MFP-YBCO and MFP-BSCCO samples exhibited the best control of nano- and macrostructure, further analyses were carried out on these samples. To quantify the porosity, BET was carried out on both samples at 77 K. For MFP-YBCO, a type-IV isotherm was observed with a hysteresis between the adsorption and desorption branches of the isotherm, which is presented in Figure 5.15a. Despite evidence of the Type-IV isotherm, the hysteresis loop was classified as a H4 type, and closed at p/p_0 0.4, which suggested that only a small amount of the sample consisted of slit-like pores with a diameter of 2.2 nm. A pore size distribution was calculated using the Barrett–Joyner–Halenda (BJH) method, which indicated a broad distribution of mesopores, with a modal pore size of 4.8 ± 1.3 nm. BJH modal pore size distribution is found in Figure 5.15b. However, this indicated a cumulative pore volume of $0.01 \, \mathrm{cm^3 \, g^{-1}}$ and therefore implies that the majority of the pores in the sample are a result of macropores. Similarly, the MFP-BSCCO sample exhibited a Type-III isotherm, which indicated little to no interaction with the adsorbate, or that the sample is mostly formed of macropores (Figure 5.15c). The samples were found to have surface areas of $4.22 \, \mathrm{m^2 \, g^{-1}}$ and $9.62 \, \mathrm{m^2 \, g^{-1}}$ for MFP-YBCO and MFP-BSCCO respectively.

The low surface areas can be inferred from the SEM, as there are large voids interspersed with small connecting struts. These large voids make no contribution to the overall surface area of the sample, thus resulting in a small surface area. Additionally, BET is best at analysing samples with micro- to mesopores, and generally has a upper pore size limit of 10 µm From the SEM, the samples looked to be macroporous, so an alternative method at quantifying the porosity was sought out - Hg-porosimetry. Data is found in Figure 5.16. The Hg-porosimetry cumulative pore size plot shows that MFP-YBCO was highly porous, with a calculated porosity of 82 %. The pore size distrubution plot in Figure 5.16b shows the distribution of different pore sizes throughout the sample, with pore diameters of 2.3 µm, 37 µm and 104 µm. This is consistent with the BET data, and confirms that MFP-YBCO is predominantly macroporous. For MFP-BSCCO, the sample was similarly highly porous and was determined to be 78 % porous. This sample consisted of predominantly larger pore sizes, with pore sizes of 2.2 µm, 43 µm and 118 µm.

Next, to analyse the superconductive properties of the samples, two methods were also employed - resistance measurements and SQUID magnetometry. For the four-point resistance measurements, strips of aluminium tape were laid over the sample as a mask, followed by a brief argon etch of the samples and then 100 nm of gold was evaporated on top of the sample in four strips. Gold wires were then attached to these gold strips with Dupont silver paint. As the sponge was an uneven shape, the resistivity was impossible to measure, so characterisation of the resistance was carried out instead. Images of the MFP-YBCO sample before measurement are available in Appendix A.5. From the plots in Figure 5.17, it can be seen that for the unannealed sponges, the MFP-YBCO sponge did eventually reach a resistance of zero, with an apparent onset T_c ($\mathrm{T}_{c \, onset}$) at 92 K. The insulating nature prior to the transition could be due to impurity phases within the sample which impede the flow of current through the network of thin wires, or due to
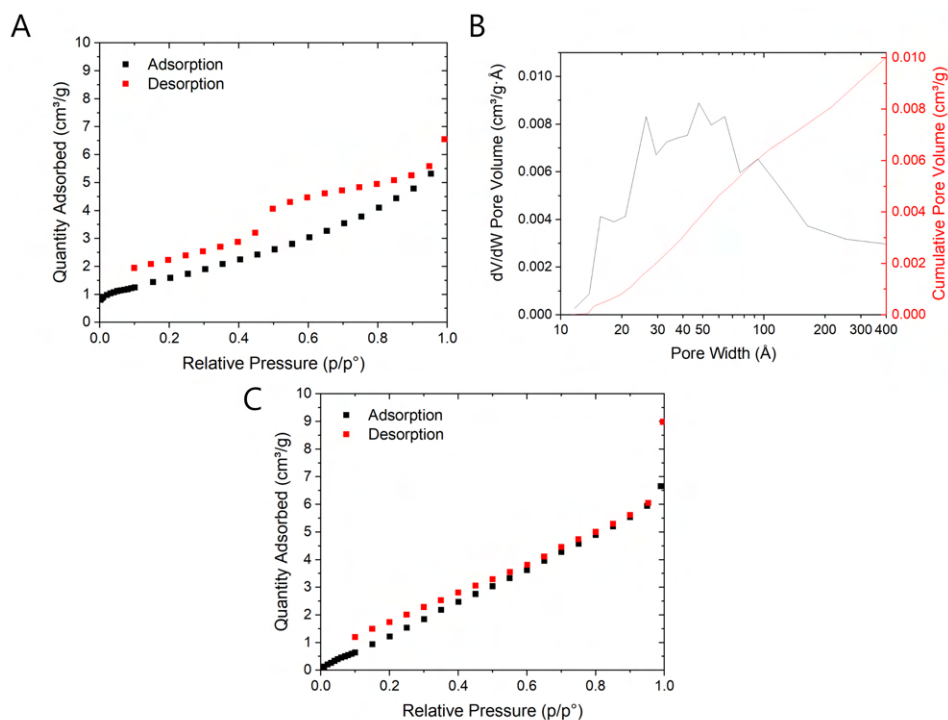
Figure 5.15: (a) BET data from MFP-YBCO, depicting the Type-IV isotherm of MFP-YBCO. (b) BJH plot depicting the pore-size distribution of MFP-YBCO. (c) BET data from MFP-BSCCO depicting the Type-III isotherm.
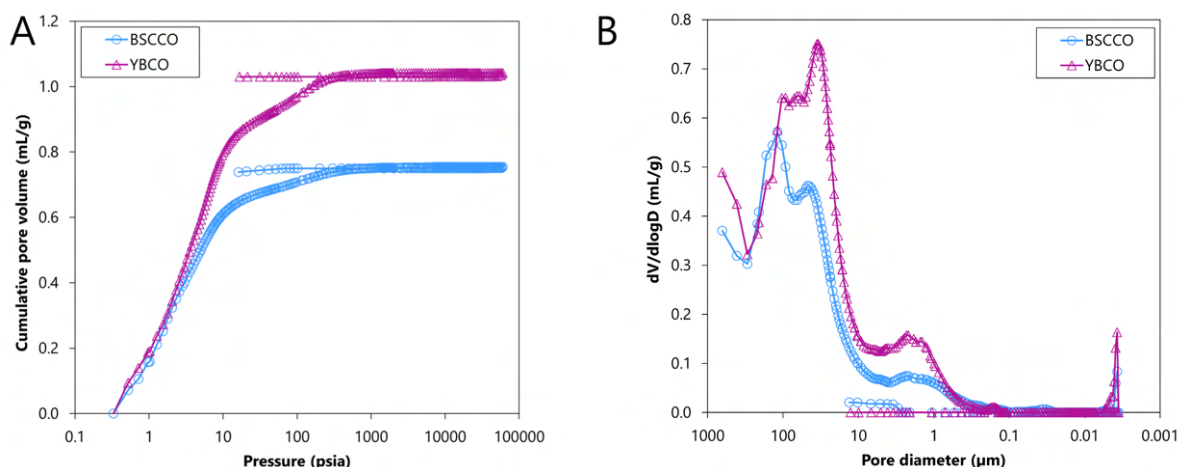
Figure 5.16: Overlay plots for the porosimetry data for MFP-YBCO (purple) and MFP-BSCCO (purple) (a) Cumulative pore volume plot. The samples were determined to be 82 % and 78 % porous for YBCO and BSCCO respectively. (b) Pore size distribution plot the two samples.
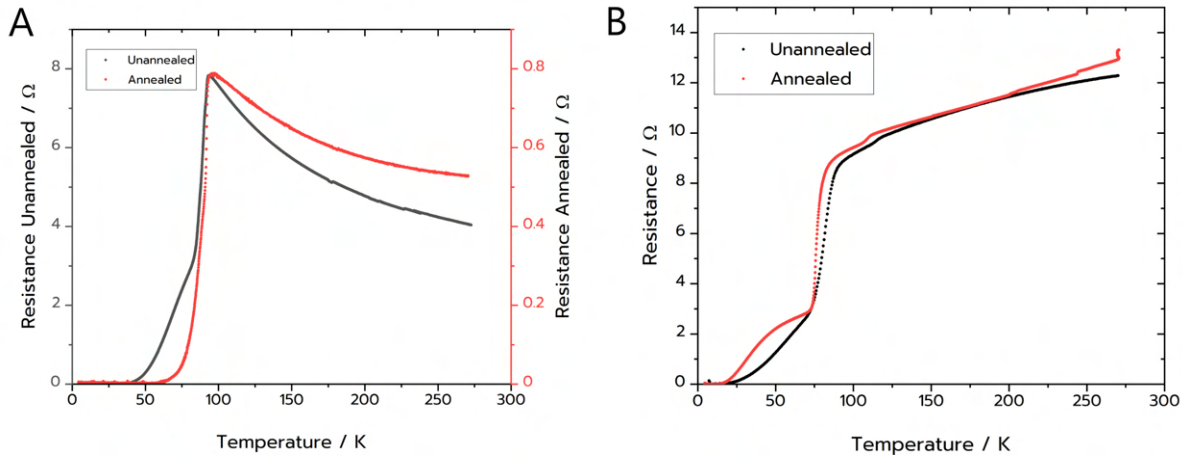
Figure 5.17: (a) Resistance data from (black) unannealed MFP-YBCO and (red) annealed MFP-YBCO. (b) Resistance data from (black) unannealed MFP-BSCCO and (red) annealed MFP-BSCCO.

the inherent resistance at grain boundaries. As current flows through the path of least resistance, measuring the resistance of a sample does not necessarily represent the bulk behaviour of the sample. If there is a path that current can flow down with zero resistance, the current will flow through that route. It can be seen that, after the transition at 92 K, there is a shoulder in the resistance behaviour of the sample at 60 K. This indicates that there is residual resistance within the sample, perhaps due to the reticulated nature of the sponge structure resulting in resistance between grains of Y-123. In order to sharpen this transition, annealing of the sponge at 500 °C under an atmosphere of flowing oxygen for 48 hours was carried out, and the resistance measurement re-attempted. Unfortunately, due to the fragile nature of the sponge, this was not able to be undertaken on the exact sample that had been characterised previously, though the samples were from the same parent sponge. It can be seen from the resulting resistance plot in Figure 5.17 that the sample exhibits an insulating nature prior to a superconducting transition at 92 K. Unlike the unannealed sample, the annealed resistance measurement exhibits no shoulder, and instead just a sharp drop in resistance.

In the case of MFP-BSCCO, it was found that the sample was more fragile than the MFP-YBCO sample, and it was thus difficult to attach wires to the sample. In the MFP-BSCCO sample, the resistance measurements show a sharp drop in resistance at 86 K, which is a little higher than would be expected for Bi-2212 but lower than would be expected for $Bi_2Sr_2Ca_2Cu_3O_{10+x}$ (Bi-2223). It is possible that the phase present is a mix between the two. Despite this, the drop in resistance is gradual and does not reach zero until about 25 K, indicating residual resistance in the sample. In an attempt to sharpen the transition, annealing of the sample in air at 830 °C for 24 hours was carried out. Similarly to MFP-YBCO, the annealed sample was not the exact sample that was analysed for the unannealed sample measurements but was from the same parent sponge. Also, for this sample, the gold wires were attached directly to the sponge without

135

prior evaporation of gold contacts on top of the sample. Interestingly, the annealed sample shows a decreased onset of T_c of 82 K, and a shoulder in the graph has been observed. This is possibly due to additional impurity phases forming during the annealing step, which are impeding the flow of current through the network of connecting struts of the sample.

To further analyse the superconductivity of these MFP samples, Superconducting Quantum Interference Device (SQUID) magnetometry was carried out on each sample. The resulting data can be shown in Figure 5.18. The magnetic susceptibilities reported were calculated by using the crystallographic density of Y-123 and the mass of the sample that has been measured and applied to equation 1.2.

Where M is the moment in Am^2, ρ is the crystal density in gm^{-3}, m is the mass in g and H is the magnetic field in Am^{-1}. In this case, the magnetic susceptibility χ is dimensionless and represents the volume susceptibility. Using the density of the unit cell means that the volume calculated is an estimate of the volume of the sponge material, and does not include the volume of the voids in the material. A susceptibility using the so-called envelope volume of the sponge could be estimated from the mercury porosimetry data, by using the value for the envelope density of the sample, but it was decided that the susceptibility of the material using its crystal density would allow for a more valuable estimate of the percentage of the actual material that was superconducting.. From the data presented in Figure 5.18, it can be seen that MFP-YBCO exhibits an onset superconductive transition at 92 K. Similarly to the resistance data, it can be seen that this transition is relatively broad. The data shows that the minimum volume susceptibility reached in the measurement is -0.4 for the annealed compared to -0.3 for the unannealed sample. This implies that more of the sample is superconducting in the annealed case.

Interestingly, the SQUID data for MFP-BSCCO indicates a similar trend, with more of the sample superconducting in the annealed sample compared to the unannealed sample. This appears to contradict with the resistance data, where the resistance reached zero at a much lower temperature for the annealed sample compared to the unannealed sample. The data appear to show that, despite the longer transition as in the case of the resistance measurements, more of the annealed sample is actually superconducting. Additionally, the onset T_c for this sample is lower than the onset T_c for the unannealed sample, which is consistent with what was observed with the resistance measurements. It appears from this additional data, that annealing the sample has improved the bulk superconductive properties of the sample, despite reducing the ability for current to flow throughout the sample.
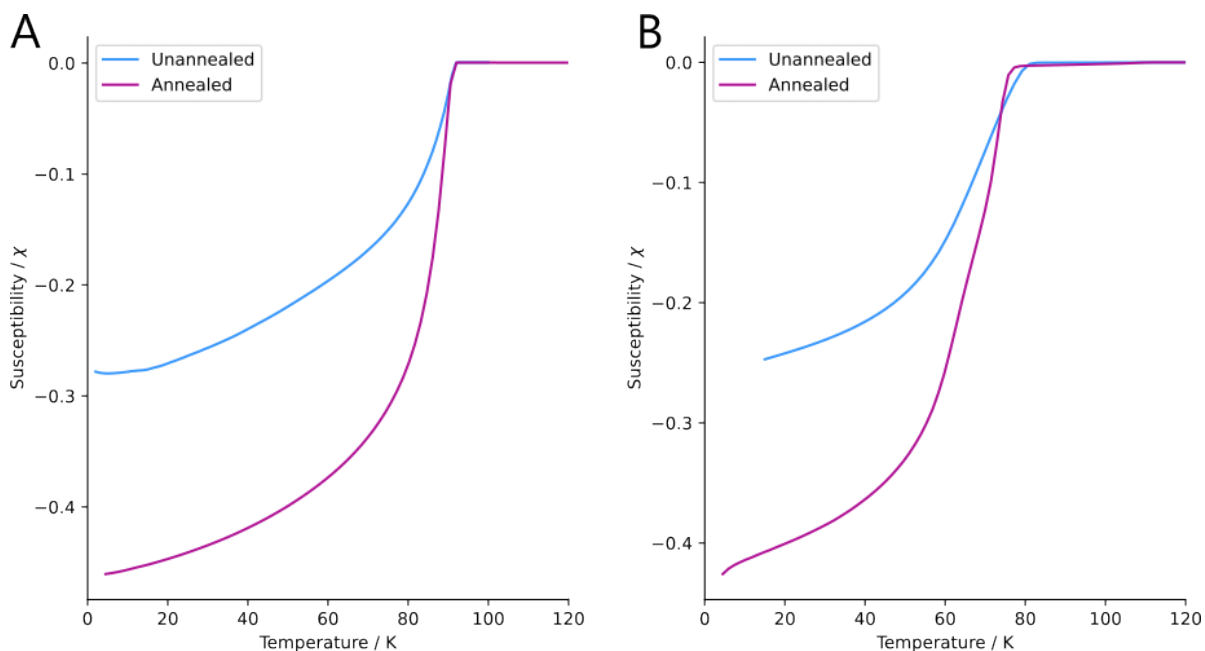
Figure 5.18: (a) SQUID magnetometry data from (blue) unannealed MFP-YBCO (purple) annealed MFP-YBCO. (b) SQUID magnetometry data from (blue) unannealed MFP-BSCCO and (purple) annealed MFP-BSCCO.

5.2.4   Summary

Through this chapter, three different methods of synthesising porous high-temperature superconductors with MF as a templating agent have been attempted. These three different synthesis methods have explored the effect of utilising the MF template by itself, the effect of combining it with additional chelating agents, and the effect of changing the solvent in the synthesis of Y-123 and Bi-2212. In doing so, some intricacies of this synthesis method were discovered, including the interaction of the sponge with the solvent and metal ions in the solution and the thermal resistance of the sponge.

When the sponge by itself was used, MF-YBCO was found to exhibit poor purity but did exhibit some control of the macromorphology of the sample. In contrast, MF-BSCCO presented excellent purity of 86 %, but with little to no control over the resultant morphology of the sample.

When synthesised by first using sodium alginate as an additional biopolymer, it was found that there was some replication of nanostructure for YBCO sample, along with a marked increase in purity of the target phase. The BSCCO sample synthesised by this method was less pure than the sample synthesised with just the MF sponge, and also yielded little to no replication of nanostructure. Despite some porosity of this sample, the resulting structure was not consistent with the starting material.

The final synthesis attempted was that of the sample synthesised by a modified Pechini method. In this case, the amount of citric acid used was ten times less than the literature reported

value. This is because it was found that the sponge had the propensity to decompose with addition of the literature-reported molar amount. Using FTIR it was discovered that this was likely due to the acidic nature of the solution resulting in a hydrolysis reaction of the MF, thus breaking the polymer chains into smaller chains, or the monomeric units. These samples synthesised by a modified Pechini method appeared to show the best compromise between the desired morphology of the sample and the purity. Both samples exhibited a good replication of the starting material, combined with a majority of the sample being formed of the target phase. It is possible that the purity of the Bi-2212 sample could be improved further by adjusting the synthesis parameters, for example by lengthening the dwell time of the synthesis. Due to the desired morpholgy being prevalent in both materials, further analysis was undertaken for these samples to probe their porosity and electronic properties. BET determined that both samples were essentially macroporous, though a slight mesoporous character was found for MFP-YBCO. Following this, the macroporosity of both samples was interrogated by Hg-porosimetry, and it was found that the samples were 82 % and 78 % porous for MFP-YBCO and MFP-BSCCO respectively. Analysis of the superconductivity for both samples was also carried out, and resistance measurements determined that the samples were indeed superconducting, though the transitions were broad, indicative of some residual resistance within the material - possibly due to resistance at grain boundaries of the crystallites. When annealed, the superconductive transition for MFP-YBCO was sharpened and SQUID showed that more of the sample was superconducting than in the unannealed sample. When MFP-BSCCO was examined with the resistance measurements, we observed a wide transition with a relatively high $T_{c,onset}$ of 86 K. After annealing the $T_{c,onset}$ was lowered, and an additional shoulder to the graph was found, though SQUID data appeared to show that a higher percentage of the sample was superconducting in the annealed sample case.

While the methods used herein have been aimed at the synthesis of the high-temperature superconductors, Y-123 and Bi-2212, it is also possible that these syntheses could be applicable to other metal oxides. Should a reticulated foam ceramic metal oxide be desired, these synthesis methods could be utilised in the synthesis. These experiments explored the templating power of MF sponges, but the effect of changing the morphology of the MF can be changed in the future.

Table 5.1: Table with the results from the multiphase Rietveld refinements for the YBCO samples presented in this chapter.

Phase	MF-YBCO Quantity / %	MFA-YBCO Quantity / %	MFP-YBCO Quantity / %	Aqueous control Quantity / %	Alginate control Quantity / %	Pechini control Quantity / %
$YBa_2Cu_3O_{7-\delta}$	36.5	64.8	69.3	29.3	59.3	50.7
Y_2BaCuO_5	16.6	12.7	3.8	13.3	17.6	22.1
$Ba_{0.98}CuO_{2.07}$	18.2	8.1	8.6	23.0	0.7	–
$Y_2Cu_2O_5$	4.1	1.4	8.4	10.7	–	3.7
CuO	11.9	8.7	7.3	20.6	15.9	23.6
$BaCO_3$	3.7	4.1	2.6	3.0	6.5	–
$YBa_4Cu_3O_9$	9.1	–	–	–	–	–
R_{wp}	6.93	4.01	3.37	5.71	7.21	6.45

Table 5.2: Table with the results from the multiphase Rietveld refinements for the BSCCO samples presented in this chapter.

Phase	MF-BSCCO Quantity / %	MFA-BSCCO Quantity / %	MFP-BSCCO Quantity / %	Aqueous control Quantity / %	Alginate control Quantity / %	Pechini control Quantity / %
$Bi_{2.09}Sr_{1.9}CaCu_2O_{8.22}$	86.5	64.8	55.7	4.9	–	62.7
$Bi_{10}Sr_{10}Cu_5O_{29}$	5.5	16.6	3.8	17.5	16.3	6.1
$Sr_{6.27}Ca_{4.73}Bi_6O_{22}$	6.0	4.9	8.6	24.5	13.6	16.9
CuO	0.1	–	8.4	34.2	3.0	2.1
$CaCO_3$	1.8	13.7	7.3	–	11.4	12.1
$SrCO_3$	–	–	–	18.9	–	–
$Na_3Ca_2BiO_6$	–	–	–	–	22.4	–
R_{wp}	6.93	4.01	3.37	8.61	7.21	6.45

CHAPTER

6

Conclusions and future work

This work has explored the synthesis of metal oxides primarily through sol-gel methods with increasing complexity and dimensionality. In the wider space of functional metal oxides, this work matches with current drives for synthetic control of nanostructures through a bottom-up approach. Examples of this drive for nanostructural control can be found in recent reviews on nanostructured supercapacitors, cathode materials for sodium-ion batteries and nanostructured materials for biosensing applications.[316–318] The pressure for ever-shrinking components for use in small devices compounds this, thus the control of nanostructures are becoming more important in everyday life. The work presented in this thesis also fits with the general themes of greener technology, both as a focus of synthesis methods which are less energy-intensive, and with respect to the applications of the researched materials themselves. These are themes that are commonly researched in recent functional material research, from the synthesis of novel green energy sources such as perovskite solar cells, to the reduction of firing time in ceramic syntheses through sol-gel or bio-templated techniques.[319–321] The excellent capabilities of deep eutectic solvents in the facile synthesis of functional materials is an important current area of research in the field of functional metal oxides, which can allow the synthesis of functional metal oxides at lower temperatures, and without the need for harsh organic solvents.[322]

Throughout this project, several synthetic techniques have been explored, such as the use of a natural deep eutectic solvent (NADES) or dextran as a biopolymer in a completely new synthesis of $Na_3Ni_2BiO_6$ (NNB), and $Na_3Ca_2BiO_6$ (NCB); a novel solid-state method of nanowire synthesis; and the use of a melamine formaldehyde (MF) sponge as a new templating agent in the synthesis of metal oxide materials. All techniques were carried out on a much shorter timescale than conventional solid-state syntheses, enabling a less energy intensive approach to the synthesis of functional metal oxides that would ordinarily require many days of high-temperature sintering.

141

Research into superconductive materials is also still prevalent, despite being known about for over 100 years, although the current focus is on high-pressure and low temperature systems, such as LaH_{10}. Despite this, a drive to the discovery of novel superconductive materials is that of high-throughput computational techniques, such as those discussed in Chapter 3. Despite the lack of success at discovering superconductivity in the potential candidates identified by the machine learning algorithm, there have been many more candidates identified by new algorithms since that could be explored in the future.[323,324]

The work herein focussed on the synthesis of superconductors, whether that was the well-established Y-Ba-Cu-O (YBCO) and Bi-Sr-Ca-Cu-O (BSCCO) families or materials predicted to be superconductive such as NNB, NCB and $KBa_6Zn_4Ga_7O_{21}$ (KBZGO). In a broader scope, this work focuses on synthesis techniques which allow control of the nanostructures of materials.

6.1 Conclusions

6.1.1 Rapid sol-gel syntheses of honeycomb-layered and orthorhombic metal oxides

Two synthetic techniques were utilised in the synthesis of NNB and NCB and were found to be successful overall. These techniques aimed to reduce the synthesis time of the materials while still retaining good purity of the product. This aim was achieved, as both materials only required a two-hour dwell time to yield a product with at least 70 % purity. A known problem with NNB is its propensity to develop stacking defects in the crystal structure during its crystallisation, resulting in a poorly ordered structure. This disorder was found to occur to some degree for all the samples synthesised and was characterised by an asymmetrical powder X-ray diffraction (pXRD) peak from the (020) reflection, and, in very disordered samples, a lack of peaks belonging to the hexagonal superlattice altogether. A sample synthesised from a low molecular weight dextran exhibited good intensity hexagonal superlattice peaks, with only slight asymmetry to the (020) reflection. This was interesting, as this ordered sample was synthesised without the necessity for additional annealing steps, as is typical for the synthesis of this material. Additionally, all syntheses of NNB and NCB were facile, with standard furnaces and syntheses carried out in ambient atmospheres. The precursor materials were also benign without needing harmful organic solvents.

The most effective synthesis of NNB was found to be the low molecular weight, dextran-mediated synthesis. This synthesis method resulted in both the purest sample of NNB, and the most ordered sample. Despite this, the NADES synthesis still resulted in good purity of product (76 % of the sample consisting of the target phase), and the sample was somewhat porous after the synthesis, which could be applicable as a porous electrode in future applications. The optimum temperature for both synthesis methods was 800 °C, despite the original synthesis requiring 700 °C with a subsequent anneal at 750 °C. For the NADES synthesis, it seemed that

the irreproducibility of generating the ordered polymorph was due to minute details within the furnace - such as slight differences in the atmosphere inside. A synthesis carried out in an open tube furnace did result in the ordered polymorph, indicating that preventing the build-up of CO_2 within the furnace is key for the formation of the target phase. It was also found that an aqueous synthesis in the absence of any biopolymer resulted in no target phase, and when $1000\,mg$ of dextran was used, the target phase also did not form. When $300\,mg$ was used, the disordered polymorph of NNB formed. This confirms the theory that the synthesis of NNB depends on the atmospheric conditions within the furnace; too much dextran appears to yield a disordered phase or none of the target phase whatsoever. However, it also appears that some chelating agent is required, as, in its absence, the target phase also does not form. A final observation from these syntheses was the note that a common impurity phase from this synthesis was a rare polymorph of Bi_2O_3, $R-Bi_2O_3$. The reasons for which this polymorph can form with these reaction conditions are yet unknown; perhaps it could be due to NiO being a very stable structure, resulting in the formation of a bismuth oxide over a mixed bismuth-nickel-oxide as what was observed for NCB.

For NCB, the most effective synthesis in terms of phase purity was also the low molecular weight dextran synthesis, where the sample consisted of $79\,\%$ of the target phase when synthesised at $800\,°C$. Interestingly, using the higher molecular weight presented no advantage over the control synthesis with no dextran at all. The synthesis with NADES was directly comparable, with a phase purity of $76\,\%$, indicating that there was very little difference between the synthesis techniques. Again, the synthesis of the NADES resulted in a porous product, consistent with what was observed for NNB. Typical impurity phases were $Ca_4Bi_6O_{13}$ and $Ca_6Bi_6O_{15}$, and there was no evidence of any formation of $R-Bi_2O_3$ in contrast to what was observed for the syntheses of NNB.

Finally, both NNB and NCB were analysed by Superconducting Quantum Interference Device (SQUID) magnetometry. From these studies, it was confirmed that the NNB was indeed antiferromagnetic, with a low ordering temperature of $11.9\,K$, as was observed in its initial study. The Curie-Weiss temperature of this sample, $0.79\,K$ indicated that the material was indeed frustrated. However, the overall degree of frustration was low (as was shown by the low magnitude of the Curie-Weiss temperature). The source of the magnetic signal was also confirmed to be due to the nickel ions by calculating the effective moment, μ_{eff}, to be $2.90\,\mu_B$. The analysis of NCB was less straightforward, as the magnetic susceptibility indicated a paramagnetic material, but the overall signal was minimal. Following the same Curie-Weiss analysis as was carried out with NNB, it was determined that the magnetic signal was arising from only $0.18\,\%$ of the sample, which is likely due to impurities within the sample.

Despite attempting several different synthetic techniques, KBZGO was not successfully synthesised during this work. Instead, most syntheses resulted in the formation of $BaGa_2O_4$ instead.

6.1.2 The synthesis of nanowires of high-temperature superconductors

The prospect of manufacturing the conditions necessary for the microcrucible mechanism of nanowire growth for the high-temperature superconductor $Bi_2Sr_2CaCu_2O_{8+x}$ (Bi-2212) was investigated. Because Bi-2212 is a quinternary metal oxide, it was realised that a solid-state method of nanowire synthesis would require five different elements and the flux to come into contact simultaneously for a nanowire to grow, resulting in a 6th order reaction. As such, two different methods were devised that exploited mixed-metal oxide or carbonates to reduce the reaction's order. These two methods took inspiration from a previous study into the phase evolution of Bi-2212, to examine the most important phases by which Bi-2212 forms, thereby identifying two potential routes for the synthesis. These were: using Bi_2O_3 and CuO with $Sr_xCa_{1-x}CO_3$ nanoparticles and a flux; and combining $Bi_2Sr_2CuO_6$ (Bi-2201) with $CaCu(OAc)_4 \cdot 6H_2O$ and a flux.

The first method examined various fluxes, dwell temperatures and dwell times to examine the final morphology and composition of the samples. The three fluxes examined were NaCl, Na_2CO_3 and Ca_Cl_2. These enabled an examination of the effect of changing both counterions for the salts used. NaCl was the least successful method, with very few wires observed throughout the samples. Na_2CO_3 was more promising and resulted in interesting samples where the wires had appeared to bent during growth, indicating some strain on the wires as they grew. Interestingly, this phenomenon was not observed for any of the other wires throughout this work, which could indicate that the bending was due in part to the Na_2CO_3 flux. Unfortunately, these wires were rarely found throughout the sample, so an examination of their exact crystal structure by transmission electron microscopy (TEM) was not carried out. Finally, using $CaCl_2$ as a flux yielded samples where wires had grown. However, the wires that were observed were found to exist within a very short dwell window, where the wires were not observed at all when the furnace had dwelled for 1 h, and evidence of wires which had grown and subsequently melted together was observed at 2 h.

The second method was examined with a NaCl flux. Interestingly, a synthesis of Bi-2201 with a NaCl flux also resulted in the synthesis of numerous nanowires, possibly due to NaCl partially melting the Bi-2201 and enabling wires to grow. The synthesis, which combined Bi-2201, $CaCu(OAc)_4 \cdot 6H_2O$ and the NaCl flux, also yielded nanowires. In this sample, it was found that wires were prevalent throughout the surface of the sample when 30 % NaCl flux was used. Further examination of these wires with TEM confirmed that they were a BSCCO phase but could not conclusively state whether the material was Bi-2212 or Bi-2201. The presence of calcium within the wires was confirmed by energy dispersive X-ray analysis (EDXA). However, the overall percentage of this was low, and there was also evidence that the wire was abundant in strontium. It is likely that the wire is a mixed phase and was therefore not conclusively confirmed to be either stoichiometry. It should also be noted that each wire is not necessarily made from the same stoichiometry, leading to further uncertainty about these samples.

The final study carried out in this chapter was the attempt to utilise a heating stage on the TEM view nanowire growth *in-situ*. The first was to examine the reaction of Bi-2201 with NaCl. Unfortunately, no nanowire growth was observed with this experiment, and it became evident that calibrating the heating stage would be required for future syntheses. Further experiments, therefore, studied $YBa_2Cu_3O_{7-\delta}$ (Y-123), as nanowires have been observed to grow from this material previously. After this calibration experiment (where no wire growth was observed), two further studies were performed with a controlled ramp rate of $5\,°C\,min^{-1}$. The first of these experiments showed several key events where the substrate moved or where features appeared to be about to grow out from the bulk before disappearing. The second experiment was interesting, as minimal transformation was observed during the heating, but the growth of nanowires was observed during the cooling of the sample. Examination of the final material after the synthesis indicated that the wires were made from Y_2BaCuO_5 (Y-211), which is promising as this coincides with what was observed in work by Boston *et al.* [143]

6.1.3 The synthesis of sponge-architectures of high-temperature superconductors

A highly porous MF sponge was explored for its ability to behave as a template in the synthesis of YBCO and BSCCO. Through this work, three different syntheses of increasing complexity were attempted to utilise a MF sponge as a template.

The first method attempted utilised the sponge alone as a templating agent to the metal nitrate ions in solution. It was found that this showed good templating for the Y-123 sample synthesised through this method, but with poor purity. On the other hand, the Bi-2212 sample exhibited poor templating, and most of the material showed no direction of shape. It exhibited excellent purity, however, possibly showing the good potential of MF as a phase-directing agent for Bi-2212.

The second method coated the sponge with sodium alginate prior to metal chelation and calcination. Despite a good reticulated sponge-like structure being observed for the Y-123 sample synthesised through this method, it was extremely fragile. In this case, the percentage of the sample due to the target phase was much better. The Bi-2212 sample was porous but did not exhibit exact replication of the sponge nanostructure and was less pure than the sample synthesised from the sponge alone.

The final method was that of the modified Pechini method. It was found that this method enabled an excellent replication of the nanostructure of the initial sponge. The resulting structures were highly porous with a reticulated structure for both Y-123 and Bi-2212. However, the small grain sizes of the products were also likely detrimental to the superconductive properties. When resistance measurements were carried out, it was found that both samples showed broad transitions, with the resistance reaching zero at much lower temperatures than at the start of the transition. SQUID magnetometry also showed that the volume susceptibility reached a minimum

145

of -0.4 for both samples, indicating that the whole of the sample was not superconducting.

6.2 Future Work

6.2.1 Rapid sol-gel syntheses of honeycomb-layered and orthorhombic metal oxides

These materials were chosen to be synthesised due to the prediction by Stanev *et al.* of their superconductivity. Unfortunately, from the data, the materials were observed not to be super-conductive. Nevertheless, there is some potential for superconductivity to be induced into the sample by doping the materials. A potential idea for alliovalent doping of NNB could be to replace the Bi^{5+} with an ion that has a +6 oxidation state, such as Te. This would hopefully push the oxidation state of some of the nickel ions in the lattice to form the Ni^+ oxidation state, which is an uncommon oxidation state for nickel. This would emulate the d^8 electron configuration found in undoped copper oxides, possibly yielding a material that emulates that of the cuprate superconductors, thus inducing superconductivity. This phenomenon was observed for a so-called infinite-layered nickelate in 2019.[325]

With the ability to synthesise NCB with higher purity and through a more facile synthesis, it is possible to study its properties further. Examination of its conductivity should be carried out to determine if there is any interesting behaviour at different temperatures. When synthesising this material, it was observed that it was orange in colour, which indicates a lack of conductivity due to the indication of a larger band gap. However, this is merely an observation until conductivity testing is carried out.

Another potential avenue of exploration is to further simplify the synthetic process by util-ising sodium alginate as the biopolymer in the synthesis. This would likely result in a more straightforward synthesis, where sodium salts are not required to be added at all, and would further examine the process by which these metal oxides form.

With regards to KBZGO, despite the lack of success at its synthesis, there are still plenty of avenues to explore in the future. One observation from the studies was that many of the syntheses resulted in little to no potassium phases in the product. A further experiment, therefore, would be to attempt the synthesis with an excess of potassium salts. This would be similar to the case with the syntheses of NNB and NCB, where the sodium salt is added at 3 % excess. In the initial study where KBZGO was synthesised, the potassium oxide was added in a large excess, presumably to behave as some form of flux during the synthesis. Therefore, adding an excess of potassium in future synthetic studies should be explored. Other biopolymers and deep eutectic solvent (DES) could also be tested; for example, potassium alginate could be examined as a potential biopolymer in a future synthesis. Alternatively, a DES based on malonic acid and choline chloride has also succeeded in synthesising barium titanate.[326] It is likely that a challenge with KBZGO in

particular is the fact that it is a quinternary metal oxide and thus requires that the quinternary phase is more energetically favourable to form than other metal oxides.

6.2.2 The synthesis of nanowires of high-temperature superconductors

Both synthesis methods attempted herein could be adjusted for future work to tailor further the nanowires produced. In particular, the samples synthesised with a Na_2CO_3 flux and the first synthetic method could be examined further. The key aim of this further work would be to increase the density of nanowires formed, allowing the exact crystal structure of the wires to be elucidated with TEM and selected-area electron diffraction (SAED). Additionally, this would be an ideal sample to examine with environmental scanning electron microscopy (SEM), as *in-situ* examination of the growth of these wires would allow the viewing of the bending of the wires as they grow as well. It would also be interesting to examine if this choice of flux encourages the growth of bent wires or if it is another factor that yields them.

The method which combined Bi-2201, NaCl and $CaCu(OAc)_4 \cdot 6H_2O$ needs to be tailored to ensure an extreme excess of calcium is present during the synthesis, in the hope that the wires would therefore contain more calcium and be closer in composition to the desired Bi-2212 phase. Attempts have already been made to utilise $CaCl_2$ as a flux for these samples by Sorrel Haughton; however, a similar issue was observed to the mixed metal carbonate method, where the wires observed were highly deficient in bismuth. Alternatively, instead of using just $CaCu(OAc)_4 \cdot 6H_2O$ one could simply include additional calcium acetate or explore its addition as a potential flux instead of NaCl. The wires that have already been synthesised with this method should also be examined for their potential as a THz emitter, which could be done by irradiating a wire with microwave radiation while it is in the superconductive state and measuring the potential difference across the wire. If the wire consists of intrinsic Josephson-junction (JJ)s, the irradiation of the wire should induce an alternating current and thus potential difference across the JJs within the structure, which can be subsequently measured.

Finally, the *in-situ* TEM experiments should be taken further to enable the observation of nanowire growth in more systems than just YBCO. Now that reasonable control of the experimental parameters has been achieved through manual control of the heating current, more systems can be examined, such as continuing studies of YBCO or initiating studies of La-Ba-Cu-O (LaBCO) or Bi-2212. These experiments are challenging due to the necessity for all phases to be present in close proximity, along with the potential for the evaporation or sublimation of the constituent phases during the heating. As such, many parameters need to be examined further - such as the behaviour of the phases during heating under a vacuum. Now that some success has been seen for the YBCO sample, the observation of nanowire growth in this system should be repeated to ensure that the wires are not growing due to extraneous features such as the decomposition of the gold grid.

6.2.3 The synthesis of sponge-architectures of high-temperature superconductors

Several future avenues could be explored in this work. The modified Pechini method was found to be excellent in the synthesis of a porous structure. However, the relative purity of the Bi-2212 in particular was not ideal, with only 56 % of the sample consisting of the target phase. This is reflected in the critical temperature (T_c) of the sponge as well, as the transition is quite broad. There are several changes to the synthetic method that could be attempted in order to potentially access better purity of product. The first is to alter the furnace conditions for the synthesis, potentially by lengthening the dwell time or raising the dwell temperature. This longer synthesis time could enable all reactions within the furnace to proceed to completion and potentially yield a more pure product. An alternative method could be to alter the solvent used in the synthesis, perhaps by utilising the NADES method that was carried out in both Chapter 3 and 4 to dissolve the metal salts, followed by soaking a MF sponge in this solution.

In the future, the modified Pechini method samples should also be tested to determine whether these porous structures can shorten the annealing time necessary. As the anneal is a diffusion-based process, the smaller struts and more porous nature of the high-temperature superconductor sponges could shorten this process. As such, examining whether the anneal can be carried out over progressively shorter timeframes would be interesting to attempt. This could be attempted with MFP-YBCO by affixing electrodes to an unannealed sponge before measuring its resistance against temperature. This sample can then be annealed for several hours and then re-analysed for its resistive properties. This can be repeated until no change in the resistance against temperature graph is observed, indicating the completion of the annealing.

This work also sets up MF as a potential new templating agent for other metal oxide materials. It is possible, providing the metal salts are soluble in ethylene glycol, that highly porous reticulated foams of other metal oxides could be synthesised through the modified Pechini method. Additionally, the MF did behave as a good templating agent, so it is possible that further experiments could be carried out to synthesise YBCO and BSCCO in different morphologies based on different potential MF morphologies.

[1]   S. R. Elliott, *The physics and chemistry of solids*, J. Wiley, 1998.

[2]   S. Banerjee and A. K. Tyagi, *Functional Materials*, Elsevier Inc., 2012.

[3]   J. F. Vincent, O. A. Bogatyreva, N. R. Bogatyrev, A. Bowyer and A. K. Pahl, *Biomimetics: Its practice and theory*, Royal Society, 2006, vol. 3, pp. 471–482.

[4]   G. D. Mestral, *Separable Fastening Device*, U.S. Patent 3009235A, 1952.

[5]   C. T. Foo, B. Omar and I. Taib, *MATEC Web of Conferences*, 2017, **135**, 00019.

[6]   T. Stegmaier, M. Linke and H. Planck, *Philosophical Transactions of the Royal Society A: Mathematical, Physical and Engineering Sciences*, 2009, **367**, 1749–1758.

[7]   C. B. Carter and M. G. Norton, *Ceramic materials: Science and engineering*, Springer New York, 2013, pp. 1–766.

[8]   R. Riedel and I. W. Chen, *Ceramics Science and Technology*, Wiley-VCH Verlag GmbH & Co. KGaA, 2011.

[9]   J. Li, Y. Pan, Y. Zeng, W. Liu, B. Jiang and J. Guo, *International Journal of Refractory Metals and Hard Materials*, 2013, **39**, 44–52.

[10]   L. H. da Silva, E. de Lima, R. B. de Paula Miranda, S. S. Favero, U. Lohbauer and P. F. Cesar, *Brazilian Oral Research*, 2017, **31**, 133–146.

[11]   S. K. Sahoo, B. Manoharan and N. Sivakumar, *Perovskite Photovoltaics: Basic to Advanced Concepts and Implementation*, 2018, 1–24.

[12]   D. H. Lindsley, *Oxide Minerals*, De Gruyter, 1991.

[13]   K. P. Kepp, *ChemPhysChem*, 2020, **21**, 360–369.

[14]   T. Misawa, K. Hashimoto and S. Shimodaira, *Corrosion Science*, 1974, **14**, 131–149.

[15]   Z. L. Wang and J. Song, *Science*, 2006, **312**, 242–246.

[16] M. Acosta, N. Novak, V. Rojas, S. Patel, R. Vaish, J. Koruza, G. A. Rossetti and J. Rödel, *Applied Physics Reviews*, 2017, **4**, 41305.

[17] J. G. Bednorz and K. A. Müller, *Z. Phys. B-Condensed Matter*, 1986, **64**, 267–271.

[18] C. Hammond, *The Basics of Crystallography and Diffraction*, Oxford University PressOxford, 2015.

[19] E. A. Moore and L. E. Smart, *Solid State Chemistry*, CRC Press, Fifth edition. | Boca Raton : CRC Press„ 5th edn., 2020.

[20] R. Purohit and P. Venugopalan, *Resonance*, 2009, **14**, 882–893.

[21] S. Yoshioka and Y. Kitano, *Geochemical Journal*, 1985, **19**, 245–249.

[22] G.-T. Zhou, Q.-Z. Yao, S.-Q. Fu and Y.-B. Guan, *European Journal of Mineralogy*, 2010, **22**, 259–269.

[23] E. H. Lee, *Asian Journal of Pharmaceutical Sciences*, 2014, **9**, 163–175.

[24] L. Yu, G. A. Stephenson, C. A. Mitchell, C. A. Bunnell, S. V. Snorek, J. J. Bowyer, T. B. Borchardt, J. G. Stowell and S. R. Byrn, *Journal of the American Chemical Society*, 2000, **122**, 585–591.

[25] C. R. Gardner, C. T. Walsh and Örn Almarsson, *Nature Reviews Drug Discovery*, 2004, **3**, 926–934.

[26] R. A. V. Santen, *Journal of Physical Chemistry*, 1984, **88**, 5768–5769.

[27] J. J. de Yoreo, *Proceedings of the National Academy of Sciences of the United States of America*, 2022, **119**, e2121661119.

[28] S. Ghedia, T. Locherer, R. Dinnebier, D. L. Prasad, U. Wedig, M. Jansen and A. Senyshyn, *Physical Review B - Condensed Matter and Materials Physics*, 2010, **82**, 024106.

[29] J. Potticary, L. R. Terry, C. Bell, A. N. Papanikolopoulos, P. C. Christianen, H. Engelkamp, A. M. Collins, C. Fontanesi, G. Kociok-Köhn, S. Crampin, E. D. Como and S. R. Hall, *Nature Communications*, 2016, **7**, 11555.

[30] J. Potticary, C. Hall, V. Hamilton, J. F. McCabe and S. R. Hall, *Crystal Growth and Design*, 2020, **20**, 2877–2884.

[31] S. Thomas and A. Thankappan, *Perovskite Photovoltaics*, Elsevier, 2018, pp. 1–501.

[32] A. M. Glazer, *Acta Crystallographica Section A*, 1975, **31**, 756–762.

[33] C. F. Buhret, *The Journal of Chemical Physics*, 1962, **36**, 798–803.

[34] M. Gaudon, *Polyhedron*, 2015, **88**, 6–10.

[35] T. Sato, S. Takagi, S. Deledda, B. C. Hauback and S. I. Orimo, *Scientific Reports*, 2016, **6**, 1–10.

[36] X. C. Liu, R. Hong and C. Tian, *Journal of Materials Science: Materials in Electronics*, 2009, **20**, 323–327.

[37] C. W. Chu, L. Z. Deng and B. Lv, *Physica C: Superconductivity and its Applications*, 2015, **514**, 290–313.

[38] C. McDonald, C. Ni, P. Maguire, P. Connor, J. Irvine, D. Mariotti and V. Svrcek, *Nanomaterials*, 2019, **9**, 1481.

[39] D. K. Palchayev, S. K. Gadzhimagomedov, Z. K. Murlieva, M. K. Rabadanov and R. M. Emirov, author, 2018, p. 012076.

[40] R. G. Jones, C. K. Ober, T. Hayakawa, C. K. Luscombe and N. Stingelin, *Pure and Applied Chemistry*, 2020, **92**, 1861–1891.

[41] H. S. Virk, *Nanomaterials : Basic Concepts and Applications*, Trans Tech Publishers, 2015, p. 239.

[42] S. Zeng, D. Baillargeat, H. P. Ho and K. T. Yong, *Chemical Society Reviews*, 2014, **43**, 3426–3452.

[43] H. Goesmann and C. Feldmann, *Angewandte Chemie International Edition*, 2010, **49**, 1362–1395.

[44] T. Darmanin and F. Guittard, *Materials Today*, 2015, **18**, 273–285.

[45] P. Vukusic and J. R. Sambles, *Nature 2003 424:6950*, 2003, **424**, 852–855.

[46] R. C. Schroden, M. Al-Daous, C. F. Blanford and A. Stein, *Chemistry of Materials*, 2002, **14**, 3305–3315.

[47] Y. Chen, L. Li, Q. Xu, W. Chen, Y. Dong, J. Fan and D. Ma, *Solar RRL*, 2021, **5**, 2000541.

[48] Q. Fu, W. Yu, G. Bao and J. Ge, *Nature Communications*, 2022, **13**, 1–9.

[49] A. Kumar and A. Singh, *Materialia*, 2021, **15**, 101034.

[50] C. Xu, P. R. Anusuyadevi, C. Aymonier, R. Luque and S. Marre, *Chemical Society Reviews*, 2019, **48**, 3868–3902.

[51] K. Zhu, Y. Ju, J. Xu, Z. Yang, S. Gao and Y. Hou, *Accounts of Chemical Research*, 2018, **51**, 404–413.

[52]   S. Mugiraneza and A. M. Hallas, *Communications Physics*, 2022, **5**, 95.

[53]   J. M. D. Coey, *Magnetism and Magnetic Materials*, Cambridge University Press, 2001, vol. 9780521816144, pp. 1–617.

[54]   A. P. Ramirez, *Annual Review of Materials Science*, 1994, **24**, 453–480.

[55]   M. P. Shores, E. A. Nytko, B. M. Bartlett and D. G. Nocera, *Journal of the American Chemical Society*, 2005, **127**, 13462–13463.

[56]   D. Van Delft and P. Kes, *Physics Today*, 2010, **63**, 38–43.

[57]   M. N. Wilson, *IEEE Transactions on Applied Superconductivity*, 2012, **22**, 3800212–3800212.

[58]   V. L. Ginzburg, *Soviet Physics - Uspekhi*, 1991, **34**, 283–288.

[59]   W. Meissner and R. Ochsenfeld, *Die Naturwissenschaften*, 1933, **21**, 787–788.

[60]   J. Bardeen, *Physical Review*, 1950, **80**, 567–574.

[61]   A. P. Drozdov, M. I. Eremets, I. A. Troyan, V. Ksenofontov and S. I. Shylin, *Nature*, 2015, **525**, 73–76.

[62]   R. Kleiner and W. Buckel, *Superconductivity: An Introduction*, Wiley-VCH Verlag GmbH Co. KGaA, Weinheim, Germany, 2016.

[63]   F. S. Henyey, *Physical Review Letters*, 1982, **49**, 416.

[64]   H. Fröhlich, *Physical Review*, 1950, **79**, 845–856.

[65]   J. Bardeen, L. N. Cooper and J. R. Schrieffer, *Physical Review*, 1957, **106**, 162–164.

[66]   *The Nobel Prize in Physics 1972*, https://www.nobelprize.org/prizes/physics/1972/summary/.

[67]   A. Narlikar, in *Superconductors*, Oxford University Press, 2014, pp. 15–30.

[68]   S. Speller, *A materials science guide to superconductors and how to make them super*, Oxford Unversity Press, 1st edn., 2022, p. 207.

[69]   G. R. Stewart, *Advances in Physics*, 2017, **66**, 75–196.

[70]   P. W. Atkins and J. de Paula, *Physical Chemistry, 9th ed*, Oxford University Press,, 2010.

[71]   M. V. Salapaka and S. M. Salapaka, *IEEE Control Systems*, 2008, **28**, 65–83.

[72]   B. D. Josephson, *Physics Letters*, 1962, **1**, 251–253.

[73] C. A. Hamilton and S. P. Benz, *IEEE MTT-S International Microwave Symposium Digest*, 2001, **2**, 853–856.

[74] Z.-R. Li and B.-H. Chen, *Superconductor Science and Technology*, 2016, **29**, 080502.

[75] W. E. Pickett, *Reviews of Modern Physics*, 1989, **61**, 433–512.

[76] M. K. Wu, J. R. Ashburn, C. J. Torng, P. H. Hor, R. L. Meng, L. Gao, Z. J. Huang, Y. Q. Wang and C. W. Chu, *Physical Review Letters*, 1987, **58**, 908–910.

[77] W. J. Nuttall, R. H. Clarke and B. A. Glowacki, *Nature*, 2012, **485**, 573–575.

[78] A. Schilling, M. Cantoni, J. D. Guo and H. R. Ott, *Nature*, 1993, **363**, 56–58.

[79] C. W. Chu, L. Gao, F. Chen, Z. J. Huang, R. L. Meng and Y. Y. Xue, *Nature*, 1993, **365**, 323–325.

[80] P. A. Lee, N. Nagaosa and X. G. Wen, *Reviews of Modern Physics*, 2006, **78**, 17.

[81] M. Łuszczek, *Physica Status Solidi (b)*, 2010, **247**, 104–108.

[82] H. A. Blackstead, D. B. Chrisey, J. D. Dow, J. S. Horwitz, A. E. Klunzinger and D. B. Pulling, *Physics Letters A*, 1995, **207**, 109–112.

[83] J. D. Jorgensen, M. A. Beno, D. G. Hinks, L. Soderholm, K. J. Volin, R. L. Hitterman, J. D. Grace, I. K. Schuller, C. U. Segre, K. Zhang and M. S. Kleefisch, *Physical Review B*, 1987, **36**, 3608–3616.

[84] K. Kanoda, T. Takahashi, T. Kawagoe, T. Mizoguchi, S. Kagoshima and M. Hasumi, *Japanese Journal of Applied Physics*, 1987, **26**, L2018–L2020.

[85] E. S. Reddy and G. J. Schmitz, *Superconductor Science and Technology*, 2002, **15**, L21–L24.

[86] D. K. Namburi, Y. Shi and D. A. Cardwell, *Superconductor Science and Technology*, 2021, **34**, 053002.

[87] A. Molodyk, S. Samoilenkov, A. Markelov, P. Degtyarenko, S. Lee, V. Petrykin, M. Gaifullin, A. Mankevich, A. Vavilov, B. Sorbom, J. Cheng, S. Garberg, L. Kesler, Z. Hartwig, S. Gavrilkin, A. Tsvetkov, T. Okada, S. Awaji, D. Abraimov, A. Francis, G. Bradford, D. Larbalestier, C. Senatore, M. Bonura, A. E. Pantoja, S. C. Wimbush, N. M. Strickland and A. Vasiliev, *Scientific Reports*, 2021, **11**, 2084.

[88] C. Michel, M. Hervieu, M. M. Borel, A. Grandin, F. Deslandes, J. Provost and B. Raveau, *Zeitschrift für Physik B Condensed Matter*, 1987, **68**, 421–423.

[89] H. Maeda, Y. Tanaka, M. Fukutomi and T. Asano, *Japanese Journal of Applied Physics*, 1988, **27**, L209–L210.

[90] S. Zhou, H. Wang, Y. Wang, Z. Fei, B. Sun and Y. Qi, *Journal of Superconductivity and Novel Magnetism*, 2014, **27**, 383–388.

[91] L. A. Bendersky, R. S. Roth and C. J. Rawn, *Journal of Materials Research*, 1990, **5**, 46–52.

[92] J. Darriet, F. Weill, B. Darriet, X. F. Zhang and J. Etourneau, *Solid State Communications*, 1993, **86**, 227–230.

[93] H. Maeda and Y. Yanagisawa, *IEEE Transactions on Applied Superconductivity*, 2014, **24**, year.

[94] L. Rossi, *Superconductor Science and Technology*, 2010, **23**, 034001.

[95] M. Sawicki, W. Stefanowicz and A. Ney, *Semiconductor Science and Technology*, 2011, **26**, 064006.

[96] H. L. Huang, D. Wu, D. Fan and X. Zhu, *Science China Information Sciences*, 2020, **63**, 1–32.

[97] L. Ozyuzer, A. E. Koshelev, C. Kurter, N. Gopalsami, Q. Li, M. Tachiki, K. Kadowaki, T. Yamamoto, H. Minami, H. Yamaguchi, T. Tachiki, K. E. Gray, W.-K. Kwok and U. Welp, *Science*, 2007, **318**, 1291–1293.

[98] A. Molodyk, S. Samoilenkov, A. Markelov, P. Degtyarenko, S. Lee, V. Petrykin, M. Gaifullin, A. Mankevich, A. Vavilov, B. Sorbom, J. Cheng, S. Garberg, L. Kesler, Z. Hartwig, S. Gavrilkin, A. Tsvetkov, T. Okada, S. Awaji, D. Abraimov, A. Francis, G. Bradford, D. Larbalestier, C. Senatore, M. Bonura, A. E. Pantoja, S. C. Wimbush, N. M. Strickland and A. Vasiliev, *Scientific Reports*, 2021, **11**, 2084.

[99] M. Stemmle, F. Merschel, M. Noe and A. Hobl, author, 2013, pp. 323–326.

[100] M. Stemmle, F. Merschel, M. Noe, L. Hofmann and A. Hobl, *Physics Procedia*, 2012, **36**, 884–889.

[101] *New superconductor technology for the transmission grid*, 2018, `https://phys.org/news/2018-07-superconductor-technology-transmission-grid.html`.

[102] P. G. Cheetham, W. Kim, C. H. Kim, S. V. Pamidi, L. Graber and H. Rodrigo, *IEEE Transactions on Dielectrics and Electrical Insulation*, 2017, **24**, 191–199.

[103] J. Stodart and M. Faraday, *The Philosophical Magazine*, 1820, **56**, 26–35.

[104] C. Xu, S. De, A. M. Balu, M. Ojeda and R. Luque, *Chemical Communications*, 2015, **51**, 6698–6713.

[105] A. I. Tok, F. Y. Boey and X. L. Zhao, *Journal of Materials Processing Technology*, 2006, **178**, 270–273.

[106] S. K. Gupta and Y. Mao, *Progress in Materials Science*, 2021, **117**, 100734.

[107] J. Boltersdorf, N. King and P. A. Maggard, *CrystEngComm*, 2015, **17**, 2225–2241.

[108] D. E. Bugaris and H.-C. zur Loye, *Angewandte Chemie International Edition*, 2012, **51**, 3780–3811.

[109] S. Oishi, K. Teshima and H. Kondo, *Journal of the American Chemical Society*, 2004, **126**, 4768–4769.

[110] M. Kakihana, *Journal of Sol-Gel Science and Technology*, 1996, **6**, 7–55.

[111] J. Livage, *Current Opinion in Solid State and Materials Science*, 1997, **2**, 132–138.

[112] L. L. Hench and J. K. West, *Chemical Reviews*, 1990, **90**, 33–72.

[113] A. E. Danks, S. R. Hall and Z. Schnepp, *Materials Horizons*, 2016, **3**, 91–112.

[114] W. F. Chen, S. S. Mofarah, D. A. H. Hanaor, P. Koshy, H. K. Chen, Y. Jiang and C. C. Sorrell, *Inorganic Chemistry*, 2018, **57**, 7279–7289.

[115] C. Su, B.-Y. Hong and C.-M. Tseng, *Catalysis Today*, 2004, **96**, 119–126.

[116] A. Douy and P. Odier, *Materials Research Bulletin*, 1989, **24**, 1119–1126.

[117] Y. Han, S. Li, X. Wang and X. Chen, *Materials Research Bulletin*, 2004, **39**, 25–32.

[118] S. Lu, J. Shao and F. Wu, *Journal of Sol-Gel Science and Technology*, 2022, 1.

[119] S. Sakka, *Handbook of Advanced Ceramics*, Elsevier, 2013, pp. 883–910.

[120] J. Krzak, A. Szczurek, B. Babiarczuk, J. Gąsiorek and B. Borak, in *J. Krzak, A. Szczurek, B. Babiarczuk, J. Gąsiorek and B. Borak*, Elsevier, 2020, pp. 111–147.

[121] K. Abe, Y. Sanada and T. Morimoto, *Journal of Sol-Gel Science and Technology*, 2001, **22**, 151–166.

[122] S. Alberti and J. Jágerská, *Frontiers in Materials*, 2021, **8**, 629822.

[123] M. U. Pechini, *Method of preparing lead and alkaline earth titanates and niobates and coating method using the same to form a capacitor*, U.S. Patent US3330697A, 1967.

[124] L. Dimesso, *Pechini Processes: An Alternate Approach of the Sol–Gel Method, Preparation, Properties, and Applications*, Springer International Publishing, 2016, pp. 1–22.

[125] J. Lin, M. Yu, C. Lin and X. Liu, *Journal of Physical Chemistry C*, 2007, **111**, 5835–5845.

[126] A. M. Huízar-Félix, T. Hernández, S. de la Parra, J. Ibarra and B. Kharisov, *Powder Technology*, 2012, **229**, 290–293.

[127] Y. J. Lin, Y. H. Chang, W. D. Yang and B. S. Tsai, *Journal of Non-Crystalline Solids*, 2006, **352**, 789–794.

[128] L. Kozielski, A. Wilk, M. M. Bućko and J. Banys, *Materials*, 2020, **13**, 1620.

[129] T. Grzyb and S. Lis, *Inorganic Chemistry*, 2011, **50**, 8112–8120.

[130] Z. S. Peng, Z. Q. Hua, Y. N. Li, J. Di, J. Ma, Y. M. Chu, W. N. Zhen, Y. L. Yang, H. J. Wang and Z. X. Zhao, *Journal of Superconductivity and Novel Magnetism*, 1998, **11**, 749–754.

[131] S. C. Zhang, G. L. Messing, W. Huebner and M. M. Coleman, *Journal of Materials Research*, 1990, **5**, 1806–1812.

[132] Z. Schnepp, *Angewandte Chemie International Edition*, 2013, **52**, 1096–1108.

[133] Z. Schnepp, S. C. Wimbush, S. Mann and S. R. Hall, *CrystEngComm*, 2010, **12**, 1410–1415.

[134] G. T. Grant, E. R. Morris, D. A. Rees, P. J. Smith and D. Thom, *FEBS Letters*, 1973, **32**, 195–198.

[135] S. Hall, *Advanced Materials*, 2006, **18**, 487–490.

[136] D. C. Green, M. R. Lees and S. R. Hall, *Chemical Communications*, 2013, **49**, 2974–2976.

[137] R. Boston, Z. Schnepp, Y. Nemoto, Y. Sakka and S. R. Hall, *Science*, 2014, **344**, 623–626.

[138] D. C. Green, R. Boston, S. Glatzel, M. R. Lees, S. C. Wimbush, J. Potticary, W. Ogasawara and S. R. Hall, *Advanced Functional Materials*, 2015, **25**, 4700–4707.

[139] Y.-Y. Kim, K. Hore, S. R. Hall, D. Walsh, D. Walsh, Y.-Y. Kim, K. Hore and S. R. Hall, *Small*, 2009, **5**, 913–918.

[140] A. A. Said and R. M. Hassan, *Polymer Degradation and Stability*, 1993, **39**, 393–397.

[141] E. Culverwell, S. C. Wimbush and S. R. Hall, *Chem. Commun.*, 2008, 1055–1057.

[142] M. Darroudi, M. Bagherpour, H. A. Hosseini and M. Ebrahimi, *Ceramics International*, 2016, **42**, 3816–3819.

[143] R. Boston, Z. Schnepp, Y. Nemoto, Y. Sakka and S. R. Hall, *Science*, 2014, **344**, 623–626.

[144] M. Y. Lui, L. Crowhurst, J. P. Hallett, P. A. Hunt, H. Niedermeyer and T. Welton, *Chemical Science*, 2011, **2**, 1491–1496.

[145] K. Ghandi, *Green and Sustainable Chemistry*, 2014, **04**, 44–53.

[146] T. P. T. Pham, C.-W. Cho and Y.-S. Yun, *Water Research*, 2010, **44**, 352–372.

[147] D. Zhao, Y. Liao and Z. Zhang, *CLEAN – Soil, Air, Water*, 2007, **35**, 42–48.

[148] S. S. de Jesus and R. M. Filho, *Renewable and Sustainable Energy Reviews*, 2022, **157**, 112039.

[149] A. P. Abbott, D. Boothby, G. Capper, D. L. Davies and R. K. Rasheed, *Journal of the American Chemical Society*, 2004, **126**, 9142–9147.

[150] E. L. Smith, A. P. Abbott and K. S. Ryder, *Chemical Reviews*, 2014, **114**, 11060–11082.

[151] Q. Zhang, K. D. O. Vigier, S. Royer and F. Jérôme, *Chemical Society reviews*, 2012, **41**, 7108–46.

[152] D. Carriazo, M. C. Serrano, M. C. Gutiérrez, M. L. Ferrer and F. del Monte, *Chemical Society Reviews*, 2012, **41**, 4996–5014.

[153] H. G. Liao, Y. X. Jiang, Z. Y. Zhou, S. P. Chen and S. G. Sun, *Angewandte Chemie - International Edition*, 2008, **47**, 9100–9103.

[154] E. R. Cooper, C. D. Andrews, P. S. Wheatley, P. B. Webb, P. Wormald and R. E. Morris, *Nature 2004 430:7003*, 2004, **430**, 1012–1016.

[155] D. C. Green, S. Glatzel, A. M. Collins, A. J. Patil and S. R. Hall, *Advanced Materials*, 2012, **24**, 5767–5772.

[156] Y. Song, Y. Li, T. Zhao, Y. Wang, T. Cui, Y. Sheng, K. Zheng, X. Zhou, H. You and H. Zou, *Journal of Colloid and Interface Science*, 2017, **487**, 281–288.

[157] C. Zhang, J. Chen, Y. Zhou and D. Li, *The Journal of Physical Chemistry C*, 2008, **112**, 10083–10088.

[158] O. Gómez Rojas, I. Sudoh, T. Nakayama and S. R. Hall, *CrystEngComm*, 2018, **20**, 5814–5821.

[159] O. G. Rojas, T. Nakayama and S. R. Hall, *Ceramics International*, 2019, **45**, 8546–8552.

[160] O. Długosz, *Materials*, 2023, **16**, 627.

[161] J. Wei, K. Rong, X. Li, Y. Wang, Z.-A. Qiao, Y. Fang and S. Dong, *Nano Research*, 2022, **15**, 2756–2763.

[162] I. Moraes, G. Evans, J. Sanchez-Weatherby, S. Newstead and P. D. S. Stewart, *Biochimica et Biophysica Acta (BBA) - Biomembranes*, 2014, **1838**, 78–87.

[163] H. N. Chapman, P. Fromme, A. Barty, T. A. White, R. A. Kirian, A. Aquila, M. S. Hunter, J. Schulz, D. P. DePonte, U. Weierstall, R. B. Doak, F. R. N. C. Maia, A. V. Martin, I. Schlichting, L. Lomb, N. Coppola, R. L. Shoeman, S. W. Epp, R. Hartmann, D. Rolles, A. Rudenko, L. Foucar, N. Kimmel, G. Weidenspointner, P. Holl, M. Liang, M. Barthelmess, C. Caleman, S. Boutet, M. J. Bogan, J. Krzywinski, C. Bostedt, S. Bajt, L. Gumprecht, B. Rudek, B. Erk, C. Schmidt, A. Hömke, C. Reich, D. Pietschner, L. Strüder, G. Hauser, H. Gorke, J. Ullrich, S. Herrmann, G. Schaller, F. Schopper, H. Soltau, K.-U. Kühnel, M. Messerschmidt, J. D. Bozek, S. P. Hau-Riege, M. Frank, C. Y. Hampton, R. G. Sierra, D. Starodub, G. J. Williams, J. Hajdu, N. Timneanu, M. M. Seibert, J. Andreasson, A. Rocker, O. Jönsson, M. Svenda, S. Stern, K. Nass, R. Andritschke, C.-D. Schröter, F. Krasniqi, M. Bott, K. E. Schmidt, X. Wang, I. Grotjohann, J. M. Holton, T. R. M. Barends, R. Neutze, S. Marchesini, R. Fromme, S. Schorb, D. Rupp, M. Adolph, T. Gorkhover, I. Andersson, H. Hirsemann, G. Potdevin, H. Graafsma, B. Nilsson and J. C. H. Spence, *Nature*, 2011, **470**, 73.

[164] M. J. Bogan, *Analytical Chemistry*, 2013, **85**, 3464–3471.

[165] M. Gemmi, E. Mugnaioli, T. E. Gorelik, U. Kolb, L. Palatinus, P. Boullay, S. Hovmöller and J. P. Abrahams, *ACS Central Science*, 2019, **5**, 1315–1329.

[166] A. A. Bunaciu, E. gabriela Udriştioiu and H. Y. Aboul-Enein, *Critical Reviews in Analytical Chemistry*, 2015, **45**, 289–299.

[167] D. G. Porob and T. N. G. Row, *Journal of Chemical Sciences*, 2001, **113**, 435–444.

[168] A. Guinier, *X-ray Diffraction in crystals, imperfect crystals, and amorphous bodies*, W. H. Freeman, 1963.

[169] N. L. Wu and J. Phillips, *Surface Science*, 1987, **184**, 463–482.

[170] A. R. Bushroa, R. G. Rahbari, H. H. Masjuki and M. R. Muhamad, *Vacuum*, 2012, **86**, 1107–1112.

[171] E. H. K. Stelzer, *Nature*, 2002, **417**, 806–807.

[172] R. Heintzmann and G. Ficz, *Briefings in Functional Genomics and Proteomics*, 2006, **5**, 289–301.

[173] D. Chescoe and P. Goodhew, *The Operation of Transmission and Scanning Electron Microscopes*, Oxford University Press, 1990.

[174] J. I. Goldstein, D. E. Newbury, P. Echlin, D. C. Joy, A. D. Romig, C. E. Lyman, C. Fiori and E. Lifshin, *Scanning Electron Microscopy and X-Ray Microanalysis*, Springer US, 1992, p. 1 online resource (829 pages).

[175] K. L. Scrivener, *Cement and Concrete Composites*, 2004, **26**, 935–945.

[176] H. Seiler, *Journal of Applied Physics*, 1983, **54**, R1–R18.

[177] I. Andrusenko, V. Hamilton, E. Mugnaioli, A. Lanza, C. Hall, J. Potticary, S. R. Hall and M. Gemmi, *Angewandte Chemie - International Edition*, 2019, **58**, 10919–10922.

[178] R. L. Fagaly, *Review of Scientific Instruments*, 2006, **77**, 101101.

[179] E. J. Luke, J. Potticary, L. R. Terry, H. V. Doan, R. Hinoplen, S. Cross, V. P. Ting, S. Friedemann and S. R. Hall, *Nanoscale Advances*, 2022, **4**, 3101–3108.

[180] E. J. Luke, J. Potticary, S. Friedemann and S. R. Hall, *Dalton Transactions*, 2023, **52**, 3188–3194.

[181] E. M. Seibel, J. H. Roudebush, H. Wu, Q. Huang, M. N. Ali, H. Ji and R. J. Cava, *Inorganic Chemistry*, 2013, **52**, 13605–13611.

[182] A. Zelati, A. Amirabadizadeh and A. Kompany, *International Journal of Chemical Engineering and Applications*, 2011, 299–303.

[183] D. Wang, J. Song, S. Lin, J. Wen, C. Ma, Y. Yuan, M. Lei, X. Wang, N. Wang and H. Wu, *Advanced Functional Materials*, 2019, **29**, 1901009.

[184] N. Doebelin and R. Kleeberg, *Journal of Applied Crystallography*, 2015, **48**, 1573–1580.

[185] K. Momma and F. Izumi, *Journal of Applied Crystallography*, 2008, **41**, 653–658.

[186] M. Klinger, *Journal of Applied Crystallography*, 2017, **50**, 1226–1234.

[187] A. Agrawal and A. Choudhary, *APL Materials*, 2016, **4**, 053208.

[188] C. Hardin, T. V. Pogorelov and Z. Luthey-Schulten, *Current Opinion in Structural Biology*, 2002, **12**, 176–181.

[189] A. R. Oganov and C. W. Glass, *The Journal of chemical physics*, 2006, **124**, 244704.

[190] R. Matsumoto, Z. Hou, H. Hara, S. Adachi, H. Takeya, T. Irifune, K. Terakura and Y. Takano, *Applied Physics Express*, 2018, **11**, 093101.

[191] R. Matsumoto, Z. Hou, M. Nagao, S. Adachi, H. Hara, H. Tanaka, K. Nakamura, R. Murakami, S. Yamamoto, H. Takeya, T. Irifune, K. Terakura and Y. Takano, *Science and Technology of Advanced Materials*, 2018, **19**, 909–916.

[192] H. Liu, I. I. Naumov, Z. M. Geballe, M. Somayazulu, J. S. Tse and R. J. Hemley, *Physical Review B*, 2018, **98**, 100102.

[193] A. P. Drozdov, P. P. Kong, V. S. Minkov, S. P. Besedin, M. A. Kuzovnikov, S. Mozaffari, L. Balicas, F. F. Balakirev, D. E. Graf, V. B. Prakapenka, E. Greenberg, D. A. Knyazev, M. Tkacz and M. I. Eremets, *Nature*, 2019, **569**, 528–531.

[194] S. M. O'Mahony, W. Ren, W. Chen, Y. X. Chong, X. Liu, H. Eisaki, S. Uchida, M. H. Hamidian and J. C. Davis, *Proceedings of the National Academy of Sciences of the United States of America*, 2022, **119**, e2207449119.

[195] K. P. Murphy, *Machine learning : a probabilistic perspective*, MIT Press, 2012, p. 1067.

[196] J. Padmanabhan and M. J. Johnson Premkumar, *IETE Technical Review*, 2015, **32**, 240–251.

[197] I. Kononenko, *Artificial Intelligence in Medicine*, 2001, **23**, 89–109.

[198] E. Gawehn, J. A. Hiss and G. Schneider, *Molecular Informatics*, 2016, **35**, 3–14.

[199] D. Xue, P. V. Balachandran, J. Hogden, J. Theiler, D. Xue and T. Lookman, *Nature Communications*, 2016, **7**, 1–9.

[200] S. Curtarolo, G. L. Hart, M. B. Nardelli, N. Mingo, S. Sanvito and O. Levy, *Nature Materials 2013 12:3*, 2013, **12**, 191–201.

[201] V. Stanev, C. Oses, A. G. Kusne, E. Rodriguez, J. Paglione, S. Curtarolo and I. Takeuchi, *npj Computational Materials*, 2018, **4**, 29.

[202] E. Gehle and H. Sabrowsky, *Zeitschrift für Naturforschung B*, 1975, **30**, 659–661.

[203] M. R. Norman, *Science*, 2011, **332**, 196–200.

[204] I. V. Puzdrjakova, R. B. Macquart, M. D. Smith and H. C. Z. Loye, *Acta Crystallographica Section E: Structure Reports Online*, 2007, **63**, i95–i96.

[205] K. Takada, H. Sakurai, E. Takayama-Muromachi, F. Izumi, R. A. Dilanian and T. Sasaki, *Nature*, 2003, **422**, 53–55.

[206] A. J. Brown, Q. Xia, M. Avdeev, B. J. Kennedy and C. D. Ling, *Inorganic Chemistry*, 2019, **58**, 13881–13891.

[207] A. Jain, S. P. Ong, G. Hautier, W. Chen, W. D. Richards, S. Dacek, S. Cholia, D. Gunter, D. Skinner, G. Ceder and K. A. Persson, *APL Materials*, 2013, **1**, 011002.

[208] H. Yamane, H. Takahashi, T. Kajiwara and M. Shimada, *Acta Crystallographica, Section C: Crystal Structure Communications*, 2000, **56**, 1177–1178.

[209] C. Wang, G. Zhang, W. Qu, H. Wang, S. Zhang and C. Deng, *Journal of Materials Chemistry A*, 2019, **7**, 1797–1809.

[210] *Press release: The Nobel Prize in Chemistry 2019*, 2019, `https://www.nobelprize.org/prizes/chemistry/2019/press-release/`.

[211] R. Aalund, B. Endreddy and M. Pecht, *Frontiers in Chemical Engineering*, 2022, **4**, 12.

[212] Q. Wang, B. Mao, S. I. Stoliarov and J. Sun, *Progress in Energy and Combustion Science*, 2019, **73**, 95–131.

[213] J. Zhang, L. Zhang, F. Sun and Z. Wang, *IEEE Access*, 2018, **6**, 23848–23863.

[214] M. Loveridge, G. Remy, N. Kourra, R. Genieser, A. Barai, M. Lain, Y. Guo, M. Amor-Segan, M. Williams, T. Amietszajew, M. Ellis, R. Bhagat and D. Greenwood, *Batteries*, 2018, **4**, 3.

[215] A. Lee, *Lithium Crisis Threatens Electric Car Boom After 500Bloomberg*, 2022, `https://www.bloomberg.com/news/features/2022-05-25/lithium-the-hunt-for-the-wonder-metal-fueling-evs`.

[216] J. Y. Hwang, S. T. Myung and Y. K. Sun, *Chemical Society Reviews*, 2017, **46**, 3529–3614.

[217] M. Sawicki and L. L. Shaw, *RSC Advances*, 2015, **5**, 53129–53154.

[218] D. S. Bhange, G. Ali, D.-H. Kim, D. A. Anang, T. J. Shin, M.-G. Kim, Y.-M. Kang, K. Y. Chung and K.-W. Nam, *Journal of Materials Chemistry A*, 2017, **5**, 1300–1310.

[219] D. Yuan, X. Liang, L. Wu, Y. Cao, X. Ai, J. Feng, H. Yang, D. Yuan, L. Wu, Y. Cao, X. Ai, H. Yang, X. Liang and J. Feng, *Advanced Materials*, 2014, **26**, 6301–6306.

[220] J. Ma, S.-H. Bo, L. Wu, Y. Zhu, C. P. Grey and P. G. Khalifah, *Chemistry of Materials*, 2015, **27**, 2387–2399.

[221] E. Zemlyanushin, K. Pfeifer, A. Sarapulova, M. Etter, H. Ehrenberg and S. Dsoke, *Energies*, 2020, **13**, 6498.

[222] J. Liu, L. Yin, L. Wu, J. Bai, S. M. Bak, X. Yu, Y. Zhu, X. Q. Yang and P. G. Khalifah, *Inorganic Chemistry*, 2016, **55**, 8478–8492.

[223] B. E. Warren, *Physical Review*, 1941, **59**, 693–698.

[224] M. Leoni, *Zeitschrift für Kristallographie*, 2008, **223**, 561–568.

[225] D. Walsh, S. C. Wimbush and S. R. Hall, *Superconductor Science and Technology*, 2009, **22**, 015026.

[226] Y. Y. Kim, C. Neudeck and D. Walsh, *Polymer Chemistry*, 2010, **1**, 272–275.

[227] L. Miersch, M. Schlesinger, R. W. Troff, C. A. Schalley, T. Rüffer, H. Lang, D. Zahn and M. Mehring, *Chemistry – A European Journal*, 2011, **17**, 6985–6990.

[228] Y. Hoshino, T. Utsunomiya and O. Abe, *Bulletin of the Chemical Society of Japan*, 1981, **54**, 1385–1391.

[229] D. A. Nissen and D. E. Meeker, *Inorganic Chemistry*, 1983, **22**, 716–721.

[230] R. Bradshaw and D. Meeker, *Solar Energy Materials*, 1990, **21**, 51–60.

[231] M. Saiduzzaman, S. Akutsu, N. Kumada, T. Takei, S. Yanagida, H. Yamane and Y. Kusano, *Inorganic Chemistry*, 2020, **59**, 4950–4960.

[232] A. Vu, Y. Qian, A. Stein, A. Vu, Y. Qian and A. Stein, *Advanced Energy Materials*, 2012, **2**, 1056–1085.

[233] B. Neu, R. Wenby and H. J. Meiselman, *Biophysical Journal*, 2008, **95**, 3059–3065.

[234] X. Li, F. Deng, Y. Hua, A. Qiu, C. Yang and S. Cui, *Carbohydrate Polymers*, 2008, **72**, 160–168.

[235] R. D. Shannon, *Acta Crystallographica Section A*, 1976, **32**, 751–767.

[236] M. Scheikowski and H. Müller-Buschbaum, *ZAAC - Journal of Inorganic and General Chemistry*, 1994, **620**, 155–159.

[237] C. C. Pye, A. D. Hendsbee, K. D. Nizio, B. L. Goodall, J. P. Ferguson, J. D. Masuda and J. A. Clyburne, *Polyhedron*, 2021, **197**, 115040.

[238] J. Macklin, *M.Sc. thesis*, University of Bristol, 2020.

[239] L. L. Noto, D. Poelman, V. R. Orante-Barrón, H. C. Swart, L. E. Mathevula, R. Nyenge, M. Chithambo, B. M. Mothudi and M. S. Dhlamini, *Physica B: Condensed Matter*, 2018, **535**, 268–271.

[240] V. Kahlenberg, R. X. Fischer and J. B. Parise, *Journal of Solid State Chemistry*, 2000, **154**, 612–618.

[241] H. Christodoulou, *M.Sc. thesis*, University of Bristol, 2020.

[242] S. Haughton, *M.Sc. thesis*, University of Bristol, 2022.

[243] J. Potticary, E. J. Luke, E. M. S. Christodoulou, R. Davies, S. Haughton, C. Feuillet-Palma, E. Recoba-Pawlowski, B. Leridon, S. Griffin and S. R. Hall, *Small Structures*, 2023.

[244] L. Eeckhout, *IEEE Micro*, 2017, **37**, 4–5.

[245] J. Ko, R. Berger, H. Lee, H. Yoon, J. Cho and K. Char, *Chemical Society Reviews*, 2021, **50**, 3585–3628.

[246] T. Ito and S. Okazaki, *Nature*, 2000, **406**, 1027–1031.

[247] M. S. Krishna, S. Singh, M. Batool, H. M. Fahmy, K. Seku, A. E. Shalan, S. Lanceros-Mendez and M. N. Zafar, *Materials Advances*, 2022.

[248] I. Holzman and Y. Ivry, *Advanced Quantum Technologies*, 2019, **2**, 1800058.

[249] R. M. Lutchyn, E. P. A. M. Bakkers, L. P. Kouwenhoven, P. Krogstrup, C. M. Marcus and Y. Oreg, *Nature Reviews Materials*, 2018, **3**, 52–68.

[250] N. Abid, A. M. Khan, S. Shujait, K. Chaudhary, M. Ikram, M. Imran, J. Haider, M. Khan, Q. Khan and M. Maqbool, *Advances in Colloid and Interface Science*, 2022, **300**, 102597.

[251] H. D. Yu, M. D. Regulacio, E. Ye and M. Y. Han, *Chemical Society Reviews*, 2013, **42**, 6006–6018.

[252] M. D. Platzer and J. F. Sargent, *Current Politics and Economics of the United States, Canada and Mexico*, 2017, **19**, year.

[253] A. Biswas, I. S. Bayer, A. S. Biris, T. Wang, E. Dervishi and F. Faupel, *Advances in Colloid and Interface Science*, 2012, **170**, 2–27.

[254] A. Fasoli and W. Milne, *Materials Science in Semiconductor Processing*, 2012, **15**, 601–614.

[255] X. Jiang, T. Herricks and Y. Xia, *Nano Letters*, 2002, **2**, 1333–1338.

[256] M. Ek and M. A. Filler, *Accounts of Chemical Research*, 2018, **51**, 118–126.

[257] R. S. Wagner and W. C. Ellis, *Applied Physics Letters*, 1964, **4**, 89–90.

[258] K. S. Shankar and A. K. Raychaudhuri, *Materials Science and Engineering C*, 2005, **25**, 738–751.

[259] A. I. Persson, M. W. Larsson, S. Stenström, B. J. Ohlsson, L. Samuelson and L. R. Wallenberg, *Nature Materials*, 2004, **3**, 677–681.

[260] T. J. Trentler, K. M. Hickman, S. C. Goel, A. M. Viano, P. C. Gibbons and W. E. Buhro, *Science*, 1995, **270**, 1791.

[261] S. Rackauskas and A. G. Nasibulin, *ACS Applied Nano Materials*, 2020, **3**, 7314–7324.

[262] Z. A. C. Schnepp, S. C. Wimbush, S. Mann and S. R. Hall, *Advanced Materials*, 2008, **20**, 1782–1786.

[263] P. Badica, K. Togano, S. Awaji, K. Watanabe and H. Kumakura, *Superconductor Science and Technology*, 2006, **19**, 81–99.

[264] J. Potticary, *Ph.D. thesis*, University of Bristol, 2018.

[265] C. Sirtori, *Nature*, 2002, **417**, 132–133.

[266] V. Petrov, T. Kurner and I. Hosako, *IEEE Communications Magazine*, 2020, **58**, 28–33.

[267] Y. Huang, Y. Shen and J. Wang, *Engineering*, 2022.

[268] G. Valušis, A. Lisauskas, H. Yuan, W. Knap and H. G. Roskos, *Sensors*, 2021, **21**, 4092.

[269] D. Cimbri, J. Wang, A. Al-Khalidi and E. Wasige, *IEEE Transactions on Terahertz Science and Technology*, 2022, **12**, 226–244.

[270] S. Kumar, *IEEE Journal on Selected Topics in Quantum Electronics*, 2011, **17**, 38–47.

[271] R. Kleiner and H. Wang, *Journal of Applied Physics*, 2019, **126**, 171101.

[272] U. Welp, K. Kadowaki and R. Kleiner, *Nature Photonics*, 2013, **7**, 702–710.

[273] L. Ozyuzer, A. E. Koshelev, C. Kurter, N. Gopalsami, Q. Li, M. Tachiki, K. Kadowaki, T. Yamamoto, H. Minami, H. Yamaguchi, T. Tachiki, K. E. Gray, W.-K. Kwok and U. Welp, *Science*, 2007, **318**, 1291–1293.

[274] T. Kashiwagi, H. Kubo, K. Sakamoto, T. Yuasa, Y. Tanabe, C. Watanabe, T. Tanaka, Y. Komori, R. Ota, G. Kuwano, K. Nakamura, T. Katsuragawa, M. Tsujimoto, T. Yamamoto, R. Yoshizaki, H. Minami, K. Kadowaki and R. A. Klemm, *Superconductor Science and Technology*, 2017, **30**, 074008.

[275] G. R. Paz-Pujalt, *Physica C: Superconductivity*, 1990, **166**, 177–184.

[276] R. Ropp, *Group 14 (C, Si, Ge, Sn, and Pb) Alkaline Earth Compounds*, Elsevier, 2013, pp. 351–480.

[277] Z. Xia and D. Chen, *Journal of the American Ceramic Society*, 2010, **93**, 1397–1401.

[278] R. B. Lewis, P. Corfdir, H. Küpers, T. Flissikowski, O. Brandt and L. Geelhaar, *Nano Letters*, 2018, **18**, 2343–2350.

[279] D. A. Langs and C. R. Hare, *Chemical Communications (London)*, 1967, **4**, 890–891.

[280] E. A. Klop, A. J. M. Duisenberg and A. L. Spek, *Acta Crystallographica Section C Crystal Structure Communications*, 1983, **39**, 1342–1344.

[281] D. E. Hibbs, U. Kolitsch, P. Leverett, J. L. Sharpe and P. A. Williams, *Mineralogical Magazine*, 2002, **66**, 459–464.

[282] S. Li, I. Huskić, N. Novendra, H. M. Titi, A. Navrotsky and T. Friščić, *ACS Omega*, 2019, **4**, 5486–5495.

[283] H. Henstock, *Transactions of the Faraday Society*, 1933, **29**, 1101.

[284] G. M. McKelvy, G. L. Gilbert and C. McWherter, *Journal of Chemical Education*, 1998, **75**, 55–56.

[285] J. E. Brandenburg, M. D. Fox and R. H. Garcia, *Ethanol based gel fuel for a hybrid rocket engine*, US. Patent no US8101032B1, 2008.

[286] A. A. Levin, Y. I. Smolin and Y. F. Shepelev, *Journal of Physics: Condensed Matter*, 1994, **6**, 3539–3551.

[287] T. M. Shaw, S. A. Shivashankar, S. J. L. Placa, J. J. Cuomo, T. R. McGuire, R. A. Roy, K. H. Kelleher and D. S. Yee, *Physical Review B*, 1988, **37**, 9856–9859.

[288] Z. Zhang and D. Su, *Ultramicroscopy*, 2009, **109**, 766–774.

[289] J. W. Dunlop and P. Fratzl, *Scripta Materialia*, 2013, **68**, 8–12.

[290] J. Rouquerol, D. Avnir, C. W. Fairbridge, D. H. Everett, J. M. Haynes, N. Pernicone, J. D. F. Ramsay, K. S. W. Sing and K. K. Unger, *Pure and Applied Chemistry*, 1994, **66**, 1739–1758.

[291] P. Liu and G. Chen, *General Introduction to Porous Materials*, Elsevier, 2014, pp. 1–20.

[292] E. M. Flanigen, J. M. Bennett, R. W. Grose, J. P. Cohen, R. L. Patton, R. M. Kirchner and J. V. Smith, *Nature*, 1978, **271**, 512–516.

[293] M. E. Davis, *Nature*, 2002, **417**, 813–821.

[294] P. Z. Moghadam, A. Li, S. B. Wiggin, A. Tao, A. G. Maloney, P. A. Wood, S. C. Ward and D. Fairen-Jimenez, *Chemistry of Materials*, 2017, **29**, 2618–2625.

[295] J. L. Rowsell and O. M. Yaghi, *Microporous and Mesoporous Materials*, 2004, **73**, 3–14.

[296] N. Stock and S. Biswas, *Chemical Reviews*, 2012, **112**, 933–969.

[297] S. Dworakowska, D. Bogdał, F. Zaccheria and N. Ravasio, *Catalysis Today*, 2014, **223**, 148–156.

[298] T. D. Bennett, F. X. Coudert, S. L. James and A. I. Cooper, *Nature Materials 2021 20:9*, 2021, **20**, 1179–1187.

[299] A. Vinu, T. Mori and K. Ariga, *Science and Technology of Advanced Materials*, 2006, **7**, 753–771.

[300] R. Tournier, E. Beaugnon, O. Belmont, X. Chaud, D. Bourgault, D. Isfort, L. Porcar and P. Tixador, *Superconductor Science and Technology*, 2000, **13**, 886–895.

[301] D. M. Gokhfeld, M. R. Koblischka and A. Koblischka-Veneva, *Physics of Metals and Metallography*, 2020, **121**, 936–948.

[302] R. Liang, D. A. Bonn and W. N. Hardy, *Physical Review B - Condensed Matter and Materials Physics*, 2006, **73**, 180505.

[303] S. M. Khalil and A. Sedky, *Physica B: Condensed Matter*, 2005, **357**, 299–304.

[304] M. R. Koblischka and A. Koblischka-Veneva, *AIMS Materials Science*, 2018, **5**, 1199–1213.

[305] D. J. Merline, S. Vukusic and A. A. Abdala, *Polymer Journal*, 2013, **45**, 413–419.

[306] X. Liu, J. Hao and S. Gaan, *RSC Advances*, 2016, **6**, 74742–74756.

[307] H. Liao, H. Li, Y. Liu and Q. Wang, *Polymer International*, 2019, **68**, 410–417.

[308] W. Zhang, X. Zhai, T. Xiang, M. Zhou, D. Zang, Z. Gao and C. Wang, *Journal of Materials Science*, 2017, **52**, 73–85.

[309] S. Bône, C. Vautrin, V. Barbesant, S. Truchon, I. Harrison and C. Geffroy, *CHIMIA*, 2011, **65**, 177.

[310] Y. Feng and J. Yao, *Industrial & Engineering Chemistry Research*, 2018, **57**, 7322–7330.

[311] C. Ruan, K. Ai, X. Li and L. Lu, *Angewandte Chemie International Edition*, 2014, **53**, 5556–5560.

[312] X. Chen, J. A. Weibel and S. V. Garimella, *Industrial & Engineering Chemistry Research*, 2016, **55**, 3596–3602.

[313] D. de Leeuw, C. Mutsaers, R. Steeman, E. Frikkee and H. Zandbergen, *Physica C: Superconductivity and its Applications*, 1989, **158**, 391–396.

[314] R. E. Gladyshevskii and R. Flükiger, *Acta Crystallographica Section B: Structural Science*, 1996, **52**, 38–53.

[315] M. Onoda and M. Sato, *Solid State Communications*, 1988, **67**, 799–804.

[316] M. Kandasamy, S. Sahoo, S. K. Nayak, B. Chakraborty and C. S. Rout, *Journal of Materials Chemistry A*, 2021, **9**, 17643–17700.

[317] V. K. Tiwari and R. K. Singh, *Chemical Engineering Journal*, 2023, **471**, 144592.

[318] S. Yuan, X. Duan, J. Liu, Y. Ye, F. Lv, T. Liu, Q. Wang and X. Zhang, *Recent progress on transition metal oxides as advanced materials for energy conversion and storage*, 2021.

[319] Y. Gao, Y. Hu, C. Yao and S. Zhang, *Advanced Functional Materials*, 2022, **32**, year.

[320] K. Kajihara, K. Kanamori and A. Shimojima, *Journal of the Ceramic Society of Japan*, 2022, **130**, 22078.

[321]

[322] J. Richter and M. Ruck, *Molecules*, 2019, **25**, 78.

[323] B. Roter and S. V. Dordevic, *Physica C: Superconductivity and its Applications*, 2020, **575**, year.

[324] T. Konno, H. Kurokawa, F. Nabeshima, Y. Sakishita, R. Ogawa, I. Hosako and A. Maeda, *Physical Review B*, 2021, **103**, 14509.

[325] D. Li, K. Lee, B. Y. Wang, M. Osada, S. Crossley, H. R. Lee, Y. Cui, Y. Hikita and H. Y. Hwang, *Nature*, 2019, **572**, 624–627.

[326] R. Boston, P. Y. Foeller, D. C. Sinclair and I. M. Reaney, *Inorganic Chemistry*, 2017, **56**, 542–547.

[327] J. Nagamatsu, N. Nakagawa, T. Muranaka, Y. Zenitani and J. Akimitsu, *Nature*, 2001, **410**, 63–64.

[328] Z. Z. Sheng and A. M. Hermann, *Nature*, 1988, **332**, 138–139.

[329] S. N. Putilin, E. V. Antipov, O. Chmaissem and M. Marezio, *Nature*, 1993, **362**, 226–228.

[330] Y. Kamihara, H. Hiramatsu, M. Hirano, R. Kawamura, H. Yanagi, T. Kamiya and H. Hosono, *Journal of the American Chemical Society*, 2006, **128**, 10012–10013.

[331] Y. Kamihara, T. Watanabe, M. Hirano and H. Hosono, *Journal of the American Chemical Society*, 2008, **130**, 3296–3297.

[332] R. Zhi-An, L. Wei, Y. Jie, Y. Wei, S. Xiao-Li, Zheng-Cai, C. Guang-Can, D. Xiao-Li, S. Li-Ling, Z. Fang and Z. Zhong-Xian, *Chinese Physics Letters*, 2008, **25**, 2215–2216.

[333] F. C. Hsu, J. Y. Luo, K. W. Yeh, T. K. Chen, T. W. Huang, P. M. Wu, Y. C. Lee, Y. L. Huang, Y. Y. Chu, D. C. Yan and M. K. Wu, *Proceedings of the National Academy of Sciences of the United States of America*, 2008, **105**, 14262–14264.

[334] J.-F. Ge, Z.-L. Liu, C. Liu, C.-L. Gao, D. Qian, Q.-K. Xue, Y. Liu and J.-F. Jia, *Nature Materials*, 2015, **14**, 285–289.

[335] F. Steglich, J. Aarts, C. D. Bredl, W. Lieke, D. Meschede, W. Franz and H. Schäfer, *Physical Review Letters*, 1979, **43**, 1892–1896.

[336] H. R. Ott, H. Rudigier, Z. Fisk and J. L. Smith, *Physical Review Letters*, 1983, **50**, 1595–1598.

[337] C. Geibel, U. Ahlheim, C. D. Bredl, J. Diehl, A. Grauel, R. Helfrich, H. Kitazawa, R. Köhler, R. Modler, M. Lang, C. Schank, S. Thies, F. Steglich, N. Sato and T. Komatsubara, *Physica C: Superconductivity and its applications*, 1991, **185-189**, 2651–2652.

[338] C. Petrovic, P. G. Pagliuso, M. F. Hundley, R. Movshovich, J. L. Sarrao, J. D. Thompson, Z. Fisk and P. Monthoux, *Journal of Physics Condensed Matter*, 2001, **13**, L337.

[339] J. L. Sarrao, L. A. Morales, J. D. Thompson, B. L. Scott, G. R. Stewart, F. Wastin, J. Rebizant, P. Boulet, E. Colineau and G. H. Lander, *Nature*, 2002, **420**, 297–299.

[340] A. F. Hebard, M. J. Rosseinsky, R. C. Haddon, D. W. Murphy, S. H. Glarum, T. T. Palstra, A. P. Ramirez and A. R. Kortan, *Nature*, 1991, **350**, 600–601.

[341] K. Tanigaki, T. W. Ebbesen, S. Saito, J. Mizuki, J. S. Tsai, Y. Kubo and S. Kuroshima, *Nature*, 1991, **352**, 222–223.

APPENDIX

A

APPENDIX

Table A.1: Data of the various superconductors that have been discovered. Used to generate Figure 1.4.

| Material	Discovery date	T_c	Pressure at T_c	Type	Reference
Hg	1911	4.2	Ambient	Conventional	58
Pb	1913	7.2	Ambient	Conventional	58
Nb	1930	9.2	Ambient	Conventional	58
Nb_3Sn	1954	18.1	Ambient	Conventional	58
Nb_3Ge	1973	23.9	Ambient	Conventional	58
MgB_2	01/03/2001	39	Ambient	Conventional	327
H_2S	17/08/2015	203	155 GPa	Conventional	61
LaH_{10}	22/05/2019	250	170 GPa	Conventional	193
LaBaCuO	02/03/1986	30	Ambient	Cuprate	17
YBaCuO	02/03/1987	92	Ambient	Cuprate	76
$Bi_2Sr_2CuO_6$	30/06/1987	22	Ambient	Cuprate	88
$Bi_2Sr_2CaCu_2O_{8+x}$	02/02/1988	105	Ambient	Cuprate	89
TlCaBaCuO	10/03/1988	120	Ambient	Cuprate	328
$HgBa_2CuO_{4+x}$	18/03/1993	94	Ambient	Cuprate	329
$HgBa_2Ca_2Cu_3O_{1+x}$	04/03/1994	133	Ambient	Cuprate	78
$HgBaCa_{m-1}Cu_mO_2$	01/08/1994	164	45 GPa	Cuprate	79
LaFeAsO	16/07/2006	4	Ambient	Iron Pnictide / Chalcogenide	330
LaOFFeAsO	23/02/2008	26	Ambient	Iron Pnictide / Chalcogenide	331
$Sm_{[O1-xFx]}FeAs$	24/04/2008	55	Ambient	Iron Pnictide / Chalcogenide	332
FeSe	28/07/2008	8	Ambient	Iron Pnictide / Chalcogenide	333
FeSe thin film	24/11/2014	100	Ambient	Iron Pnictide / Chalcogenide	334
$CeCu_2Si_2$	17/12/1979	0.5	Ambient	Heavy fermion	335
UBe_{13}	16/05/1983	0.85	Ambient	Heavy fermion	336
UPd_2Al_3	01/12/1991	2	Ambient	Heavy fermion	337
$CeCoIn_5$	29/03/2000	2.3	Ambient	Heavy fermion	338
$PuCoGa_5$	21/11/2002	18	Ambient	Heavy fermion	339
K_3C_{60}	18/04/1991	18	Ambient	Organic / doped	340
$Cs_xRb_yC_{60}$	18/07/1991	33	Ambient	Organic / doped	341
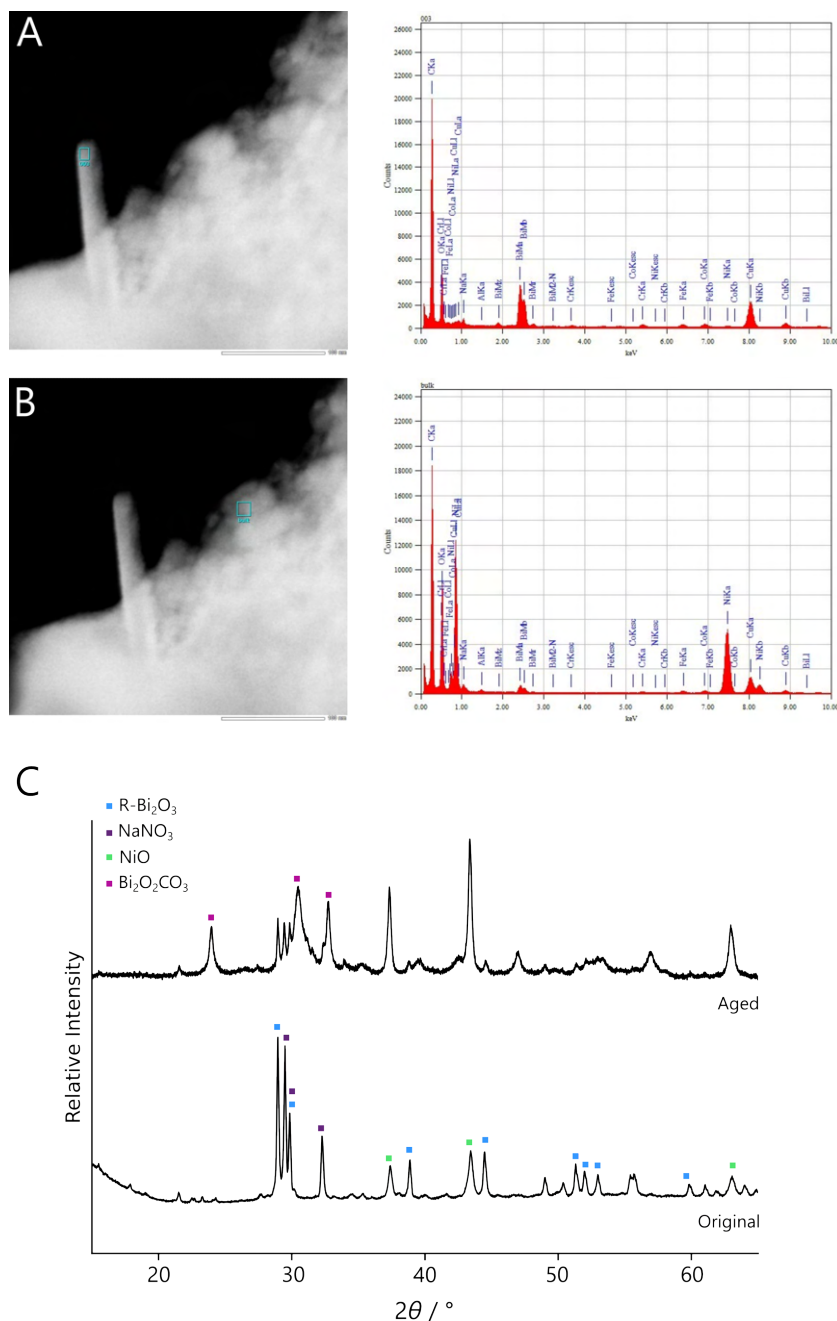
Figure A.1: a) and b) EDXA of two main features observed in the NNB sample synthesised at 600 °C, where a) is a flakey material and observed to consist mainly of Bismuth and Oxygen, and b) is the bulk material observed consist of mainly nickel and oxygen. c)Indexed powder X-ray diffraction pattern of the NNB sample synthesised at 600 °C (bottom) at time of synthesis and (top) after ageing for 1 year.
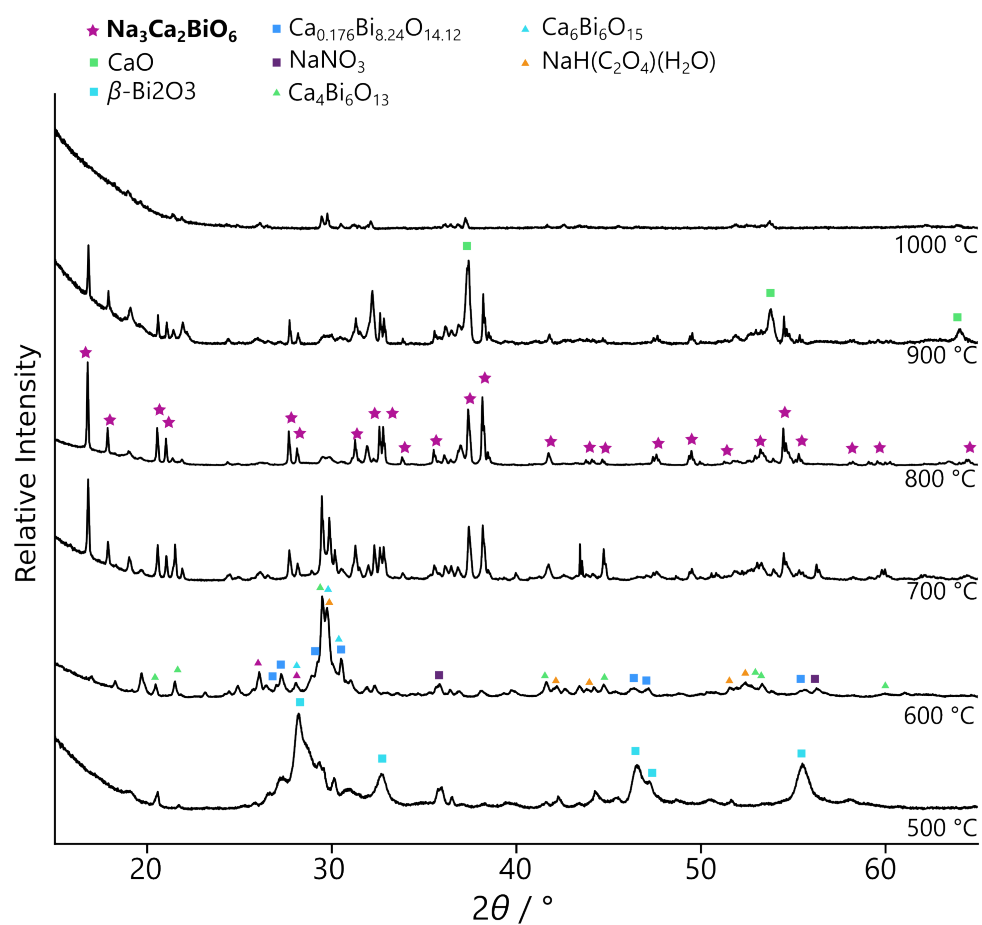
Figure A.2: Indexed powder X-ray diffraction pattern of the NCB samples synthesised with the 'high fraction' dextran
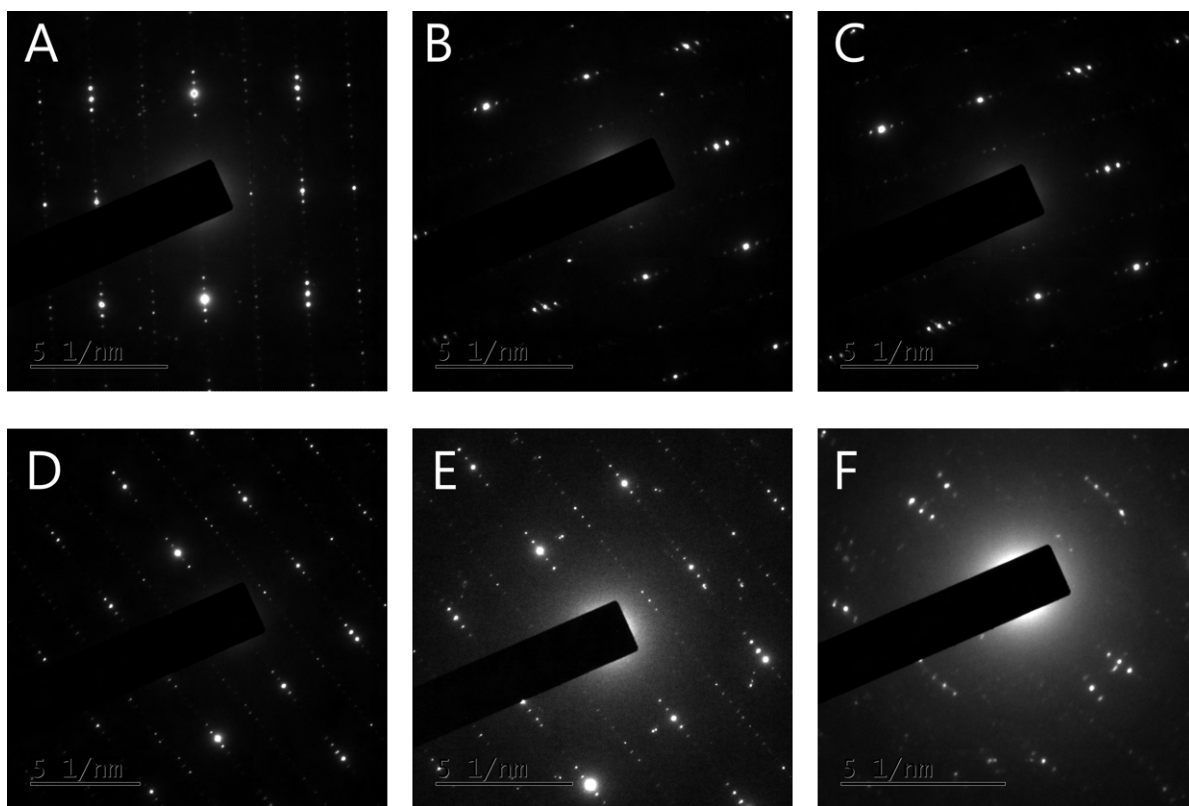
Figure A.3: Additional selected area electron diffraction data from the same sample as presented in Figure 4.18. The details of the indexed samples are presented in table 4.2.
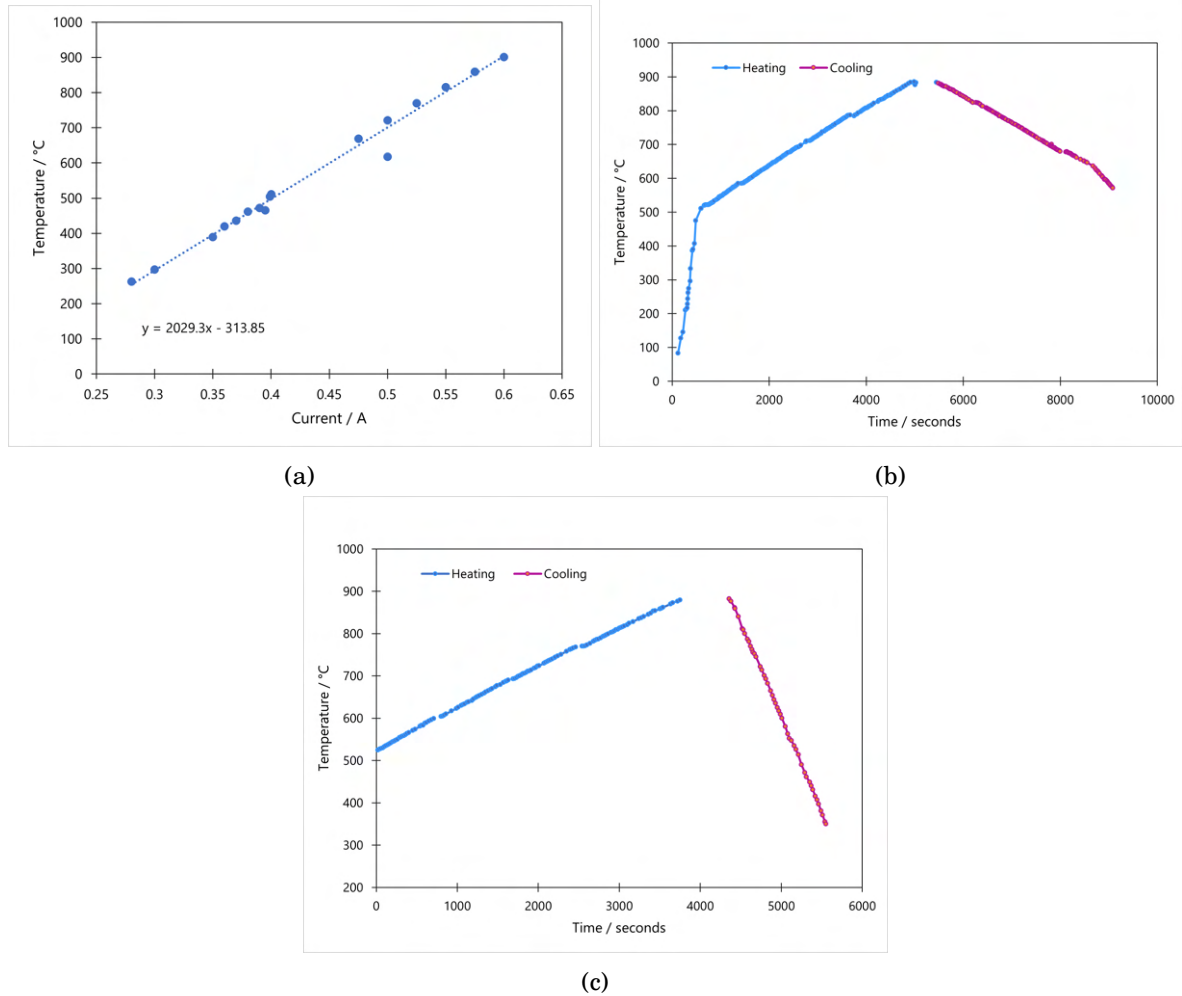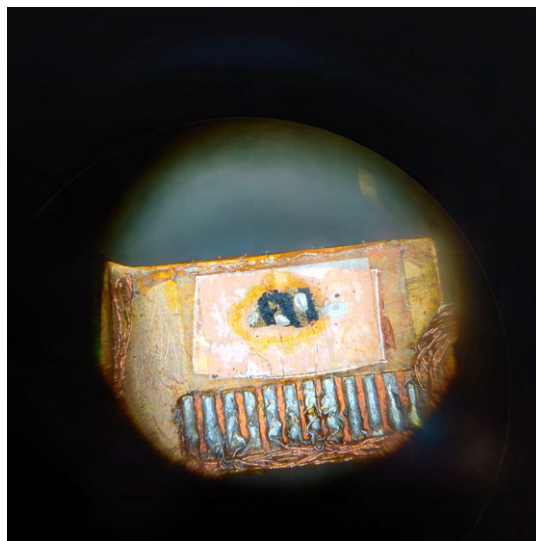
(a)

(b)

(c)

Figure A.4: a) Plot of temperature against current as a calibration for the heating stage. b) and c) Plots of temperature against time for the heating stage experiments, where (b) is the sample where the cooling rate was slow and (c) is the sample with a faster cooling rate.
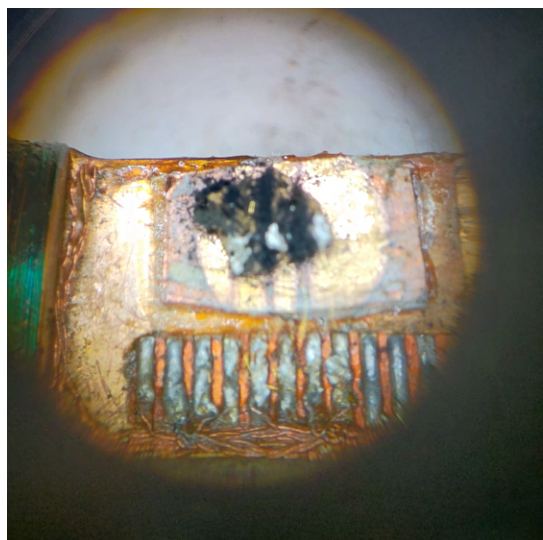
(a)   (b)

Figure A.5: Photos of the setup for the (a) 2-point resistance measurement for Y-123 sponge. (b) 4-point measurement of the annealed Y-123 sponge.

(a)   (b)

Figure A.6: Photos of the setup for the (a) 4-point resistance measurement for Bi-2212 sponge. (b) 4-point measurement of the annealed Bi-2212 sponge